Characterisation and functional analysis of actin cytoskeleton components and development of a novel hydrostatic pressure live cell imaging system.

Thesis submitted to the University of Kent for the degree of Doctor of Philosophy (Ph.D.) in the faculty of Science, Technology and Medical studies.

2017

Holly Brooker

Declaration

No part of this thesis has been submitted in support of an application for any degree qualification from the University of Kent or any other University or Institute of learning.

Acknowledgments

Firstly, I would like to express my sincere gratitude to my principle supervisor Dr Dan Mulvihill for the continuous support of my Ph.D. study and related research, for his patience, motivation, and immense knowledge. I would also like to thank my supervisors; Professor Mike Geeves and Dr Jenny Tullet for all of their expert guidance in addition to all of my fellow lab-mates and collaborators.

A special thank you to my parents, brothers, family and friends for their love and support throughout my entire education and to my wonderful boyfriend Jonathan for all of his love and encouragement.

Abstract

The main aims of this project were to use a variety of techniques to study various components of the actin cytoskeleton using *Caenorhabditis elegans* and *Schizosaccharomyces pombe,* in addition to developing a novel hydrostatic pressure imaging system.

The function and localisation of the *C. elegans* class I myosins: HUM-1 and HUM-5, were first explored using fluorescent protein fusions and phenotype analysis. The impact of a conserved phosphorylation event on myosin Ie function and localisation was then examined in *C. elegans* and *S. pombe* HUM-1 and Myo1 respectively. The results show HUM-1 and HUM-5 are non-essential, with HUM-1 expressed in a variety of tissues whereas HUM-5 was expressed exclusively in the nervous system. Loss of HUM-1 reduces maximal brood size, inducing delayed embryo release. The conserved serine residue is required for the function and localisation of both HUM-1 and Myo1. Mutations of the residue altered HUM-1 localisation in a tissue specific manner and abolished Myo1 membrane association in addition to inducing spore formation.

In vitro and *in vivo* studies were next undertaken to explore the impact of fluorescent protein fusions and temperature sensitive mutations upon the the stability and function of *S. pombe* tropomyosin. While both Ts mutants, Cdc8-27 and Cdc8-110, had a two-step thermal unfolding transition lower than that of wild-type Cdc8, fluorescent fusions did not impact stability. Amino- terminal fusions however, mimic acetylation whereas carboxyl terminal fusions abolished polymerisation, localisation and functionality. The final part of this project used a methodical approach to develop a hydrostatic imaging system that could be used to follow fluorescently labelled protein dynamics in a live cell context. Preliminary data revealed the application of 100 bar of pressure induced a cell cycle delay in both *S. pombe* and *Candida albicans,* however the current limitations of the system make it incompatible with fluorescence microscopy.

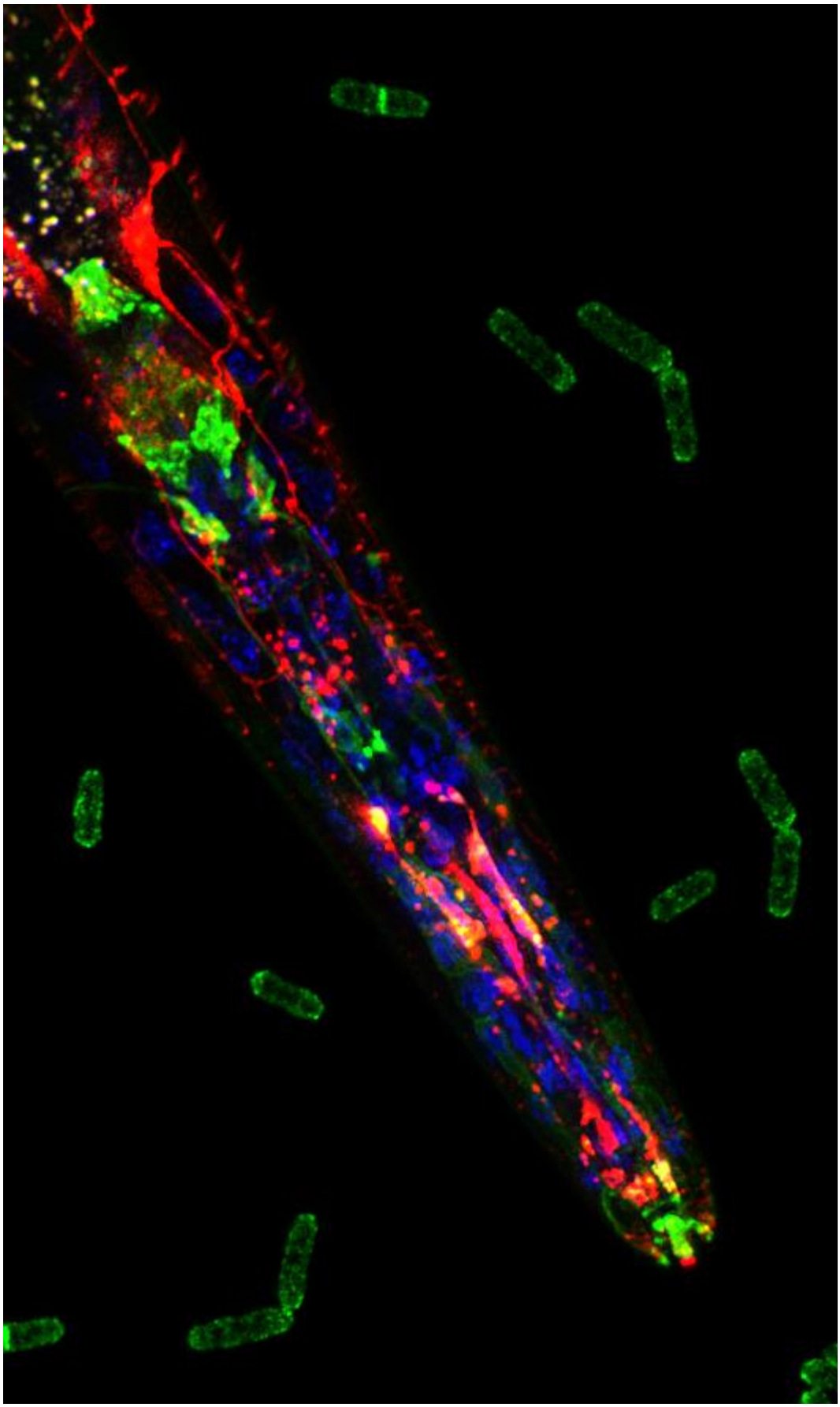

Table of Contents

List of figures and tables

List of abbreviations

Aa: Amino acids
ABP: Actin binding proteins
Ac-CoA: Acetyl-coenzyme A
ADF: Actin depolymerising factor
Arp: Actin-related protein
ATP: Adenosine triphosphate
BSA: Bovine serum albumin
C- terminus: Carboxyl terminus
Ca^{2+}: Calcium
CAR: Contractile acto-myosin ring
Cer3: Cerulean3
CD: Circular dichroism
CGC: Caenorhabditis genetics centre
CI: Chemotaxis index
cSt: Centistokes
dH_20: Deionised water
DNA: Deoxyribonucleic acid
EMMG: Edinburgh minimal medium with glutamic acid
ER: Endoplasmic reticulum
F-actin: Filamentous actin
FH: Formin homology domain
FP: Fluorescent protein
FPLC: Fast protein liquid chromatography
FT: Flow through
FUDR: 5-fluoro-2′-deoxyuridine
G0: Resting phase
G1: Gap phase one
G2: Gap phase two
G418: Geneticin
G-actin: Globular actin
GFP: Green fluorescent protein

GTP: Guanosine-5'-triphosphate

HEK: Human embryonic kidney cells

HMW: High molecular weight

HUM: Human unconventional myosin

IPTG: Isopropyl-β-D-1 thiogalactopyranoside

kanMX: Kanamycin

kDa: Kilodalton

LB: Luria bertani broth

LMW: Low molecular weight

MAPs: Microtubule associated proteins

M phase: Mitosis

Mb: Mega basepairs

mCh: mCherry

MOPS: 3-(N-morpholino) propanesulfonic acid

MTs: Microtubules

MTOC: Microtubule organising centre

NA: Numerical apertures

N terminus: Amino terminus

Nat: N-a-acetyltransferase

NGM: Nematode growth medium

OD_{260}: Optical density at 260 nm

OD_{280}: Optical density at 280 nm

OD_{600}: Optical density at 600 nm

ORF: Open reading frame

PBS: Phosphate-buffered saline

PCR: Polymerase chain reaction

PH: Pleckstrin-homolgy domain

PHYRE2: Protein Homology/analogY Recognition Engine V 2.0

PTMs: Post-translational modifications

RPM: Reps per minute

S phase: Synthesis phase

SC: Synthetic complete medium

SDS-PAGE: sodium dodecyl sulfate polyacrylamide gel electrophoresis

SPB: Spindle pole body

Sp-Ut: Spermathecal – uterine valve

SH3: Src-homolgy domain

TbsMTs: Tubular body singlet microtubules

TCA: Trichloroacetic acid

TH: Tail-homology domain

T_m: Mid-point melting temperature

Tpm: Tropomyosin

Ut: Uterine toroid epithelial cells

Utse: Uterine seam-cell

UV: Ultra violet

V: Vaults

WASp: Wiskott–Aldrich Syndrome protein

WT: Wild type

YES: Yeast extract plus supplements

ΔA: Differential absorption

Chapter 1: Introduction

Discovered by Robert Hooke in 1665, the cell is the most basic structural and functional unit of all living organisms (Gest 2009). Believed to be descended from a single ancestral cell three to four billion years ago, cells can be biologically classified into the three domains; archaea, bacteria and eukaryote (Woese & Fox 1977; Cooper 2000). The first two domains archaea and bacteria, are single celled prokaryotes with relatively simple cytological properties whereas the third domain eukaryote, is characterised by a high degree of cellular complexity and forms an in-exhaustive list of organisms (Spang et al. 2015).

Highly conserved throughout all eukaryotes, cells are involved in maintaining structure and stability as well as providing an ideal environment for critical processes such as the production of energy, gas exchange and genetic replication (Cooper 2000). Architecturally complex, eukaryotes are composed of one or more cells containing numerous internal organelles and structures that are organised into discrete interior compartments (Alberts et al. 2014). Contained within a membrane bound nucleus, the genetic material of all eukaryotes encodes the information required for each cell to grow and divide and is therefore central to heredity. As cells can only arise by the division of existing cells, it is essential that the replication of the genetic material and segregation into the two new daughter cells is a highly controlled and tightly regulated process (Morgan 2007).

1.1 The cell cycle

The eukaryotic cell cycle is a highly complex sequence of cellular events that involves cell growth, DNA replication, distribution of duplicated chromosomes and cell division (Smith 1982). With each stage of the process typically defined on the basis of chromosomal events, the cell cycle can be divided into two major phases: Interphase in which the new DNA is synthesised and the chromosomes are replicated; and mitosis, during which the chromosomes are equally distributed into two nuclei in preparation for cell division (O'Conner, C. 2008; Alberts, B et al 2002).

With 95% of the cell cycle spent in interphase, this period can be further divided into three discrete phases: gap phase 1 (G1); synthesis phase (S); and gap phase 2 (G2) (Smith 1982) (Figure 1.1). Characterised by active protein synthesis, G1 is a relatively short phase during which the cell grows in size and is primed for DNA replication. In mid to late G1 the cell reaches its first major checkpoint known as the G1/S phase checkpoint (Morgan 2007). If conditions are un-favourable, insufficient growth has occurred or a specific threat to genome integrity is perceived, the cell is signalled to exit the cell cycle and moves into a state of dormancy known as GO phase. If, however the cell has met the size/ nutritional requirements and conditions are ideal for proliferation, the cell enters S phase and is signalled to commit to continued division.

During S phase the cell begins replicating its DNA leading to chromosome duplication. Once replication is complete, proteins such as histones and cohesin are deposited along the strands to help package the DNA, resulting in the formation of two identical sister chromatids (Alberts, B et al 2002). Upon completion of S phase, the cell then enters G2 which provides additional time for growth as well as the second key check point before the cell can proceed into mitosis.

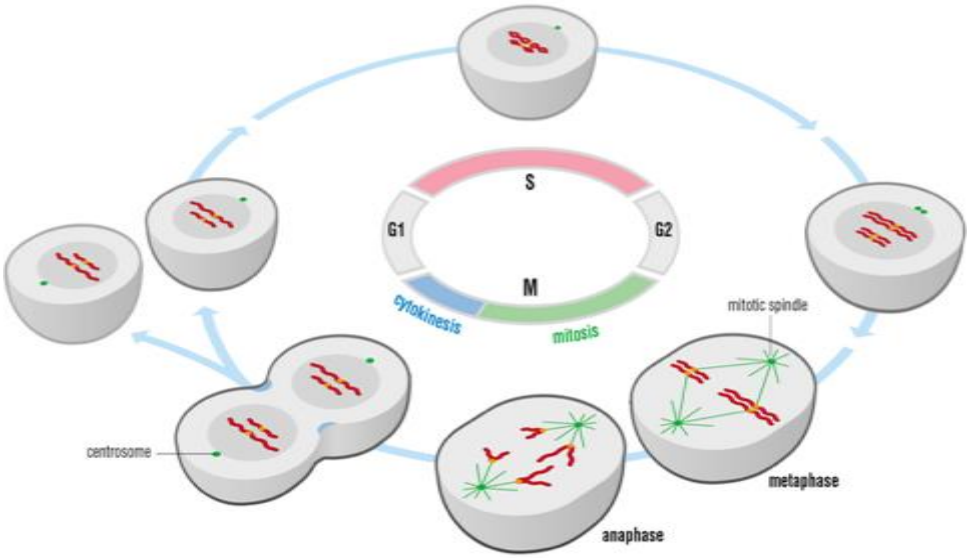

Figure 1.1 Overview of the cell cycle**.** The eukaryotic cell cycle has two major phases, S phase during which the chromosomes are replicated followed by mitosis, during which the chromosomes segregate and the cell undergoes cytokinesis to form two identical daughter cells. G1 and G2 comprise the gap phases between M and S phase and serve as major checkpoints for cell cycle progression. (Morgan 2007).

The G2 checkpoint senses any un-replicated or damaged DNA, generating a signal that leads to cell cycle arrest. If the DNA is irrevocably damaged the cell will be unable to proceed into mitosis, if however DNA replication is incomplete the cell will remain in G2 until the genome is fully replicated (Morgan 2007). Once there are two accurate copies of the entire genome the cell is triggered to proceed into mitosis (M) phase (Gautier et al. 1988). Although a continuous process, M phase can be further divided into several sub phases (Purves et al. 2003) (Figure 1.2). The first stage is prophase,

during which the chromosomes condense, centrosome separation occurs and the spindle assembly begins (Morgan 2007). The cell then moves into pro-metaphase when the nuclear envelope is broken down and the sister chromatids become attached to the spindle. Following this is metaphase, the last stage of mitotic entry when the sister chromatids are fully attached to the spindle and await the signal to separate (O'Conner, C. 2008). The metaphase to anaphase transition is the last major checkpoint of the cell cycle, during which the initiation of sister-chromatid separation can be blocked if the spindle is not fully assembled (Novak, B. et al 2002). Once the cell receives signals to proceed through the cell cycle it enters the first stage of mitotic exit known as anaphase.

During anaphase, the sister chromatids are separated by the mitotic spindle and are moved to opposite poles of the cell (Williams & Stoeber 2012). This is followed by telophase, the final stage of mitosis when the spindle is disassembled, the chromosomes condense and the nuclear envelope reforms (Morgan 2007). Once the cell has completed the cell cycle, it undergoes cytokinesis by forming a new cell membrane, known as the division septum at the cell equator. As the contractile actin ring starts to constrict, the septum is synthesised behind it, dividing the duplicated nuclei and cytoplasmic components equally into two daughter cells (O'Conner, C. 2008).

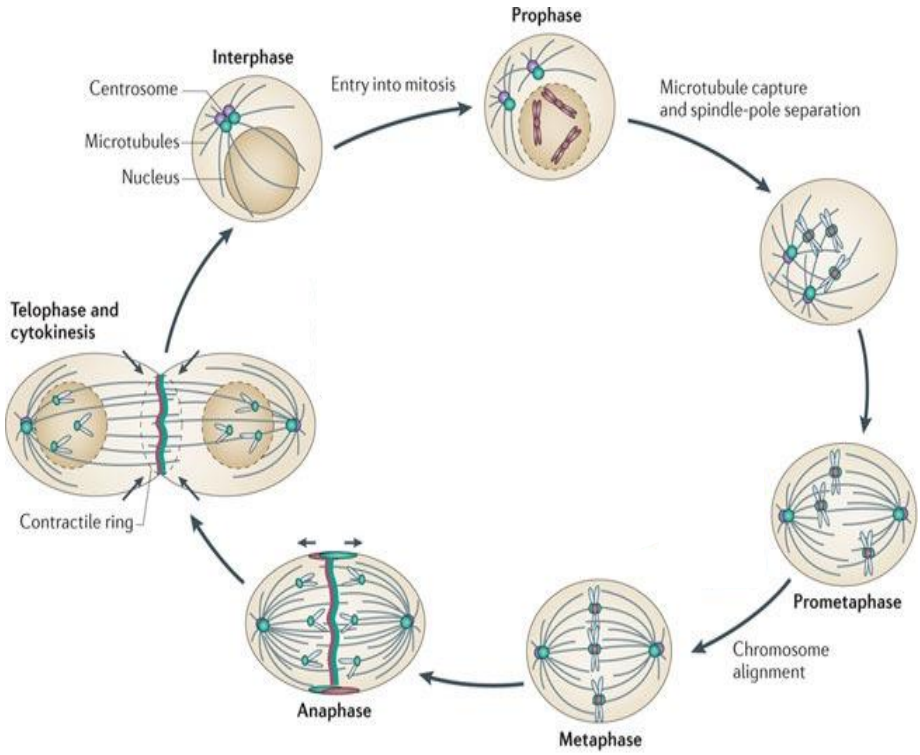

Figure 1.2 Stages of mitosis. During prophase chromosomes condense, centrosome separation and spindle assembly begin. The cell then moves into prometaphase, when the nuclear envelope is broken down and the sister chromatids become attached to the spindle. Sister chromatids become fully attached to the spindle during metaphase and are then segregated by the mitotic spindle during anaphase. Telophase is the final stage of mitosis when the spindle is disassembled and sister chromatid pairs dissociate. The cell then undergoes cytokinesis, separating into two identical daughter cells (Rath & Kozielski 2012).

1.1.1 *Schizosaccharomyces pombe* overview and life cycle

Widely studied around the world, *Schizosaccharomyces pombe* (*S. pombe*) is a non-motile, rod shaped unicellular organism, that has been successfully used as a model system for the study of eukaryotic molecular genetics and cellular biology for over 50 years (Nurse et al. 1976). Amongst the simplest of eukaryotes*, S. pombe* was first sequenced in 2002 and shown to contain a small genome of 13.8 Mb distributed over three chromosomes, encoding 5,123 genes (Wood et al. 2002). Sharing numerous cellular features with metazoan cells, many processes were shown to be conserved from yeast to humans, as well as many genes that when mutated, amplified or deleted resulted in the development of disease (Wood et al. 2002).

Displaying a cell cycle reminiscent of those seen in higher eukaryotes, *S. pombe* development consists of asexual or sexual phases, allowing proliferation of the organism in both a haploid or diploid state (Hagan & Nurse 2016). Cylindrical in shape with roughly hemispherical ends, cells typically measure 3 - 4 µm in diameter and 8 - 14 µm in length and are usually vegetatively growing haploid cells, carrying a single homolog of each chromosome (Moreno et al. 1991). With a generation time of between 2 – 4 hours, once cells reach ~15 µm in length they undergo a closed mitosis with a transverse septum laid down medially shortly after nuclear division, producing two daughter cells of ~8 µm long which continuously grow through most of the cell cycle without width change (Hagan & Nurse 2016).

In addition to vegetative growth, cells can also undergo a sexual lifecycle, during which two haploid cells of appropriate mating types respond to starvation by mating to form a diploid cell carrying two homologs of each chromosome (Figure 1.3). Normally the diploid cell then enters the meiotic pathway and produces four haploid spores which germinate and develop into vegetative cells (Forsburg 1991). Truly wild-type fission yeast strains are homothallic h^{90} and possess three copies of information at the mating

type locus enabling them to self-fertilise by the frequent switching between mating types, providing greater protection for surviving starvation conditions (Hoffman et al. 2015). As well as being homothallic, *S. pombe* can also be heterothallic; h^+ or h^-, requiring a h^{90} mating partner or one of the opposite mating type for proliferation. Due to its ease of genetic manipulation, simple culture conditions, typical phenotype and high degree of conservation with higher eukaryotes, *S. pombe* has become an ideal model organism for the study of genes involved in fundamental mechanisms such as DNA replication, cell cycle control, cell growth and signal transduction (Takegawa, K. et al 2009).

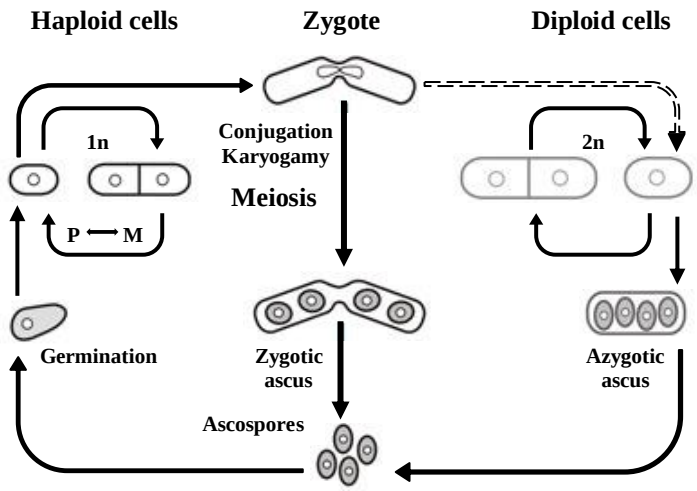

Figure 1.3 *S. pombe* cell cycle. Vegetative cells are predominantly haploid (1n) however during nutrient deprivation zygote formation and/or meiosis can occur. Conjugation requires cells of opposite mating types, whereas meiosis requires expression of opposite mating type genes in the same cell. Homothallic switch of mating type (P « M) occurs during vegetative growth. Adapted from www1.bio.ku.dk.

1.1.2 *Caenorhabditis elegans* overview and life cycle

Found in temperate soil environments all over the world, *Caenorhabditis elegans* (*C. elegans*) is a small free-living, non-parasitic, un-segmented, vermiform with a cylindrical body that tapers at both ends (Brenner 1974). The first multi-cellular organism to have its entire genome sequenced, *C. elegans* was found to contain an estimated 20,444 protein-coding genes with at least ~38% of these found to have predicted orthologues in the human genome (*C. elegans* Sequencing Consortium 1998).

Androdioecious, *C. elegans* has a rapid life cycle and can reproduce either by self-fertilizing hermaphrodites (XX), producing around 300 to 350 offspring, or by hermaphrodites breeding with males (X0) producing more offspring with at least 50% of progeny males (Stewart & Phillips 2002). Embryogenesis in *C. elegans* involves two main stages; proliferation followed by organogenesis and morphogenesis (Figure 1.4) (Clay & Sherwood 2015). During proliferation, the zygote is encased in a virtually impermeable eggshell, allowing the embryo to develop completely independently of the mother until the ~24 cell stage at which time the embryo is laid.

The cells then continue ex-utero development until becoming 558 essentially undifferentiated cells at which point the embryo hatches becoming a first stage L1 Larva (Brenner 1974). Following proliferation is organogenesis and morphogenesis; the continued growth of cells without additional cell divisions during larval development stages L1 – L4. During this time the nematode matures, growing from 0.25 mm in length to a 1 mm, fully formed adult with entirely differentiated tissues and organs. Two notable examples of organogenesis and morphogenesis are the establishment of the egg laying apparatus, which includes the vulva and formation of the uterine-vulval attachment and the expansion and shaping of the gonad as shown in Figure 1.4 (Clay & Sherwood 2015; Newman et

al. 1996). The time spent in each stage of development is dependent on media, genotype and temperature, however when grown at 22°C on NGM media under favourable conditions, the L1 stage is approximately 12 hours long, with stages L2 - L4 only 8 hours, with each stage ending with a sleep-like period of inactivity called lethargy. During lethargy the nematode moults the old cuticle and a new outer cuticle is formed (Corsi et al. 2015).

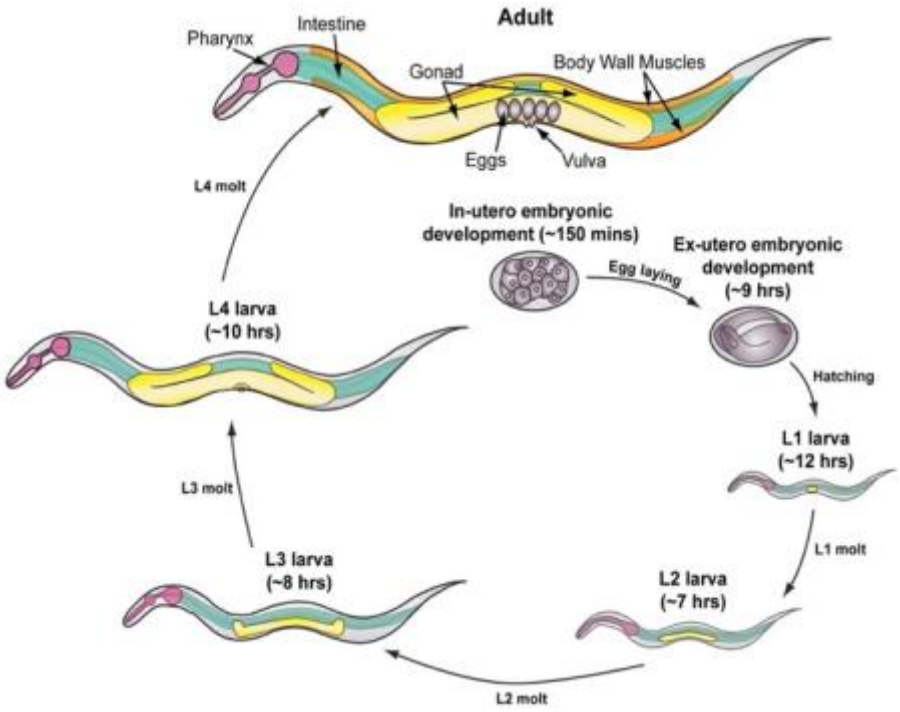

Figure 1.4 Overview of *C. elegans* development. Embryogenesis involves two stages: (A) a proliferative stage that includes gastrulation and (B) organogenesis and morphogenesis. Larval development consists of four stages (L1–L4), each separated by a lethargic stage during which the new outer cuticle is made (Clay & Sherwood 2015).

Roughly 10 hours after the L4 moult, adult hermaphrodites begin producing progeny for a period of 2 - 3 days until they have utilized all of their self-produced sperm (Clay & Sherwood 2015). After the reproductive period, hermaphrodites can live several more weeks before dying of senescence. If conditions are un-favourable L2 larvae activate an alternative life cycle and moult into a dauer larva, during which the cuticle completely surrounds the animal and plugs the mouth preventing the animal from eating and thereby arresting development. This provides the nematode with greater protection against environmental stresses and caustic agents such as chemicals, allowing larvae to survive for many months until conditions become favourable once more (Brenner 1974).

Widely studied over the last 60 years, the experimental attributes of *C. elegans*, such as its small size, transparency for ease of genetic manipulation and observation, short lifecycle, easy cultivation conditions and high degree of conservation with more complex eukaryotes has led to the nematode becoming an attractive model system for research into the processes of development, neurobiology and ageing relevant to human biology and disease.

1.2 The cytoskeleton

An essential component of all eukaryotic cells is the cell cytoskeleton; an interconnected network of protein filaments and regulatory proteins which extends throughout the cytoplasm determining cell shape and providing the structural framework of the cell (Fletcher & Muschel 2006). Involved in cell movements, cell division, transport of intracellular cargo and internal organisation (Evangelista et al. 2003), the cell cytoskeleton is a dynamic and adaptive structure whose component polymers are constantly undergoing re-organisation in response to both internal and external cues (Fletcher &

Muschel 2006). Formed by the three major cytoskeletal structures; microtubules, microfilaments and a group of polymers known collectively as intermediate filaments (Figure 1.5), the cytoskeleton is a highly conserved, complex structure tightly controlled by several classes of regulatory proteins.

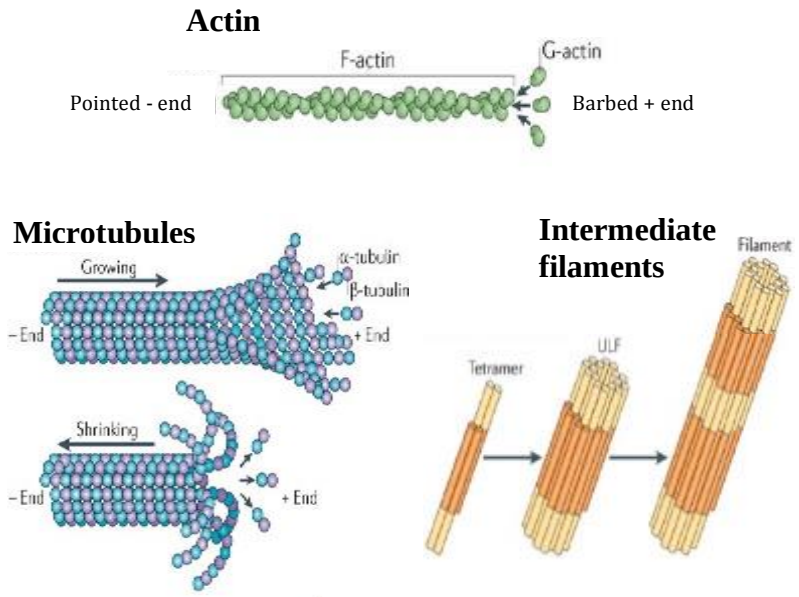

Figure 1.5 Components of the cell cytoskeleton. Globular (G) actin polymerizes to form actin microfilaments. Microtubules are formed from the polymerization of the two polypeptides α- and β tubulin. Intermediate filaments are composed of smaller strands in the shape of rods. Eight rods are aligned in a staggered array with another eight rods, and these components all twist together to form the rope-like conformation of an intermediate filament (Mostowy & Cossart 2012).

1.2.1 Microtubule Cytoskeleton

Composed of 13 parallel proto-filaments assembled around a hollow core, microtubules (MTs) are the largest of the 3 major cytoskeletal components with an overall diameter of 25 nm. Cylindrical in structure MTs are formed through the polymerization of tubulin; a heterodimer composed of the two polypeptides α and β tubulin. Polar structures, MTs have two distinct ends: a fast-growing plus end to which the β tubulin is orientated, and a slow-growing minus end to which the α tubulin is orientated (Morgan 2007).

Nucleated at microtubule organising centres (MTOCs) by the initiation of γ-tubulin (de Forges et al. 2012), microtubules exhibit dynamic instability, continually undergoing catastrophe and rescue due to changes in the relative rates of new subunit addition and hydrolysis of GTP bound to β-tubulin (Garcia et al. 2013). With the minus ends typically anchored within nucleating centres, rapid polymerization of MTs is achieved by the addition of GTP-bound tubulin dimers incorporating into the positive end of the filament. After a short delay the GTP is hydrolysed, which weakens the binding affinity of tubulin for adjacent molecules.

As long as the new GTP-bound tubulin molecules are added more rapidly than GTP is hydrolysed, the microtubule retains a GTP cap at its plus end and microtubule growth continues, if however, the rate of polymerization slows, the GTP bound to tubulin at the plus end of the microtubule will be hydrolysed to GDP, resulting in rapid de-polymerization and shrinkage of the microtubule.

Involved in a variety of cellular functions such as regulation of cell polarity, chromosome separation during cell division and morphogenesis, MTs provide tracks for the movement of molecular motors kinesin and dynein, which transport and/or anchor various organelles (Sloboda 2015). Microtubule associated proteins (MAPs) tightly regulate MT dynamics by modifying filament stability, effecting growth rate, frequency of catastrophe

and their association with other proteins (Sawin & Tran 2006). This tight regulation is essential as microtubules play a central role in cell division in all eukaryotes.

1.2.2 Intermediate filaments

Found in metazoan cells, intermediate filaments are composed of a variety of proteins which can be classified into six groups (I – VI) based on similarities between their amino acid sequences (Cooper 2000). With expression dependent on cell type and degree of differentiation of cells, intermediate filaments are stable non polar polymers that are generally insoluble in physiological conditions (Portet 2013).

Ranging from 40 kDa to 240 kDa in size, the primary structure of intermediate filaments has been evolutionarily well conserved, with filaments around 10 nm in diameter, containing a central α-helical rod domain of approximately 310 amino acids, flanked by variable end domains located at their amino and carboxyl termini (Chung et al. 2013). Primarily playing a structural role by providing mechanical strength to cells and tissues (Cooper & Hausman 2009), intermediate filaments also serve to anchor several organelles as well as being essential components of the actin-dependent positioning of the cell nucleus (Dupin et al. 2011).

1.2.3 Actin Cytoskeleton

Arguably the most important of the cytoskeletal components, the actin filament is highly conserved across a diverse set of eukaryotic species, remaining essentially unchanged from yeast to man (Pollard 1986; Gunning, Hardeman, et al. 2015). The universal eukaryotic force provider, the actin cytoskeleton is involved in a broad range of important cellular

functions such as providing strength and architecture, as well as playing a central role in locating/ transporting protein complexes and ordering/ shaping compartments and organelles (Gunning, Ghoshdastider, et al. 2015). A major component of the thin filament in all muscle tissues, a secondary property of actin is its ability to provide pushing and pulling forces that can be integrated into biological processes in which movement is a necessary component.

Found in many eukaryotic cells to be the most abundant protein, actin is a 43 kDa ATPase, that exists in a dynamic equilibrium between monomeric G-actin and polymerized F-actin (Oda et al. 2009). Approximately 7 nm in diameter, actin filaments are formed from the head-to-tail polymerisation of G-actin and have the appearance of a double helix due to the rotation of each monomer by 166º (Pfaendtner et al. 2010). Constantly undergoing reorganization, actin filaments are also polar structures due to the same directional orientation of each actin monomer, resulting in two distinct ends: a fast-growing barbed (+) end and a pointed (-) end.

Exhibiting dynamic instability, actin re-organisation is controlled through the ATPase activity of the protein. Rapid polymerization of filaments is achieved by the addition of ATP-bound actin monomers incorporating into the positive barbed end of actin filaments. The ATP-bound actin monomers are then hydrolysed, which weakens the binding affinity of the protomers for adjacent molecules, producing a slightly older portion of the filament bound to ADP and phosphate. The inorganic phosphate is slowly released leaving ADP bound actin at the pointed (-) end which can then dissociate from the filament. Although the dynamic properties of actin drive filament tread-milling, enabling the filament to polymerize and depolymerize in unison, it is a tightly controlled process regulated by a number of actin regulatory proteins (Lee et al. 2010).

1.3 Actin Binding Proteins

Actin binding proteins (ABPs) are a large group of proteins which bind to actin and modulate actin dynamics through a variety of activities. Based on function, ABPs can be grouped broadly into four categories: actin polymerisation factors, which initiate and polymerise filament formation; depolymerisation factors, which disassemble filaments; bundling proteins and stabilising proteins (Chen et al. 2000).

1.3.1 Actin-related protein 2/3 complex

Highly conserved throughout all eukaryotes, the Actin-related protein (Arp) 2/3 complex is an actin-polymerising complex involved in assembling and cross-linking actin filaments to produce a diverse array of structures (May 2001). Unable to homo-polymerize the Arp 2/3 complex is formed by the stable assembly of seven protein subunits, including two Arp proteins; Arp 2 and Arp 3 and five novel proteins (May 2001). Localised to the cytoplasm the Arp 2/3 complex binds to the side of pre-existing actin filaments where it is activated by the interaction of a nucleation promoting factor, such as the Wiskott–Aldrich syndrome protein (WASp)/ Scar family of proteins (Mullins et al. 1998) (Figure 1.6).

The nucleation promoting factor induces a conformational change in the complex (Mullins et al. 1998), which results in the interaction of the Arp2 and Arp3 subunits, increasing the proteins ability to bind an actin monomer to its barbed (+) end (Muller et al. 2005). The binding of the first actin monomer combined with ATP initiates the synthesis of a new actin daughter strand at a constant angle of approximately ± 70° to the mother strand (Mullins et al. 1998).

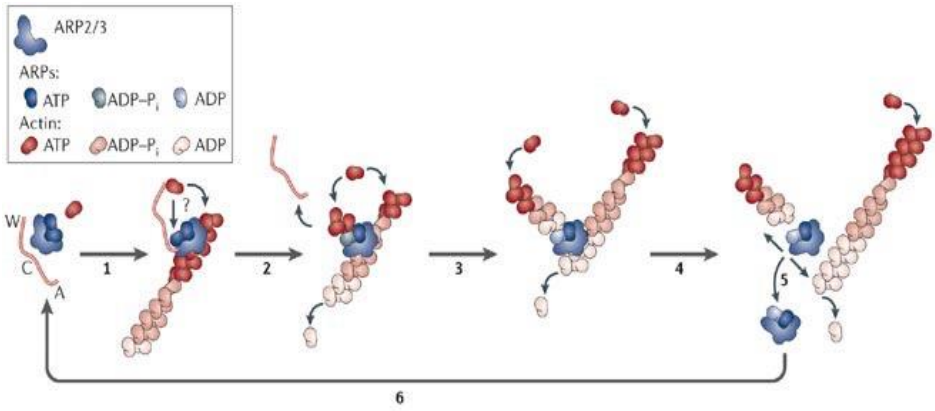

Figure 1.6 Actin polymerization by the Arp2/3 complex. The Arp2/3 complex binds to the side of the mother strand and is activated by a nucleating promoting factor. The activated complex then initiates the synthesis of a new daughter strand at a 70 ° angle to the mother strand (Goley & Welch 2006).

1.3.2 Formins

Composed of two highly conserved adjacent formin homology (FH) domains; FH1 and FH2 and typically a Rho-binding (FH3) domain, formins are a diverse family of multi-domain proteins that promote the rapid assembly of linear, un-branched actin filaments in all eukaryotes (Evangelista et al. 2003; Sawin 2002). Involved in determining the sub-cellular localisation of the formin as well as regulating its activity, the FH3 domain is required for protein activation by a membrane bound Rho-GTPase (Evangelista et al. 2003). Once activated the proline rich FH1 domain begins increasing the local concentration of actin by binding actin monomers, which it then delivers to

the FH2 domain to rapidly nucleate actin polymers at the barbed end (+) of the filament (Paul et al. 2008).

1.3.3 ADF/ Cofilin

An essential group of proteins, the actin-depolymerizing factor (ADF)/cofilin-family are low molecular weight actin modulating proteins that promote dissociation of actin monomers (Nakano & Mabuchi 2006). Ubiquitous among eukaryotes, ADF/ cofilin enhances the turnover of actin filaments by either severing filaments, binding and contacting two actin monomers and imparting a conformational twist on the actin filament or by increasing the dissociation of monomers from the pointed end of the actin filaments. ADF/ cofillin activity is regulated by reversible phosphorylation, with phosphorylation of a serine in the NH2-terminal region inactivating the protein (Carlier et al. 1997; Ichetovkin et al. 2000).

1.4 Tropomyosin

Conserved throughout the fungal and animal kingdoms, tropomyosins (Tpms) are a family of highly abundant actin associating proteins which are essential for the normal functioning of the actin filament system in both muscle and non-muscle cells (Gunning et al. 2008). Regarded as the actin gatekeeper; tropomyosin cooperates with a range of actin binding proteins to form complexes with differing functional outputs in both a collaborative and independent manner, regulating actin mechanical and dynamic properties (Dominguez 2011). First discovered as a component of the skeletal muscle contractile system, the complexity of Tpm isoform diversity has been shown to be closely linked to the increased complexity of animals during evolution (Vrhovski et al. 2008). Simple unicellular eukaryotes, such

as the fission yeast *S. pombe* and budding yeast *S. cerevisiae,* encode one and two Tpm genes respectively. The *S. pombe cdc8*$^{+}$ gene produces only one essential Tpm isoform, whereas *S. cerevisiae* contains two Tpm genes; *TPM1* and *TPM2* which encode only two Tpm isoforms with non-overlapping functions (Drees et al. 1995).

More complex eukaryotes such as the soil nematode *C.elegans* also encodes a single Tpm gene *tmy-1,* however is able to generate four isoforms using external and internal promoters (Anokye-Danso et al. 2008). Similarly, the arthropod *Drosophila melanogaster* contains two Tpm genes; *Tm1* and *Tm2* which to date are known to generate at least 13 distinct polypeptides, although splicing predictions indicate the potential for the expression of 18 isoforms with most remaining uncharacterized (Cho et al. 2016; Goins & Mullins 2015).

Highly organized multicellular vertebrates such as amphibians, avians and mammals contain 4 distinct Tpm genes which by the use of different promoters and alternatively expressed exons can produce over 40 Tpm isoforms (Vrhovski et al. 2008). The human genome contains the four separate tropomyosin genes; *TPM1, TPM2, TPM3* and *TPM4* (Gunning et al. 2008). Mutations in *TPM1* are thought to be responsible for familial type-3 hypertrophic cardiomyopathy and have been directly linked to the growth and spread of cancer. Mutations in *TPM2* and *TPM3* have been linked to nemaline myopathies (Sahota et al. 2009).

Regulation of isoform expression is decided by the timing and tissue specificity of gene expression, mRNA, protein localisation and subtle differences in protein function, with some mammalian cells found to express as many as 7 isoforms at once (Goins & Mullins 2015). The functional specificity of each Tpm protein is related to the collaborative interactions of the isoform with various actin binding proteins such as the Arp 2/3 complex, cofilin and myosin motors, allowing Tpm isoforms to accumulate to actin

structures where they have the highest affinity and are most stable (Gunning et al. 2008).

1.4.1 Tropomyosin structure

Although muscle Tpms show a preference for heterodimer formation, current evidence suggests cytoskeletal Tpms exclusively form homodimers which associate in parallel and register to form amphipathic, alpha-helical super coils up to 400 angstroms long (Gunning, Hardeman, et al. 2015). Differing in length and sequence, Tpms can be classified as high molecular weight (HMW) corresponding to ~284 amino acids (aa) organised into seven pseudo repeats of 40 aa, or low molecular weight ~248 aa in length containing between 4 and 6 of such repeats (Jampani et al. 2012). Shown to bind cooperatively along the major groove of most actin filaments, each Tpm peptide is formed by the uninterrupted hepta-peptide repeat *(a-b-c-d-e-f-g)* (Figure 1.7) (Gunning et al. 2008; Lin et al. 2008).

Residues in positions *a* and *d* are generally a-polar and form a left-handed stripe along the surface of right-handed helices, packing into a “knobs into holes” fashion along the interior of the structure, conferring stability and forming the hydrophobic core of the Tpm molecule (Nitanai et al. 2007; Hitchcock-DeGregori 2008). An unusual feature found within this core is the alanine stagger; areas of high alanine content clustered into small regions with ~35% of these commonly found to occupy the *d* position (Brown et al. 2001). Low resolution crystal structures of Tpm have revealed these areas of alanine clusters along with axially in-register chains rich in canonical leucine - type residues, appear to create relatively sharp bends in the axis of the Tpm creating a source of semi-flexibility for the molecule and promoting shape complementarity to the actin filament (Brown 2010).

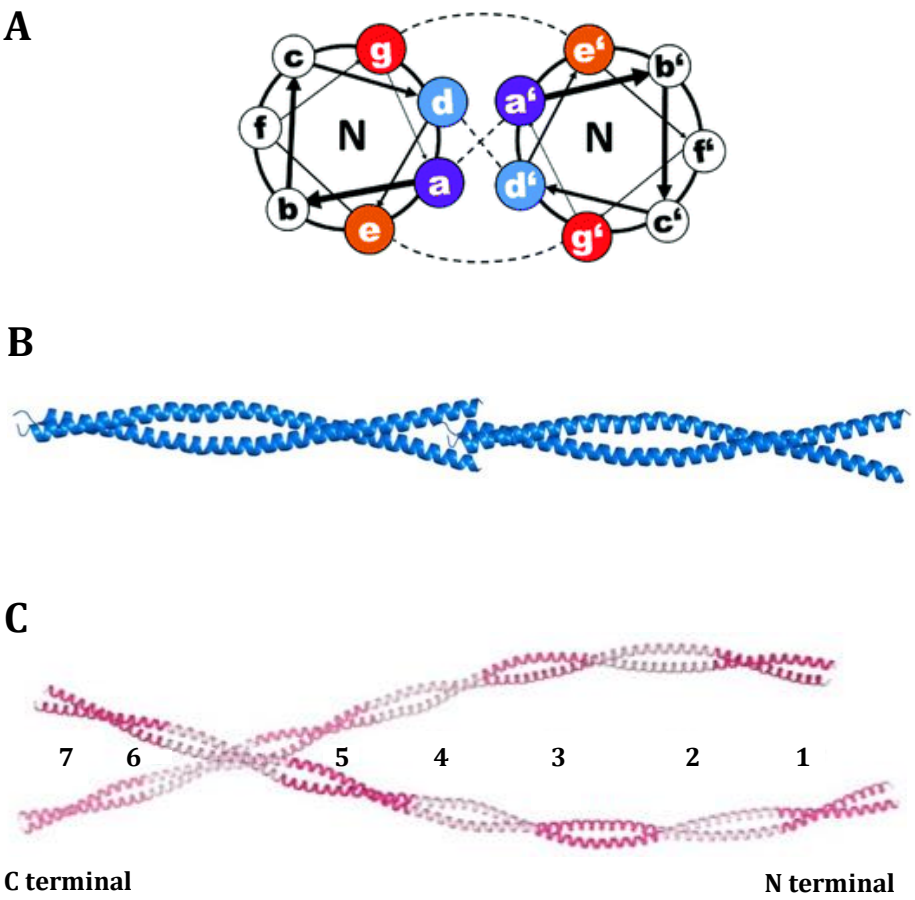

Figure 1.7 Structure of smooth muscle tropomyosin. A) Helical wheel representation of the heptad repeat *a-b-c-d-e-f-g* found in each Tpm peptide. Amino acid residues at positions *a* and *d* are a-polar and form the hydrophobic core of the molecule. Residues at positions *e* and *g*, are often occupied by charged amino acids which form salt bridges between the two chains (Ljubetič et al. 2016). B) Head to tail complex, showing the tail of one Tpm dimer and the amino-terminal region of the next dimer overlapping by ~ 8 – 9 amino acids. C) Model of full length Tpm bound symmetrically along the two long pitch helices of 7 actin filament subunits (Jampani et al. 2012).

Residues found in positions *e* and *g* are often occupied by charged amino acid residues which form salt bridges between the two neighbouring chains, defining the parallel orientation of each strand and further stabilising the coiled-coil structure (Jampani et al. 2012). The *b, c* and *f* positions are usually polar or charged residues on the surface of the molecule facing the surrounding aqueous environment, available for the binding of other proteins (Barua 2013).

1.4.2 Tropomyosin overlap complex

Like the actin filament, Tpm polymerizes to form a polar, filamentous macro-molecular assembly with the overlap complex shown to be an interleaved four-chained structure in which the chains of the carboxyl- terminus spread apart to form a cleft in which 11 residues of the amino- terminus of the adjacent molecule are inserted (Jampani et al. 2012; Frye, Klenchin & Rayment 2010a). As a result the planes of the two ends are rotated by 90 degrees relative to each other allowing the hypothesized actin binding repeats to be retained from one dimer to the next (Hitchcock-DeGregori 2008). Although the head to tail arrangement is a universal attribute of all Tpm isoforms, the overlap domain has been shown to differ widely among different family members (X. E. Li et al. 2014).

As a single dimer, the intrinsic affinity of Tpm to an actin filament is very low, with the Tpm appearing to rest in the major groove of the actin polymer, relying on ionic interactions to stabilise the Tpm-actin interface (Gunning et al. 2008). As a polymer however, some Tpm isoforms are subject to post translational modification such as amino-terminal acetylation and phosphorylation. Acetylation of the amino-terminal methionine has been shown to be necessary for overlap formation as well as coiled–coil stability and for greatly increasing the affinity of Tpm for actin, enhancing the stability

of the Tpm-actin interaction (Frye, Klenchin & Rayment 2010b). Phosphorylation of Tpm has been shown to enhance the ability of Tpm to form head to tail interactions and has also been linked to protein regulation and associated actin remodelling, although the significance of Tpm phosphorylation is still poorly understood (Schevzov et al. 2014; Rao et al. 2009).

1.4.3 Tropomyosin function

In muscle cells the key function of Tpm is to associate with F-actin and stabilise actin filaments as well as regulate the acto-myosin system by steric hindrance of myosin in the absence of calcium. This is achieved via a proposed three-state model, in which Tpm forms an actin-troponin-tropomyosin complex that adopts a 'blocked state' preventing the binding of myosin S1, a 'closed state' which allows S1 to bind weakly or an 'open state' in which the S1 can both bind and undergo an isomerization on to a more strongly bound rigor–like conformation (McKillop & Geeves 1993).

In non-muscle cells however, tropomyosin is important for various actin cytoskeletal functions including intracellular–vesicle movement, cell motility, cytokinesis, apoptosis and cell proliferation which is reflected in the diversity of the Tpm isoforms (Gunning et al. 2008). In addition, Tpm also plays a central role in regulating actin dynamics by stabilising filaments, inhibiting both the rate of polymerization and de-polymerisation by making fewer ends available for subunit addition and lowering the off rate constant from the pointed end of actin filaments without preventing elongation (Gunning, Hardeman, et al. 2015).

The complexity of the tropomyosin gene family makes *in vivo* or *in situ* studies of tropomyosin challenging, therefore unique model systems such as yeast organisms have been used to look at eukaryotic biology due to

their amenability to cell, molecular, biochemical and genetic approaches.

1.4.4 Tropomyosin in fission yeast

S.pombe has a single, essential Tpm gene, *cdc8*$^{+}$*,* that encodes a protein composed of 161 amino acids and 18.96 kDa in size (Balasubramanian et al. 1992). Containing only one Tpm isoform, *cdc8*$^{+}$ is found at constant expression levels throughout the cell cycle, with post-translational acetylation of its amino- terminal methionine found to greatly affect its actin affinity *in vitro* and localisation within the cell. With around 80% of Cdc8 existing in the acetylated form, it predominantly polymerizes around the actin filaments that form longitudinal cables during interphase and the CAR during cell division with smaller amounts in actin patches (Skoumpla et al. 2007). The binding of Cdc8 to actin in a 'closed' position, stabilizes a particular configuration which prevents various myosin proteins from binding strongly, therefore enhancing its ability to regulate myosin motor activity throughout the cell cycle.

1.5 Myosin

Present in all eukaryotic cells possessing an actin-based cytoskeleton, myosins are a super-family of evolutionarily conserved motor proteins that can efficiently convert chemical energy into mechanical work via the hydrolysis of nucleotide phosphates (Odronitz & Kollmar 2007). Engaged in a plethora of tissue-specific cellular functions, there are at least 35 distinct groups of myosins, classified based on the phylogenetic analysis of the head domains, located at the amino- terminus of the polypeptide (Odronitz & Kollmar 2007; Walklate et al. 2016). Implicated in a number of important cellular processes, the human genome is thought to encode around 40

known or predicted myosin isoforms (Odronitz & Kollmar 2007), which can be grouped into 12 subfamilies and further divided into the 2 major groups; unconventional myosins and conventional class II myosins. Although no class of myosin appears to be universally expressed in all phyla, eukaryote myosins are highly conserved proteins, composed of one of more heavy chains, organised into three structurally and functionally different domains and several light chains (Figure 1.8) (Lodish H. et al 2000).

The conserved heavy chain consists of a globular head domain typically consisting of ~ 800 amino acids, located at the amino– terminus which contains a conserved catalytic domain that binds actin filaments and ATP in an ATPase-dependent manner (Walklate et al. 2016). The ATPase cycle is coupled to conformational changes within the head domain that are translated into movement (J. Li et al. 2016), changing the actin binding capability of the motor domain, allowing the protein to exert force against actin (Berg, J. et al 2001. East, D. et al 2011). The head domain is followed by the neck region or lever arm, which consists of various numbers of IQXXXRGXXXR (IQ) motifs, which form a continuous α-helix to which calmodulin or calmodulin-like light chains associate in a Ca^{2+} dependent manner (Sellers 2000).

This association of a light chain with the IQ motifs increases the stiffness of this ‘lever arm’ and prevents the tail region from folding back on itself into an ‘off’ state. It also increases the rigidity of the neck region, which allows amplification of the power stroke generated from the motor domain. In the majority of myosins the neck region is immediately followed by the tail domain; a sequence of variable lengths that diverges substantially between the different myosin classes. Found at the carboxyl- terminus of the protein the tail domain can form several distinct types of structures and contains the binding sites that specify the targeting, oligomeric state and function of the specific myosin (Lodish H. et al 2000).

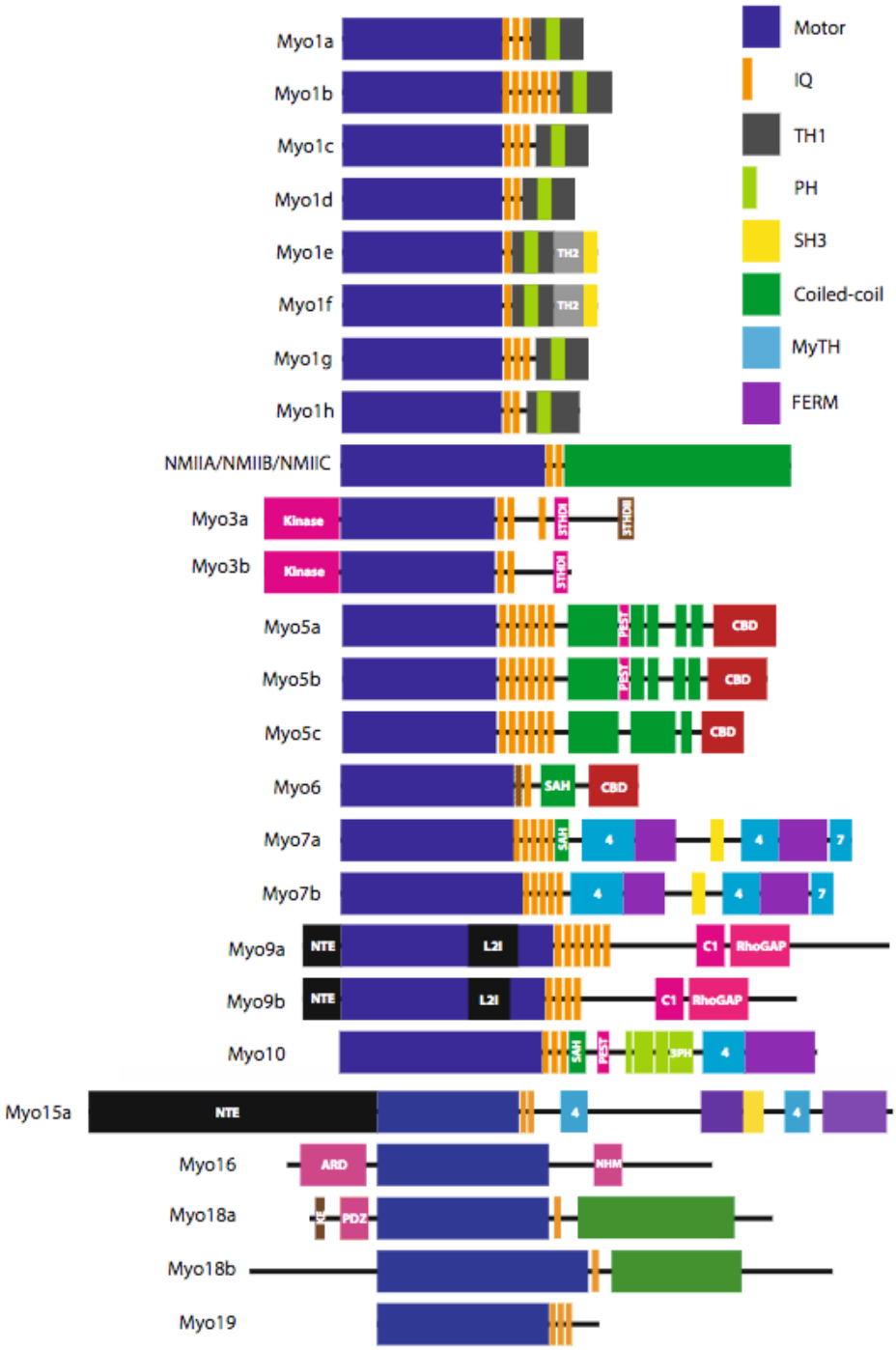

Figure 1.8 Structural domains of myosin motors expressed in humans. Each myosin contains a motor head domain with variable neck and tail domains. (Masters et al. 2017).

Uniquely suited for the specific functions of each motor protein, some myosin tails such as the class II and class V myosins contain heptad repeat sequences that can form α-helical coiled-coils and allow the heavy chains to dimerize, resulting in formation of two-headed motors that are able to move processively along actin filaments (Syamaladevi et al. 2012). Other myosin proteins however, such as those belonging to class I, II and IX do not contain coiled-coil motifs and have either been shown or presumed to be single headed (Krendel & Mooseker 2005; J. Li et al. 2016).

1.5.1 Myosin Regulation

As cells often possess a repertoire of myosin proteins from different classes, finely balanced regulatory mechanisms are required to determine the mechano-enzymology, oligomerization, interactome and cellular localisation of each myosin in order to meet the changing demands of cellular functions (Hartman & Spudich 2012). Myosin regulation occurs at three different levels; transcriptional regulation which affects the extent of myosin gene expression and alternate splicing in response to intracellular and extracellular cues, regulation by substrate or effector binding and finally by versatile post-translational modifications (Heissler & Sellers 2016).

Actin-linked regulation is an example of substrate binding regulation. In response to signal transduction cascades, actin binding proteins diversify and dynamically compartmentalise the cell cytoskeleton inducing higher order actin structures with different signatures which can directly influence a myosins track selectivity and mechano-chemistry (Gunning, Ghoshdastider, et al. 2015). Tethering of cargo to the myosin tail domain provides binding partner regulation as myosin-cargo interactions determine the oligomerization and localisation of the motor complex. An example of regulation by post-translational modification is phosphorylation which often occurs on the heavy chain and the associated light chains, induced by the

finely balanced interplay of kinases and phosphatases (Sellers 2000). Regulation by auto-inhibition is a non-covalent allosteric mechanism at the single protein level which is associated with reduced myosin catalytic activity, with relief often achieved via phosphorylation of the regulatory light chain (Heissler & Sellers 2016). Isoforms can be present in cells in an equilibrium between primary functional and non-functional states, due to conformational restrictions imposed by the interaction of the motor domain and tail, shifting the myosin into a kinetically inert and assembly-incompetent state.

Divalent cations such as Ca^{2+} are also regulators and integrators of myosin function either directly or indirectly via interactions with the heavy chain, associated light chains or via binding to troponin, a component of the tropomyosin-troponin complex that lies in the groove of the actin coiled-coil. Interactions with the associated light chains can trigger conformational rearrangements that result in the dissociation of the light chain from the IQ domain or result in a higher affinity for particular IQ motifs (McKillop & Geeves 1993).

1.5.2 Myosin I

First discovered in lower eukaryotes (Pollard et al. 1973), the class I myosins comprise the second largest myosin family in vertebrates with isoforms sharing a high degree of sequence conservation and similar structural organization (Greenberg & Ostap 2013). Higher vertebrates express eight distinct members of the myosin-I family, six of which encode short-tailed isoforms (Myo1a, b, c, d, g, and h) and two of which encode long-tailed isoforms (Myo1e, f) (Figure 1.9) (Kim & Flavell 2008; Berg et al. 2001). Comprised of a motor domain, a light chain binding domain that binds one to six calcium sensitive calmodulin or calmodulin-like light chains and a tail domain, class I myosins are single headed motor proteins, unable

to dimerize or form filaments due to the termination of the coiled coil at the globular cargo binding region. The tail domain of myosin I, which shows the most sequence divergence amongst isoforms can be divided into three tail-homology (TH) subdomains based on sequence motifs that have been termed TH1, TH2, and TH3. All characterised myosin I tail domains contain a positively charged, polybasic TH1 domain which features an embedded pleckstrin-homolgy (PH) domain capable of binding to lipid membranes (Doberstein & Pollard 1992).

Point mutations in the PH domain of vertebrate Myo1c, Myo1f, Myo1g, and Myo1b disrupt *in vivo* membrane binding but only moderately affect membrane binding and localisation of Myo1e. Similarly, a mutation of a conserved PH domain residue found in *Acanthamoeba* myosin-IC, has only moderate effects on membrane binding. These results show there is substantial diversity in the binding of the various myosin I isoforms to membranes and indicates interactions with membrane lipids are likely mediated through specific interactions by the PH domain and by non-specific electrostatic interactions mediated by basic residues in other regions of the tail domain (Feeser et al. 2010). Only long tailed class I myosins contain a proline rich TH2 domain that binds actin and regulates actin dynamics and a TH3 domain consisting of a Src-homolgy (SH3) domain that putatively binds cytoskeletal regulatory proteins (Figure 1.10).

It has been hypothesized that it is the tail–ligand interactions that target the different myosin I isoforms to various intracellular locations and/ or adapt them to different actin dependent processes (Lee et al. 2000). As the cellular localisation of myosin I proteins is based on their structural and functional peculiarities, expression of different isoforms has been found to vary across different tissues (McIntosh & Ostap 2016).

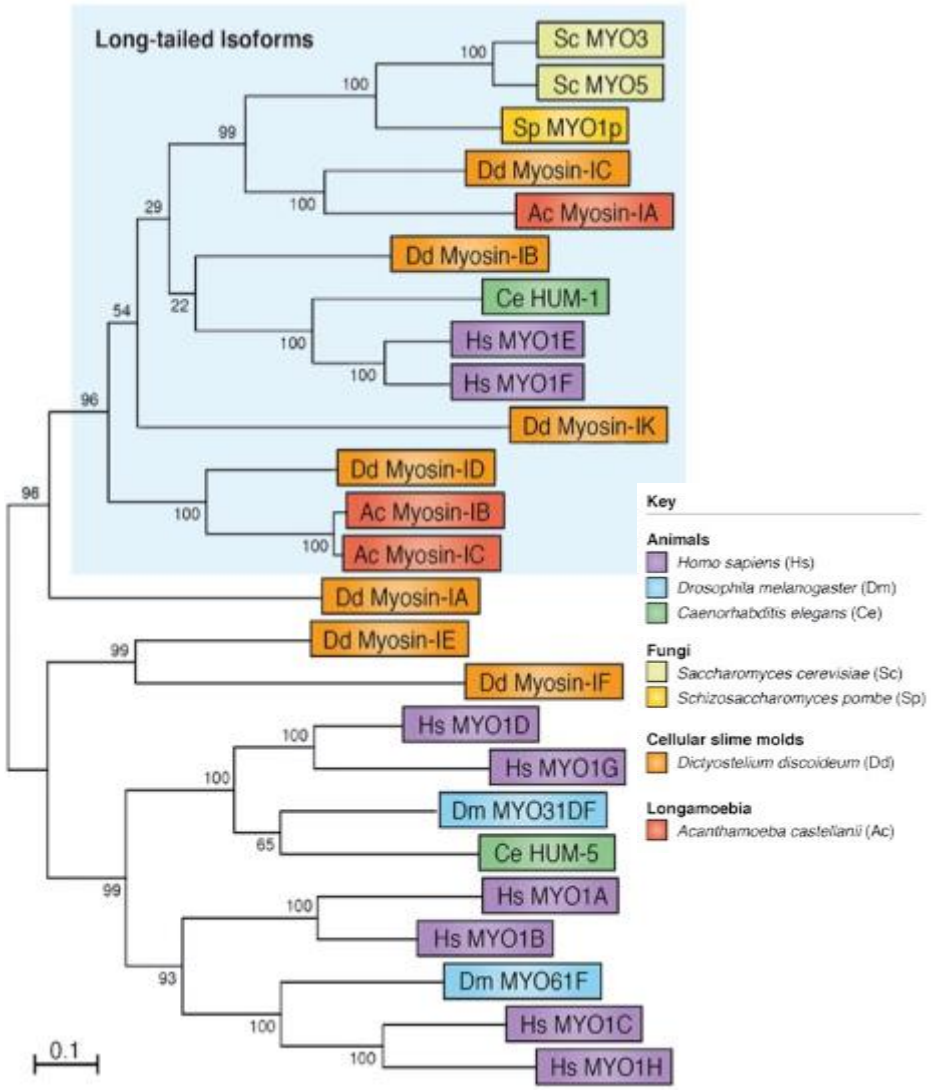

Figure 1.9 Myosin I isoforms from model organisms. Evolutionary histories based on the JTT matrix based model of full length myosin I sequences. Statistical confidence is listed at each branch point. Branch length are measured in the number of substitutions per site. Adapted from McIntosh, B. et al 2016.

Figure 1.10 Schematic of a short and long tailed class I myosin. Each myosin contains a motor domain (blue), variable neck (purple) region and a TH1 domain (red) with an embedded pleckstrin-homology (yellow) domain. Long tailed myosins have an additional TH2 domain (orange) and SH3 domain (green). Scale bar represents 250 aa.

Myo1a is most highly expressed in the small intestine and colon where it is thought to be involved in trafficking of Golgi-derived vesicles as well as providing structural integrity to brush border microvillus by connecting the plasma membrane with the underlying bundle of cross-linked actin filaments. Myo1a knockout mice display membrane herniation in intestinal epithelial cells with mutations in Myo1a also associated with colon cancer and hearing loss (Mazzolini et al. 2012; Donaudy et al. 2003). Myo1b, Myo1c, and Myo1e are widely expressed and found in most cell types. Myo1b participates in trafficking endosomes, lysosomes and multi-vesicular bodies as well as stabilising plasma membrane tension. Deletion of Myo1b leads to increased plasma membrane blebbing, reduced cell movement and directionality (McIntosh & Ostap 2016; Salas-Cortes et al. 2005).

Myo1c has been implicated in a diverse range of functions including vesicle trafficking, exocytosis, endocytosis, lipid raft arrangements and adaptation in hair cell bundles, loss of Myo1c has been associated with kidney disease and deafness (Sielski et al. 2014; Zadro et al. 2009).

Found in a wide range of tissues, Myo1d is highly expressed in the central and peripheral nervous system (Benesh et al. 2012) and is involved in fusion of early endosomes, establishing or maintaining plasma membrane tension and establishment of left-right asymmetry during drosophila development. Myo1d knockdown mice show morphological changes in oligodendrocytes however the understanding of function in the context of vertebrate physiology remains largely unexplored (Benesh et al. 2012; Yamazaki et al. 2016). Ubiquitously expressed, Myo1e is found in regions of high actin concentrations including phagocytic cups, adherens-type intracellular junctions and clathrin-containing puncta, where it is involved in establishing cell-cell contacts, membrane dynamics, regulated secretion and endocytosis (Cheng et al. 2012; El-Mezgueldi et al. 2002). Loss of Myo1e is associated with focal segmental glomerulosclerosis 6 and arteriosclerosis and has also been found to be a core component of cancer invadosomes (McIntosh & Ostap 2016; Krendel et al. 2009).

Predominantly expressed in the hematopoietic tissues, Myo1f is involved in modulating adhesion to the extracellular matrix by preventing excessive exocytosis and inappropriate cell spreading and is the third myosin I isoform to be involved in deafness (Kim et al. 2006). Myo1g is a hematopoietic-specific myosin expressed mainly by lymphocytes and has been shown to have a role in exocytosis, endocytosis, intracellular membrane trafficking and nuclear organization (Maravillas-Montero et al. 2014). Loss of Myo1g in B-lymphocytes leads to decreased cell stiffness due to a loss of cortical tension affecting cell adhesion, spreading, phagocytosis and endocytosis (McIntosh & Ostap 2016).

Myo1h is highly expressed in the testes with expression also seen in adipocytes and the heart (McIntosh & Ostap 2016). Although Myo1h has no known function it has been shown to contribute to mandibular prognathism (Tassopoulou-Fishell et al. 2012). Most myosin I isoforms contain numerous regulation signatures which increases protein diversity and provides several mechanisms for the cell to regulate the activity and cellular localisation of each myosin protein.

Regulations by heavy chain phosphorylation of amoeboid myosin I molecules occurs predominantly at a residue exposed on the surface loop in the myosin motor domain. Typically, this residue is either a Thr (T), Glu (E), Asp (D) or a Ser (S), therefore it was termed the TEDS – site. The addition of a phosphate group stabilizes and constrains the TEDS-loop, modulating the proteins affinity for actin allosterically accelerating the weak-to-strong transition of the myosin kinetic cycle (Bement & Mooseker 1995).

Observations of phosphorylation sites in the tail domain of amoeboid myosin I heavy chains are also believed to play an important role in determining protein function however to date none have been well characterised. Unlike class I myosins from less complex organisms, vertebrate class I myosins contain a negatively charged amino acid at the TEDS-site that supersedes the phosphorylation requirement (Heissler & Sellers 2016).

As myosins are a highly-conserved group of proteins, many of their specific roles may be hypothesized based on the functions of their homologs in other simpler eukaryotic species. *S. pombe* and *C. elegans* therefore offer ideal model systems for the study of the myosin family of proteins, encoding only one and two class one myosin proteins respectively (Egel, R. 2004).

1.5.3 Myosin I in *Schizosaccharomyces pombe*

First identified during the fission yeast genome sequencing project, *S. pombe myo1*$^{+}$ encodes a typical long tailed class I myosin 136 kDa in size, comprised of a motor domain, two calmodulin-binding IQ domains and a long tail region which contains all three tail homology domains (TH1, 2 & 3) (Toya et al. 2001; Lee et al. 2000). A homolog of human Myo1e, Myo1 plays an important role in stimulating Arp 2/3 complex-dependent actin polymerization, working in parallel pathways with Wsp1, the yeast homolog of WASp to regulate the activation of Arp 2/3 and the distribution of cortical actin patches at the sites of new cell growth and at the cell equator during cytokinesis (Lee et al. 2000). In addition to promoting actin polymerization, Myo1 also plays a key role in membrane re-modelling and endocytosis (Attanapola et al. 2009). Although not essential for cell viability, disruption of *myo1*$^{+}$ causes abnormal morphology with cells lacking a polarized distribution of cortical actin patches and loss of polarized cell growth (Lee et al. 2000).

Myo1 activity and function is predominantly regulated by actin binding proteins and by the association of calmodulins to the IQ motifs, however the mechanisms by which fission yeast Cam1 regulates Myo1 are only just starting to be elucidated (East & Mulvihill 2011). Although numerous phosphorylation sites have been observed throughout the Myo1 heavy chain, regulation of Myo1 activity as a consequence of phosphorylation has only been explored for the conserved TEDS motif within the motor domain. Mutations within the TEDS site to a phospho-mimic, were found to affect the ability of Myo1 to bind to longer actin cables allowing it to bypass the inhibitory effects of tropomyosin, resulting in the decoration of actin cables throughout the cell (East & Mulvihill 2011).

1.5.4 Myosin I in *Caenorhabditis elegans*

C. elegans encodes at least ten unconventional myosin motor proteins from classes I, V, VI, VII and XII. Heavy chain Unconventional Myosin (HUM) 1 and HUM-5, are two structurally distinct unconventional class I myosins (Baker & Titus 1997). A known homolog of human Myo1e and mouse Myo1f, *hum-1* encodes a protein of 124 kDa in size, most closely related to the amoeboid myosin I subclass (Baker & Titus 1997). Presenting a typical class I structure, the motor domain of HUM-1 is found at the amino–terminal end of the protein adjacent to the neck region which contains a single IQ motif.

Similar to other class I myosins, HUM-1 contains a residue known as the TEDS site in the head domain, located at the tip of the actin-binding surface loop, 16 residues upstream of the conserved DALAK (347 - 351) sequence (Bement & Mooseker 1995). Unlike amoeboid myosin Is however, HUM-1 has a charged residue (Glu 331) at this position which supersedes the need for phosphorylation. The neck region is immediately followed by a highly positively charged polybasic domain (aa 729 to 824), a GPA domain rich in the amino acids Gly, Pro, Ala, Glu and Asn that binds to actin in an ATP-insensitive manner and an SH3 domain at the very carboxyl–terminus of the protein (amino acid residues 1073 to 1099) (Baker & Titus 1997; Pollard 1991; Senda et al. 2001).

Although not much is known about protein localisation and function, the genetic position of *hum-1* maps the gene near two larval lethal alleles and a single mutant defective in its ability to lay eggs (Baker & Titus 1997). Phylogenetic analysis shows that HUM-1 and HUM-5 belong to the same class of myosins, however HUM-5 represents a separate subclass which includes rat myr4 and *Drosophila* IA (Baker & Titus 1997). With a molecular weight of 117 kDa, HUM-5 is composed of motor domain, 2 IQ motifs in the neck region and a short basic tail. A homolog of Myo1d, not much is known

about the protein localisation or function of *hum-5* although it has been hypothesized HUM-1 and HUM-5 offer a unique opportunity to study individual and overlapping functions, at the genetic level, of two distinct subclasses of myosin I motor proteins.

1.6 Post-translational modifications

Post-translational modifications (PTMs) are fundamental mechanisms for modulating protein function, with reversible or irreversible chemical modifications such as phosphorylation, ubiquitination and acetylation found to influence nearly all aspects of normal cell biology and pathogenesis (F. Li et al. 2011). Essential for increasing proteomic diversity and dynamically coordinating signalling networks, PTMs are often mediated by the enzymatic activity of kinases, phosphatases, ligases and transferases and occur at distinct amino acid side chains or peptide linkages. The addition or removal of functional groups often alters protein function via changes in the protein structure and dynamics or by regulating binding to partner proteins that recognise the modified residue (S. Li et al. 2010). Mutations of post-translational target sites have been found to be directly involved in diseases such as heart disease, human hereditary lethal disease and cancer, highlighting the importance of PTMs in maintaining normal cellular states (Y.-C. Wang et al. 2013).

1.6.1 Acetylation

Carried out by N-a-acetyltransferase (Nat) complexes, amino- terminal acetylation is a ubiquitous protein modification affecting up to 98% of proteins in eukaryotes, both co- and post- translationally (M. Johnson et al. 2010). A multifunctional regulator, amino- terminal acetylation has diverse effects

upon protein structure, stability and function, acting as a protein degradation signal, an inhibitor of endoplasmic reticulum (ER) translocation and as a mediator of protein complex formations (Starheim et al. 2012; M. Johnson et al. 2013). In some instances, acetylation also determines the subcellular localisation for certain proteins such as Cdc8 in the fission yeast (Drazic et al. 2016).

Currently eukaryote cells are thought to possess up to six distinct classes of Nat complexes (Nat A-F), which transfer an acetyl group from acetyl-coenzyme A (Ac-CoA) to the a-amino group of the first amino acid residue of a protein, according to its amino-terminal dipeptide. In addition to impacting a large number of cellular processes including cell cycle progression, cytoskeletal organisation and apoptosis, amino-terminal acetylation also plays a role in disease states such as heart disease, epithelial cancers and fragile X syndrome (Timmermann et al. 2001).

1.6.2 Phosphorylation

An important, ubiquitous cellular regulatory mechanism in eukaryotic cells, phosphorylation is a reversible post-translational modification regulated independently by the two types of enzymes; protein kinases and protein phosphatases. Structurally and functionally diverse with highly conserved catalytic domains, protein kinases phosphorylate proteins by catalysing the transfer of the γ-phosphate of ATP (γ-PO32-) to the nucleophilic (-OH) side chains of the specific amino acid residues; serine, threonine and tyrosine (L. N. Johnson 2009). The introduction of a charged and hydrophilic group alters the overall charge of the residue resulting in conformational changes that often activate or inactivate the substrate protein by altering its activity, subcellular localisation, binding properties or association with other proteins.

Some proteins contain multiple phosphorylation sites, facilitating complex multi-level regulation, making this type of modification a flexible mechanism for cells to respond to external signals and environmental conditions (Y. Wang et al. 2014). Protein phosphatases catalyse de-phosphorylation through the removal of phosphate groups from the substrates. Although phosphorylation by protein kinases provides an efficient and effective means to regulate most physiological activities, including metabolism, transcription, cell cycle progression, differentiation, cytoskeleton arrangement cell proliferation and apoptosis, aberrant regulation of kinases has been implicated in many diseases including cancer, inflammatory diseases, diabetes and neurological disorders (López-Otín & Hunter 2010)

1.7 Hydrostatic pressure

Within the biosphere, hydrostatic pressure can range over four orders of magnitude, from 1 bar at the surface to 1200 bar in extreme environments such as the deep-sea (Gross & Jaenicke 1994). A key physical parameter affecting cellular physiology, hydrostatic pressure has influenced the evolution of numerous micro- and macro- organisms throughout time, yet the exact mechanisms adopted to survive and adapt to pressure stress are still largely unknown (Bartlett 2002).

1.7.1 Principles of pressure perturbation

Le Chatelier's principle states that an increase in pressure shifts the chemical equilibrium of a reaction towards the direction in which the net volumes of the reacting molecules become smaller. However, folded proteins are highly incompressible with near zero changes in volume seen to accompany protein transitions (Hillson et al. 1999). This is due to a

complex interplay between the intramolecular architecture of the protein, its hydration and its thermal volume (Akasaka & Matsuki 2015). Instead, the reduction in the overall volume of the system is a result of pressure induced conformational changes altering the dynamic structure of water particles interacting with proteins, complexes and polymers. These changes often lead to protein denaturation, protein dissociation, dissociation of protein−nucleic acid complexes and disassembly of aggregates such as amyloids (Figure 1.11) (Silva et al. 2009).

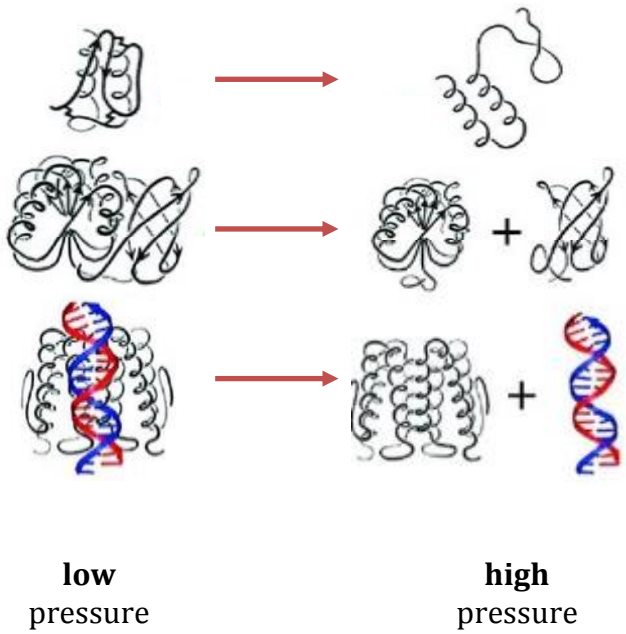

Figure 1.11 Hydrostatic pressure effects. Pressure often promotes protein conformational changes which may induce protein denaturation, protein dissociation and dissociation of protein−nucleic acid complexes. This allows the system to shift the equilibrium of the reaction in the direction in which the net volumes of the reacting molecules become smaller. Adapted from (Silva et al. 2009)

At low pressures water, macromolecules and therefore tissues are largely incompressible because water will balance the tendency of forming an open structure from directional hydrogen bond interactions, with the tendency to pack as Lennard–Jones particles to reduce its volume. Upon the application of pressure, this balance is shifted affecting the dynamic fluctuations of a protein in an aqueous solvent (Hillson et al. 1999; Zonia & Munnik 2007).

As pressure increases, it acts at the level of driving a system from a lower density to a higher density, often denaturing proteins, protein-protein interactions or aggregates via solvation of peptide groups or by partial disappearance of large intra-globular voids (Zonia & Munnik 2007). Denaturation by solvation occurs when the transfer of a peptide group from the protein interior to water becomes increasingly favorable. This decreases protein stability / protein-protein interactions enabling free water to penetrate the hydrophobic core of the molecule. This results in a decrease in the overall volume of the system due to the water molecules packing as Lennard-Jones particles, decreasing in the amount of disordered free water (J. A. Kornblatt & M. J. Kornblatt 2002).

Conversely, denaturation by the disappearance of intra-globular voids increases protein stability and occurs when the transfer of nonpolar side chains from the protein interior to water becomes more un-favourable. The absence of structural constraints results in tighter packing of the protein interior than when in its native state (Akasaka & Matsuki 2015). Compression of proteins is often not an uniform event as some tertiary structures such as helices are more compressible than loops and strands, therefore peptide groups engaged in intra-helical hydrogen bonds in an isolated peptide occupy a smaller volume than when forming hydrogen bonds with water. If a protein-protein or protein-ligand has a high equilibrium constant, applying pressure will have little effect; however, if the equilibrium constant is low, applying pressure will perturb the system more readily.

1.7.2 Applications of hydrostatic pressure

Pressure is a fundamental thermodynamic variable as important as temperature, which has been gradually gaining in popularity (Zonia & Munnik 2007). Historically, hydrostatic pressure had been extensively explored within food science as it offers a method in which it is possible to keep the heat, sensory, and nutritional attributes of a product, whilst inactivating microorganisms and enzymes responsible for shortening shelf life. This yields products of better quality than those processed using traditional methods (Balny, Masson & Heremans 2002b).

In addition to use within the food industry, hydrostatic pressure has been utilised for the production of synthetic materials such as alginate gels, and in recent years has been employed in methods as a less “invasive” perturbation to disclose the multiple-conformational and dynamic reality of bio-macromolecules, notably high-pressure NMR and X-ray scattering/ crystallography, This has contributed to a more in-depth understanding of protein structures and life phenomena such as motility, physiology/disease and adaptation/evolution (Akasaka & Matsuki 2015). The strategic and efficient use of hydrostatic pressure has also been explored for applications within the health industry where it has already been found to act as a mechanical stimuli for cartilage development, offering a promising approach for the regeneration of damaged tissues (San Martín et al. 2002).

1.7.3 Use of hydrostatic pressure as a molecular probe

Although widely used within the fields of physic-chemical biochemistry and biotechnology, use of hydrostatic pressure to investigate cellular responses is considerably less frequent due to the technical difficulties associated with pressure studies (Balny, Masson & Heremans 2002a). When compared to

conventional methods of perturbing systems such as temperature and/or chemical composition of the medium, hydrostatic pressure offers a number of advantages to modulate samples under investigation.

Perturbations caused by variables such as temperature have been found to cause simultaneous changes in the volume and thermal energy in a way which makes it difficult to separate their effects (Roche et al. 2013). This is due to biological macromolecules being flexible molecules that maintain secondary, tertiary and quaternary structure by bonds of strengths not much greater than thermal energy. The application of pressure however, offers a method that perturbs internal interactions exclusively by changes in the distances of the components, not significantly affecting the total energy of the system (Barciszewski et al. 1999).

Hydrostatic pressure perturbations in an *in vitro* or *in vivo* environment also provide an excellent method for probing the structure/function relationship of various proteins and protein conjugates as the effects of pressure are often fully reversible with more conventional methods such as pH changes often inducing a number of stress responses which have non-reversible and destructive effects upon the cell / molecule under investigation. Although it has been found that moderate pressures (>200 bar) are relatively benign to cell viability, specific processes in the cell are very sensitive to changes in pressure. Small molecule model systems have given information on the effects of pressure on non-covalent intermolecular interactions and have shown high hydrostatic pressure stabilises hydrogen bonds and destabilizes hydrophobic interactions that play a substantial role in stabilizing protein tertiary structures and protein–protein interactions (Athanasiou et al. 2015).

In the context of the larger field of protein structure and dynamics, hydrostatic pressure has been shown to disrupt cellular systems such as cytoskeleton assembly/disassembly, both actin and microtubules,

ribosome assembly and muscle contraction although much remains unclear (Fortune et al. 1991). The ability to combine conventional fluorescent microscopy based techniques with a hydrostatic pressure system offers a method to expand the utility of pressure perturbations, allowing the dynamic changes of various intracellular components and how each alters in response to pressure changes in the environment to be followed in real time, aiding in the characterization of fundamental cellular processes. The use of hydrostatic pressure to dissect the cellular functions of proteins also offers a number of advantages over conventional methods.

1.8 Objectives of Investigation

The main aims of this study were to investigate various components of the actin cytoskeleton using a variety of microscopy based techniques.

The first part of the project focused on determining the localisation and function of the class I myosin motor proteins in *Caenorhabditis elegans* testing the hypotheses: HUM-1 and HUM-5 have discrete localisations and HUM-1 and HUM-5 have discrete functions. In addition, homologs of Myo1e found in *Caenorhabditis elegans* and *Schizosaccharomyces pombe* were used to explore the role of a conserved phosphoserine residue within the TH1 domain, testing the hypotheses: phosphorylation of this conserved serine is required for protein localisation and protein function.

Next, *Schizosaccharomyces pombe* Cdc8 was used to explore the biochemical and functional properties of tropomyosin in both temperature sensitive mutants and fluorescent protein fusions. The final part of the project was spent developing a novel hydrostatic pressure imaging system which would allow fluorescently tagged protein dynamics to be followed within living cells under pressure.

Chapter 2: Materials and Methods

2.1 Materials

2.1.1 Enzymes and kits.

Enzymes used for molecular biology techniques were purchased from New England Biolabs or Promga and all DNA purification kits were from Qiagen.

2.1.2 Buffers

The buffer compositions are stated in the context of their use. A compiled full description of the buffers is listed in appendix.

2.1.3 *Escherichia coli* strains

DH10β competent cells were used for plasmid DNA amplification. BL21 DE3 and BL21 DE3 NatB competent cells (M. Johnson et al. 2010) were used for protein expression and amino-terminally acetylated protein expression respectively.

2.1.4 *Caenorhabditis elegans* strains

Strain	Genotype	Short annotation
N2	*C. elegans* wild type (ancestral)	N2
RB1557	*hum-5(ok1885) III*	*hum-5*
RB818	*hum-1(ok634) I*	*hum-1* (RB818)
JMT6	*hum-1(ok634) I*	*hum-1*
JMT8	*hum-1(ok634) I; hum-5(ok1885) III*	*hum-1;hum-5*
JMT12	*[Phum-1::gfp::hum-1 S734D::hum-1 3'UTR]*	*gfp::hum-1S734D*
JMT15	*[Phum-1::gfp::hum-1 S734A::hum-1 3'UTR]*	*gfp::hum-1S734A*
JMT19	*[Phum-1::gfp::hum::hum-1 3'UTR]*	*gfp::hum-1*
JMT24	*hum-1(ok634) I; [Phum-1::gfp::hum::hum-1 3'UTR]*	*hum-1;gfp::hum-1*
JMT25	*hum-1(ok634) I; [Phum-1::gfp::hum-1 S734A::hum-1 3'UTR]*	*hum-1;gfp::hum-1S734A*
JMT26	*hum-1(ok634) I; [Phum-1::gfp::hum-1 S734D::hum-1 3'UTR]*	*hum-1;gfp::hum-1S734D*
XW8490	*yqIs100(Pced-1mCHERRY::ACT-1)*	XW8490
JMT38	*hum-1(ok634)I;[Phum-1::gfp::hum::hum-1 3'UTR] yqIs100(Pced-1mCHERRY::ACT-1)*	*hum-1;gfp::hum-1;mCh::act-1*
JMT39	*hum-1(ok634) I; hum-5(ok1885) III; [Phum-1::gfp::hum::hum-1 3'UTR] [Phum5::mCHERRY ::hum::hum-5 3'UTR]*	*hum-1;gfp::hum-1;hum-5;mCh::hum-5*

JMT40	*[Phum5::mCHERRY::hum::hum-5 3'UTR]*	*mCh::hum-5*

Table 1.1 *C. elegans* strains used throughout this project. Column 1 gives the lab stock name. All listed JMT strains were generated within the lab for this project. Column 2 provides strain genotypes; gene mutations are given names consisting of three italicised letters and an italicized Arabic number, followed by an italicised Roman numeral to indicate the linkage group on which the gene maps. Gene deletions are given a single allele name eg. *ok634.* Prefix P refers to extra-chromosomal plasmid, *Is* refers to integrated transgenes. Column 3 gives the short annotation that will be used when referring to that particular strain.

2.1.5 *Schizosaccharomyces pombe* strains

Strain	Genotype	Short name
201	*myo1:leu2 ura4-d18 leu1-32*	*myo1:leu2*
333	*cdc8-110 (IH3417)*	*cdc8-110*
360	*leu1-32 ura+) (ts)*	TM011
365	*ura4-d18 leu+ His+*	ura4-d18
761	*ura4-d18*	*ura4-d18*
829	*myo1::kanMX6 leu1-32 ura4-d18 his3-d1 ade6-M216*	*myo1::kanMX6*
968	*myo1::kanMX6 leu1+ ura4.d18*	*myo1::leu1+*

1202	*cdc8::kanMX6/cdc8+ ade6.M210/ade6.M216 ura4.d18/ura4.d18 leu1.32/leu1.32 V358*	*cdc8::kanMX6/cdc8+ pSPO*
1875	*ura4-d18*	*ura4-d18*
1929	prototroph	prototroph
2129	*cam1-gfp:kanMX6 prototroph*	*cam1-gfp:kanMX6*
2150	*leu1-32*	*leu1-32*
2217	*hht-cgfp:NAT*	*hht-cgfp prototroph*
2410	*cdc8-110his2-ura4.d18leu1.32 pREP41NtermeGFP*	*cdcd-110 pREP41NtermeGFP*
2411	*cdc8-110 his2- ura4.d18 leu1.32 pREP41cdc8-his6-cerulean3*	*cdc8-110 pREP41cdc8 HisCerulean3*
2412	*cdc8-110 his2- ura4.d18 leu1.32 pREP41cerulean3-Hiscdc8 (v675)*	*cdc8-110pREP41 cerulean3-His cdc8*
2423	*pREP41His6-cdc8-cerulean3*	*cdc8-cerulean3-*
2424	*pREP41cerulean3-Hiscdc8*	*pREP41cerulean3-His cdc8- (2150 675)*
2441	*nop1-gfp-his1*	*Candida Albicans*
2446	*cdcd-110 his2-ura4.d18 leu1.32pREP41-cdc8*	*cdc8-110 pREP41cdc8 clone 3 (v99)*
2470	*cdc8-110 his2- ura4.d18 leu1.32 myo52-cherry:hphMX6*	*cdc8-110 myo52 cherry*
2478	*myo2-mCherry:hphMX6 ura4.d18 his2- leu1.32*	*myo2-mCherry cdc8-110*
2481	*cdc8-110 his2- ura4.d18 myo52-cherry:hphMX6 2471 v99*	*cdc8-110 Myo52 cherry v99*
2502	*cdc8-110 his2- ura4.d18 myo52-cherry:hphMX6 2471 v675 clone 1*	*cdc8-110 Myo52 cherry cer3-cdc8*

2504	*cdc8-110 his2- ura4.d18 myo52-cherry:hphMX6 2471 v674 clone 1*	*cdc8-110 Myo52 cherry cdc8-cer3*
2512	*myo2-mCherry:hphMX6 ura4.d18 his2- Cdc8-cer3*	*myo2-mCherry cdc8-110 v674*
2514	*myo2-mCherry:hphMX6 ura4.d18 his2- Cdc8*	*myo2-mCherry cdc8-110 v99*
2516	*myo2-mCherry:hphMX6 ura4.d18 his2- Cer3-cdc8*	*myo2-mCherry cdc8-110 v675*
2614	*mNeongreen-myo1:ura4 ura4.d18*	*mNeongreen-myo1* proto
2633	*mNeongreen-myo1:ura4 sid4-tdTomato:hphMX6 ura4.d18*	*mNeongreen-myo1 sid4-tdTomato*
2710	*myo1S782A*	*myo1S782A* proto
2750	*myo1::kanMx6V810mNgS782Amyo1*	
2762	*myo1::KanMX6 ade6-M210 leu1-32 ura4-d18*	*myo1::kanMX6*
2765	*myo1S782A ade6-M210 leu1-32 (V810)*	*myo1S782A*
2767	*myo1S782D ade6-M210 leu1-32 (v812)*	*myo1S782D*

Table 1.2 *S. pombe* strains used throughout this project. Column 1 gives the lab stock number. Column 2 provides strain genotypes. Column 3 gives a short annotation. Gene names are expressed as a three letter, italic name followed by a number. Deletions indicated by ::.

2.1.6 Plasmids used in this study

Stock	Plasmid	Source
9	pREP41nGFP	Craven, 1998.
11	pREP41cGFP	Craven, 1998.
80	pJC20*cdc8*	This Lab
99	pREP41*cdc8*	This Lab
241	pREP41*TPM1*	This Lab
652	pMKRQ-Nde1-*cdc8-cerulean3*-G3H6-BamH1	GeneArt
653	pMKRQ-Nde1-H6G3*cerulean3-cdc8*-BamH1	GeneArt
660	pJC20*cerulean3-cdc8*	This Lab
662	pJC20*cdc8-cerulean3*	This Lab
674	pREP41*cdc8-cerulean3*His6	This study
675	pREP41His6*cerulean3-cdc8*	This study
677	pJC20*cdc8-A18T*	This Lab
678	pJC20*cdc8-27E129K*	This Lab
679	pJC20*cdc8-E31K*	This Lab
680	pJC20*cdc8-110A18TE31K*	This Lab
710	pTOPO500US*mCherrymyo1*-Ura4	This Lab
725	pMA-T-*myo1flank-Ura4*	GeneArt
727	pMK-RQ-*gfp-hum1ds*	This study
728	pUC18-*gfp-downst*	This study
731	pMK-RQ-*hum-1*	Geneart
733	pET151DTOPO-*myo1IQ12S782ATH1*	This Lab
734	pGEM-T-*hum-1promoter*	This study
737	pET151DTOPO-*myo1IQ12S782DTH1*	This Lab
743	pUC18	This study

749	pUC18-*promoter-gfp -downst*	This study
755	pET151DTOPO-*myo1IQ12S782Atail*-Ura4	This study
761	pTOPO*myo1-S782A*-URA4	This study
763	pUC18-*promoter-gfp-hum1-downst*	This study
764	pMA-T-*hum-1*	This study
767	pET151DTOPO-*myo1IQ12S782Dtail*-Ura4	This study
769	pMA-T-*hum-1S734A*	This study
773	pMA-T-*hum-1S734D*	This study
776	pUC18-*promoter-gfp-hum1S734A-downst*	This study
782	pUC18-*promoter-gfp-hum1S734D-downst*	This study
792	pTOPO*myo1-S782D*-Ura4	This study
810	pTOPO-*500USNeongreenmyo1S782A*-Ura4	This study
812	pTOPO-*500USNeongreenmyo1S782D*-Ura4	This study
819	pMX-K-*Utr-mCherry-dsutr*	Geneart
820	pMX-K-*hum-5*	Geneart
821	pMX-K-*Utr-mCherry-hum5-dsutr*	This stusy
823	pUC18-*Utr-mCherry-hum5-dsutr*	This study
M13	pTOPO*myo1:ura4*	This Lab
M74	pINT41-*gfp-myo1*	This Lab
pGEM	pGEM-T-easy	Promega

Table 1.3 Plasmids used throughout this project. Column 1 gives the lab stock number. Column 2 provides plasmid information. Column 3 indicates which plasmids were made during this study.

2.1.7 Oligonucleotide primers

Oligo	Annotation	Sequence 5' – 3'
293F	Myo1 700bp	TAT CAA TTC ACC AAG AGC
294F	Myo1 1400bp	CAA TAA AGT TGT ATG TG
295F	Myo1 2100bp	AGC AAA GTT TTC ATT AAA
296F	Myo1 2800bp	AAA CTG TTA AGA CGG C
540F	5' Nde1-myo1	CAT ATG GCC ATC CTT AAG AGA ACA AAC CGC GCG
541R	3' Sal1-myo1	GTC GAC TCA CCA ATC TTC TTC TTC ATC ACT ACC ACG
552F	Nru1hum1F	TCG CGA ATG GCG TTC CAC TGG CAA TC
553R	Not1hum1R	GCG GCC GCT TAT TCT TTG ACA TAA TTT CCG GG
554F	Xma1hum1promF	CCC GGG CTC ATT TTTCTG TAT ATT TCG CC
555R	BamH1hum1promR	GGA TCC AAT GAA CCA CCG GCG TAT TTA C
564F	Hum1 S734A	GGC GCT ACG CGT TAA ACC GAA ACT TTG TCG GAG ATT ACA TTG GAC

565R	Hum1 S734A	TCG AGT CCA ATG TAA TCT CCG ACA AAG TTT CGG TTT AAC GCG TAG CGC
566F	Hum1 S734D	GGC GCT ACG ATT TAA ACC GAA ACT TTG TCG GAG ATT ACA TTG GAC
567R	Hum1 S734D	TCG AGT CCA ATG TAA TCT CCG ACA AAG TTT CGG TTT AAA TCG TAG CGC
588F	Myo1 600bp US	GCG TTA TAA TAA TCT GCG GC
590F	Hum-5 F	TGG TGA AGC AAT TGG CAC
591I	Hum-5 I	TCA GAG ATG TTC GCC GAA TG
592R	Hum-5 R	CGA CAA TGT CGT TAT CGC CA

Table 1.4 Oligonucleotide primers used throughout this project. Column 1 gives the lab stock number, F refers to forward, R refers to reverse direction of primer. Column 2 provides plasmid short annotation. Column 3 gives oligonucleotide sequence.

2.1.8 Media and stock solutions

NGM medium

Reagent	Quantity 1L	[Final]
Bactopeptone	2.5 g	0.25 %
NaCl	3 g	0.05 M
Agar	17 g	1.7 %
KPO_4 · (1M pH 6.0)	25 mL	1 mM
$MgSO_4$ · (1M)	1 mL	1 mM
$CaCl_2$ · (1M)	1 mL	1 mM
Cholesterol (5 mg/ml)	1 mL	5 ug

YES medium

Reagent	Quantity 1L	[Final]
Yeast extract	5 g	0.5 %
Glucose	30 g	3.0 %
Supplements	*	*

Minerals (10,000×)

Reagent	Quantity 1L	[Final]
Boric acid	5 g	80.9 mM
MnSO4	4 g	23.7 mM
ZnSO4 · 7H2O	4 g	13.9 mM
FeCl2 · 6H2O	2 g	7.40 mM
Molybdic acid	0.4 g	2.47 mM
KI	1 g	6.02 mM
CuSO4 · 5H2O	0.4 g	1.60 mM
Citric acid	10 g	47.6 mM

Vitamins (1000×)

Reagent	Quantity 1L	[Final]
Pantothenic acid	1 g	4.2 mM
Nicotinic acid	10 g	81.2 mM
Inositol	10 g	55.5 mM
Biotin	10 mg	40.8 uM

LB medium

Reagent	Quantity 1L	[Final]
Yeast extract	5 g	0.5 %
Tryptone	10 g	1.0 %
NaCl	10 g	171 mM

Salt stock (50 x)

Reagent	Quantity 1L	[Final]
$MgCl_2 \cdot 6H_2O$	52.5 g	0.26 M
$CaCl_2 \cdot 2H_2O$	0.735 g	4.99 mM
KCl	50 g	0.67 M
Na_2SO_4	2 g	14.1 mM

EMMG medium

Reagent	Quantity 1L	[Final]
Glucose	20 g	111 mM
Glutamic acid	3.38 g	20 mM
Na_2HPO_4	2.2 g	15.5 mM
$C_8H_5KO_4$	3 g	14.7 mM
NH_4Cl	5 g	93.5 mM
Vitamins (1000x)	1 mL	1x
Minerals (10,000x)	0.1 mL	1x
Salt	20 mL	1x

SC Complete medium

Reagent	Quantity 1L	[Final]
$C_4H_6O_4$	10 g	
NaOH	6 g	
$(NH_4)_2SO_4$	5 g	
SC-Complete	1.39	
Glucose	20 g	
YNB (w/o amino acids / $(NH_4)_2SO_4$)	1.7 g	

* Appropriate supplements of 5 mM thiamine and 150 mg/ml of amino acids (leucine, adenine, uracil and histidine) were added as required.

2.2 Cultures

2.2.1 *S. pombe* cultures

Cells were grown in either the complex rich medium Yeast Extract plus Supplements (YES) or Edinburgh Minimal Medium with Glutamic acid (EMMG) with the relevant amino acids supplements to a final concentration of 150 mg/L (leucine, uracil, histidine or adenine) using standard culture methods (Moreno et al. 1991). Addition of 2% agar to media prior to autoclaving was used to prepare solid media plates. Repression of the nmt41 promoter was achieved using thiamine to a final concentration of 5 µM in EMM (Forsburg & Rhind 2006).

2.2.2 *E. coli* cultures

Cultures were grown at 37°C in Luria Bertani (LB) broth with plasmid selection achieved by the addition of ampicillin, chloramphenicol or kanamycin at a final concentration of 100 µg/ml.

2.2.3 *C. elegans* cultures

C. elegans were maintained on 60 mm petri dishes using standard culture methods (Brenner 1974). Nematode Growth Medium (NGM) agar plates were seeded with 200 µl of *E. coli* OP50 (Stiernagle 2006). Strains used were kept at 20ºC unless otherwise stated. All strains were maintained in a well fed and clean state for at least two generations before use in any experiments. Repression of progeny growth was achieved by the addition of 50 µg/ml of 5-fluoro-2′-deoxyuridine (FUDR) to agar plates.

2.2.4 *C. albicans* cultures

Cells were grown in Synthetic Complete (SC) medium supplemented with a complete mix of amino acids and vitamins in addition to 2% glucose. Addition of 2% agar to media prior to autoclaving was used to prepare solid media plates.

2.2.5 *S. pombe* growth curves

20ml cultures of *S. pombe* cells were grown at 25°C in EMMG lacking leucine in the presence and absence of 5 µM thiamine. Once cells reached mid-log ($2x10^6$) they were diluted to 0.05 OD600 and 1 ml was transferred into the wells of a Cellstar® 24 well culture plate. Growth curves were generated by monitoring OD^{600} at 25°C and 36°C with shaking at 200 RPM using a plate reader connected to a PC running software.

2.2.6 Cdc8 expression in *E.Coli*

Cdc8 proteins were expressed from pJC20 based plasmids in either BL21 DE3 or BL21 DE3 pNatB *E. coli* cells. 1L of LB media containing 0.1 mg/ml of the appropriate antibiotic was inoculated using 3 ml of an overnight starter culture. Cells were cultured in a 220 RPM shaking incubator at 37°C until reaching an OD_{600} of between 0.6 and 0.8. Isopropyl-β-D-1 thiogalactopyranoside (IPTG) was then added to a concentration of 0.1 mg/ml to induce expression of the T7 promoter, with cells cultured for a further 2 hours. Cells were harvested by centrifugation at 4000 RPM for 20 minutes at 4°C. Pellets were then re-suspended for protein extraction or frozen at – 20°C.

2.3 Molecular biology techniques

2.3.1 *C. elegans* standard genetic cross

Three NGM plates containing 10 L4 worms were heat shocked at 37°C for 4 hours to produce males. As a general ratio one hermaphrodite to seven males were then placed on an NGM plate containing a small spot of OP50. Crosses were conducted at 20°C. Picked strains with disrupted genes were confirmed with genotyping.

2.3.2 *E. coli* transformation

40µl aliquots of chemically competent *E. coli* cells stored at - 80°C were thawed on ice. 5 µl of plasmid DNA was added to the cells, mixed gently and incubated on ice for 30 minutes. Cells were heat shocked in a 42°C water bath for 90 seconds then placed back on ice for 2 minutes. 100 ml of LB was added and cells were incubated in a 36°C 220 rpm shaker for 1 hour then plated onto LB agar containing the appropriate antibiotic and placed at 36°C.

2.3.3 *S.pombe* transformation

Mid-log *S. pombe* cells were washed in 0.1 M lithium acetate pH 4.9, and then re-suspended in 100 µl lithium acetate per transformation. Cells were incubated at 25°C for 1 hour, then added to 100 µl of 70% PEG 4000 containing 5 µl of DNA and mixed by vortexing. Cells were incubated at 25°C for 1 hour then heat shocked for 10 minutes in a 42°C water bath. Cells were washed and re-suspended in EMMG then plated onto EMM agar with appropriate supplements.

2.3.4 *S. pombe* DNA extraction for PCR

10 ml of mid-log *S. pombe* cells were pelleted in an Eppendorf tube at 3 000 RPM for 5 minutes. Cells were re-suspended in 100 µl of 200 mM Lithium Acetate with 1% SDS and heated to 75°C for 10 minutes. 300 µl of 100% ethanol was added and cells were vortexed and spun down at 13 000 RPM for 3 minutes. The pellet was then washed with 70% ethanol, air dried for 10 minutes then re-suspended in 50 µl of dH_2O. The mixture was then centrifuged for 2 minutes at 13 000 RPM. 1 or 2 µl of supernatant was used for subsequent PCRs.

2.3.5 *C. elegans* single worm PCR lysis

To amplify DNA sequences of interest, worm samples were first prepared for PCR by typically immersing one adult worm in 5 µl proteinase K lysis buffer (50 mM KCl, 10 mM Tris (pH 8.3), 2.5 mM $MgCl_2$, 0.45% Nonidet P-40, 0.045% Tween-20, 0.01% (w/v) gelatinin, 100 ug/ml proteinase K). Worms were then lysed using a standard lysis protocol; 65°C for 1 hour, 95°C for 15 mins, 4°C final hold.

2.3.6 Standard *C. elegans* genotyping PCR

To genotype the various strains, three primers were designed such that the internal forward flanking primer (F2) and reverse flanking primer (R1) would amplify sequence at the 3' end of the gene of interest as shown in Figure 2.1. The forward external flanking primer (F1) was designed to recognise upstream sequence of the gene of interest, therefore highlighting gene deletions (Figure 2.1). Thermal-cycler conditions were optimised for each set of primers. Standard reaction mixes were; 3 µl primer, 5 µl worm lysis, 2 µl dH_2O, 15 µl GoTaq ® DNA polymerase.

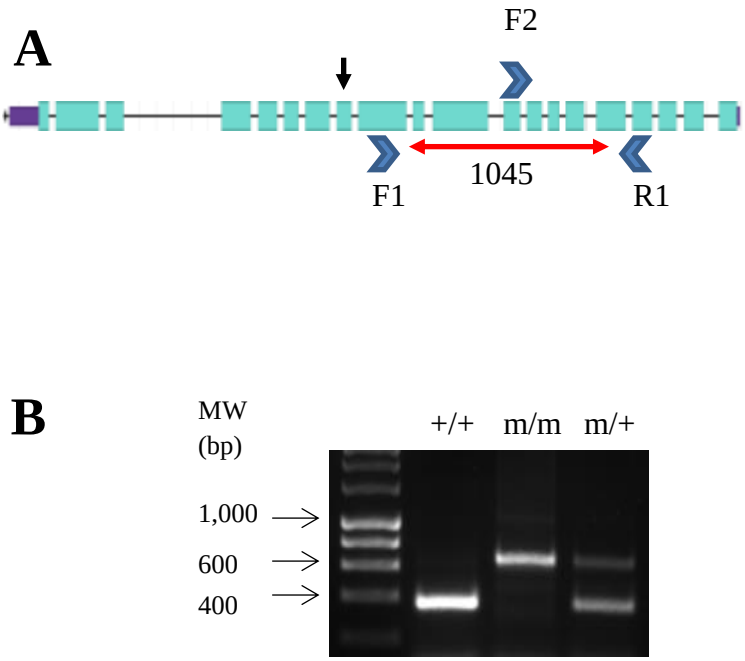

Figure 2.1 Standard PCR genotyping procedure for *C. elegans*. A) Schematic overview of primer location in relation to the gene of interest, indicated by the red double headed arrows. B) Example DNA agarose gel showing genomic PCR product. Primers F2 + R1 produce a ~ 355 bp N2 specific product (+/+). Primers F1 + R1 give a ~ 622 bp homozygote mutant specific product (m/m). Heterozygous strains produce a band for each size (m/+).

2.3.7 Back-crossing of the *hum-1 (ok634)* deletion strain

The first step in the back-crossing process required a homozygous *hum-1(ok634)* hermaphrodite from strain *hum-1* (RB818) to be crossed with a wild-type N2 male using a standard genetic cross protocol. First generation (F^1) hermaphrodite progeny were isolated onto separate NGM plates and left to populate. Once populated, the genotype of maternal hermaphrodites is confirmed by PCR using primers specific to the gene of interest (Figure 1).

PCR product for homozygous wild-type *hum-1* worms gave a predicted 355 bp fragment; homozygous *hum-1(ok634)* worms gave a predicted 622 bp mutant specific product. Heterozygous progeny gave a PCR band at each size (Figure 2.1). Hermaphrodites found with heterozygous expression of the *hum-1(ok634)* were selected and the subsequent progeny (F^2) were isolated onto separate NGM plates and again left to populate.

Once third generation progeny were present (F^3), the maternal hermaphrodites (F^2) were genotyped. Hermaphrodites found with homozygous expression of the *hum-1* deletion were selected, as all subsequent progeny would also be *hum-1(ok634)* homozygous (F^3). Step two then required the cross of an isolated homozygous *hum-1(ok634)* F^3 hermaphrodite from the first back-cross to be crossed with a N2 wild-type male. The back-crossing process was performed a further four times so the resulting homozygous *hum-1* strain shared approximately < 95% genetic identity with the lab N2 wild-type strain.

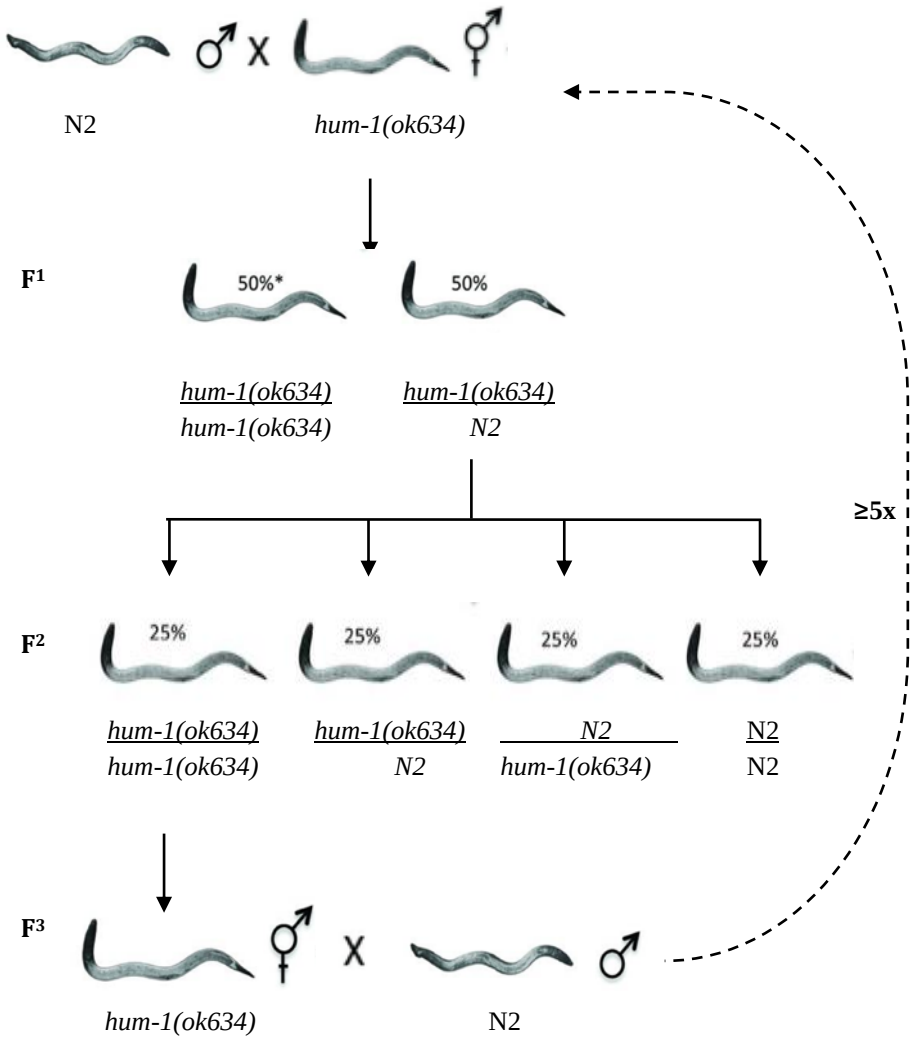

Figure 2.2 hum-1(ok634) back-crossing strategy. Step 1: N2 male is crossed with a *hum-1(ok634)* homozygous hermaphrodite. Heterozygous F^1 progeny are isolated and the F^2 generation tested for the presence of homozygous *hum-1(ok634)* by PCR. Step 2: A homozygous *hum-1(ok634)* F^3 hermaphrodite was crossed with an N2 male. This process was repeated a further 4 times. Following the back-crossing, the resulting homozygous *hum-1(ok634)* strain should share < 95% genetic identity with the lab N2 strain. Adapted from (Zuryn & Jarriault 2013).

2.3.8 Transgenic *C. elegans* genetic crosses

For strains containing the *gfp::hum-1* transgenes, the standard genetic cross protocol was used. However only rolling progeny containing the identification marker *rol6*$^{+}$ were selected. For strains containing endogenously tagged proteins, nematodes containing both the transgene and *rol6*$^{+}$ marker were first isolated then subsequent progeny were screened for stable homozygous expression of the endogenously tagged protein. Stable expression is achieved when 100% of progeny express the endogenously tagged protein.

2.3.9 Plasmid DNA preparation

Plasmid DNA from *E. coli* was extracted using a Qiagen - QIAprep spin miniprep kit, following the manufacturer's protocol. Plasmid DNA was then eluted into 50 µl of sterile elution buffer (10 mM Tric-Cl, pH 8.5) and stored at – 20°C.

2.3.10 Preparation of DNA

DNA was prepared using a typical digest mixture (10 µl DNA, 10 µl buffer, 2 µl enzyme 1, 2 µl enzyme 2, 76 µl dH2O) and incubated in a 37°C hot plate overnight. DNA fragments were then separated by electrophoresis on a 1% agarose gel and visualised by a UV transluminator. Desired bands were carefully excised from the gel using a razor blade and purified using a QIAquick gel extraction kit. The purified DNAs were subsequently ligated into the destination vector using a typical ligation mixture (2 µl vector, 6 µl insert, 1 µl buffer, 1 µl T4 DNA ligase) at 4°C overnight. Following ligation, reactions were amplified and purified from *E. coli*.

2.3.11 Electrophoretic separation of DNA

1% gels were prepared by dissolving 1 g of molecular biology grade agarose in TAE (40 mM Tris-acetate, 1 mM EDTA) by heating in a microwave at maximum power. The gel solution was then slightly cooled and poured into a casting tray of appropriate size, ethidium bromide was added to a final concentration of 0.5 µg/ml and the gel was left to set at room temperature. DNA loading buffer (0.25% bromophenol blue and 40% sucrose in dH_2O) was diluted 1:5 in sample DNA and samples loaded into gel wells. Samples were run alongside a 1 kb DNA ladder at 50 V for 30 to 60 minutes and visualized using a UV transluminator operated by Genesys 1.5.2 image acquisition software.

2.3.12 Cloning of *gfp::hum-1*

The *hum-1* 2 kb upstream promoter region was amplified from *C. elegans* cDNA using a typical PCR reaction with oligos 554 and 555, then cloned into a pGEM-T-Easy vector and confirmed by sequencing. Using Geneart, the GFP-downstream region was synthesized and inserted into a pUC18 plasmid using a BamHI, SalI digest and ligation. The promoter region was then excised and inserted into the pUC18-GFP-downstream construct via a SandI, BamHI digest. Genart synthesized *hum-1* was then cloned into the pUC18-prom-GFP-downstream by a NotI, NruI digest to make the final construct; pUC18-prom-GFP-HUM1-downstream.

2.3.13 Cloning of *gfp::hum-1* phosphoserine mutants

The two restriction sites; Nae1 and Xho1 were introduced into the synthesized *hum-1* gene either side of the conserved serine residue 734. The DNA was prepared by using a Nae1, Xho1 digest then ligated with PCR

product from oligonucleotides 564 and 565, which carried the S – A mutation. The introduction of this portion of DNA also introduced an Mlu1 site for correct clone identification. Once the S734A mutant was attained, it was digested using a Nae1, Xho1 digest and ligated with PCR product from oligonucleotides 566 and 567, which carried the S – D mutation. Correct clones would no longer carry the Mlu1 site allowing for quick identification.

2.3.14 Cloning of *mCherry::hum-5*

The two restriction sites PvuI and NruI were introduced into the synthesized *hum-5* gene. The DNA was prepared by using a PvuI, NruI digest and ligated into the synthesized promoter-mCherry-downstream vector. The DNA was then excised as a BamHI, SalI fragment and cloned into a pUC18 based vector.

2.3.15 *C. elegans* micro-injections

Strains containing the extra chromosomal *gfp::hum-1, gfp::hum-1S734A, gfp::hum-1S734D* or *mCherry::hum-5* transgenes were generated by co-injecting the plasmid DNA into the distal arm of the gonad of day one adult wild-type (N2) nematodes. The distal germ line contains a central core of cytoplasm that is shared by many germ cell nuclei therefore, DNAs injected here can be delivered to many progeny. DNA is injected at a concentration of 50 ng/μl along with *rol-6* at a concentration of 100 ng/μl. The identification marker *rol-6* carries the dominant collagen mutation, *rol6*$^{+}$ *(su1006)* which causes animals to roll and move in circles, a behaviour that can be easily recognised (Kramer et al. 1990). A minimum of two stable injection lines were isolated and a comparison of expression was made. One line, representative of protein expression was then chosen to take forward for all

experiments. All microinjections in this project were carried out by Marina Ezcurra from University College London.

2.3.16 Cloning of Cdc8 plasmids

The *cdc8-cerulean3-his$_6$* carboxyl *and his$_6$-cerulean3-cdc8* amino terminal *cdc8$^+$* fusions were synthesised as Nde1- BamH1 fragments (ThermoFisher) and cloned into pJC20 and pREP41 bacterial and fission yeast expression vector respectively. Plasmids containing mutated cdc8 alleles were amplified from genomic DNA preparations of *cdc8-27* and *cdc8-110* cells, cloned into pGEM-T-easy vectors and confirmed by sequencing. This procedure was repeated twice from independent genomic preps. *pJC20cdc8$^+$* was described previously (Skoumpla et al. 2007). *cdc8-A18T*, *cdc8-E31K, cdc8-A18TE31K* and *cdc8-E129K* were synthesised as Nde1 – BamH1 fragments (ThermoFisher) and cloned into the pJC20 (Clos & Brandau 1994) bacterial expression vector.

2.3.17 Cloning of *myo1$^+$* phosphoserine mutants

DNA containing the *myo1$^+$ S782A* and S782*D* mutations was synthesised by IDT and cloned using HpaI, AvrII into M13; a nutritionally marked ura4 vector replacing a portion of the existing wild type *myo1*. The presence of the S782 mutation was confirmed by the introduction of a HindiIII restriction site. For fluorescent versions of the S782 mutants, the *myo1S782* DNA was further cloned as an AflII, AvrII fragment into an M13 vector containing mNeon-green and a 500 bp upstream region of the *myo1* gene.

2.4 Biochemical techniques

2.4.1 Cdc8 extraction from *E. coli*

E. coli pellets containing cerulean Tpm constructs were re-suspended in 20 ml of lysis buffer pH 8.0 (50 mM Tris, 100 mM NaCl, 1 mM PMSF, 10 mM Imidazole, 2 mM EGTA). *E. coli* pellets containing mutant and WT Tpm were re-suspended in 20 ml of lysis buffer pH 7.5 (20 mM Tris - HCl pH 8.0, 100 mM NaCl, 2 mM EGTA, 5 mM $MgCl_2$). Lysates were sonicated for 3 minutes (30 sec pulse on, 59 sec pulse off). Mutant and WT Cdc8 samples were then heated to 65°C and 85°C for 10 minutes respectively.

Samples were centrifuged at 15,000 rpm for 10 minutes to remove cell debris and denatured proteins. Soluble mutant and WT Cdc8 was isolated by isoelectric precipitation at pH 4.55. The solution was then centrifuged at 15,000 rpm for 10 minutes, the supernatant was disregarded and crude Cdc8 pellets were frozen at – 20°C or re-suspended for purification. The supernatant of cerulean Tpm samples was incubated with 10 µg/ml DNase and RNase and 10 mM $MgCl_2$ at 4°C for 30 minutes.

2.4.2 Cdc8 purification by Nickel affinity gel

Cerulean Tpm samples were loaded onto a HIS-Select® Nickel Affinity Gel column. Wash buffer (50 mM Tris pH 8.0, 100 mM NaCl, 10 mM Imidazole, 2 mM EGTA) was passed through the column followed by elution buffer (50 mM Tris pH 8.0, 100 mM NaCl, 150 mM Imidazole, 2 mM EGTA, 1 mM PMSF). The samples were then exchanged into FPLC running buffer (5 mM TRIS, 100 mM NaCl pH 7.0) for purification.

2.4.3 Cdc8 purification by fast protein liquid chromatography (FPLC)

Mutant and WT Cdc8 pellets were re-suspended in FPLC running buffer (5 mM TRIS, 100 mM NaCl pH 7.0) and incubated with 10 ug/ml DNase and RNase and 10 mM $MgCl_2$ at 4°C for 30 minutes. All Cdc8 proteins were purified using two 5 ml GE Healthcare HiTrap-Q HP columns in tandem and eluted using a gradient of 100 – 900 mM NaCl. Using the UV 280 nm reading, the appropriate fractions were collected. Cerulean Cdc8 was exchanged back into FPLC running buffer using an Amicon Ultra-15 centrifugal filter unit with an ultracel-3 membrane for subsequent purification. Mutant and WT Cdc8 were isolated using HCl isoelectric precipitation at pH 4.55 and centrifugation, then re-suspended in FPLC running buffer for subsequent purification. FPLC purification was typically used three times. After the final elution, Cdc8 was re-suspended in the appropriate buffer, snap frozen in liquid nitrogen and stored at –80°C. Protein concentration was determined using a Bradford protein assay.

2.4.4 Bradford protein assay

Eight dilutions of bovine serum albumin (BSA) from 0.0 mg/ml to 1.2 mg/ml were prepared by diluting the stock of BSA (10 mg/ml) in the same buffer as the unknown protein samples. Proteins under investigation were diluted 1:6 and 1:8 in the same buffer as the unknown protein samples. 33 μl of each dilution was transferred to a 1.6 ml semi-micro cuvette made of polystyrene, then 1 ml of Bradford reagent was added. The mixture was left to incubate at room temperature for 10 minutes. The absorbance at 595 nm was measured using a spectrophotometer with an empty cuvette used as the blank. The net absorbance against the protein concentration of each standard was plotted in Excel. The protein concentrations of the unknown samples are then determined by comparing the absorbance against the standard curve and averaging.

2.4.5 SDS-PAGE Gel

SDS – PAGE was performed using Novex™ 4-20% Tris-Glycine precast polyacrylamide gels. Gels were assembled in the gel tank containing NuPAGE® MOPS SDS running buffer. Samples were mixed with SDS loading buffer (0.02% Bromophenol Blue, 5% β-Mercaptoethanol, 30% glycerol, 10% SDS, 250 mM Tric-Cl pH 6.8) at a ratio of 1:5 then heated to 85°C for 10 minutes using a hot plate. 15 µl of sample was then loaded and gels run at 150V for 50 minutes. Following this, gels were immersed in coomassie staining solution (0.1% coomassie brilliant blue, 50% methanol, 10% acetic acid) and incubated for 2 hours with gentle agitation. After staining, gels were put into de-staining solution (50% methanol, 10% acetic acid) overnight.

2.4.6 Western blot genomic DNA extraction

20 ml of mid-log *S. pombe* cells were pelleted in a falcon tube at 3 000 RPM for 5 minutes. Cells were then re-suspended in STOP buffer pH 8.0 (150 mM $NaCl_2$, 10 mM EDTA, 1 mM NaN_3) and transferred to a 2 ml screw top mechanical lysis tube and centrifuged at 13 000 RPM for 1 minute at 4°C. 200 µl 20% Trichloroacetic acid (TCA) was added to the pellet with 0.5 ml of glass beads. Cells were lysed in a FastPrep® Instrument at full power for 45 seconds, then 400 µl of 5% TCA added. The sample was then centrifuged at 3 500 RPM for 1 minute. Once the supernatant was removed the pellet was re-suspended in 50 µl of 5 X SDS loading buffer (0.02% Bromophenol Blue, 5% β-Mercaptoethanol, 30% glycerol, 10% SDS, 250 mM Tric-Cl pH 6.8) and heated to 80°C for 10 minutes, then centrifuged at 13 000 RPM for 2 minutes. The sample was then ready for gel loading.

2.4.7 Western blots

S. pombe cell extracts were separated using Novex™ 4 - 20% Tris-Glycine precast polyacrylamide gels at 150 V for 50 minutes and blotted onto methanol activated PVDF membrane using a BioRad Trans-Blot® semi-dry electro blotter at 10 V for 30 minutes. After blotting membranes were blocked with 3% skimmed milk powder in Phosphate-buffered saline (PBS) for 1 hour at room temperature with gentile agitation. Subsequently membranes were incubated at room temperature with anti-Myo1 antibody (antigen region AKDETTKDYDYYKSG) at a 1:100 dilution in PBS with 3% skimmed milk powder overnight with gentle agitation then washed 3 times in PBST (PBS + 0.2% Tween^{20}) for 10 minutes with gentle agitation.

Membranes were then incubated at room temperature with an anti-rabbit IgG alkaline phosphatase secondary antibody (Sigma-Aldrich) in PBS with 3% skimmed milk powder for 1 hour with gentle agitation. Membranes were subsequently washed 3 times in PBST for 10 minutes with gentle agitation followed by incubation with western blot detection buffer (0.1 M Tris pH 9.6, 0.1 M NaCl, 5 mM $MgCl_2$) for 5 minutes. Excess buffer was disregarded and 2 ml of BCIP®/NBT-Purple Liquid Substrate (Sigma) was added to membranes and incubated at room temperature with gentle agitation. The reaction was stopped by washing with de-ionised water.

2.4.8 Mass spectrometry

Samples were analysed by Kevin Howland, using electrospray mass spectrometry (Bruker MicroTOF-Q) and Bruker compass data analysis 4.1 software.

2.4.9 Circular Dichroism

Tpm proteins were diluted in CD buffer (10 mM K phosphate, 500 mM NaCl, 5 mM MgCl2, pH 7.0) to a concentration of 0.1 mg/ml. Samples were loaded into a 1 mm quartz cuvette and CD was performed using a Jasco 715 spectropolarimeter. Thermal unfolding data were obtained by monitoring the CD signal at 222 nm with a heating rate of 1°C/min. At completion of the melting curve the sample was cooled at a rate of 20°C/min. CD spectra are presented as differential absorption (∆A). Melting curves are reported as fraction of unfolded protein by normalizing the CD signal between 10ºC and 50ºC.

2.4.10 Co-sedimentation and densitometric analysis

Co-sedimentation assays were performed by mixing 10 µM actin with increasing concentrations of Tpm, diluted in Tpm binding buffer (20 mM MOPS, 5 mM $MgCl_2$, 100 mM KCl, pH 7.0) to a total volume of 100 µl. Reactions were incubated at room temperature for 30 minutes. Samples were then centrifuged at 100,000 RPM for 20 minutes at 4°C using a Beckman ultracentrifuge. Actin along with any bound Tpm would pellet, leaving the remaining unbound Tpm in the supernatant. The supernatant and pellet were separated and the pellet was re-suspended in 100 µl of H_2O. 20 µl of SDS-PAGE loading buffer was added and samples were heated to 85°C for 10 minutes. 15 µl of each sample were separated using SDS-PAGE, gels were stained using Coomassie Blue and scanned using an Epsom perfection 1640 SU scanner with a transparency adaptor attached to a PC. Quantification of the co-sedimentation assay was achieved by densitometric analysis using Scion Image software (Scion Corp) and Origin. The $K_{50\%}$ value was determined by fitting the data with a non-linear Hill equation.

2.4.11 Viscosity

Cdc8 samples were re-suspended in viscosity buffer (20 mM MOPS, 5 mM $MgCl_2$, pH 7.0) and prepared to 20 µM. 1 ml of each sample was run in a Cannon-Manning semi-microviscometer at 23°C with NaCl increasing in concentration from 0 to 250 mM. Kinematic viscosity was then calculated using the manufacturer's predetermined microviscometer kinematic viscosity constant (0.03235) and the average efflux time, calculated from five observations per sample at each NaCl concentration.

2.5 Microscopy

2.5.1 Wide-field Microscopy

Samples were visualised using an Olympus IX71 microscope with PlanApo 100x OTIRFM-SP 1.45 NA lens mounted on a PIFOC z-axis focus drive (Physik Instrumente, Karlsruhe, Germany), and illuminated using LED light sources (Cairn Research Ltd, Faversham, UK) with appropriate filters (Chroma, Bellows Falls, VT). An Optosplit device (Cairn Research Ltd) was used to allow simultaneous acquisition of signals from two fluorophores that emitted light of different wavelengths. Samples were visualised using either a QuantEM (Photometrics) or ProEM 1024B (Princeton Instruments) EMCCD camera, and the system was controlled with Metamorph software (Molecular Devices).

Each 3D-maximum projection of volume data was calculated from 21 z-plane images, each 0.4 µm apart, and analysed using Metamorph. Digital deconvolution was performed using MediaCybernetics Autoquant X software. During live-cell imaging, cells were cultured in Edinburgh minimal media using 20 mM L-Glutamic acid as a nitrogen source (EMMG). Cells were grown exponentially at 25 ºC for 48 hr before being mounted (without centrifugation) onto lectin (Sigma L2380; 1 mg/ml) coated coverslips with

an a Bioptechs FCS2 (Bioptechs, Butler, PA), fitted onto an ASI motorised stage (ASI, Eugene, OR) on the above system, with the sample holder, objective lens and environmental chamber held at the required temperature.

2.5.2 Confocal Microscopy

For image acquisition, a Nikon A1si confocal laser scanning microscope (CLSM) was used with a plan-apochromatic VC 1.4 NA 60x magnifying oil-immersion objective (Nikon Corp., Tokyo, Japan), CFI Plan Apochromat VC 60XOil N2 NA 1.4 WD 0.13mm, CFI PlanFluor 40X oil N.A. 1.30 W.D. 0.2mm and a CFI Plan Apochromat VC 20X N.A 0.75, W.D. 1.0mm

Images were acquired in three channels, using one-way sequential line scans: Alexa Fluor 488 (GFP) was excited at 488 nm with laser power 7.8 AU, its emission collected at 525/50 nm with a PMT gain of 140 AU; Alexa Fluor 555 (mCherry) signal was excited at 561 nm with laser power 2.1 AU, and collected at 595/50 nm with a PMT gain of 117 AU; differential interference contrast images were acquired using the transmitted light detector at a gain of 103 AU.

In all cases no offset was used and the scan speed was ¼ frames/s (galvano scanner). The pinhole size was 34.5 µm, approximating 1.2 times the airy disk size of the 1.4 NA objective at 525 nm. Scanner zoom was centred on the optical axis and set to a lateral magnification of 55 nm/pixel. Axial step size was 140 nm, with 30–50 image planes per z-stack. 50–70 cells with average to fair signal strength in all channels were examined.

2.6 *C. elegans* phenotyping assays

2.6.1 Brood size assay

Brood size assays were performed at 20°C. A two-hour timed egg lay using 20 gravid hermaphrodites was conducted on NGM plates seeded with *E. coli* OP50 2 days prior to the brood size assay to synchronise nematode cultures. The progeny populated the corresponding plates until the L4 larvae stage. Once reaching the L4 larvae stage and the ovaries of the hermaphrodites had begun to develop, individual worms were transferred onto new NGM plates containing a fresh drop of *E. coli* OP50. Nematodes were then transferred to fresh plates every 24 hours. As self-progeny brood sizes are determined by the number of self-sperm, plates were incubated at 20°C for 48 hours in order to distinguish between sterile and fertile eggs. Fertile eggs and therefore hatched juveniles were counted as offspring, while visibly infertile eggs were excluded from brood size counts.

2.6.2 Lifespan Assay

Lifespan assays were performed at 20°C. Five gravid hermaphrodites were left to lay eggs overnight on NGM plates seeded with E. coli OP50. The progeny populated the corresponding plates until the L4 larvae stage. L4 larvae were then transferred onto fresh NGM plates seeded with *E. coli* OP50, containing 50 µM 5-fluoro-2′-deoxyuridine (FUDR). FUDR inhibits DNA synthesis and therefore reduces egg production and prevents eggs from hatching. A total of 5 plates containing 20 nematodes on each are used per strain, per lifespan assay. Day 0 of the lifespan assay was counted as the day the first eggs were laid. The adult population were then scored every other day. Plates were maintained at 20°C until all the worms on the plate had died. Animals that died as a consequence of crawling up the wall of the petri dish or internal hatching of larvae were censored and therefore not included in lifespan measurements. As worms near the end of their life often

become stationary with occasional movement of their head or tail, animals are only scored as dead when they show absence of any movement and failed to respond to a gentle prodding in the head region with a platinum wire.

2.6.3 Chemotaxis assay

Adapted from (Margie et al. 2013). Chemotaxis assays were performed at 20°C. Five gravid hermaphrodites were left to lay eggs overnight on NGM plates seeded with *E. coli* OP50. Once progeny were synchronized to young adults they were ready to harvest. A petri dish containing chemotaxis agar (2% agar, 5 mM KPO_4 pH6, 1 mM $CaCl_2$, 1 mM $MgSO_4$) was divided into four quadrants; two opposite quadrants were marked “Test” and two were designated Control. In each Test quadrant, 2 µl of diluted diacetyl (1:100 with water) and 2 µl of 0.5 M sodium azide were added. In the two control quadrants, 2 µl of distilled water and 2 µl of 0.5 M sodium azide were added. Each chemotaxis assay was undertaken in triplicate.

Worms were harvested by dropping 1 ml of M9 onto the surface of one of the stock plates. The plate was carefully tilted back and forth several times to wash the entire surface of the plate. Worms were then removed and transferred to a 1.5 ml eppendorf tube. Worms were left to settle to the bottom of the tubes for 2 minutes. The supernatant was then carefully removed and worms were again washed in 1 ml of M9. The wash step was repeated a further 3 times. After the final wash step as much of the supernatant as possible was removed. Using a pipette, the worms were then placed in the center of the plate with a circle marked around the origin to ensure that non-motile worms were ignored. Petri dish lids were immediately added and plates were left to incubate for 1 hour. After 1 hour, the worms in each quadrant were counted the chemotaxis index (CI) was calculated using the equation shown below.

$$CI = \frac{(\#\ \text{Worms in Both Test Quadrants} - \#\ \text{Worms in Both Control Quadrants})}{(\text{Total \# of Scored Worms})}$$

A + 1.0 score indicates maximal attraction towards the target and represents 100% of the worms arriving in the quadrants containing the chemical target. An index of - 1.0 is evidence of maximal repulsion.

2.6.4 Gentle touch mechanosensing assay

C. elegans responds to gentle touch to the nose by initiating backward locomotion, mediated by the ASH, OLQ and FLP sensory neurons. During a nose touch assay an eyebrow hair attached to the end of a pick is sterilized by dipping it into a 70% ethanol solution then shaking it dry. Animals are placed on standard NGM plates with thin bacterial lawns as response on food is more robust and is therefore preferred. As the animal moves forward, the hair is laid on the surface of the plate in front of the animal in such a way that the nematode makes contact with the hair with the tip of the nose perpendicular to the direction of the movement (Chalfie et al. 2014).

Normal animals immediately initiate backward locomotion. Defective animals either hurdle over the hair or slide their nose along the hair. An individual animal is tested no more than 10 times in a row to avoid inducing habituation. The hair is wiped off every few trials to eliminate bacteria and water that may adhere. Between 20 – 30 worms are assayed in triplicate; a positive score was given if the animal initiated backwards locomotion. Gentle touch to the posterior of the body is sensed by six sensory neurons (ALML/R, PLML/R, AVM, and PVM) with sensitivity measured by stroking the animals with an eyebrow hair across the body just before the anus.

Between 20 – 30 worms are assayed in triplicate; a positive score was given if the animal initiated forwards locomotion (Chalfie et al. 2014).

2.6.5 Harsh touch mechanosensing assay

Sensation of harsh body touch requires the PVD neurons; two non-ciliated neurons that extend long anterior and posterior processes almost the entire length of the worm, located between the mid-body and the tail. As the animal matures, these processes develop elaborate dendritic branches that cover most of the surface of the animal (Bounoutas & Chalfie 2007), therefore only fully formed gravid adults were assayed.

Anterior harsh touch is determined by probing non-moving gravid adults anterior to the vulva whereas posterior harsh touch is determined by probing non-moving gravid adults just posterior to the vulva. Animals that initiate forward or backward locomotion for posterior and anterior respectively, give a positive response and are therefore scored 1. “Touch abnormal” animals do not respond and are scored 0 (Chalfie et al. 2014).

Chapter 3: Characterization of the localisation and function of the *Caenorhabditis elegans* class I myosins

3.1 Introduction

Present in all fungal and animal species, the class I myosins constitute a group of highly conserved, non–filamentous, single-headed actin-binding motor proteins, implicated in a number of essential cellular processes (Kim & Flavell 2008; Coluccio 2007). The human genome encodes eight distinct members of the myosin-I family (*Myo1a-h*), with mutations in these genes associated with a number of human diseases including kidney disease, deafness and cancer (Mazzolini et al. 2012; Sielski et al. 2014; Zadro et al. 2009).

Over the past 30 years, *C. elegans* has become a popular model organism to study a variety of biological processes including cell signalling, the cell cycle, cell polarity, gene regulation and ageing, due to its conservation of many molecular and cellular pathways found in higher, more complex eukaryotes. Subsequent comparison of the nematode and human genomes confirmed a large number of human disease genes and disease pathways are conserved in *C. elegans* (Kaletta et al. 2006). Although mutations in class I myosin motor proteins have been linked to a number of human diseases, the pathophysiology in most cases is still poorly understood, therefore *C. elegans* offers an ideal model system to further explore the role of class I myosins and their regulation.

C. elegans encodes two structurally distinct unconventional class I myosins; HUM-1 and HUM-5. A homolog of human myosin Myo1e, *hum-1* encodes a typical long tailed class I myosin with 1 IQ motif. RNAi screens suggest HUM-1 may be involved in regulating synapse structure and/or function however its precise function remains unknown (Sieburth et al. 2005).

Conversely HUM-5, a homolog of human Myo1d, is a short tailed myosin I with 2 IQ motifs with no role currently ascribed (Baker & Titus 1997).

Often defining the cellular localisation of a protein is an essential step towards understanding its possible functions, therefore the aim of this study was to determine the localisation of the *C. elegans* class I myosins in a live cell context. As the emergence of fluorescent protein fusions offers an attractive method for characterising protein properties and protein dynamics *in vivo,* both HUM-1 and HUM-5 were fused with recombinant reporter proteins. In addition, loss of gene function often provides insight into protein functionality therefore *C. elegans* HUM-1 and HUM-5 knockout strains were assayed to further investigate the function of each protein.

3.2 Disruption of the *hum-1* and *hum-5*

Strains containing disruption of *hum-1* or *hum-5* were acquired from the Caenorhabditis Genetics Centre (CGC). The *hum-1(RB818)* strain of *C. elegans* contained a 1045 bp deletion of the *hum-1* gene which had been replaced with a 28 bp insertion. The *hum-5* strain contained a 1523 bp deletion of the *hum-5* gene. Both gene deletions corresponded to a region of the motor domain which would shift the remaining coding sequence out of frame, therefore it is expected to render the endogenous proteins inactive (Figure 3.1). Animals received from a deletion library have the potential to contain multiple mutations in addition to the deletion of interest.

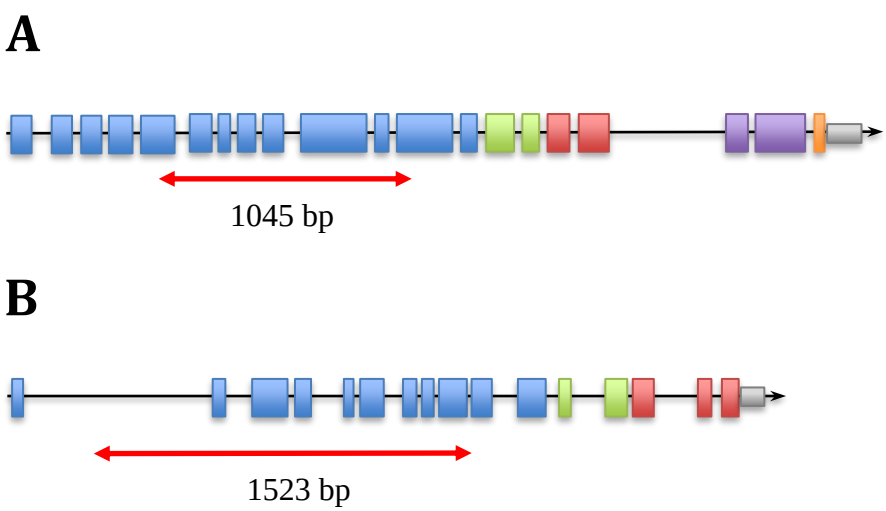

Figure 3.1 Location of mutations in the C. elegans myosin I genes. The approximate location of the A) *hum-1(ok634)* and B) *hum-5(ok1886)* deletions indicated by the red double headed arrows. Both deletions correspond to a region of the motor domain. Exons are indicated by bars; blue is the motor domain, green is the neck region, red is the TH1 domain, purple is the TH2 domain and orange is the SH3 domain, introns are indicated by black lines.

Several back-crosses of the acquired *hum-1(RB818)* strain with the lab N2 strain was therefore used to make the genetic background more equivalent to the lab wild-type. The first step in the backcrossing process was to cross a homozygous *hum-1(RB818)* hermaphrodite with an N2 male (methods). Subsequent generations of progeny with homozygous gene expression were re-isolated using genomic PCR (methods). To ensure the *hum-1* disrupted strain shared at least 95% genetic identity with the lab N2 strain the back-crossing process was carried out a further four times.

3.2.1 Generation of fluorescently labelled *hum-1* and *hum-5*

To determine the cellular localisation of each protein, HUM-1 and HUM-5 were tagged with the recombinant reporter proteins; GFP and mCherry respectively. A pUC18 based construct was generated containing *hum-1* (2 kb upstream promoter and 2 kb downstream) with DNA encoding GFP fused to the 5' end of the gene. An equivalent construct was generated for *hum-5* fused to an mCherry fluorophore (methods). These fusions allowed nematodes to be imaged using fluorescence microscopy based techniques.

3.2.2 Generation of strains

Strains containing disrupted *hum-1* or *hum-1*;*hum-5* were generated using standard genetic cross protocols (methods). Transgenic strains; *hum-1;gfp::hum-1 or hum-1;hum-5;gfp::hum-1;mCh::hum-5* containing the extra chromosomal *gfp::hum-1* or *mcherry::hum-5* constructs were generated by co-injecting the transgene DNA into day one adult N2 nematodes at a concentration of 50 ng/μl, along with the identification marker *rol6*$^{+}$ at a concentration of 100 ng/μl. Injections were carried out by Marina Ezcurra from the University College London. A minimum of two stable injection lines were isolated so a comparison of expression could be made. One line,

representative of protein expression was then chosen to take forward for all experiments. Subsequent strains with myosin I disruptions, containing extra chromosomal constructs were generated using standard genetic cross protocols however only rolling progeny could be selected (methods). For strain *hum-1;gfp::hum-1;mCh::act-1*, expressing both extra chromosomal and endogenously tagged proteins, rolling progeny were first isolated for construct selection and then screened for stable homozygous expression of the tagged endogenous protein. For strains used throughout this project see materials and methods.

3.3 Localisation of HUM-1

To determine the localisation of HUM-1, fluorescent confocal microscopy was used to image strain *hum-1;gfp::hum-1,* which expresses a *gfp*::*hum-1* transgene (methods). The transgene is expressed in a in a *hum-1* null to provide a clean background for protein localisation studies, minimising competition with the endogenous HUM-1 protein. In late L3 and adult nematodes expression of GFP signal was seen to concentrate in the chemo/odour sensory sensilla, the pharyngeal-intestinal and intestinal-rectal valves and the reproductive system. Expression of GFP::HUM-1 within the chemo/odour sensory sensilla was seen throughout cell bodies, axons and other processes of amphid neurons and inner labial neurons located in the head (Figure 3.2), which was confirmed by DiI staining, a red fluorescent lipophilic membrane dye (Figure 3.3), in addition to PHC and phasmid neurons in the tail (Figure 3.4).

In total, *C. elegans* contains 32 chemo/odour sensory neurons; 22 are paired neurons of the amphid sensilla (ADF, ADL, AFD, ASE, ASG, ASH, ASI, ASJ, ASK, AWA, AWB, AWC), 4 are paired neurons of the phasmid sensilla (PHA, PHB) and 6 are neurons of the inner labial sensilla (IL1, IL1D, IL1V, IL2, IL2D, IL2V) (Schulenburg & Ewbank 2007). A schematic overview

of the chemo / odour sensory neurons in the head can be seen in Figure 3.5 (Riddle 1997; Mori 1999). The amphids are the primary olfactory, chemo-receptive, and thermos-receptive organs in *C. elegans* and are paired lateral sensory structures at the anterior end of the nematode (Ward et al. 1975). Each amphid is typically composed of 11 sensory neurons and two support cells (Bumbarger et al. 2009). The sensory process of each neuron extends to the lip on the lateral side of the pharynx, terminating as a cilium exposed to the environment (Riddle 1997), whereas the axons of each neuron enters the neuronal commissures on each side of the terminal bulb to reach the ventral nerve cord and nerve ring (Hunt-Newbury et al. 2007).

Originating from a position anterior to the amphids, the inner labial sensilla are arranged in a six-fold symmetry, of inner labial neuron types 1 and 2 (Inglis et al. 2007). These neurons possess more seemingly degenerate basal bodies, with dendrites that terminate in shorter cilia around the apex of each lip (Inglis et al. 2007). IL1 neurons are mechano-sensory neurons involved in mediating head withdrawal in response to dorsal or ventral nose touch, whereas IL2 neurons are postulated to be chemosensory. Like amphid neurons, the cilia of IL2 neurons are exposed to the environment, whereas IL1 neurons remain embedded in the sub cuticle (Corsi et al. 2015).

In the tail, the PHC neuron and the two phasmid neurons PHA and PHB are located on the lateral side of the nematode, behind the rectum. Similar in structure to the rod-like amphid channel cilia but smaller, the cell bodies of the phasmid neurons are located at the lumbar ganglia, with cilia exposed to the external environment through holes created by socket cells (Schafer 2016). Involved in modulation of chemo-repulsion behaviour, the phasmid neurons act antagonistically with amphid neurons to regulate reversals required for escape behaviours (Bae & Barr 2008). The posterior process of the PHC neuron extends into the tail tip and is thought to be involved in modulating thermo-nociception and temperature avoidance responses

(Siddiqui & Culotti 2007). In addition to expression in the nervous system, HUM-1 also showed expression in additional tissues including the pharyngeal-intestinal and intestinal-rectal valves and within the reproductive system. The pharyngeal-intestinal valve connects the posterior of the pharynx to the anterior cells of the intestine through a multicellular valve composed of six equivalent cells; one vpi1, three vpi2 and two vpi3 (Mango 2007). These six cells form consecutive rings, producing a small epithelial channel in continuity with the pharyngeal lumen. No apparent muscular elements operate within the valve cells therefore it is thought the valve is a passively open and patent channel (www.WormBook.com).

The membrane complex of the intestinal-rectal valve is similar to that of the pharyngeal valve; formed by two small darkly staining epithelial cells (virL and virR) that occlude the lumen of the posterior intestine allowing digested material to leak into the rectum and then to the anus (Figure 3.4A). Joined at their lateral surfaces by membrane junctions, rectal valve cells have no apparent contractile elements, however are associated with the anal depressor muscle and two intestinal muscles (A. F. Bird & J. Bird 2012).

Within the reproductive system, HUM-1 was expressed in four multinucleate toroidal uterine cells (ut1-4) and in the spermatheca / spermathecal-uterine (SU) valve. The hermaphrodite uterus consists of an anterior and posterior lobe, composed of four uterine toroid epithelial syncytia; ut1 - 4. A single 'H' shaped uterine seam-cell (utse) attaches the uterus to specialized lateral epithelial cells while three mono-nucleate cells (uv1-3) connect the ut cells to the vulva on both the left and right side of the animal (Figure 3.5B) (Newman et al. 1996). Each toroid is formed when four or six cells at that anterior and posterior position fuse. The uterine toroidal cells are followed by the spermathecal – uterine valve which connects the spermatheca to the uterus, restricting mature gametes from passing from the spermatheca to the uterus or vice versa (McCarter et al. 1997).

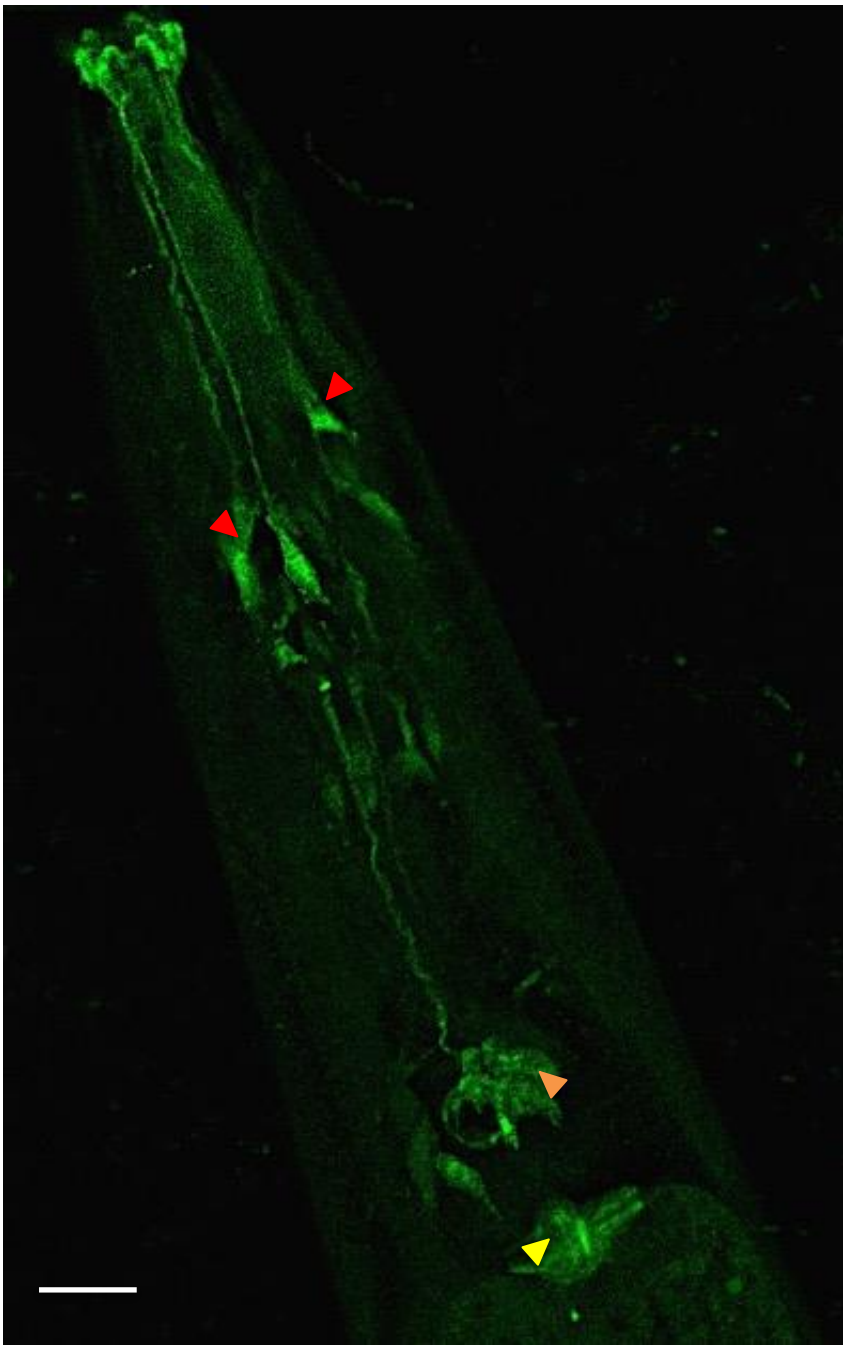

Figure 3.2 Localisation of GFP::HUM-1 within the head. Localisation of GFP::HUM-1 concentrates to the amphid sensilla (orange arrowhead), inner labial sensilla (red), pharyngeal-intestinal valve (yellow). Scale bar is 10 µm.

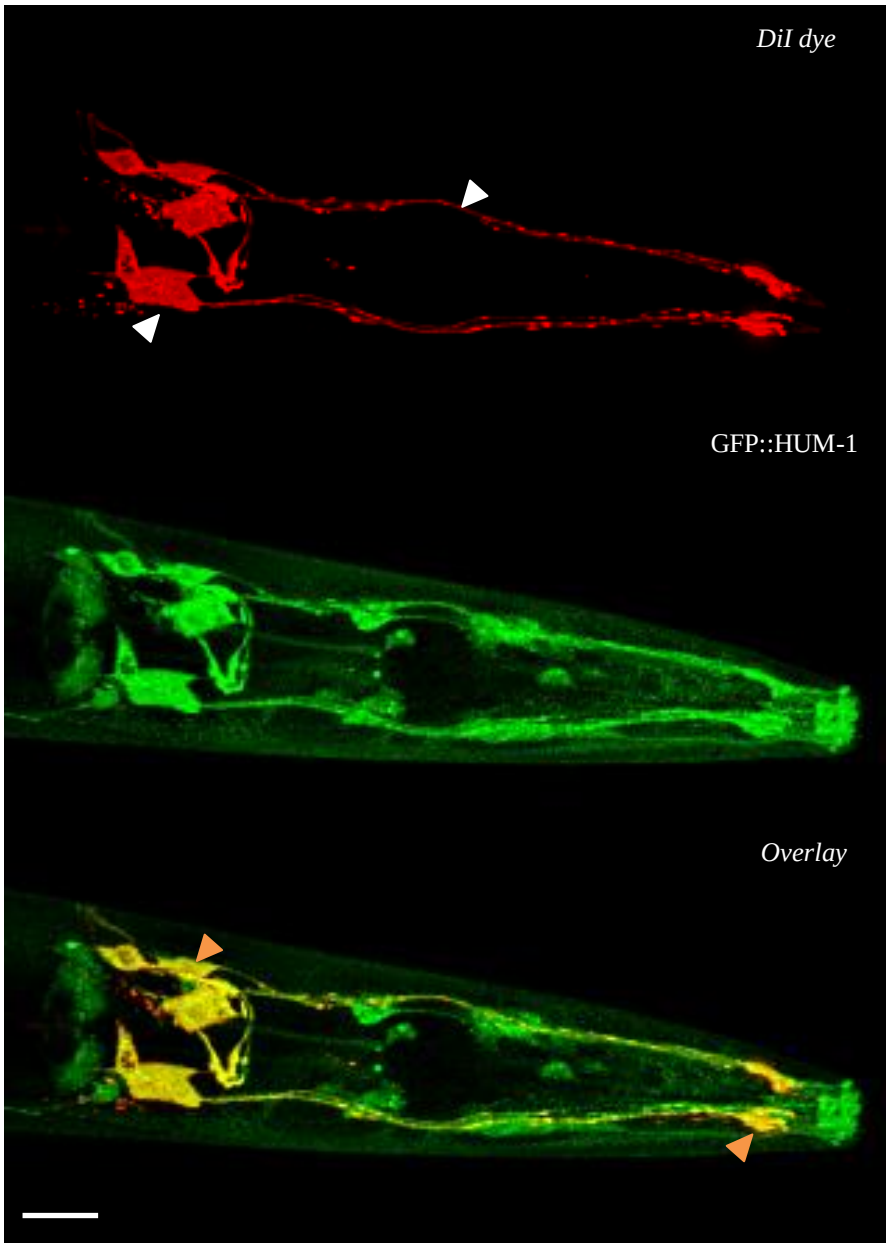

Figure 3.3 Co-localisation of GFP::HUM-1 and DiI dye. DiI dye-filling of the amphid neurons (white arrowhead) shows co-localisation with HUM-1 (orange), confirming HUM-1 expression in these structures. Scale bar is 10 µm.

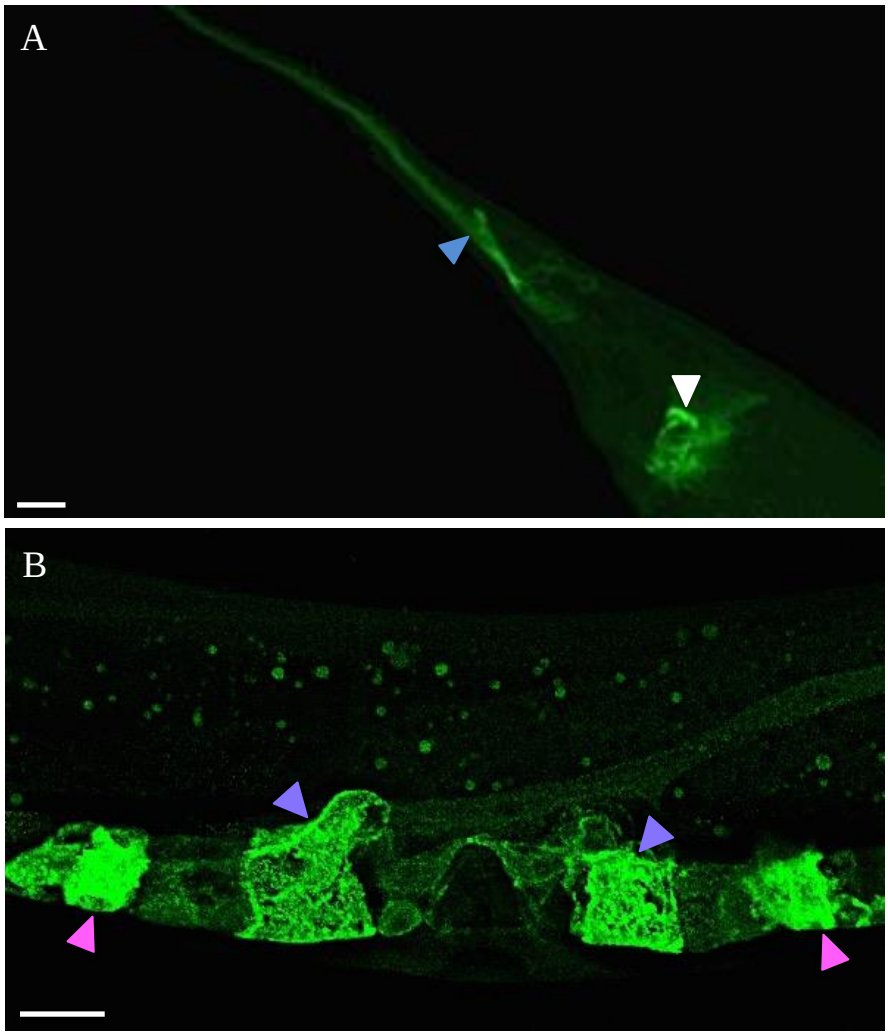

Figure 3.4 Localisation of GFP::HUM-1 in the tail and reproductive system. A) Localisation of GFP::HUM-1 within the tail concentrated to the phasmid sensilla and PHC neuron (blue arrowhead) and intestinal-rectal valve (white). Within the reproductive system, GFP::HUM-1 showed localisation to the; spermatheca/ spermatheca-uterine valve (pink) and uterine toroidal epithelial cells (purple). Scale bar is 10 µm.

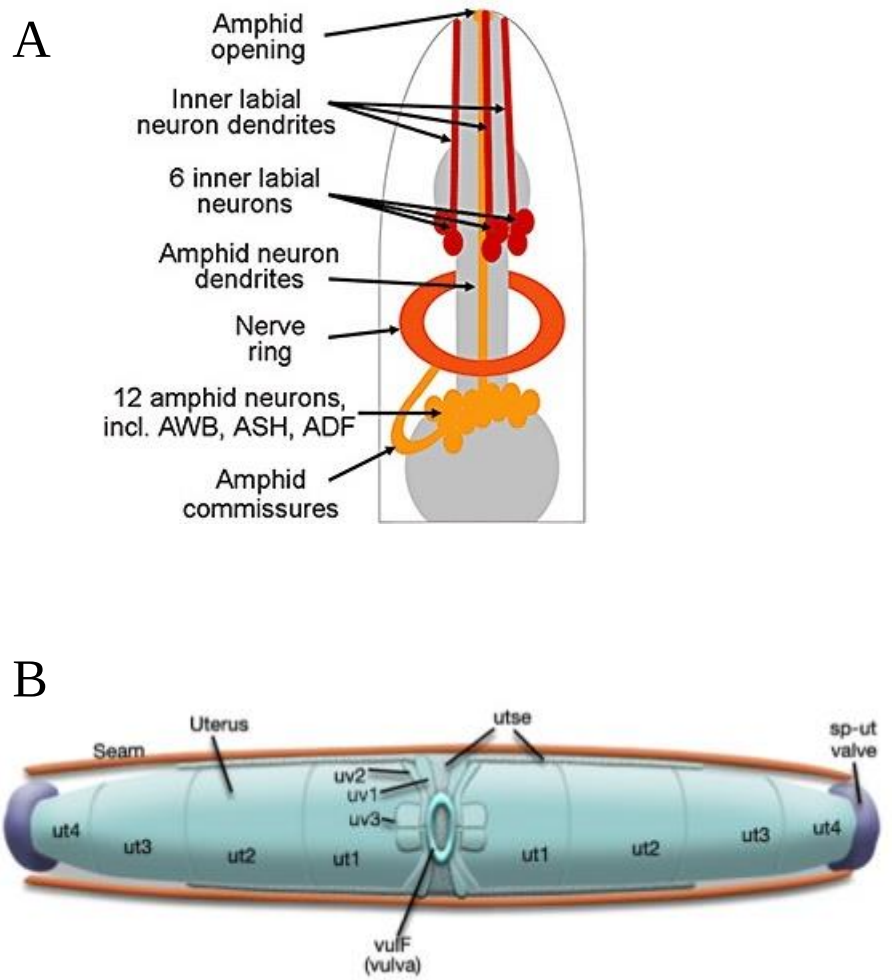

Figure 3.5 Schematic overview A) Chemosensory sensilla in the head B) The uterus. A) Two symmetrically organized amphid organs extend from outside the base of the lip to the terminal bulb (orange). Six symmetrically arranged inner labial sensilla extend from the apex of each lip to the anterior bulb (red). The pharynx with its two bulbi are given in grey. Adapted from (Schulenburg & Ewbank 2007). B) Ventral view of the uterus depicting ut toroid cells 1-4, utse cell attaching the uterus to epithelial seam cells, uv cells connecting ut cells to the vulva and the spermathecal-uterine (sp-ut) valve. Adapted from www.wormatlas.com.

The adult valve consists of a toroidal syncytium generated by the fusion of four cells, containing a ring of microfilaments that wraps around the inside face of the torus possibly acting as a sphincter to close the valve (Newman et al. 1996). The spermatheca connects the distal gonad arm to the uterus via the SU valve and is the site of oocyte fertilization, acting as a reservoir for maturing spermatids and adult sperm. The spermathecal is composed of 24 cells organised into two regional groups; distally, 8 cells form a narrow corridor and proximally, 16 cells form a wider chamber (McCarter et al. 1997)

3.3.1 HUM-1 co-localises with ACT-1 in the spermatheca and SU valve

To further explore the localisation at HUM-1, *hum-1;gfp::hum-1* hermaphrodites were crossed with males with endogenously tagged mCherry::ACT-1. The resulting strain was imaged using confocal microscopy (methods). The *C. elegans* genome encodes five actin genes (*act-1,-2,-3,-4,-5).* Primarily expressed in muscle and myofilament-containing cells, ACT-1 localisation includes the isotropic bands of the body wall muscle sarcomeres, phagocytes, spermatheca/ SU valve and the pharyngeal muscle (Dixon & Roy 2005; Huang et al. 2012; Wirshing 2017).

Within the reproductive system, ACT-1 localises to actin filaments in the spermatheca/ SU valve. HUM-1 showed co-localisation with ACT-1 in both of these structures however, no co-localisation was seen within the uterine toroid epithelial cells (Figure 3.6). Within the pharynx, ACT-1 is expressed in eight sections of muscles organised with three-fold rotational symmetry around the pharyngeal lumen (Mango 2007). Posteriorly, a toroid of six valve cells (vpi 1-6) connects the last pharyngeal muscle; pm8, to the intestine. GFP::HUM-1 showed no co-localisation with ACT-1 in any of these tissues (Figure 3.7).

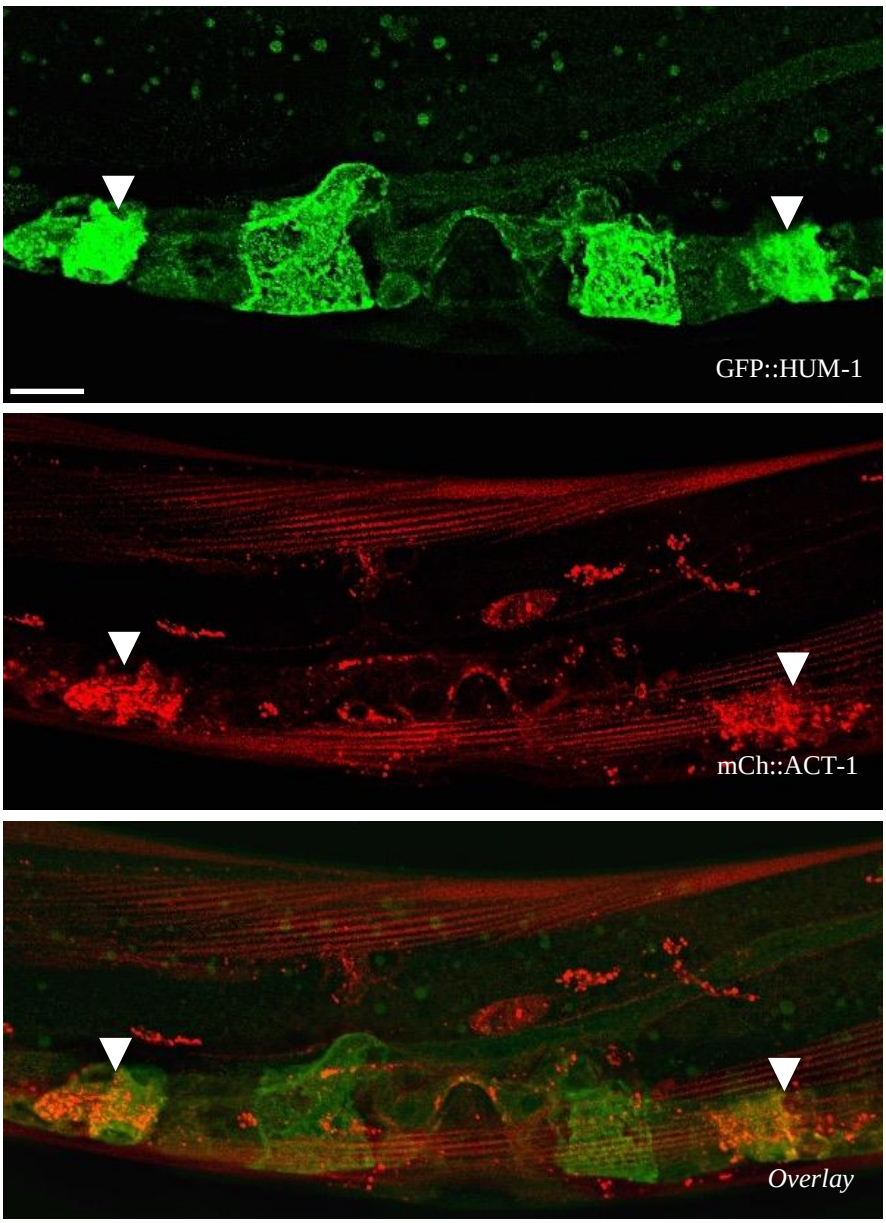

Figure 3.6 GFP::HUM-1 shows co-localisation with mCherry::ACT-1 in the spermatheca and SU valve. Overlay of GFP::HUM-1 with mCherry::ACT-1 shows protein co-localisation in the spermatheca and SU valve of the reproductive system (white arrowhead) however no co-localisation is observed within the uterine toroid epithelial cells. Scale bar is 10 µm.

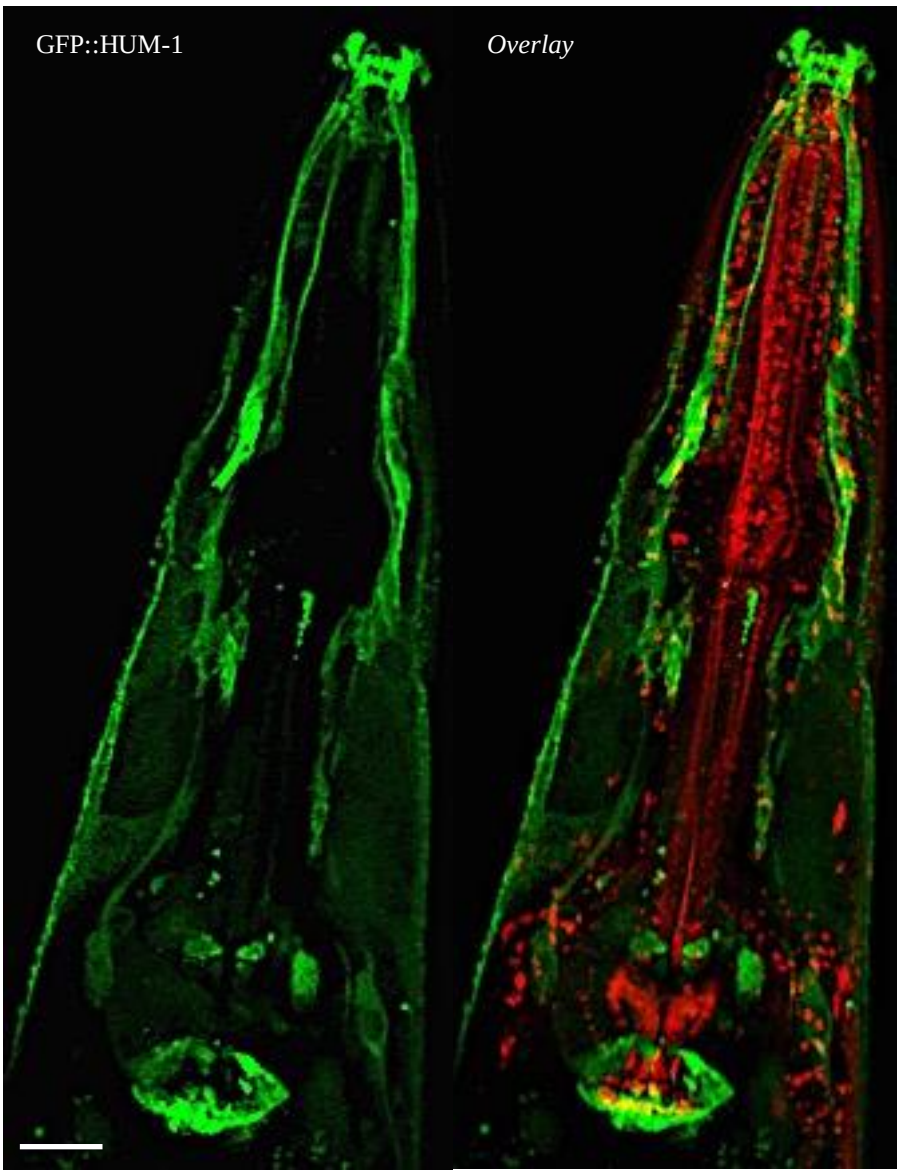

Figure 3.7 GFP::HUM-1 shows no co-localisation with mCherry::ACT-1 within the head. GFP::HUM-1 shows no co-localisation with mCherry::ACT-1in any of the chemo/odour sensory sensilla or the pharyngeal-intestinal valve within the head**.** Scale bar is 10 µm.

3.4 Localisation of HUM-5

To determine the localisation of HUM-5, a *mcherry::hum-5* transgene was generated and co-injected with a *gfp::hum-1* transgene into nematodes with a disrupted *hum1*;*hum-5* background. Nematodes were anesthetised and imaged using confocal microscopy (methods). HUM-5 is highly expressed in the Cephalic (CEP), FLP and PVD mechanosensory neurons where it localizes throughout cell bodies, axons and other processes (Figure 3.8 & 3.9). In *C. elegans*, mechanosensory neurons are responsible for diverse sensory modalities including responses to low threshold mechanical stimuli, temperature, maintenance of body posture and the feeling of pain (Albeg et al. 2011).

CEP neurons have sensory cilium distributed around the mouth which extend back to the anterior bulb (Figure 3.8). The far distal end of CEP widens and contains an amorphous, dark, microtubule-associated material (TAM) that is also found in mechano-cilia of other species (Jauregui et al. 2008). Similar in structure, FLP and PVD neurons are not part of a sensillum and instead innervate the outer envelope of the animal through bare nerve endings located in the head and body, respectively (Figure 3.9, 3.10). Topologically FLP neuron processes cover the head and neck whereas PVD neuron processes cover the body (Hall & Altun 2008).

Both neurons are developmentally controlled and grow throughout the various life stages; FLP neurons are born in the early embryo whereas PVD neurons arise in L2 stage of development (Figure 3.11). Although not much is known about the development of FLP neurons, PVD neurons develop from a single axon which emerges venrtalward from the cell body, before going rostrally within the ventral cord. The processes then emerge laterally to form multi-dendritic structures with an arborization pattern, displaying non-overlapping and regularly spaced arrays of processes once fully formed in the adult nematode (Figure 3.11) (Hall & Treinin 2011). Image overlay with GFP::HUM-1 showed no co-localisation with any of these neurons.

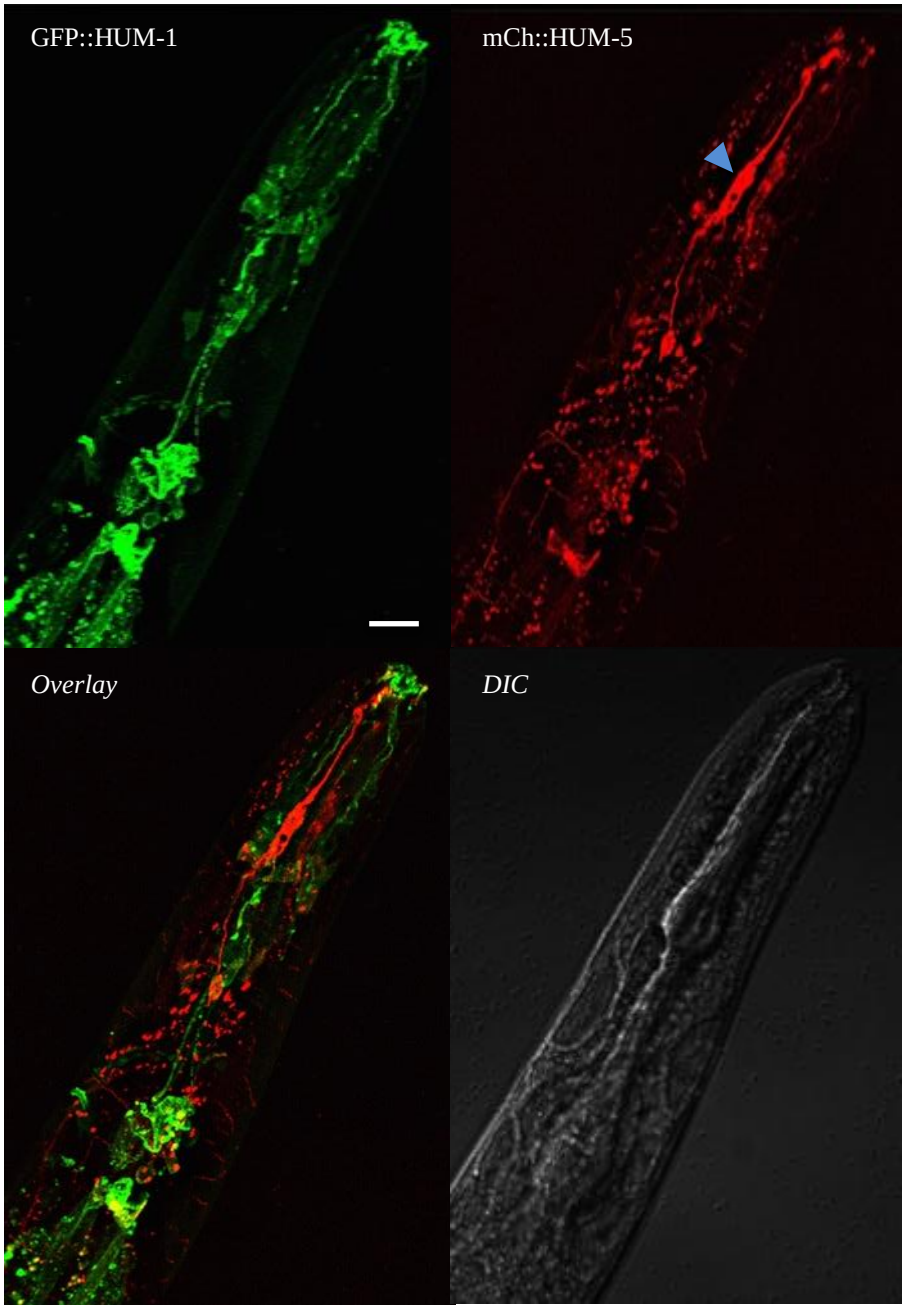

Figure 3.8 Localisation of mCherry::HUM-5 to CEP neurons. HUM-5 appears to localise to CEP mechano-sensory neurons within the nose tip (blue arrowhead). Image over-lay with GFP::HUM-1 shows no co-localisation of HUM-1 with HUM-5. Scale bar is 10 µm.

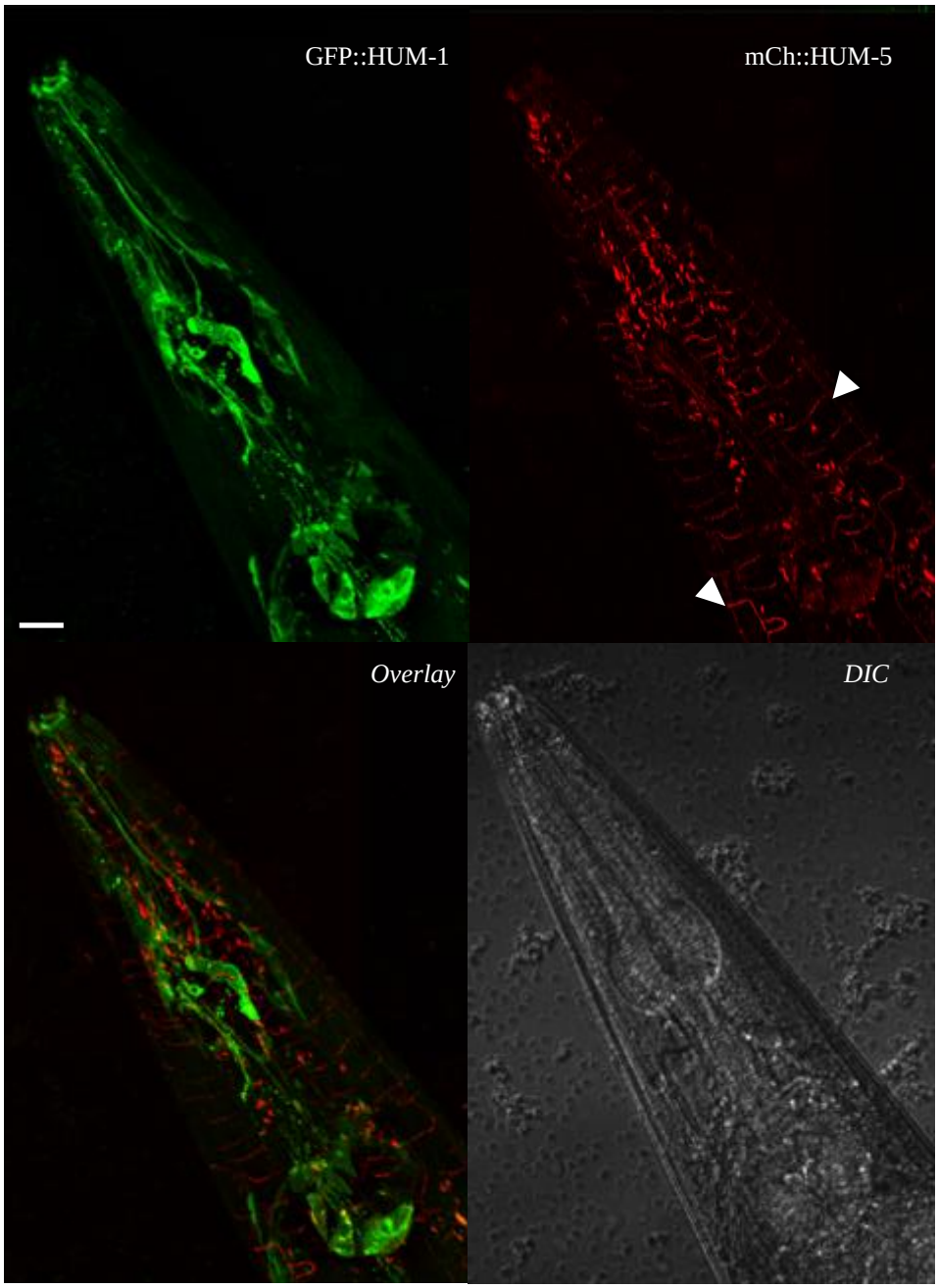

Figure 3.9 Localisation of mCh::HUM-5 to FLP neurons. HUM-5 appears to localise to FLP mechano-sensory neurons within the head (white arrowhead). Image over-lay with GFP::HUM-1 shows no co-localisation within the FLP neurons. Scale bar is 10 µm.

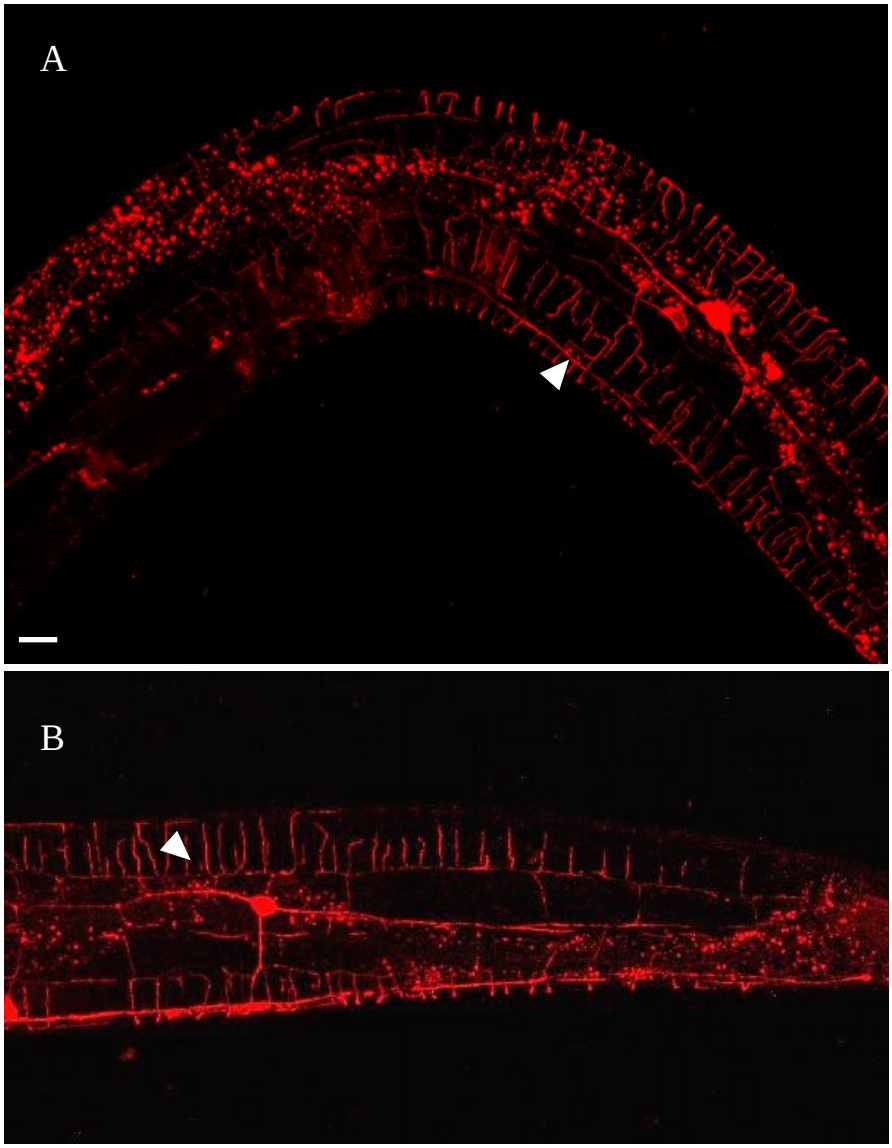

Figure 3.10 Localisation of mCherry::HUM-5 to PVD neurons within the body wall. HUM-5 localises to PVD mechano-sensory neurons within the body wall (white arrowhead) but does not co-localise with HUM-1. Scale bar is 10 µm.

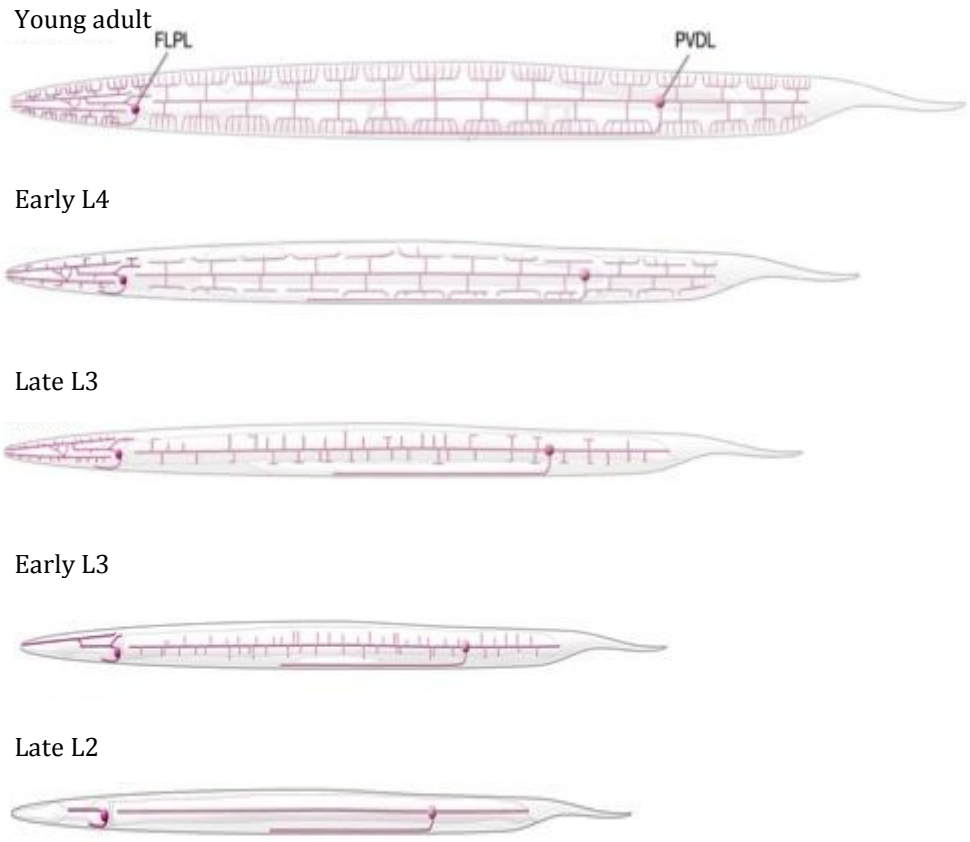

Figure 3.11 Development of FLP and PVD neurons through larval stages. Schematic diagram of the organization and development of the FLP and PVD neurons through different stages of larval development. Not much is known about the development of FLP neurons however, PVD neurons develop from a single axon which emerges venrtalward from the cell body, before going rostrally within the ventral cord. The processes then emerge laterally and form highly branched dendrites. Diagrams not to scale. (Adapted from www.wormatlas.com)

3.5 Functional analysis of *C. elegans* Myosin I

3.5.1 Myosin I is not required for nematode lifespan

To explore the role of HUM-1 and HUM-5 in regulating nematode lifespan, a lifespan assay was undertaken in triplicate using strains in which either one of the myosin I genes (*hum-1* or *hum-5)* or in which both myosin genes (*hum-1;hum-5)* were disrupted. Lab stock N2 were used as the control. Significance was set at $P < 0.05$ (two-tailed) (methods). Young adult L4 hermaphrodites were transferred to fresh NGM plates containing FUDR (methods). FUDR does not affect adult life span, however it inhibits cell division, reduces egg production, and prevents eggs from hatching. This removes the need to transfer worms every few days in order to separate maternal worms from growing larva. The first-time point (day 0) is counted as the day an L4 larva molts into an adult. The final time point is taken when all worms are classified as deceased. As worms near the end of their life often become stationary with occasional movement of their head or tail, they were only deemed as dead when they showed lack of movement when gently touched with a pick (methods).

The mean life span for the lab N2 strain was 24 days. Disruption of *hum-1* or *hum-5* did not appear to have any impact on nematode aging as the mean life span for each strain was 24 and 23 days respectively (Figure 3.12). A P value of 0.7467 for *hum-1* and 0.0585 for *hum-5* when calculated against the N2 control confirmed there was no statistical significance between the two populations (Table 3.1). Disruption of both myosin I genes however reduced the mean lifespan to 21 days. A P value of 1.8E-0.8 calculated against the N2 control confirmed the two populations are statistically significant. As HUM-1 and HUM-5 do not co-localise functional cross over is unlikely to occur, therefore the reduction in life span could be due to both myosin I genes having a synthetic interaction.

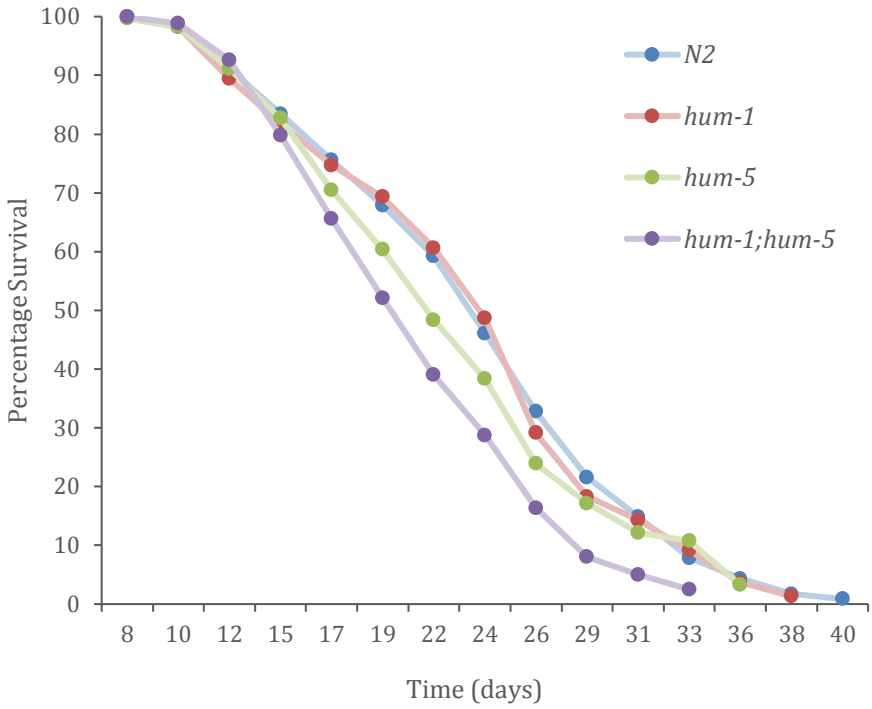

Figure 3.12 Survival curve of N2 and myosin I mutant hermaphrodites at 20°C. N2 controls showed a mean lifespan of 24 days. Disruption of the *hum-1* or *hum-5* gene alone did appear to significantly impact lifespan. Disruption to both *hum-1* and *hum-5* however decreased the mean lifespan to 21 days. When compared to the N2 control, the double mutant gave a P value of 1.8E-0.8 confirming the two populations were statistically significant.

Genotype	Mean Lifespan ± SEM 20°C (days)	Median Lifespan	75th %tile	25th %tile	P value against control	Animals scored*
N2	24.12 ± 0.41	24	29	19	-	303 (349)
hum-1	23.94 ± 0.40	24	29	17	0.7467	333 (350)
hum-5	22.99 ± 0.42	22	26	17	0.0585	267 (346)
hum-1; hum-5	21.41 ± 0.33	19	26	17	1.8E-0.8	307 (347)

Table 3.1. Lifespan assay data for N2 and myosin I deletion strains. SEM: standard error of the mean. 25th and 75th percentile refer to the day at which 25 or 75 % of the population is dead. Animals scored*; number of animals dying senescent deaths (starting sample, including animals dying non-senescent deaths).

3.5.2 HUM-1 function is required for maximum brood size

To evaluate the effects disruption of *hum-1* and *hum-5* had on progeny production a brood size assay was undertaken. A single hermaphrodite, the ovaries of which had just begun to develop (L4) (therefore did not contain any oocytes), was transferred to a fresh drop of medium daily until egg laying ceased (methods). As brood sizes in *C. elegans* are determined by the number of self-sperm with additional oocytes released unfertilized,

fertile eggs and hatched juveniles were counted as offspring, while visibly infertile eggs were excluded from brood size counts. The overall average brood size for the N2 control was 303 ± 12 which is in line with the *C. elegans* universal optimum of self-progeny (Muschiol et al. 2009). Significance was set at $t < 0.05$ (two-tailed). Disruption of *hum-1* alone caused a significant reduction in brood size with an overall average of 257 ± 7. This was confirmed by t-test (t) with *hum-1* giving a t value of 3.9E-07 when compared to the N2 control (Figure 3.13).

Disruption of *hum-5* alone had very little impact on brood size giving an average of 292 ± 9 and a t value of 0.298. Disruption of both *hum-1;hum-5* showed a significant decrease in average brood to 263 ± 16. Although this was not as substantial as the *hum-1* disruption alone, the t value was calculated at 2.8E-4 when compared to the N2 control confirming the difference in the two populations was statistically significant. These results show that HUM-1 is required for maximum brood size however HUM-5 is not.

To further investigate whether the reduction in brood size was *hum-1* dependent, a *gfp::hum-1* transgene was co-expressed with the identification marker *rol6*$^{+}$ in a disrupted *hum-1* background (methods). The introduction of the *gfp::hum-1* transgene rescued the brood phenotype, increasing the average brood size from 257 ± 7, seen in the disrupted *hum-1* strain, to 288 ± 16. This changed the t value from 3.9E-07 to 0.05 when calculated against the N2 control, confirming there was no longer any statistical significance between the two populations. In addition to showing HUM-1 is required for maximum brood size, these results also indicate the *gfp::hum-1* transgene is functional *in vivo* (Figure 3.13).

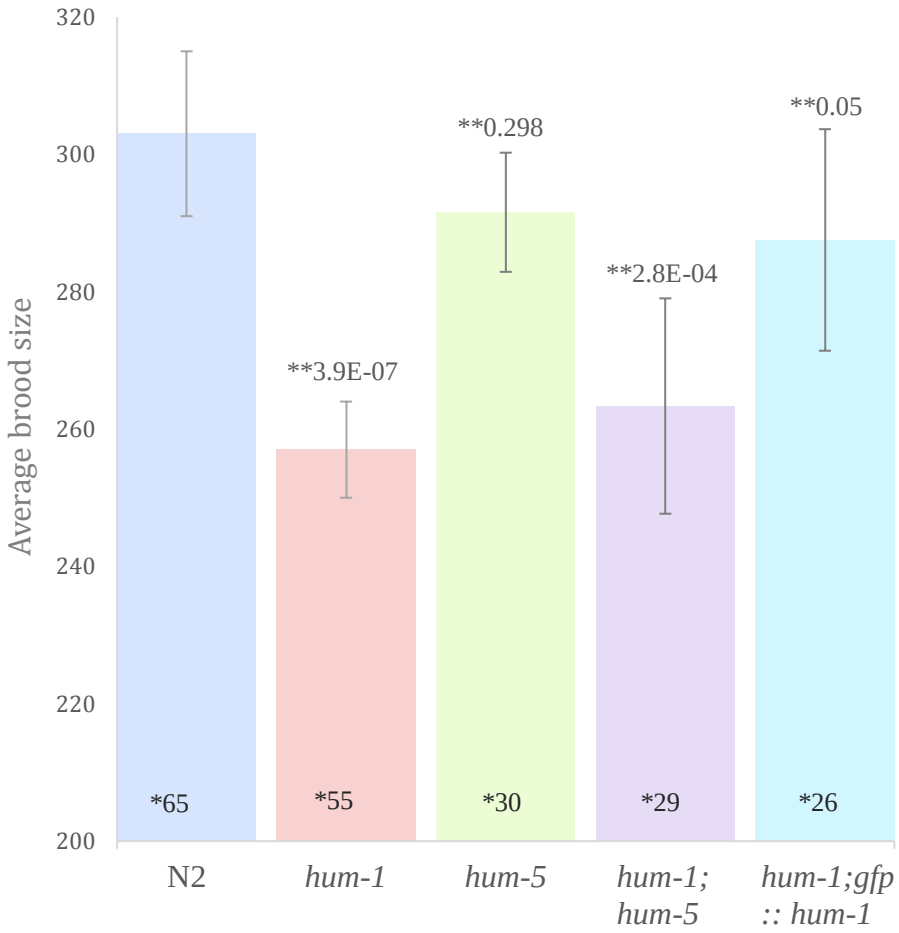

Figure 3.13 Overall average brood size. Disruption of *hum-1* showed the most significant reduction in average brood size when compared to N2. Disruption of *hum-5* alone did not appear to have any impact on brood size, however disruption of both genes in strain *hum-1;hum-5* showed a significant reduction in average brood. Introduction of the *gfp*::*hum-1* transgene appeared to partially rescue the reduced brood phenotype. * Number of maternal hermaphrodites used. ** t-test value calculated against N2 control.

3.5.3 Disruption of *hum-1* affects age-specific fecundity

To explore whether HUM-1 or HUM-5 function affects age-specific self-fertility, the results for average number of progeny laid per day were compared. Since hermaphrodites produce only a fixed number of sperm, meiotic maturation rates and embryo laying are initially highest for the first day of adulthood, but decline as sperm are used for fertilization, age-specific fecundity is therefore positively correlated with fertility on contiguous days (Brooks & T. E. Johnson 1991).

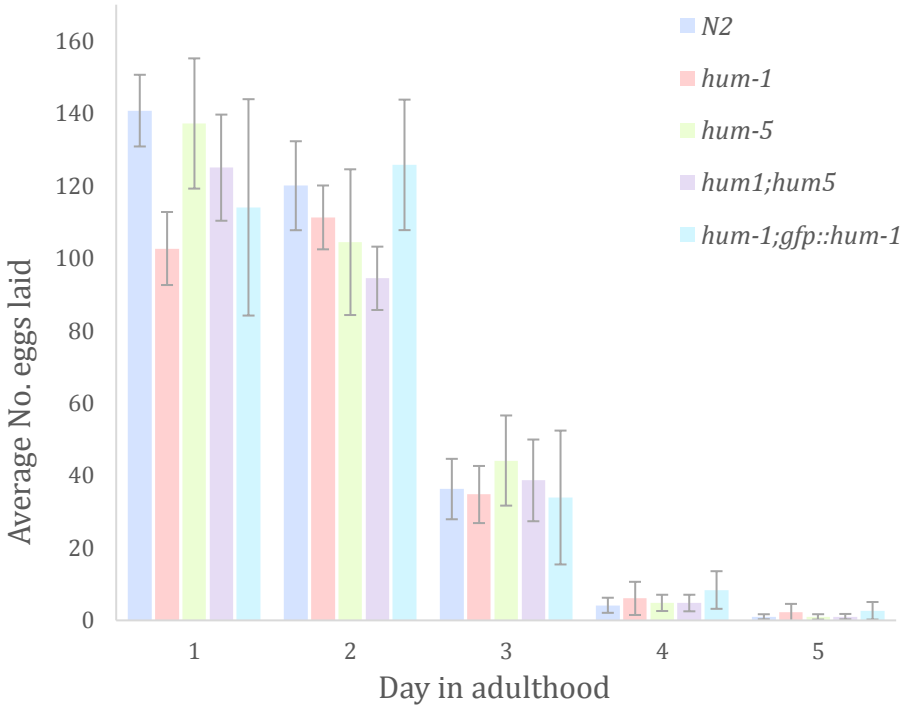

Figure 3.14 Age specific fecundity. N2 control, *hum-5* and *hum-1;hum-5* disruptions showed the highest number of progeny were laid on day 1 of adulthood, with this number decreasing with each consecutive day thereafter. Hermaphrodites with disruption of *hum-1* or those expressing the *gfp::hum-1* transgene showed a delay in embryo release with each strain showing the highest number of progeny laid on day 2.

The N2 control showed the highest average number of progeny laid on day 1 of adulthood, with each consecutive day thereafter showing a linear decrease as sperm depletes. Disruption of *hum-5* did not appear to impact age specific-fecundity and although the double mutant *hum-1;hum-5* caused a reduction in overall brood size, it also did not appear to impact age-specific fertility, with both showing the highest number of progeny laid on day 1 of adulthood (Figure 3.14). Hermaphrodites with disruption of *hum-1* and those expressing the *gfp::hum-1* transgene however appeared to have a delay in embryo release, with the highest number of progeny laid on day two. Following day two, fertility decreased on contiguous days. These results suggest that although the presence of the *gfp::hum-1* transgene is able to partially rescue the overall brood size, it is unable to rescue the age-specific fecundity phenotype (Figure 3.14).

3.5.4 Myosin I is not required for chemosensory behaviour to diacetyl

As HUM-1 was expressed in the chemo/odour sensory sensilla found within the head of *C. elegans* a chemosensory assay was undertaken to investigate whether disruption of *hum-1* affected the ability of nematodes to respond to an odorant. In general, the ASE neurons detect salts and water-soluble attractants, whereas the AWA and AWC olfactory neurons detect volatile attractants. ASH, ADL, and AWB neurons detect volatile repellents., while the additional amphid neurons ASI, ADF, ASJ, ASK and ASG make only minor contributions to behavioural chemosensory responses (Menini et al. 2010).

As expression of HUM-1 appeared to be within the two pairs of amphid sensory neurons AWC and AWA, which are required for chemotaxis to volatile odours, diacetyl was chosen as the test attractant (Bargmann 2006). The diacetyl was diluted 1:100 in water and water alone was used as the control.

$$\frac{\text{(\# Worms in Both Test Quadrants - \# Worms in Both Control Quadrants)}}{\text{(Total \# of Scored Worms)}}$$

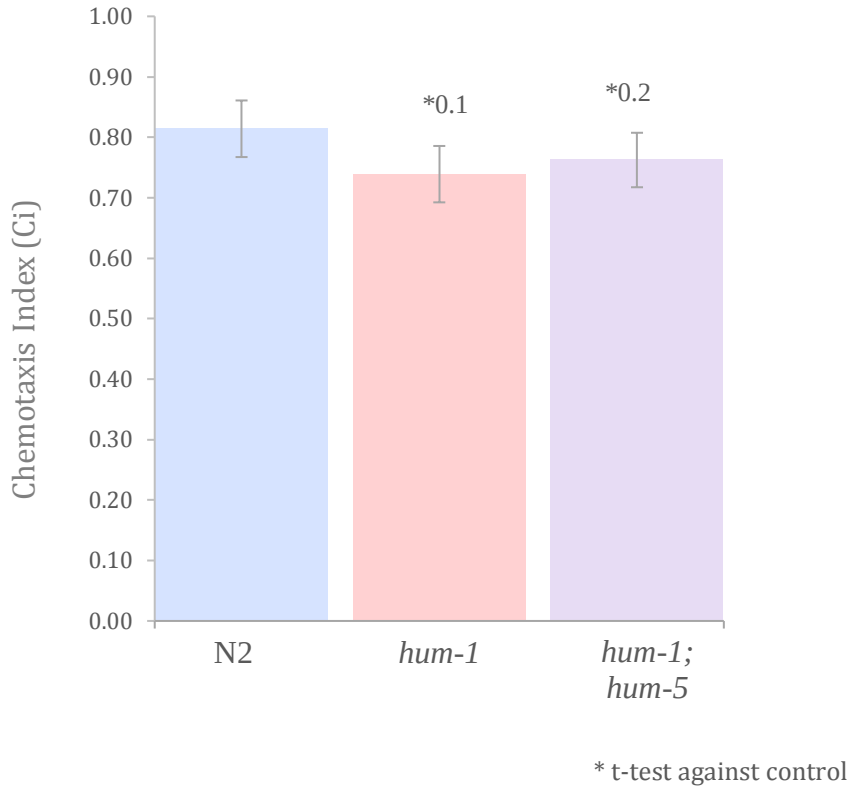

Figure 3.15 Diacetyl chemotaxis index for N2 and myosin I mutants. Equation used to calculate the chemotaxis index, # is number of worms. *t-test value when compared to N2 control. A CI value of +1 represents 100% of worms arriving in the test quadrants. A CI value of -1 represents 100% maximal repulsion. When compared to the N2 control disruption of *hum-1* or both *hum-1;hum-5* did not appear to have any impact on nematode chemosensing to the attractant odour of diacetyl.

Worms were placed in the centre of a petri dish that has been divided into four quadrants. Anaesthetic was placed in all four quadrants, with two opposite quadrants used for the test odorant and the remaining two used as the controls. A circle was marked around the origin to ensure that non-motile worms were ignored (see methods). Utilizing a four-quadrant system eliminated bias in the movement of the worms and also circumvented the worms being forced to travel through clusters of other worms.

After one hour, the movement evoked in response to the odorant was observed and the chemotaxis index (CI) calculated using the equation shown in Figure 3.15. A CI score of +1.0 represents 100% of the worms arriving in the quadrants containing the diacetyl, indicating maximal attraction towards the target. An index of -1.0 however is evidence of maximal repulsion.

The chemotaxis index calculated for the control N2 was +0.83, *hum-1* mutants gave a value of +0.76 and *hum-1;hum-5* double mutants gave a value of +0.8. After completing statistical analyses on the data with significance set at $t < 0.05$ (two-tailed), it was evident there were no significant differences seen between the N2 control and the *hum-1* and *hum-1;hum-5* populations, with each giving t values of 0.1 and 0.2 respectively (Figure 3.15). These results therefore indicate myosin I proteins are not required for chemosensory behaviour to diacetyl.

3.5.5 Myosin I is not required for gentle touch mechanosensing

In order to survive in the wild, nematodes must be able to detect physical forces produced from colliding with objects such as adjacent soil particles and other animals or forces generated by their own movement. Hermaphrodites have 30 putative mechanoreceptor neurons which initiate and modulate several behaviours in response to such stimuli.

As HUM-1 showed expression in the ASH and IL mechanosensing neurons and HUM-5 showed expression in the CEP and FLP mechanosensing neurons, a gentle touch assay was undertaken to explore the effects disruption of *hum-1* and *hum-5* had on the nematodes ability to sense mechanical stimuli.

Nematodes are assayed on very thin bacterial lawns or off food by laying a sterilised eyebrow hair on the surface of the plate in front of the animal; testing gentle nose touch responses or by stroking the animal across the body just before the anus to test for posterior touch responses (methods). Eyebrow hairs are used because they are usually not cut and are therefore finely tapered. Twenty to 30 animals were tested each time, with each strain tested at least three times independently. Animals are said to be nose touch-sensitive if they immediately initiate backward locomotion once the nose has made perpendicular contact with the hair whereas mechanosensory defective animals either hurdle over or slide their nose along the hair. Significance was set at $t < 0.05$ (two-tailed). Disruption of *hum-1* or *hum-5* had no apparent impact on nematode gentle touch nose sensing (Figure 3.16).

When compared to the N2 control *hum-1* and *hum-5* gave t values of 0.56 and 0.84 respectively. Disruption of both myosin I genes also had no notable effect on gentle nose touch, giving a t value of 0.44. Conversely animals are said to be touch-sensitive to posterior touch if they respond to stroking by moving forward away from the hair. Similarly to the gentle nose touch assay, disruption of *hum-1*, *hum-5* or *hum-1;hum-5* had no apparent impact on nematode gentle posterior sensing, giving t values of 0.58, 0.35 and 0.81 respectively, when compared to the N2 control confirming no statistical significance (Figure 3.16).

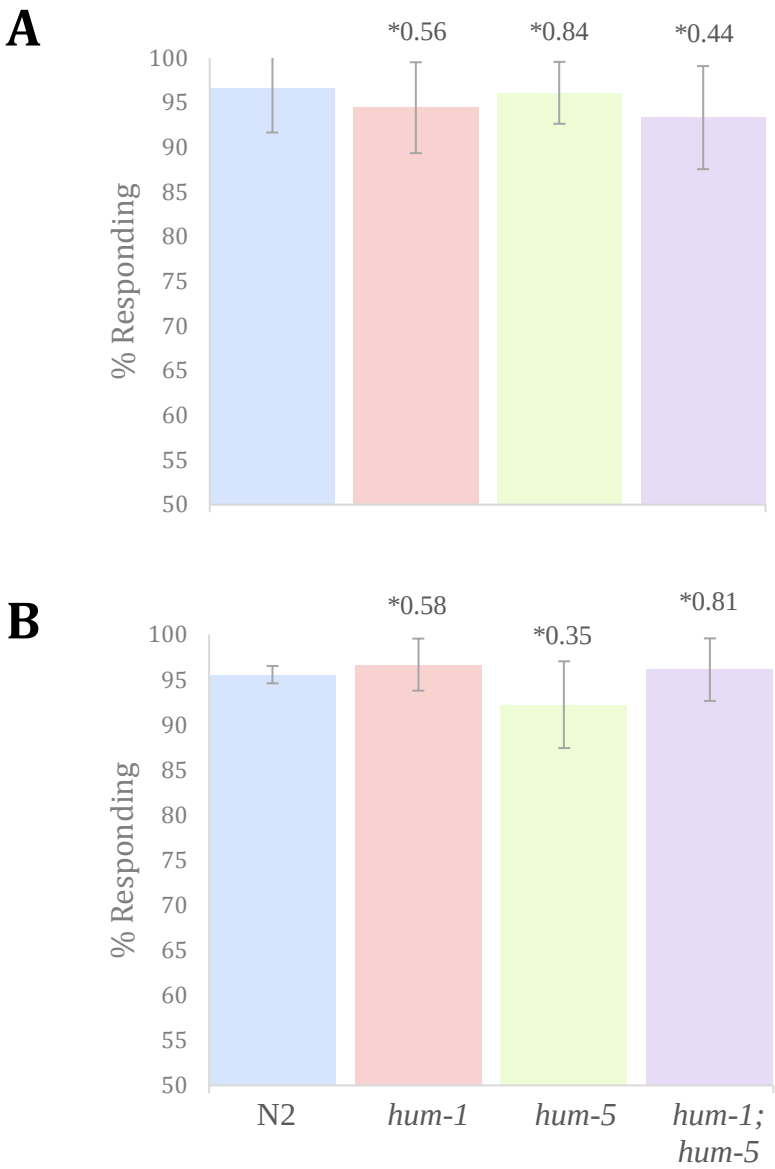

Figure 3.16 N2 and myosin mutant responses to gentle A) nose or B) posterior touch. A) Disruption of *hum-1*, *hum-5* or *hum-1;hum-5* had no significant impact on nematode response to gentle nose touch. B) Disruption of *hum-1*, *hum-5* or *hum-1;hum-5* had no significant impact on nematode gentle posterior sensing.

3.5.6 Myosin I is not required for harsh touch mechanosensing

Response to harsh touch is predominantly mediated by the PVD and FLP sensory neurons. As HUM-5 showed expression in both of these mechanosensory neurons a harsh touch assay was carried out to explore the effects disruption of *hum-5, hum-1* and *hum-1;hum-5* had on the nematodes ability to sense harsh mechanical stimuli. Harsh anterior touch is determined by probing non-moving gravid adults anterior to the vulva whereas posterior harsh touch is determined by probing non-moving gravid adults just posterior to the vulva (methods). Animals that initiate forward or backward locomotion for posterior and anterior respectively, give a positive response. Touch abnormal animals to not respond. Significance was set at $t < 0.05$ (two-tailed).

Disruption of *hum-1*, *hum-5* or *hum-1;hum-5* had no apparent impact on nematode anterior or posterior harsh touch sensing (Figure 3.17). When compared to the N2 control, anterior harsh touch responses gave t values of 0.64, 0.38 and 0.54 for *hum-1*, *hum-5* and *hum-1*;*hum-5* respectively confirming no statistical significance between the populations. Similarly, posterior harsh touch t values of 0.18, 0.13 and 0.2 for *hum-1*, *hum-5* or *hum-1;hum-5* respectively confirmed there was no statistical significance between the populations when compared to the N2 control.

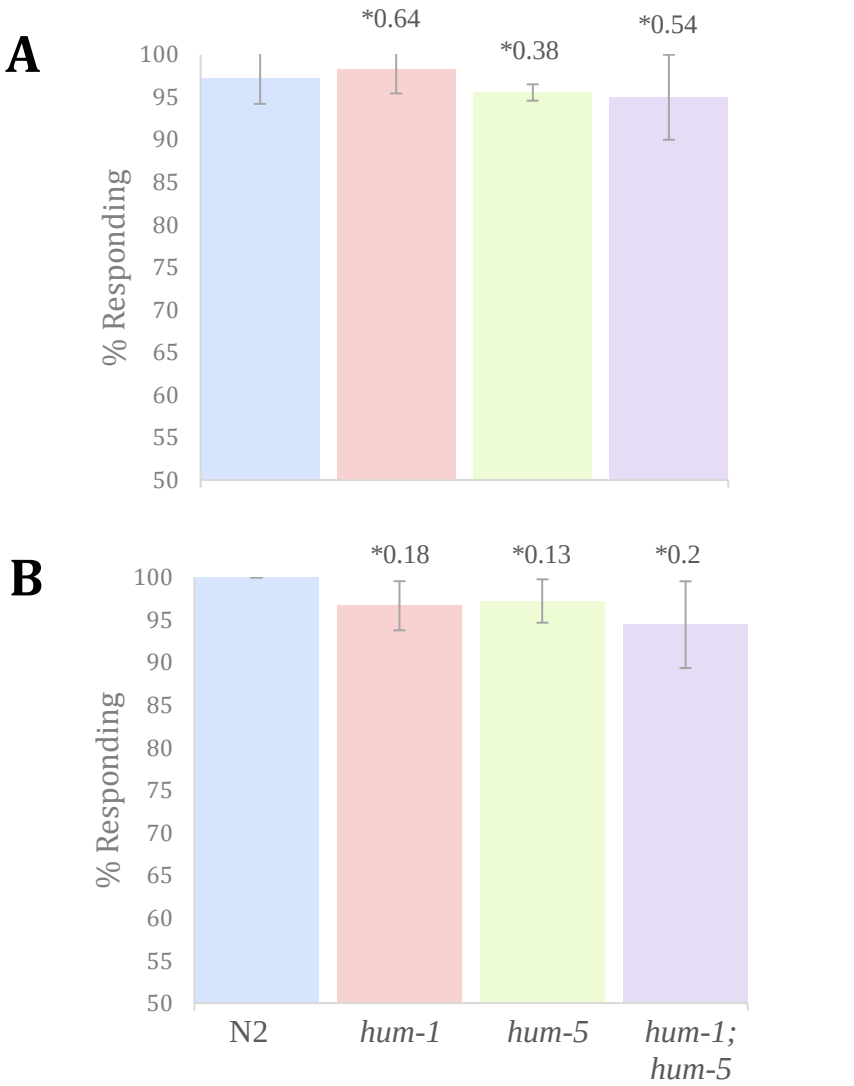

Figure 3.17 N2 and myosin mutant responses to A) harsh anterior and B) posterior touch. *C. elegans* responds to anterior and posterior harsh touch by initiating backward or forward locomotion respectively. % of worms calculated based on positive responses. Disruption of *hum-1*, *hum-5* or *hum-1;hum-5* had no significant impact on nematode responses to harsh touch. This was confirmed by t-test with all t values > 0.05.

3.6 Discussion

To further develop our understanding of class I myosin motor proteins in *C. elegans*, plasmid born copies of HUM-1 and HUM-5 were fused with the recombinant reporter proteins; GFP and mCherry respectively and co-injected with the identification marker *rol6*$^{+}$ into day one adult nematodes. Nematodes were then crossed with strains in which the endogenous *hum-1* or *hum-5* genes were disrupted to provide a clean background for protein localisation and functional studies. *In vivo* analysis using high-resolution fluorescent confocal microscopy (methods) revealed HUM-1 is highly expressed in a diverse array of tissues including chemo/odour sensory sensilla, the pharyngeal-intestinal and intestinal-rectal valves and the reproductive system, whereas HUM-5 was found to be expressed in mechanosensory neurons in the head and body only.

Considering first the nervous system; a fully formed adult hermaphrodite has 302 neurons, each with a reproducible position, morphology and cell lineage (Schafer 2016). The central nervous system consists primarily of a nerve ring that encircles the neck of the pharyngeal muscle, composed largely of the axonal and dendritic processes of neurons whose cell bodies lie in bundles positioned anterior and posterior to the nerve ring. Usually encased in lamina, cell bodies of most neurons have been shown to cluster in ganglia in the head or tail (Corsi et al. 2015).

Although not mutually exclusive, *C. elegans* neurons are classified into the three major groups: sensory neurons that possess distinct sensory dendrites of any modality, interneurons where their synaptic wiring imputes a role in relaying synaptic activity from upstream to effector downstream neurons and motor-neurons which form neuromuscular junctions onto one or more muscle cells (Sanders et al. 2013; Aamodt 2006). Expression of HUM-1 within the chemo/odour sensory sensilla was seen throughout cell bodies, axons and other processes of the amphid neurons and inner labial neurons located in the head, in addition to PHC, and phasmid neurons in

the tail. In total*, C. elegans* contains 32 chemo/odour sensory neurons; 22 are paired neurons of the amphid sensilla, 4 are paired neurons of the phasmid sensilla and 6 are neurons of the inner labial sensilla (Schulenburg & Ewbank 2007).

The amphids are the primary olfactory, chemo-receptive, and thermo-receptive organs in *C. elegans* and are paired lateral sensory structures at the anterior end of the nematode (Ward et al. 1975). Each amphid is typically composed of 11 sensory neurons and two support cells (Bumbarger et al. 2009). The inner labial sensilla are arranged in a six-fold symmetry, originating from a position anterior to the amphids (Inglis et al. 2007). IL1 neurons are mechano-sensory neurons involved in mediating head withdrawal in response to dorsal or ventral nose touch, whereas IL2 neurons are postulated to be chemosensory (Corsi et al. 2015). In the tail, the two phasmid neurons PHA and PHB are located on the lateral side of the nematode, behind the rectum and are thought to be involved in modulation of chemo-repulsion behaviour, acting antagonistically with amphid neurons to regulate reversals required for escape behaviours (Bae & Barr 2008). The PHC neuron however, is thought to be involved in modulating thermo-nociception and temperature avoidance responses (Siddiqui & Culotti 2007).

In contrast to HUM-1, which was predominantly expressed in chemo/ odour sensory neurons, high-resolution confocal data indicates HUM-5 is highly expressed in the cephalic neurons (CEP), FLP and PVD mechanosensory neurons where it localizes throughout cell bodies, axons and other processes. In the hermaphrodite, all polymodal nociceptors detect noxious signals associated with tissue damage and elicit protective responses, therefore these neurons are potentially significant to the survival of the animal (Hall & Treinin 2011). CEP and FLP neurons are located in the head of the nematode, whereas PVD neurons cover the body. Although the majority of neurons in *C. elegans* adopt a simple morphology with few branches, FLP and PVD neurons are atypical for the nematode displaying

elaborate, highly branched, multi-dendritic structures that cover the head and body (Albeg et al. 2011). The function and position of PVD branches are characteristic of mammalian poly-modal nociceptors, which are typically, highly branched with multiple sensory dendrites (Caterina & Julius 1999). The morphology and function of such neurons is also conserved in *Drosophila*, indicating this cell type is conserved throughout evolution.

Eight forms of myosin I are expressed in mammalian cells, however to date only four of these; Myo1b, Myo1c, Myo1d and Myo1e have been found in neurons (Bridgman 2004). During this study, we have shown HUM-1, the homolog of Myo1e, was expressed in a diverse array of neurons however its exact role is still to be elucidated. Previous research has shown Myo1e (myr 3) is expressed in rat brain tissue, with biochemical assays revealing interactions with proteins involved in endocytosis and actin dynamics including dynamin, synaptojanin and CARMIL-1a/Acan125 (Feeser et al. 2010). In addition, expression of the Myo1e tail in HeLa cells inhibits transferrin endocytosis, indicating Myo1e could be involved in clathrin-mediated endocytosis at the synapse (Krendel et al. 2008). *C. elegans* RNAi screens used for the systematic analysis of genes required for synapse structure and function have also implicated HUM-1 in synaptic transmission (Sieburth et al. 2005), therefore it is likely the role of Myo1e in neurons is conserved in the nematode, with HUM-1 playing a key role in actin membrane dynamics and endocytosis.

Expression of HUM-5, the homolog of Myo1d, was confined to mechanosensory neurons, with expression found to be predominantly developmentally controlled. Myo1d (myr 4) was first identified in the rat brainstem, spinal cord, cortex and cerebellum where it localised to neuronal cell bodies, dendrites and axons (Bähler et al. 1994). Expression in the brain was found to be developmentally regulated with expression levels reaching maximal values during adulthood (Bähler et al. 1994). Functional studies indicated Myo1d played a role in membrane trafficking, membrane tension and the establishment of left-right symmetry during Drosophila development

(Suter 2010; Benesh et al. 2012; Nambiar et al. 2009), however more recent studies revealed a potential association with autism, suggesting Myo1d plays an important role in nervous system tissues, neuro-development and myelination (Benesh et al. 2012; Ishii et al. 2009). Although the exact role of HUM-5 is yet to be determined, it is likely the role of Myo1d is conserved in *C. elegans*, with HUM-5 playing an important role in the membrane recycling pathway and neurodevelopment.

In addition to expression in the nervous system, HUM-1 also showed expression in additional tissues including the pharyngeal-intestinal and intestinal-rectal valves and within the reproductive system. The pharyngeal-intestinal valve is a passively open, multicellular valve that connects the posterior of the pharynx to the anterior cells of the intestine (Hall & Altun 2008), whereas the intestinal-rectal valve occludes the lumen of the posterior intestine, allowing digested material to leak into the rectum and then to the anus (A. F. Bird & J. Bird 2012).

Within the reproductive system, HUM-1 was expressed in four multinucleate toroidal uterine cells (ut1 - 4) which form the anterior and posterior lobe of the uterus, in addition to the spermatheca and spermathecal-uterine valve. The spermatheca connects the distal gonad arm to the uterus via the spermathecal-uterine valve and is the site of oocyte fertilization, acting as a reservoir for maturing spermatids and adult sperm. The spermathecal-uterine valve restricts mature fertilised gametes from passing from the spermatheca to the uterus or vice versa (Newman et al. 1996). Although the precise function of HUM-1 in these structures is unknown, studying the roles of other Myo1e homologs combined with the sub-cellular localisation of HUM-1, potentially provides further insight into its possible function.

In addition to expression in neuronal tissue Myo1e is also expressed in a variety of tissues including the spleen, kidney, small intestine, pancreas and the immune system (Krendel et al. 2009). Often found in regions of high

actin concentration, the exact role of Myo1e is thought to have evolved, enabling the protein to perform different functions depending on the environment (El-Mezgueldi et al. 2002). Localisation of Myo1e around the phagosome in the macrophage implied a role in phagosome closure, whereas localisation in F-actin rich regions at the cell-cell contact, indicates a role in regulating membrane associated actin structures (Kim & Flavell 2008). The observed enrichment of Myo1e to the inter-microvillar region of the intestinal brush border in mice, indicates Myo1e plays a central role in endocytosis (Krendel et al. 2008). This contribution to endocytosis is further substantiated by two mutations in human Myo1e leading to focal segmental glomerulosclerosis in two independent pedigrees (Mele et al. 2011), indicating Myo1e plays a key role in podocyte function and the consequent integrity of the glomerular filtration barrier (Mele et al. 2011). Myosin I proteins have also been shown to be involved in regulating endocytosis in fission yeast (East & Mulvihill 2011).

Often gene deletions can interrupt cellular processes, providing an invaluable insight into gene function. As behaviour in *C. elegans* reflects nervous system activity and is dependent on factors such as external stimuli, neuronal structure or past experience, behavioural assays were undertaken, providing simple, sensitive and powerful tools to interrogate protein function in the myosin I nulls (Hart et al. 2006). Disruption of HUM-1 or/and HUM-5 did not impact the ability of *C. elegans* to respond to harsh or gentle touch or sense the chemo attractant odour of diacetyl, therefore it is possible HUM-1 and HUM-5 are not involved in eliciting a response in these behaviours or they function in parallel pathways with other proteins which are able to compensate for the loss of myosin I function.

Individually, HUM-1 or HUM-5 are not required for nematode longevity, however disruption of both myosin I genes resulted in a slight reduction in lifespan. This could be due to each myosin I having overlapping function, however when they are both disrupted this functional cross over does not occur, conversely it could be due to a synthetic interaction between both

myosin I genes. The most significant phenotype for disruption of myosin I was seen in the brood size assay. Although disruption of HUM-5 had no observable impact on nematode brood, disruption of HUM-1 caused a significant reduction, therefore indicating HUM-1 is required for maximal brood size. In addition, disruption of HUM-1 also affected age specific fertility, causing a slight delay in embryo release. If the role of Myo1e is conserved in *C. elegans*, the reduction in brood size may be the result of reduced endocytosis leading to a loss of signalling or it could be due to reduced actin membrane dynamics in the spermatheca / spermathecal-uterine valve.

3.7 Conclusions

The results obtained during this study revealed class I myosin motor proteins are non-essential in *C. elegans.* This is surprising based on what is known about myosin I function in other systems and the dependence of the nematode on the actin cytoskeleton for growth and development. Fluorescent confocal microscopy revealed HUM-1 is expressed in a variety of different tissues, whereas HUM-5 is expressed in specific mechano-sensory neurons only. No co-localisation of HUM-1 and HUM-5 could be seen in any of these structures, indicating each gene has a different anatomical focus.

Mutations in human Myo1d and Myo1e have been associated with neuro-development defects and kidney disease respectively. Although this study cannot ascribe the exact function of HUM-1 or HUM-5, tissue expression of each protein is reminiscent of homologs found in higher eukaryotes. As proteins often function in evolutionary conserved pathways, these results offer an invaluable insight into the possible function of class I myosin proteins in human pathologies.

Chapter 4: Analysis of a conserved phosphoserine within the TH1 domain of Myosin 1e

4.1 Introduction

Myosin 1e (Myo1e) is a single headed actin binding motor-protein ubiquitously expressed in mammalian cells (Jin et al. 2013). Classified as long tailed, the tail domain of Myo1e includes a TH1, TH2 and SH3 domain. Rich in basic amino acids, the TH1 domain is required for steady-state targeting in cells and has been shown to be capable of high-affinity binding to anionic phospholipids via electrostatic interactions (Doberstein & Pollard 1992; Mazerik et al. 2014). The TH2 domain binds actin and regulates actin dynamics and the SH3 domain has been assumed to putatively bind regulatory proteins involved in endocytosis and actin dynamics (Greenberg & Ostap 2013)

Several conserved motifs within the TH1 domain have been implicated in myosin I function however, it is believed different isoforms employ distinct or additional mechanisms that govern membrane binding and targeted localisation (Mazerik et al. 2014). Deletion of the Myo1e TH1 domain only reduces co-localisation with clathrin suggesting that interactions with both lipids and proteins contribute to Myo1e localisation, however the membrane binding properties and structural motifs that govern these interactions have yet to be identified (Feeser et al. 2010).

Using phosphoproteomic screens a conserved serine residue found within the TH1 domain of Myo1e has been identified as a potential phosphorylation site (Feeser et al. 2010). Post-translational modification through the addition of a phosphate group is often employed as a fundamental mechanism for regulating the biological activity of proteins as it is fast, reversible and often highly specific. The resulting protein conformational changes serve to alternately promote or inhibit function, facilitate or disrupt protein interactions or target proteins for destruction (Huttlin et al. 2010).

The aim of this study was to therefore investigate the molecular mechanism of regulation by phosphorylation and explore the importance of this phosphoserine residue on protein structure, function and dynamics using the two Myo1e homologs; *S. pombe* Myo1 and *C. elegans* HUM-1 which show conservation of the conserved phosphoserine residue. In addition, *C. elegans* functional assays were undertaken to investigate whether expression of each mutant transgene could rescue the genetic null phenotype.

4.2 Location and modelling of the conserved phosphoserine

The conserved phosphoserine residue of human Myo1e lies at the start of the TH1 domain in position 734. Sequence alignment of Myo1e, *S. pombe* Myo1 and *C. elegans* HUM-1 shows conservation of the conserved phosphoserine between the IQ domain and pleckstrin homology (PH) domain in all species (Figure 4.1). The conserved serine in *S. pombe* Myo1 lies in position 782 whereas the equivalent in *C. elegans* HUM-1 occupies residue 734. Un-phosphorylated serine residues contain a side chain consisting of a hydroxyl-methyl group (OH) which provides polarity to otherwise hydrophobic side chains.

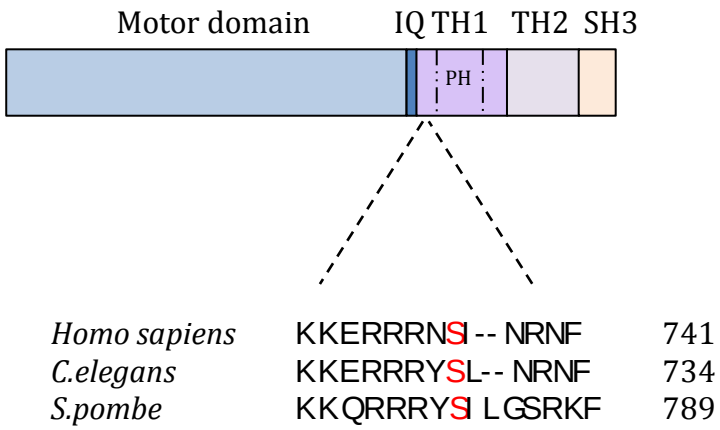

Figure 4.1 Schematic of Myo1e and TH1 domain sequence alignment. Alignment of the TH1 domain sequences of Myo1e, HUM-1 and Myo1 (Bottom) shows conservation of a conserved serine residue at the start of the TH1 domain. The serine residue mutated in this study is indicated in red. PH refers to the pleckstrin-homology domain.

The major driving forces of conformational changes upon phosphorylation are the electrostatic interactions between the negatively charged phosphate group and the surrounding charged residues. The mechanism of phosphorylation by the modifying protein kinase, indicates that this serine residue should be located on the protein surface where it is accessible to the modifying kinase (Tyanova et al. 2013).

To date the crystal structure of yeast or nematode myosin I isoforms have not been determined therefore Protein Homology/analogY Recognition Engine V 2.0 (PHYRE2) software was used to generate a prediction of the 3D structure of the Myo1e, Myo1 and HUM-1 TH1 domains enabling us to model the location of the conserved phosphoserine residue. Providing a simple bioinformatics tool, PHYRE2 uses advanced remote homology detection methods to build 3D models, based on the key principles that in evolution, protein structure is more conserved than protein sequence and that in nature there is evidence of a finite and moderately small number of unique protein folds (Kelley et al. 2015).

The PHYRE2 predicted 3D structure of the Myo1e, HUM-1 and Myo1 TH1 domain shown in Figure 4.2, shows a high degree of structural conservation between each of the TH1 domains and predicts that the phosphoserine residue is located within a conserved, highly organised alpha helical structure in all of the myosin I isoforms. An enhanced view of the conserved phosphoserine shown in Figure 4.3 displays the predicted area around the serine residue exposed at the surface of the protein, illustrated by black mesh. The absence of mesh above the residue would indicate no exposure to the protein surface. The predicted crystal structure for each of the proteins therefore indicates that the conserved serine residue is exposed to the environment in each of the myosin I isoforms, further reinforcing the prediction that this conserved phosphoserine is located at the surface interface and is thus accessible by other proteins.

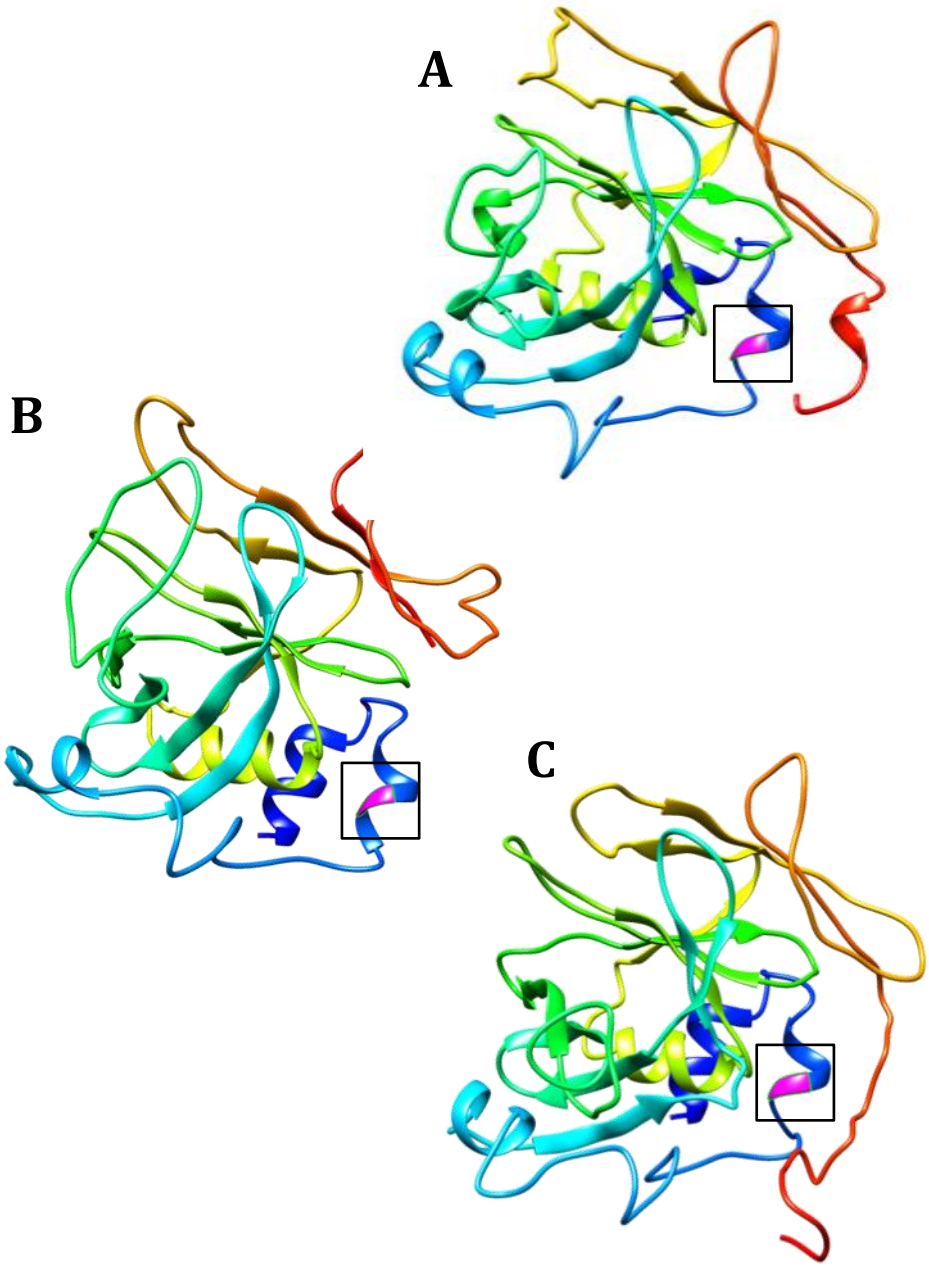

Figure 4.2 Predicted 3D structures of the A) Myo1e B) *C. elegans* HUM-1 and *S. pombe* Myo1 TH1 domain. The predicted crystal structures of the Myo1e, HUM-1 and Myo1 TH1 domains appeared to be highly conserved with similar structural arrangements. The conserved phosphoserine is highlighted in magenta. The black box highlights the area of interest explored further in Figure 4.3.

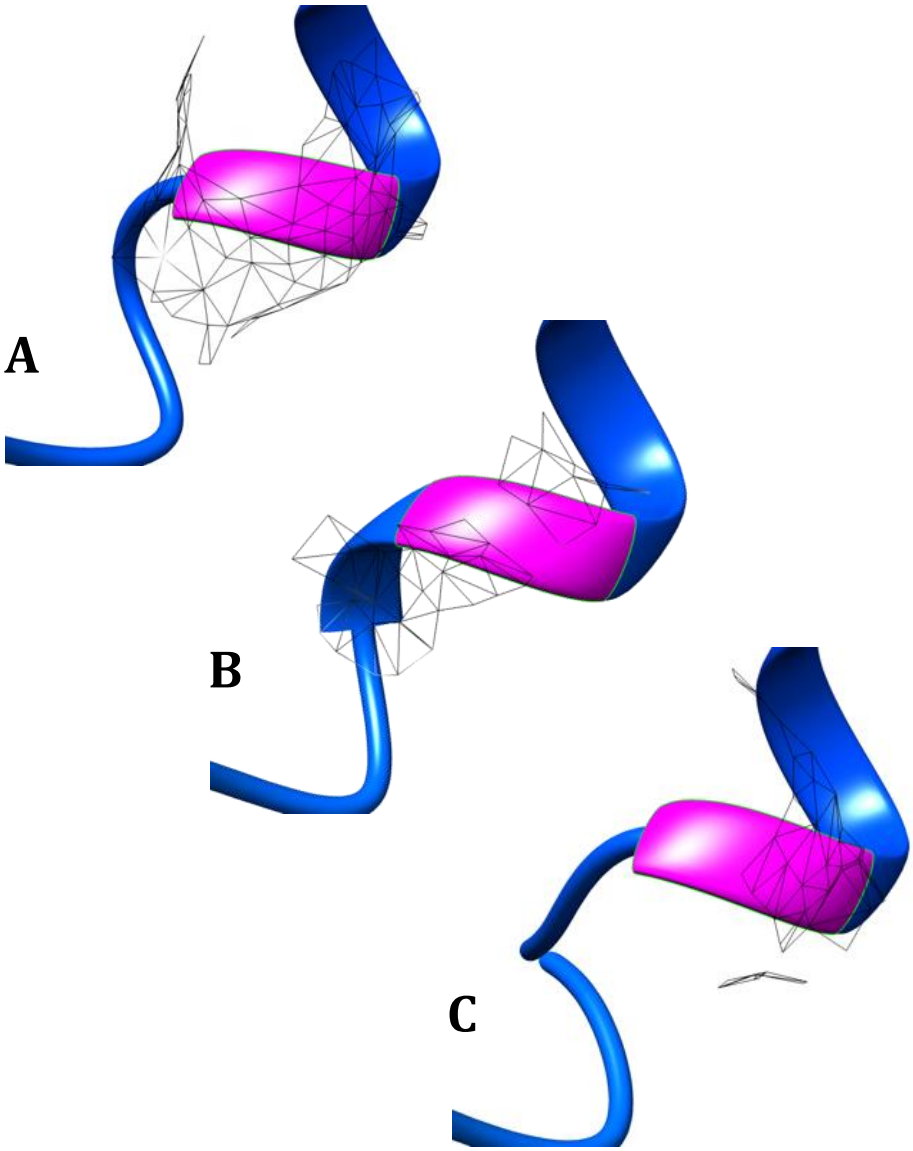

Figure 4.3 Close up of the A) Myo1e B) HUM-1 and C) Myo1 conserved phosphoserine. Close up of Myo1e Ser736, HUM-1 Ser734 and Myo1 Ser782 show in all of these isoforms, the residue is exposed at the surface of the protein, highlighted in black mesh. The large area of mesh on Myo1e indicates serine 736 is openly exposed to the environment whereas the small area of mesh around HUM-1 and Myo1indicates these residues are not as readily accessible and are more buried within the protein.

The degree of surface interface appears highest in Myo1e with HUM-1 and Myo1 appearing to have less surface exposure (Figure 4.3 B,C). As *C. elegans* and *S. pombe* are simpler eukaryotes encoding fewer proteins, less exposure of the serine residue at the surface of the protein could be employed as an additional mechanism of regulating access by other proteins and thus phosphorylation of this residue.

4.2.1 Generation of HUM-1 phosphoserine mutant constructs

As the intrinsic backbone conformation propensity of the conserved phosphoserine is mainly determined by the interactions arising from the side-chain groups and the neighbouring backbone peptide groups, mutations were introduced into the *C. elegans hum-1,* to explore the effects phosphorylation of this residue has on protein structure and function.

The first mutation substituted the conserved serine to an alanine. Serine residues are amino acids with polar uncharged side chains; substitution to an alanine introduces a non-polar hydrophobic side chain and prevents phosphorylation of the residue due to the absence of the –OH group needed for substitution with the phosphate group. The second mutation substituted the conserved serine to an aspartic acid. Substitution to an aspartic acid introduces a polar amino acid that mimics the phosphorylation of serine due to the negative charge of the –COOH group in the lateral chain that is also generated by the additional phosphate group.

In *C. elegans* the conserved phosphoserine residue is found at position 734 (Figure 4.1). Mutations were introduced into the *hum-1* gene using PCR. Fragments were inserted into a pUC18 based vector which contained a 2 kb upstream promoter and GFP fluorophore. The *S. pombe* conserved phosphoserine is found at position 782 (Figure 4.1). DNA containing the Myo1 S782 mutations was synthesised by IDT and cloned into an M13

vector containing mNeon-green and a 500 bp upstream region of the *myo1*$^{+}$ gene (methods).

4.2.2 Generation of *C. elegans* strains

C. elegans strains containing the extra chromosomal *gfp::hum-1::hum-1S734A* or *gfp::hum-1::hum-1S734D* were generated by co-injecting the plasmid DNA into day one adult N2 nematodes with the identification marker *rol6*$^{+}$ by Marina Ezcurra (methods). Generation of *hum-1::gfp::hum-1* was previously described in chapter 3. A minimum of two stable injection lines were isolated so a comparison of expression could be made. One line, representative of protein expression was then chosen to take forward for all experiments. Subsequent strains with disruption of endogenous *hum-1* containing extra chromosomal constructs were generated using standard genetic cross protocols, however only rolling progeny could be selected to follow construct expression (methods). All experiments were conducted using strains with disrupted *hum-1* unless otherwise stated, with the exception of wild-type N2.

4.2.3 Overall transgene expression levels are equivalent

To give confidence that any changes seen in localisation were a result of the phosphoserine-mutations and not due to changes in protein expression levels, images of 20 L4 worms from each of the strains expressing GFP::HUM-1, GFP::HUM-1S734A and GFP::HUM-1S734D were captured and analysed using Autoquant. A line profile was drawn around each worm and the overall pixel intensity was analysed. Using this data, the average pixel intensity for each strain could be calculated. Significance was set at $t < 0.05$ (two-tailed). The overall average pixel intensities between each of the strains gave equivalent expression levels. This was confirmed by t-test

with GFP::HUM-1S734A and GFP::HUM-1S734D giving t values of 0.86 and 0.31 respectively, when compared to GFP::HUM-1 (Figure 4.4). This indicates that there is no significant difference in protein expression levels between each strain and therefore any changes in HUM-1 localisation are a result of the phosphoserine mutation.

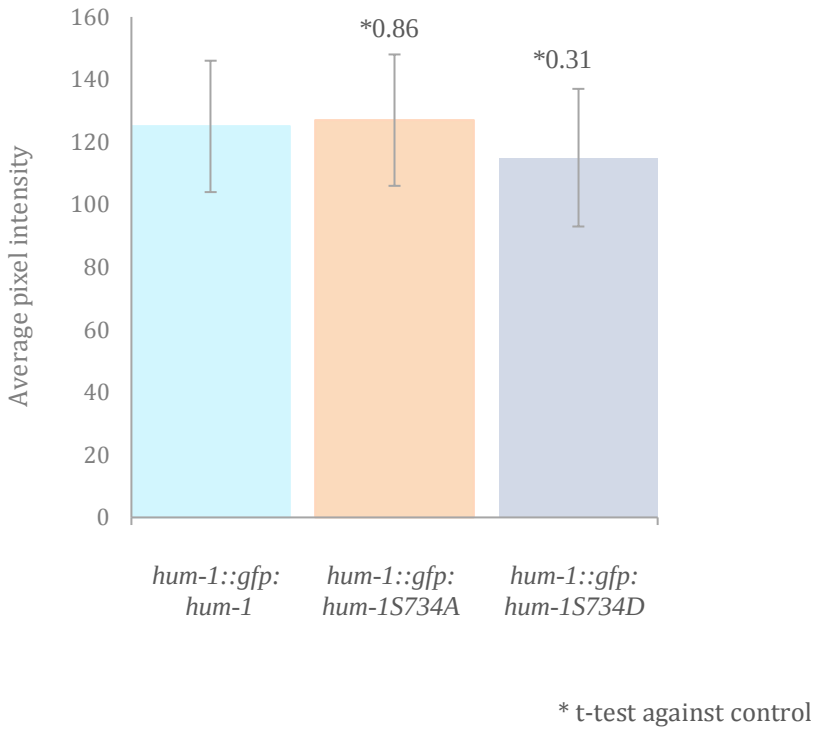

Figure 4.4 Average pixel intensity for nematodes expressing GFP::HUM-1, GFP::HUM-1S734A and GFP::HUM-1S734D. The average pixel intensity calculated using 20 L4 worms from each strain indicates that protein expression levels are comparable. t values of 0.86 and 0.31 were calculated for GFP::HUM-1S734A and GFP::HUM-1S734D respectively, confirming no statistical differences when compared to GFP::HUM-1. Any changes in localisation are therefore a result of the phosphoserine-mutations and not due to difference in protein expression.

4.3 Mutation of HUM-1 S734 alters protein localisation

Expression of GFP::HUM-1 in late L3 and adult nematodes was seen to localise to the chemo/odour-sensory sensilla, the pharyngeal-intestinal and intestinal-rectal valves and the reproductive system (Chapter 3). Although GFP::HUM-1S734A and GFP::HUM-1S734D can also be seen at each of these structures, the pattern of localisation has been altered, indicating this conserved serine residue plays a central role in modulating the ability of the HUM-1 TH1 domain to interact with different phospholipids at cellular membranes.

When compared to GFP::HUM-1 (Figure 4.5), expression of GFP::HUM-1S734A within the head chemo/odour sensory sensilla shows more cytoplasmic expression within neurons with less discrete localisation within dendrites and neuron commissures (Figure 4.6). Signal is also significantly reduced in the cilia of the neurons outside the base of the lip. In addition to changes in expression, the morphology of the neurons expressing GFP::HUM-1S734A appears to have changed, with cells showing much larger, less defined neuron commissures with less uniform axons. Expression of GFP::HUM-1S734D within the head neurons appears non-uniform and punctate. Less cytoplasmic expression can be seen within the neuronal dendrites with signal appearing much tighter to membranes. Neuronal commissures are not as well defined and expression at the terminal end of the neuron tip at the apex of the lip appears more concentrated to the membrane.

Localisation for both GFP::HUM-1S734A and GFP::HUM-1S734D can be seen in the pharyngeal – intestinal valve however when compared to GFP::HUM-1, both HUM-1 mutants show more discrete localisation to the inner membrane of the vpi cells (Figure 4.6, 4.7).

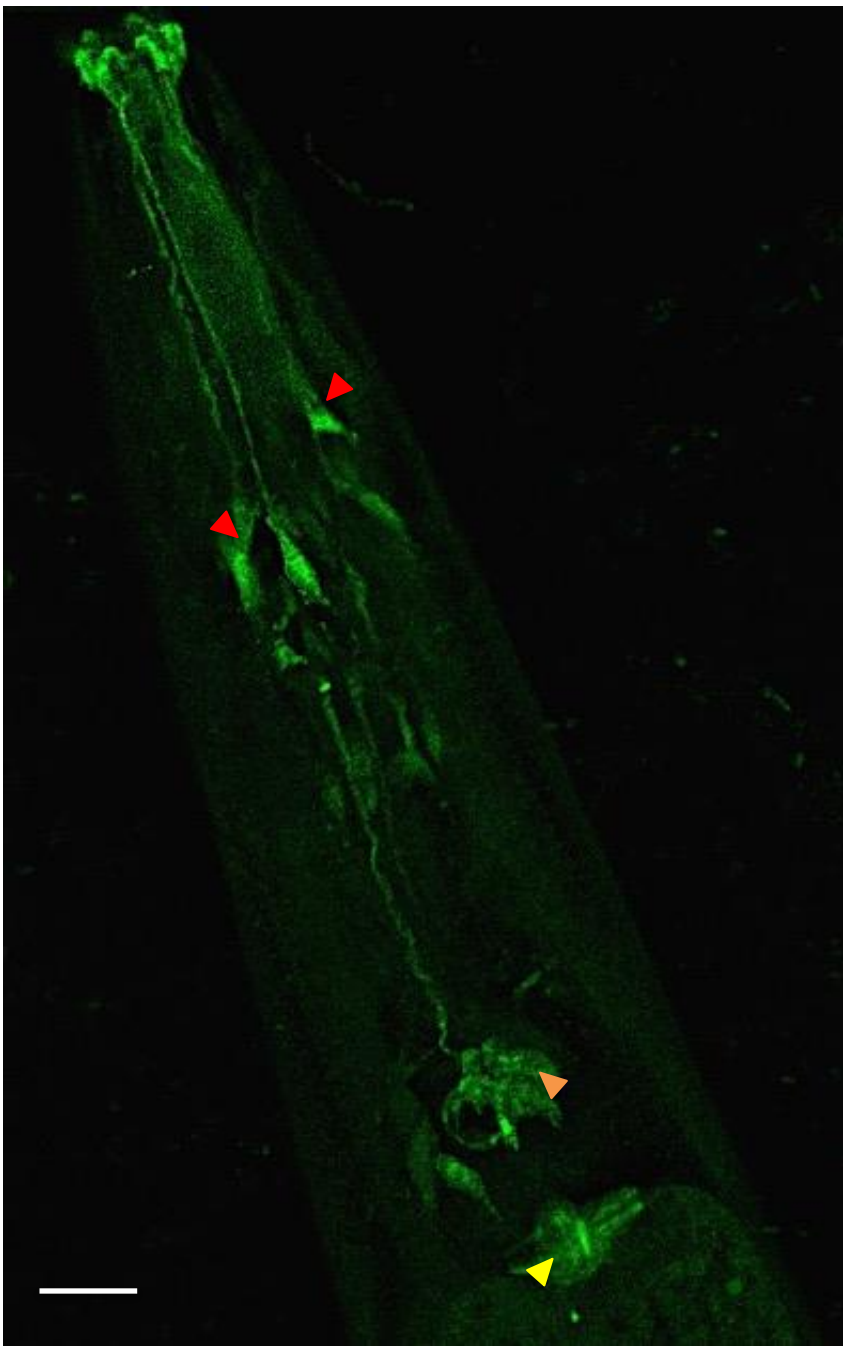

Figure 4.5 Localisation of GFP::HUM-1 within the head as previously shown in chapter 3. Expression of GFP::HUM-1 is seen throughout cell bodies, axons and other processes of the amphid sensilla (red arrowhead) and inner labial sensilla (orange). GFP::HUM-1 is also expressed in the pharyngeal-intestinal valve (yellow). Scale bar is 10 µm.

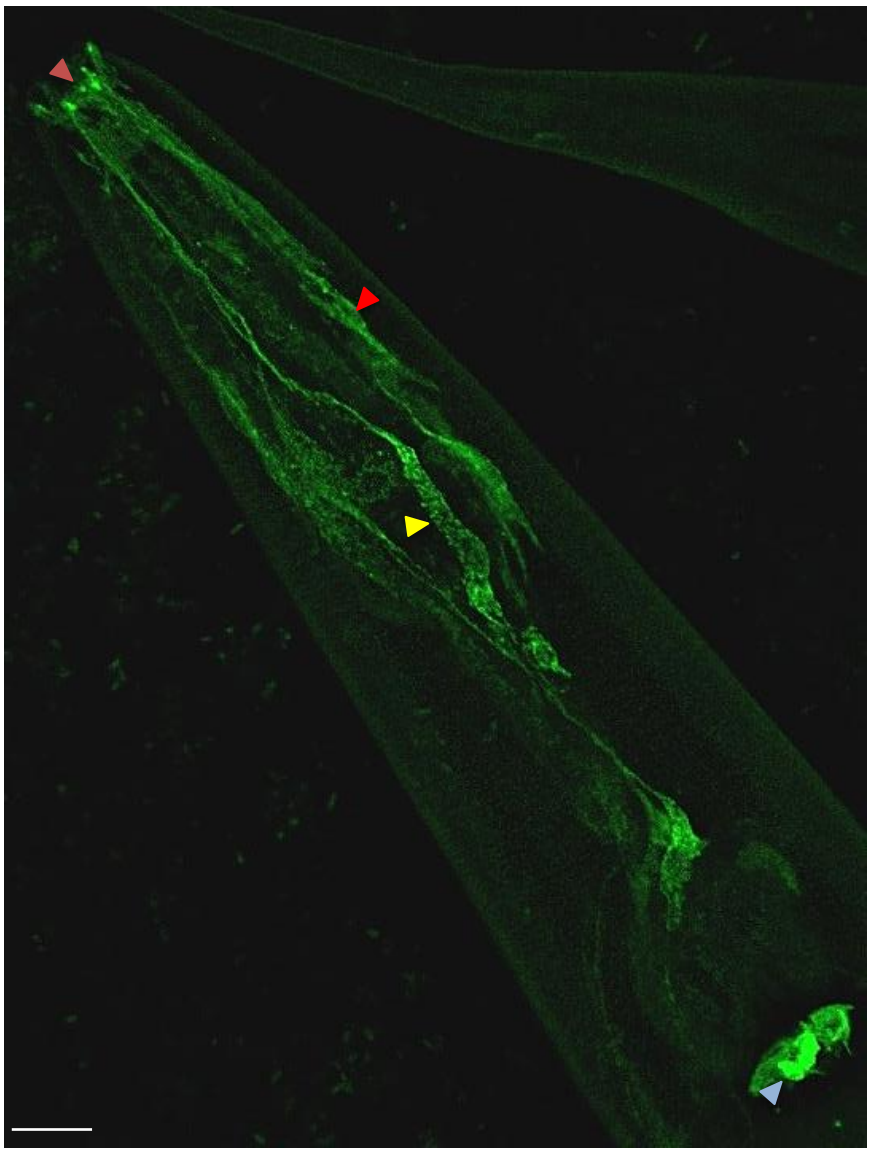

Figure 4.6 Localisation of GFP::HUM-1S734A within the head. Neurons expressing GFP::HUM-1S734A have elongated commissures (yellow arrowhead) with less uniform distribution of axons (red). Localisation appears more cytoplasmic within axons and commissures, with reduced discrete localisation in the lips (orange). Expression in the phalangeal - intestinal valve is more concentrated to the inner membrane (blue). Scale bar is 10 µm.

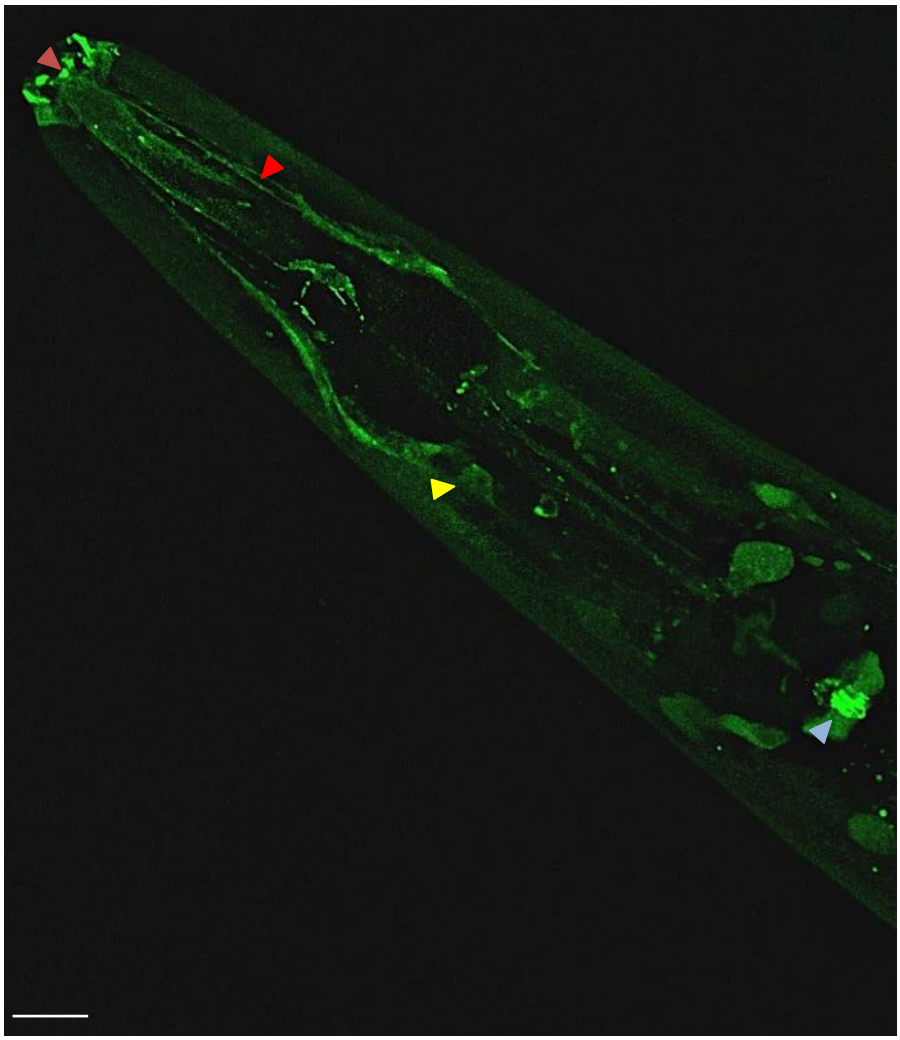

Figure 4.7 Localisation of GFP::HUM-1S734D within the head. GFP::HUM-1S734D shows less cytoplasmic and more punctate localisation in the neuronal dendrites (red arrowhead). Neuron commissures are not as well defined (yellow). Expression within the lips appears more concentrated to the neuronal tips (orange). More discrete localisation can be seen on the inner membrane of the phalangeal- intestinal valve (blue). Scale bar is 10 µm.

Within the reproductive system, less GFP::HUM-1S734A was expressed in the spermatheca and spermathecal-uterine valve with expression more evenly distributed across the uterine toroidal epithelial cells when compared to GFP::HUM-1 (Figure 4.8). In contrast, GFP::HUM-1S734D showed comparable expression in the spermatheca and spermathecal-uterine (SU) valve and uterine toroidal epithelial cells to GFP::HUM-1 however, appeared to show increased localisation to the membrane of ut1 (Figure 4.8 B).

Expression of GFP::HUM-1S734A could be seen at comparable levels to GFP::HUM-1 in the phasmid sensilla and intestinal-rectal valve, however appeared to be reduced in the PHC neuron, which extends to the tip of the tail (Figure 4.9). Conversely, expression of GFP::HUM-1S734D could be seen at comparable levels to GFP::HUM-1 in the phasmid and PHC sensilla located at the lateral sides of the tail behind the rectum and in the intestinal-rectal valve (Figure 4.9).

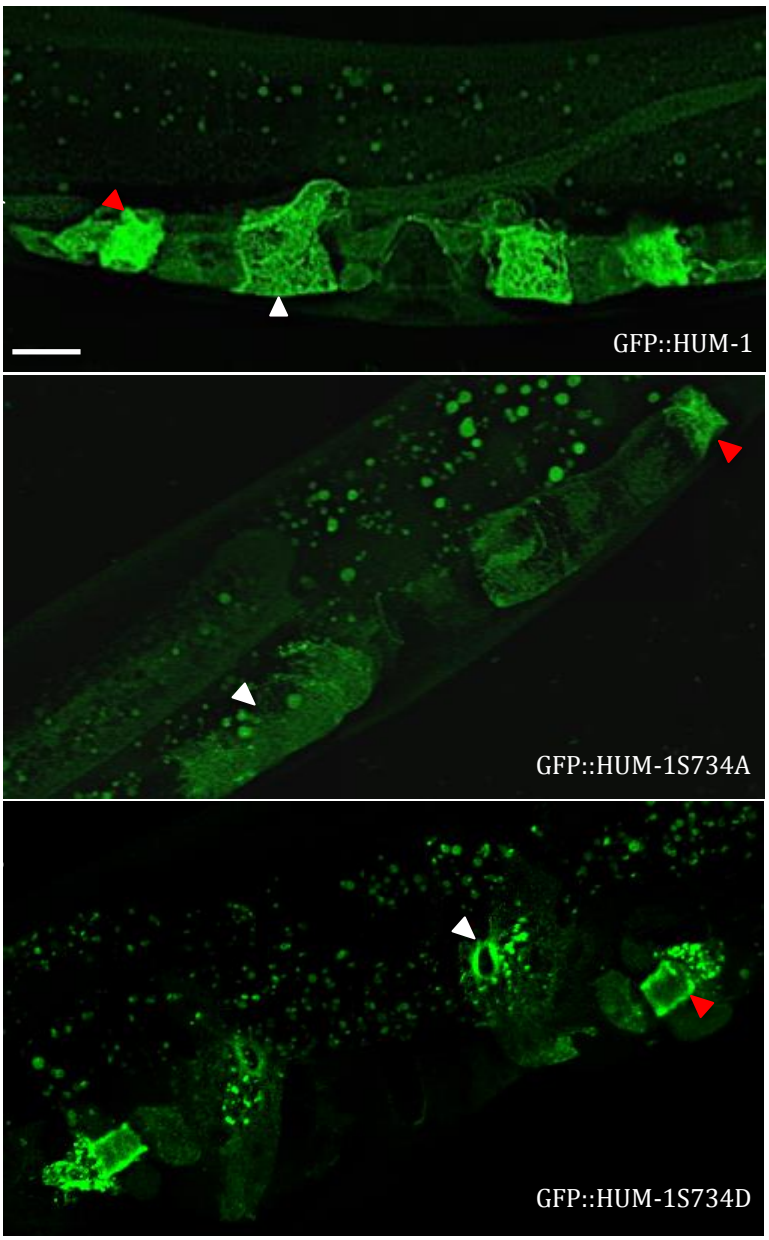

Figure 4.8 Localisation of GFP::HUM-1S734A and S734D within the gonads. GFP::HUM-1S734A shows more cytoplasmic localisation in ut cells (white arrowhead) with less expression in the spermatheca and SU valve (red). GFP::HUM-1S734D shows comparable expression to GFP::HUM-1 in the spermatheca and SU valve (red) however appears to localise more to the membrane of ut1 (white). Scale bar is 10 µm. Auto fluorescence of gut granules.

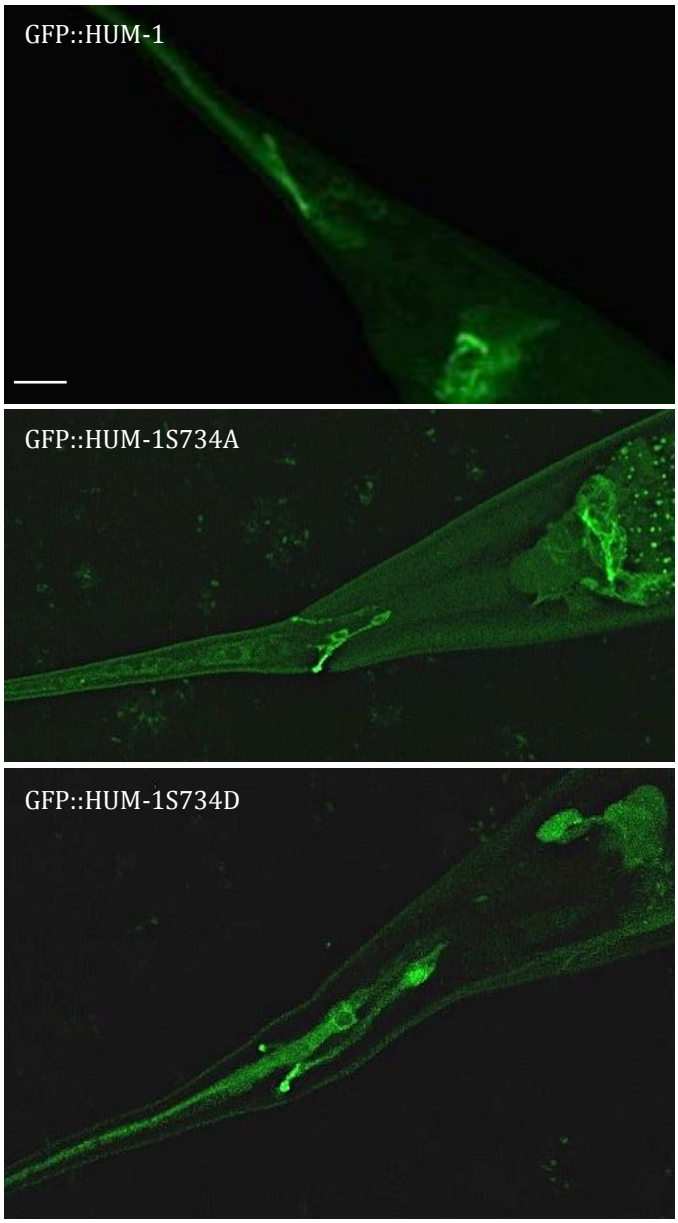

Figure 4.9 Localisation of GFP::HUM-1S734A and S734D within the tail. GFP::HUM-1S734A and S734D show comparable expression to GFP::HUM-1 in the intestinal-rectal valve and phasmid sensilla however, S734A shows reduced expression in the PHC neuron. Scale bar is 10 µm.

4.4 Functional analysis of HUM-1 phosphoserine-mutants

4.4.1 HUM-1 phosphoserine mutants fail to rescue brood size

Previously it was determined that disruption of *hum-1* caused a significant reduction in brood size when compared to the N2 control. Further investigation revealed the reduction in brood size was likely *hum-1* dependent as the introduction of a *gfp::hum-1* transgene was able to partially rescue the brood phenotype, increasing the average brood size in the disrupted *hum-1* strain to a level that was no longer statistically significant when compared to the N2 control (Chapter 3).

This partial rescue indicates that the expressed transgene is functional *in vivo*, therefore a brood size assay was undertaken using strains expressing GFP::HUM-1S734A or GFP::HUM-1S734D, in a disrupted *hum-1* background to further investigate the importance of this phosphoserine on protein function. Significance was set at $t < 0.05$ (two-tailed).

As described previously, disruption of *hum-1* alone caused a significant reduction in brood when compared to the N2 control as was confirmed by t-test. However the expression of the GFP::HUM-1 transgene partially rescued this phenotype giving a t value of 0.05. In contrast to the results obtained for the GFP::HUM-1 transgene, expression of either of the phosphoserine mutant constructs failed to rescue the brood phenotype (Figure 4.10). This was confirmed by t-test (values of 0.004 for the A mutant and 0.002 for the D mutant).

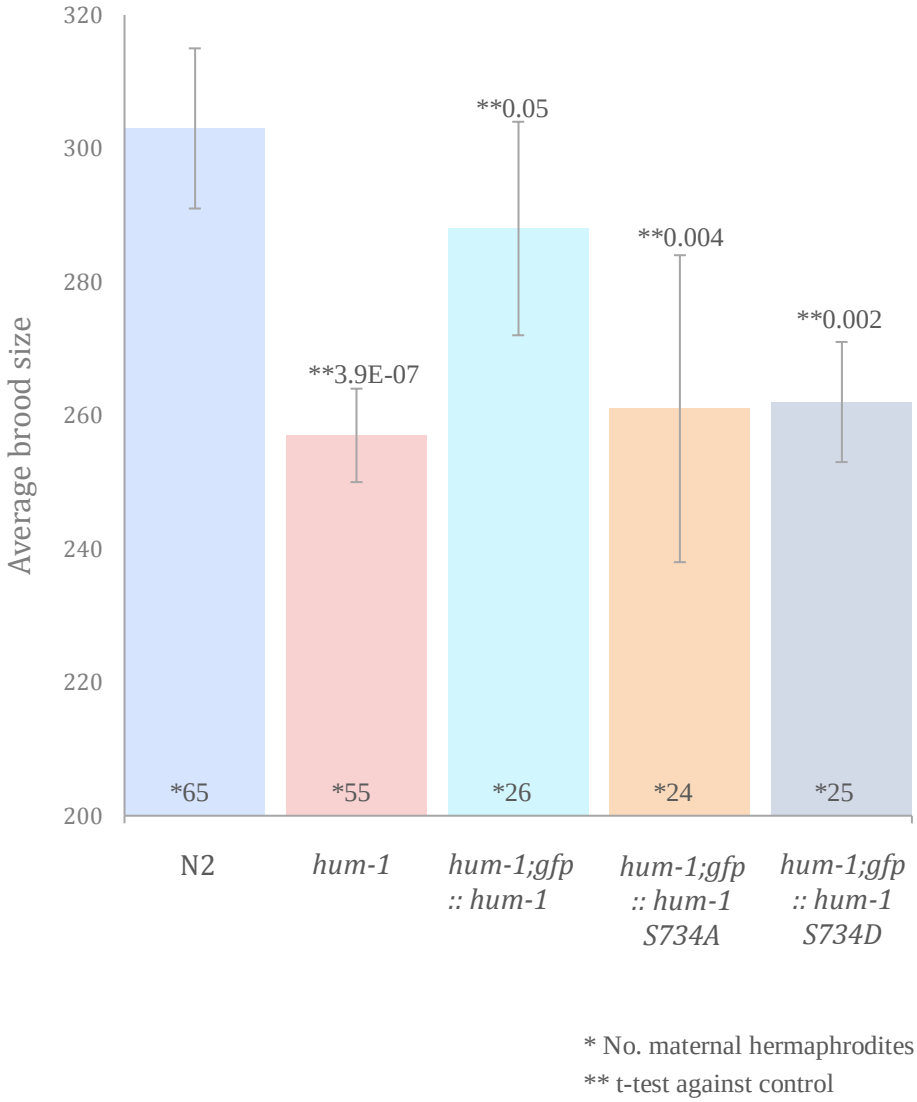

Figure 4.10 Overall average brood for nematodes expressing HUM-1 transgenes. Disruption of *hum-1* showed a significant reduction in average brood size when compared to N2. Expression of a *gfp::hum-1* transgene was able to partially rescue this phenotype. Expression of either phosphoserine mutant constructs however, had little impact on average brood. t-test confirmed both A and D mutant populations were still statistically significant when compared to the N2 control. * Number of maternal hermaphrodites used. ** t-test value calculated against N2 control.

4.4.2 HUM-1 phosphoserine mutants fail to rescue age specific fecundity

In addition to a reduction in average brood size, disruption of *hum-1* also had an impact on age-specific fecundity, resulting in delayed embryo release (Chapter 3). Results showed that even though expression of the *gfp::hum-1* transgene was able to partially rescue the overall reduction in brood size phenotype, it had little impact on rescuing age-specific fecundity.

To determine the effects of the phosphoserine mutations on age-specific fecundity, the results for average number of progeny laid per day were compared. As described previously, hermaphrodites with disruption of *hum-1* and those expressing the *gfp::hum-1* transgene displayed a delay in embryo release when compared to the N2 control. Similarly, hermaphrodites expressing the *gfp::hum-1S734A* or the gfp::*hum-1S734D* transgenes also displayed a delay in embryo release, with the highest number of progeny laid on day two.

These results also indicate disruption of age specific fecundity appears exacerbated in hermaphrodites expressing *gfp*::*hum-1S734A* which shows a notably higher number of progeny laid on day 3 when compared to the other strains (Figure 4.11) .

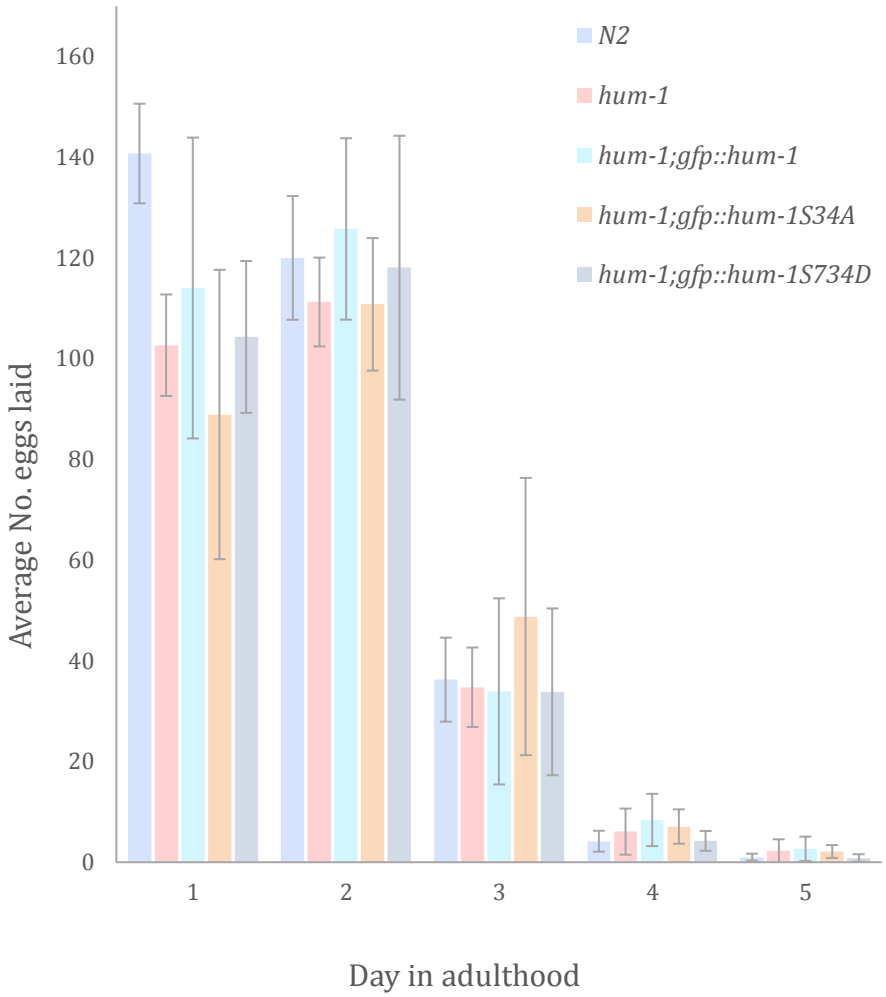

Figure 4.11 Age specific fecundity. Hermaphrodites with disruption of *hum-1* and those expressing the *gfp::hum-1* transgene displayed a delay in embryo release when compared to the N2 control. Similarly, hermaphrodites expressing GFP::HUM-1S734A or GFP::HUM-1S734D also displayed a delay in embryo release, with the highest number of progeny laid on day two. Disruption of age specific fecundity appears exacerbated in hermaphrodites expressing GFP::HUM-1S734A which show a notably higher number of progeny laid on day 3.

4.5 Generation of *S. pombe* strains

To next to explore the effects phosphorylation of the conserved serine residue has on myosin I structure and function in *S. pombe,* a lab stock strain in which the endogenous *myo1*$^+$ had been marked with leucine, was transformed with *myo1S782A*$^+$ or *myo1S782D*$^+$ constructs. This allowed for targeted integration of the episomal DNA to the homologous chromosomal *myo1*$^+$ locus. Colonies which had replaced the endogenous *leu2*$^+$ with the *ura4*$^+$ identification marker carried by the construct DNA were selected. Genomic PCR was then used to confirm isolated colonies had integrated the gene at the correct locus (methods). In addition to the *ura4*$^+$ amino acid selection marker, introduction of the S782 mutations introduced an additional Hindi III restriction site, therefore both undigested and digested PCR products were analysed using gel electrophoresis (Figure 4.12).

The expected size of the undigested PCR product for both wild type (WT) and S782 mutants was ~ 3.6 kb. A single band corresponding to ~ 3.6 kb can be seen for the WT genomic prep however, S782A and S782D mutants showed an additional band approximately ~ 3.0 kb. When digested, the additional Hindi III restriction site in the S782A and S782D DNA, cleaves the 1.7 kb fragment, producing two bands of 1.35 and 0.35 kb. When the potential S782A and S782D mutant clones were digested with Hindi III, additional bands were present that corresponded to 1.35 and 0.35 kb, with the 1.7 kb band remaining (Figure 4.12). This indicated the presence of both *myo1*$^+$ and *myo1S782*$^+$ mutations within the genome. This pattern of digest was seen for all *myo1S782*$^+$ mutant transformations however only *myo1S782A*$^+$ was taken forward for further investigation.

To check these results were not due to a mixed population of WT and S782A mutant cells, single cells were isolated using a tetrad machine and the genomic DNA from subsequent colonies was screened using PCR.

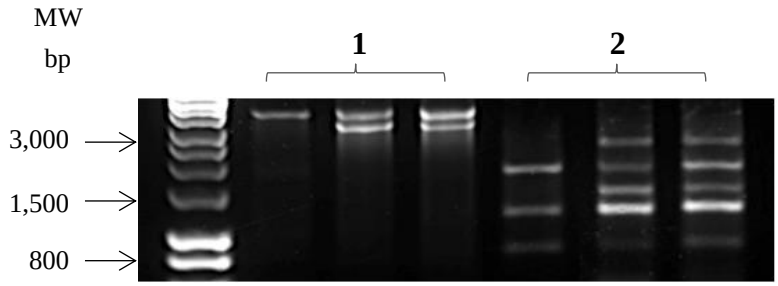

Figure 4.12 Genomic PCR check of S782 potential clones. 1) Undigested PCR product for WT, S782A and S782D clones. WT gave a single ~ 3.6 kb fragment, however both *S782*$^{+}$ clones produced an additional ~ 2.5 kb fragment. 2) If DNA has integrated correctly, the 1.7 kb fragment is cleaved to produce a 1.35 and 0.35 kb fragment. Both *S782*$^{+}$ clones showed the addition of a 1.3 kb fragment however still contained a 1.7 kb fragment indicating the presence of both *myo1*$^{+}$ and *myo1S782A*$^{+}$ or *myo1S782D*$^{+}$ within the genome.

This confirmed each clone was from a single cell however, the genomic DNA contained wild type *myo1*$^{+}$ and *myo1S782A*$^{+}$. To confirm plasmids containing the S782A mutation were correct, constructs were sent for sequencing and checked using PCR. Sequencing confirmed all of the plasmid DNA sequences were correct. Various oligonucleotide combinations were used to amplify different regions of the *myo1*$^{+}$ gene from both the original plasmids and the genomic DNA (Figure 4.13 A). All oligonucleotide combinations used to amplify the plasmid DNA gave single bands at the correct size when run alongside the parental vectors (Figure 4.13 B), further confirming the plasmid DNAs containing the S782A mutations were correct.

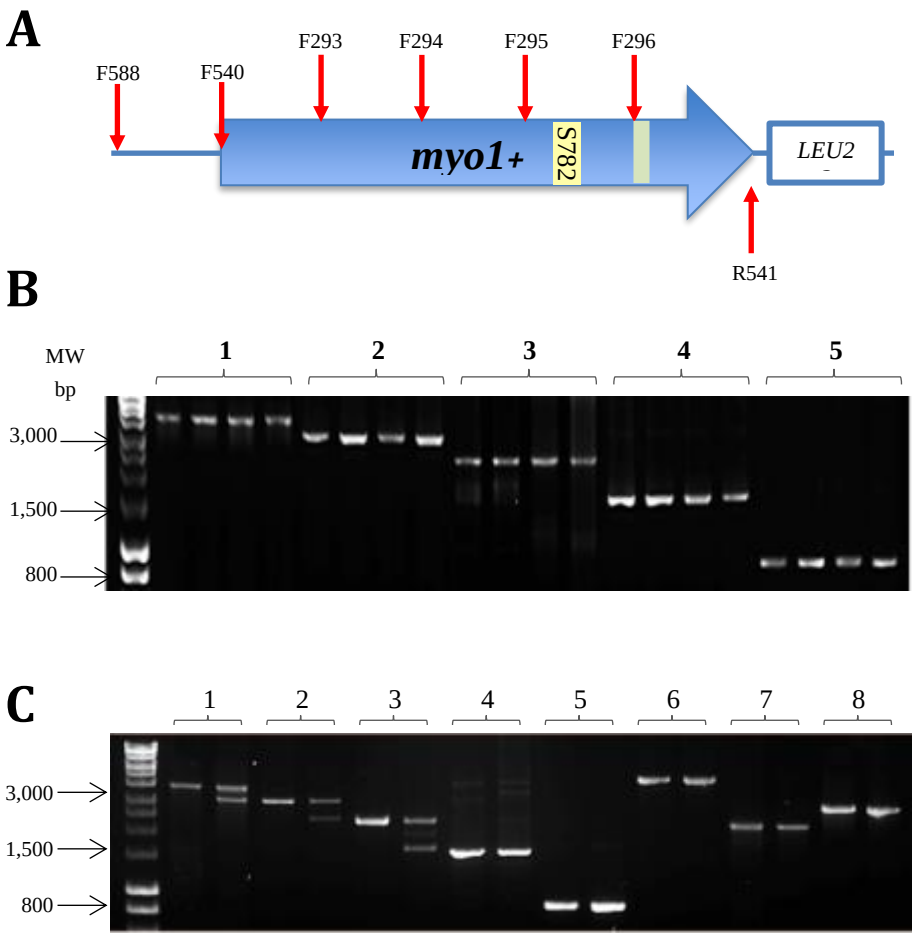

Figure 4.13 PCR check of plasmid and genomic DNA. A) Schematic of oligonucleotide locations along the *myo1+* gene. S782 highlighted in yellow. Anti-Myo1 antigen region highlighted in grey. B) PCR check on (in order) WT, mNgWT, S782A, mNgS782A plasmid DNA using combinations: 1. 540 + 541 expectant size ~ 3.6 kb. 2. 293 + 541 size ~ 2.9 kb. 3. 294 + 541 size ~ 2.2. 4 kb. 295 + 541 size ~ 1.5 kb. 5. 296 + 541 size ~ 0.8 kb. C) PCR check on (in order) WT and S782A genomic DNA using combinations. 1. 540 + 541 2. 293 + 541. 3. 294 + 541. 4. 295 + 541. 5. 296 + 541. 6. 588 + 541 size ~ 4.3 kb. Expected fragment sizes as above.

Genomic PCR however, showed double bands for oligonucleotides that recognised sequence in the motor domain, but only single bands for oligonucleotides that recognised sequence in the region of the S782 mutation (Figure 4.13 C). These results indicate that even though the episomal DNA was targeted to integrate at the chromosomal *myo1*$^+$ locus, replacing the entire Myo1 gene region, it had integrated elsewhere in the genome, therefore PCR amplified both the endogenous *myo1*$^+$ and the *myo1S782A*$^+$. In addition to integrating elsewhere in the genome, these results reveal recombination of *myo1S782A*$^+$ had resulted in the loss of ~ 0.5 kb of sequence in the region of the S782A mutation. Over 60 colonies which had the correct amino acid selection marker were checked using genomic PCR however none of the clones selected showed correct integration of *myo1S782A*$^+$.

To try and circumvent the issue of endogenous Myo1 expression, S782A DNA needed to be transformed into a *myo1::* null strain however, for targeted homologous recombination, the targeted *myo1*$^+$ locus must be largely intact. To overcome this issue, new S782A constructs were generated which contained an upstream flanking region of the *myo1*$^+$gene and an mNeongreen fluorophore tag. The *mNgmyo1-S782A*$^+$ constructs were transformed into a published lab stock strain in which the ORF of the *myo1*$^+$ gene had been disrupted and replaced with a KanMX6 cassette, which confers G418 resistance to cells. In excess of 200 colonies were screened by amino acid selection.

Although all of the colonies isolated contained the *ura4*$^+$ selection marker, none of the colonies had become susceptible to G418, indicating that the targeted integration of the episomal DNA to the *myo1*$^+$ locus had again been unsuccessful. When a Hindi III digest of genomic PCR was performed to check for integration of the S782A mutation (Figure 4.14), some of the potential clones were giving the same digest pattern that had been seen previously, when the genome contained both the endogenous *myo1*$^+$ and *myo1-S782A*$^+$, however this could not be possible if the open reading frame

(ORF) of the *myo1*$^{+}$ gene had been disrupted correctly. To investigate this further, genomic PCR was performed on the original *myo1::* deletion strain and the PCR product was compared to that acquired from a lab stock wild-type strain. Undigested and digested PCR products were analysed using gel electrophoresis (Figure 4.15). Using oligonucleotides 540 and 541, the *myo1::* deletion strain produced undigested PCR product ~ 3.6 kb, the same as expected for wild-type *myo1*$^{+}$. A series of digests were carried out to determine which portion of the *myo1*$^{+}$ gene was still present in the genome as disruption with KanMX6 would result in a change in enzyme restriction sites. All of the PCR digests from the *myo1::kanMX6* strain were identical to wild-type *myo1*$^{+}$*,* therefore the *myo1*$^{+}$ gene had not been disrupted with the *KanMX6* maker and was still present in the genome in its entirety.

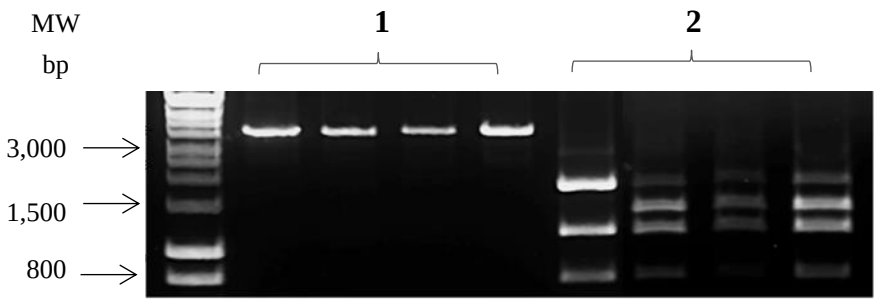

Figure 4.14 PCR check of WT and mNg-S782A genomic DNA. 1) Undigested DNA from (in order) WT and 3 potential mNgS782A clones. The expected fragment size using oligonucleotides 540 and 541 is ~ 3.6 kb. All clones display single bands at this size. 2) Hindi III digest of WT and 3 potential mNg-S782A clones. Although the mNgS782A clones show addition of a 1.3 kb band confirming the presence of the S782A mutation, a 1.7 kb fragment is still apparent indicating the presence of endogenous *myo1*$^{+}$.

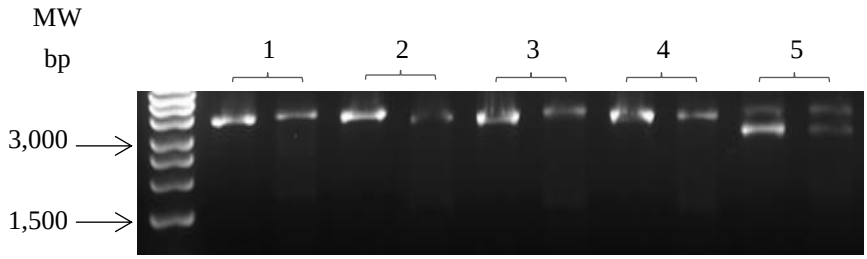

Figure 4.15 Comparison of WT and *myo1::* genomic DNA. 1) Undigested PCR product of WT and *myo1::* DNA produced a fragment at ~ 3.6 kb. Digests of (in order) WT and *myo1::* PCR products using 2) Mlu1. 3) Nco1. 4) Nru1 and 5) Nde1gave the same digest patterns, therefore the *myo1::* strain contained the entire *myo1*+ gene.

Although this confirmed the endogenous *myo1*$^+$ gene was still present, this strain has a distinctive Myo1 null phenotype therefore it is likely that the disruption with the KanMX6 is located within the promoter region and therefore silences the *myo1*$^+$ gene.

A *myo1::* deletion strain was next acquired from the Bioneer© *S. pombe* genome-wide deletion mutant library. In this strain, the *myo1*$^+$ ORF is targeted using a mutagenesis method, replacing the gene with a KanMX4 cassette which confers G418 resistance. Both *mNgmyo1-S782A*$^+$ and *mNgmyo1-S782D*$^+$ constructs were transformed then isolated using the amino acid marker *ura4*$^+$*,* introduced with the serine mutations. Correct clones were then tested for G418 susceptibility and checked using genomic PCR. Using oligos upstream and downstream of the *myo1*$^+$ locus, the *myo1::* strain gave a band at the expected size of 3.5 kb whereas each of the mutant clones gave a band of 5.5 kb, the same as for a WT strain confirming plasmid DNA had integrated into the genome at the correct locus (not shown).

4.6 Mutation of Serine 782 alters Myo1 localisation

To investigate whether Myo1 dynamic movements and distribution were regulated by post-translational phosphorylation of the conserved serine residue, cells expressing mNgMyo1-S782A and mNgMyo1-S782D were imaged using fluorescence microscopy and analysed using Autoquant (methods). Cells expressing the mutant alleles were mixed with cells expressing WT mNgMyo1 from a plasmid, in addition to Sid4tomato, marking the spindle pole body for ease of identification.

In wild-type cells, Myo1 forms highly dynamic associations with actin patches, where it promotes actin polymerisation and plays a key role in membrane remodelling and endocytosis (Attanapola et al. 2009; East & Mulvihill 2011). Cells expressing WT mNgMyo1 show discrete localisation to actin patches enriched at the tips of growing cells and at sites of cell division (Figure 4.16). Cells expressing mNgMyo1-S782A or mNgMyo1-S782D however, show no discrete localisation of Myo1 with expression appearing predominantly cytoplasmic (Figure 4.16 & 17).

Previously it has been determined that deletion of *myo1*$^{+}$ is not lethal, however cells have actin cytoskeletal defects, including loss of polarized cell growth, delocalized actin patches, and mating defects (Lee et al. 2000). Expression of both Myo1-S782A and Myo1-S782D appears to partially rescue the polarized cell growth defect phenotype however, expression of each mutant appears to induce entry into meiosis in a proportion of the population even though the parental *myo1::* strain was haploid. Upon further investigation, the spores formed in both strains were non-viable, although hochst staining (not shown) revealed all four spores contained DNA content.

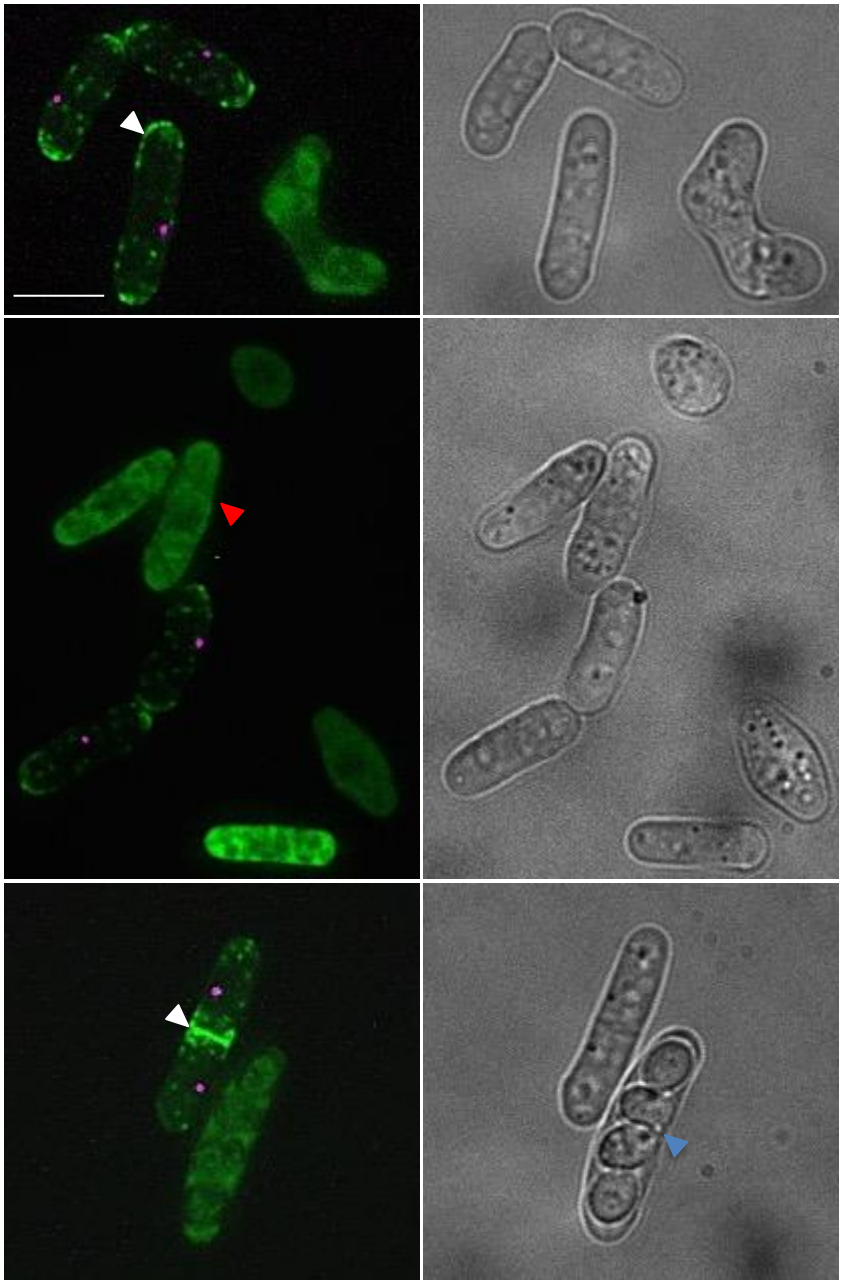

Figure 4.16 Localisation of mNgMyo1S782A. Cells expressing WT Myo1 Sid4Tom (white arrowheads) show localisation to actin patches and the division site, however discrete localisation is abolished in cells expressing Myo1-S782A (red). Myo1-S782A also appears to induce meiosis even though cells are haploid (blue). Scale bar is 5 µm.

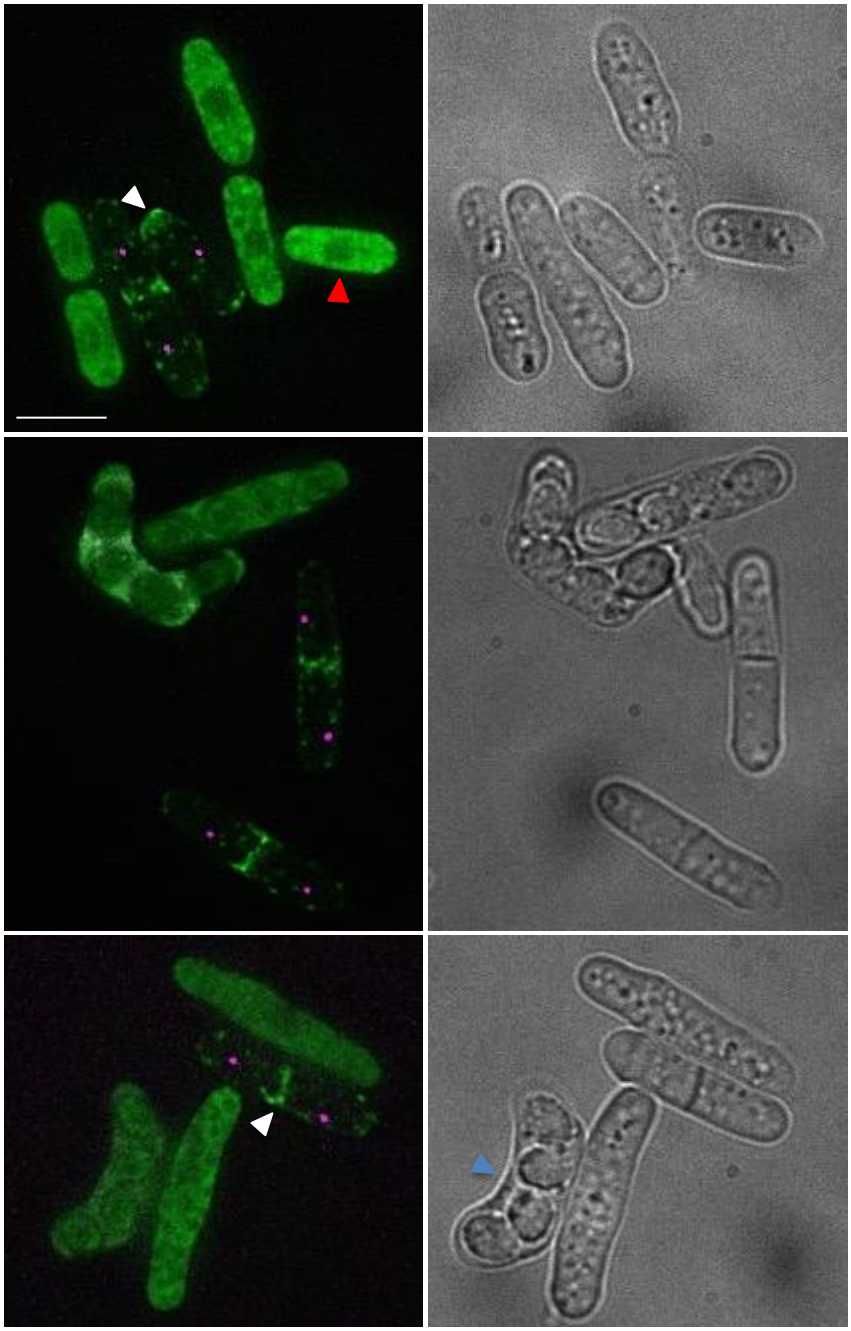

Figure 4.17 Localisation of mNgMyo1S782D. Cells expressing WT mNgMyo1 Sid4Tom (white arrowheads) show localisation to actin patches and the division site, however discrete localisation is abolished in cells expressing Myo1-S782D (red). Myo1-S782D also appears to induce meiosis even though cells are haploid (blue). Scale bar is 5 µm.

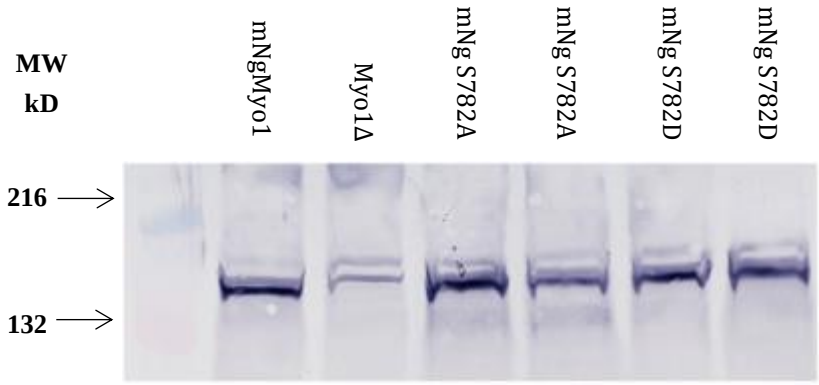

Figure 4.18 Western blot analysis of Myo1 expression levels. Cells expressing mNgMyo1, mNgS782A and mNgS782D show equivalent protein expression levels whereas no protein expression can be seen in the parental *myo1::* strain. This gives confidence that any changes in localisation are a result of the phosphoserine mutation and not changes in protein expression. Bands in *myo1::* strain are unspecific as MW of untagged Myo1 is 135 kDa.

To ensure any changes in protein localisation were a result of the serine mutations and not due to changes in expression levels, western blot analysis was performed using cell extracts (methods). The resulting blot revealed protein expression levels were equivalent in the different mutant strains and were comparable to cells expressing WT Myo1 from a plasmid (Figure 4.18), therefore giving confidence that the changes in localisation are due to the presence of the S782A and S782D mutations.

4.7 Discussion

An important feature of myosin I isoforms is their ability to bind membranes via direct interactions of the TH1 domain with anionic phospholipids however, how these interactions in Myo1e are regulated is still poorly understood. To explore how Myo1e function could be regulated by phosphorylation, mutations were introduced into a conserved phosphoserine residue found within the TH1 domain of the Myo1e homologs; *S. pombe* Myo1 and *C. elegans* HUM-1. The first substitution changed the serine to an alanine, preventing phosphorylation of the residue whereas the second introduced an aspartic acid, a phosphorylation mimic. Each mutant form of Myo1 and HUM-1 were then fused with the reporter proteins mNeongreen or GFP respectively and expressed in homologous knockouts, containing a specific deletion of the endogenous gene to provide a clean background for protein localisation and functional studies.

Modelling of the Myo1e, Myo1 and HUM-1 TH1 domain revealed a high degree of structural conservation, with the conserved phosphoserine residue predicted to be located on a highly organized alpha helix in each of the isoforms. Amphipathic alpha helices have been shown to play a key role in mediating the interaction of peptides and proteins with membranes (Sharadadevi et al. 2005), therefore location of this conserved phosphoserine residue indicates it could play a significant role in regulating the membrane binding properties of these myosin I isoforms. The importance of phosphorylation sites within a-helical loops is reflected in the conserved TEDs site found in class I myosins from lower eukaryotes such as *Saccharomyces cerevisiae* Myo3p, where it has been shown to play a key role in regulating protein dynamics and cellular functions (Grosshans et al. 2006).

These models of the region surrounding the phosphoserine residue in each on the myosin I isoforms, also reveal varying levels of predicted surface exposure. Whilst it is clear that amino acid sequence plays a key role in

phosphorylation site recognition, surface exposure is also thought to regulate accessibility of the corresponding kinases. The depicted environment around the conserved serine residue predicts Myo1e S736 to have the highest level of surface coverage which is reduced in HUM-1 S734, with *S. pombe* Myo1 S782 predicted to have the lowest exposure. As *S. pombe* is a simple eukaryote encoding fewer proteins, decreasing the level of surface exposure could be another mechanism used to regulate phosphorylation and thus protein functionality. A computational study of kinase specificity has reported that approximately 60% of the sites modified by protein kinase A lie within an α-helical region (Sharadadevi et al. 2005; Plewczyński et al. 2005). Although the kinases involved in phosphorylation of these residues are yet to be confirmed, it is possible that in addition to providing insight into the regulation and binding of Myo1e, the level of structural organisation of each of these isoforms could also provide insight into identifying the corresponding kinases.

Although the structural models indicate the conserved serine residues could have a significant role in the membrane binding properties of each isoform, it was important to investigate the effects of each mutation *in vivo*. Analysis of GFP::HUM-1, GFP::HUM-1S734A and GFP::HUM-1S734D transgene expression showed overall protein expression levels were comparable, therefore giving confidence any changes in protein localisation were a result of the phosphoserine mutation. Studies conducted in chapter 3 revealed HUM-1 is highly expressed in a diverse array of tissues including chemo/odour sensory sensilla, the pharyngeal-intestinal and intestinal-rectal valves and within the reproductive system. Although each of the phosphoserine mutants were expressed in the same tissues, protein localisation studies using high-resolution fluorescent confocal microscopy revealed mutation of the conserved serine residue alters HUM-1 localisation.

GFP::HUM-1S734A within the chemo/odour sensory sensilla shows more cytoplasmic localisation within neurons with less discrete recruitment within

dendrites, neuron commissures and cilia. This suggests phosphorylation of serine 734 is required for membrane binding of HUM-1. This is further supported with localisation across the uterine toroidal epithelial cells appearing more cytoplasmic when compared to GFP::HUM-1. Reduced GFP signal was observed in the spermatheca and spermathecal-uterine valve, with no localisation of GFP::HUM-1S734A seen in the PHC neuron, although within the phasmid sensilla and intestinal-rectal valve expression could be seen at comparable levels to GFP::HUM-1. Conversely, within the pharyngeal – intestinal valve, GFP::HUM-1S734A showed more discrete localisation to the inner membrane of the vpi cells, therefore indicating the consequence of serine 734 phosphorylation on protein recruitment and localisation is tissue specific.

Localisation of GFP::HUM-1S734D within the chemo/odour sensory sensilla appears non-uniform and punctate, showing less cytoplasmic expression within the neuronal dendrites, with signal appearing tighter to membranes. Neuronal commissures were not as well defined and expression at the cilia endings around the lips appears more concentrated to the membrane. In contrast to the S734A mutation, these results indicate phosphorylation is required for HUM-1 membrane binding or for stabilising protein interactions once recruited to the membrane. The role of S734 phosphorylation in modulating membrane interactions is further confirmed within the reproductive system where GFP::HUM-1S734D showed increased localisation to the membrane of cell ut1.

Comparable expression to GFP::HUM-1 was seen in the spermatheca and spermathecal-uterine (SU) valve and uterine toroidal epithelial cells. Similarly, at the posterior of the nematode GFP::HUM-1S734D could be seen at comparable levels to GFP::HUM-1 in the phasmid and PHC sensilla. Within the pharyngeal – intestinal valve, GFP::HUM-1S734D appeared to show more discrete localisation to the inner membrane of the vpi cells. These results further indicate that although HUM-1 is widely expressed,

tissue-specific phosphorylation fine tunes protein activity to fulfil the specific needs of each tissue.

Results obtained in chapter 3, revealed disruption of HUM-1 resulted in a reduction in maximal brood size, however this phenotype was rescued by the introduction of a HUM-1 transgene. In addition to a reduction in brood, further investigation revealed a delay in embryo release with the highest number of progeny released on day two of adulthood and not day one. Functional assays revealed both of the HUM-1 phosphoserine mutant constructs were unable to rescue the reduced brood phenotype indicating both the phosphorylated and un-phosphorylated forms of the protein are required for maximal brood size. Further analysis also showed each construct was unable to rescue age specific fertility, with the highest number of embryos laid also on day 2 of adulthood.

In line with the results obtained with HUM-1, mutation of the equivalent conserved serine (Ser 782) in *S. pombe* Myo1, significantly alters protein localisation in addition to inducing entry into meiosis. Western blot analysis of the parental deletion strain showed no detectable Myo1 protein and those expressing wild-type Myo1, Myo1S782A and Myo1S782D showed overall protein expression levels were comparable, therefore giving confidence any changes in protein localisation were a result of the phosphoserine mutation and not due to changes in expression. Previous research has shown wild type Myo1 shows discrete localisation to actin patches enriched at the tips of growing cells and at sites of cell division (Lee et al. 2000, Attanapola et al. 2009). Cells expressing mNgMyo1 also showed this pattern of localisation, however localisation appeared almost completely cytoplasmic in cells expressing Myo1S782A and Myo1S782D, with no discrete localisation to the membrane seen in either strain.

In addition to altering the subcellular localisation of Myo1, the serine 782 mutation also appeared to induce entry into meiosis in both mutant strains even though the parental *myo1::* was a heterothallic h^+ strain. Although it is possible for heterothallic h^+ cells to revert to homothallic h^{90}, it occurs at a

very low frequency (≤10^{-3}/generation) and is therefore unlikely to have occurred in all isolates of each generated mutant strain (Forsburg & Rhind 2006). Upon further investigation, the spores formed in each of the strains were non-viable, with some missing DNA content. The results therefore indicate cells did not switch mating type but the expression of mutant Myo1S782A and Myo1S782D proteins induced spore formation in the haploid strain, with subsequent spores containing insufficient DNA, leading to loss of viability.

Previously it has been shown *myo1::* cells mate with less efficiency and are defective in sporulation due to incomplete formation of the spore wall during sexual differentiation (Toya et al. 2001). Although the mechanisms behind this remain to be elucidated, introduction of the Myo1 tail domain alone significantly rescues loss of spore phenotype, with the head domain having only moderate effects (Toya et al. 2001). One possible explanation is the Myo1 tail domain is involved in modulating actin dynamics, inducing filament polymerisation to generate the pushing force required for forespore membrane formation or by mediating the closure of the forespore membrane in a manner similar to contraction of the CAR during cytokinesis (Itadani et al. 2006). Although these results indicate the tail domain of Myo1 plays a critical role in the formation of spores, this study suggests it is likely the TH1 domain regulates Myo1 activity, with both the phosphorylated and un-phosphorylated versions of serine 782 required for protein function and localisation, however further biochemical analysis is required to determine the changes in Myo1 affinity and specificity.

4.8 Conclusion

Although gene expression, protein abundance and subcellular localisation profiling uncover physiological differences among tissues, they do not address tissue-specific effects on post-translational regulation. To date, several motifs within the TH1 domain have been implicated in the membrane binding properties of Myo1e, however the results from this study suggest phosphorylation of serine 734 could play an important role in regulating protein function.

Substitutions that both prevented phosphorylation or acted as a phospho-mimic abolished discrete localisation of Myo1 in *S. pombe* suggesting the conserved serine is essential for the affinity and specificity of the protein. Similarly, mutation of the conserved serine in *C. elega*ns HUM-1 indicates specific tissues fine tune the activity of proteins by post-translational modification, creating a specialization of protein expression suited for each tissue's needs.

As mammalian tissues exhibit diverse physiology despite sharing identical genomes, these results could provide insight into the biochemical idiosyncrasies of proteins that have led to the occurrence of tissue-specific diseases such as focal segmental glomerulosclerosis, potentially providing further insight into human pathologies.

Chapter 5: Stability and function of *Schizosaccharomyces pombe* tropomyosin

5.1 Introduction

The tropomyosins (Tpm) are highly abundant actin associating proteins, conserved throughout the fungal and animal kingdoms, that are essential for the normal functioning of the actin filament system in both muscle and non-muscle cells (Frye, Klenchin & Rayment 2010b). In muscle cells the key function of Tpm is to regulate muscle contraction. Whereas in non-muscle cells Tpm plays a central role in stabilising and controlling the biophysical properties of specific actin filaments, as well as modulating its ability to interact with other proteins (Gunning, Hardeman, et al. 2015).

An evolutionarily conserved α-helical coiled-coil, Tpm associates in parallel and register along the major groove of F-actin filaments, with the amino- and carboxyl- terminus of each dimer essential for the end-to-end binding of the polymer (Hitchcock-DeGregori 2008; X. E. Li et al. 2014). With significant variation between different Tpm isoforms, the overlap region is involved in defining the structural and charge landscape of the protein, as well as determining the nature of such end-to-end interactions (Jampani et al. 2012). Post-translational modifications to the protein such as the addition of an acetyl group to the amino - terminus have been shown to modulate the ability of this protein to form end-to-end contacts (Hitchcock-DeGregori & Heald 1987), and therefore has a dramatic impact upon protein interactions and function (Frye, Klenchin & Rayment 2010b).

Due to the simple mechanistic and regulatory systems that underpin various cellular processes, *S. pombe* provides an attractive model system to facilitate diverse functional analysis of the dynamic actin cytoskeleton in a live cell context. Containing a single essential Tpm gene *cdc8*$^{+}$*,* which can be rapidly modified to introduce mutations. *S. pombe* offers a unique system to reveal key amino acids required for the proper functioning of tropomyosin

as well as define its contributions to a diverse array of cellular processes, which are often more complex in metazoans. Previous research has shown conditional lethal temperature sensitive mutants are a powerful tool for studying indispensable gene functions as well as protein functionality, however the basis of such phenotypes are often poorly understood. In this study, we aimed to investigate the molecular basis of temperature sensitivity in two fission yeast tropomyosin mutants discovered over 40 years ago (*cdc8-27* and *cdc8-110*) (Nurse et al, 1976).

In addition to modifications to the amino acid sequence, emergence of fluorescent protein fusions has also become an attractive method for following the dynamics of a plethora of proteins within a live cell. Although diverse fluorescent labelled markers exist, many have been shown to alter the behaviour and organisation of the polymers within cells with the impact of fluorescent fusions on normal protein folding and thus protein function not well characterised. It is widely known both the microtubule and actin cytoskeletons are acutely sensitive to fluorescent labelling of protein components (Snaith et al. 2010), therefore Tpm offers an attractive candidate for markers of specific actin structures, enabling filament dynamics in diverse cell types to be followed in a live cell context. To date it is unclear how fusing a fluorescent protein to the termini of the Tpm protein impacts its normal function, therefore I have undertaken a detailed *in vitro* and *in vivo* study to establish the consequence of amino and carboxyl terminal monomeric fluorescent protein fusions on Cdc8 function.

5.2 Creation and expression of fluorescently labelled Cdc8

To explore the impact of fluorescent protein fusions on normal Tpm function, Cerulean3 was fused to both the amino and carboxyl terminus of the Tpm protein. This enabled the effects of each terminal fusion to be defined. DNA encoding for Cdc8-Cerulean3-His_6 (*cdc8-cer3*) carboxyl *and* His_6-Cerulean3-cdc8 (*cer3-cdc8*) amino terminal fusions were designed and synthesised. In these fusions the monomeric Cerulean3 (Markwardt et al. 2011) fluorescent protein was linked to the Cdc8 via a poly-glycine linker. DNA fragments were synthesised as Nde1- BamH1 (ThermoFisher) and cloned into both pJC20 bacterial and pREP41 fission yeast expression vectors.

5.3 Creation and expression of WT and mutant Cdc8 proteins

Two fission yeast tropomyosin mutants (*cdc8-27* and *cdc8-110*) first described more than 40 years ago (Nurse et al. 1976) revealed mutations in $cdc8^+$ led to loss of viability when shifted to the restrictive temperature of 36^0C however, the basis of temperature sensitivity was not defined. Further investigation within this lab and others, into the molecular basis of the *cdc8-110* and *cdc8-27* mutants revealed the presence of mutations; A18T/E31K and E129K respectively (East et al. 2008; Kurahashi et al. 2002). To further explore the effects of these amino acid substitutions on Cdc8 stability, single point mutations were introduced into the $cdc8^+$ gene, corresponding to each mutation (Table 5.1).

Alanine 18 was mutated to a threonine changing it from a hydrophobic residue to a polar residue with an uncharged side chain. Ala18 is predicted to fall in the '*d'* position of the heptad repeat, residues that fall into the '*a'* or *'d'* position are frequently occupied by hydrophobic residues and confer stability. Glutamic acid 31 found in the '*c'* position was mutated to a lysine, changing it from a negative to a positive charge. Positions '*b', 'c',* and '*f'* are

usually polar or charged residues on the surface of the molecule facing the surrounding aqueous environment, available for the binding of other proteins. Within the *cdc8-27* allele the mutated glutamic acid 129 is at the '*g'* position of the heptad repeat, residues that fall into the '*e'* or *'g'* position are often charged residues that pack against the hydrophobic core. Mutation of Glu129 to a lysine, changes it from a negative to a positive charge. Bacterial expression plasmids containing the mutated *cdc8*$^{+}$ genes were introduced into *E. coli* strain BL21 + NatB (M. Johnson et al. 2010). The Cdc8 proteins were subsequently expressed and amino-terminally acetylated by the NatB complex (methods). 1ml samples of *E. coli* pre- and post-induction with IPTG were taken and separated by SDS-PAGE to verify induction (not shown).

Amino Acid substitution	**Allele Name**
Ala 18 to Thr	*cdc8-A18T*
Glu 129 to Lys	*cdc8- E129K (27)*
Glu 31 to Lys	*cdc8-E31K*
Ala 18 to Thr Glu 31 to Lys	*cdc8-A18T E31K (110)*

Table 5.1 A summary of Cdc8 amino acid substitutions. The left column details each amino acid residue selected for mutation and substitution. The right column displays the abbreviated name for each mutation. Brackets indicate temperature sensitive mutants.

5.4 Purification of Tropomyosin proteins

Cerulean-tagged Tpm proteins were expressed in *E. coli* and initially purified by nickel affinity chromatography. 10 µl of the fractions; pre-purification, flow through, wash and elution were taken and separated on an SDS-PAGE gel to verify the presence and purity of each protein (Figure 5.1). In contrast, wild type and temperature sensitive Tpm Cdc8 protein extracts were first subjected to 60°C heat treatment and isoelectric precipitation to a pH of 4.5. All Tpm proteins were then further purified via fast protein liquid chromatography (FPLC) using two 5 ml HiTrap Q columns. Each protein had two consecutive runs through the FPLC to eliminate contaminants. Figure 5.1 shows an example trace taken from the second round of purification for acetylated Cdc8-Cer3^{ACE}. The OD_{260} (red trace) and OD_{280} (blue trace) give an indication of the relative abundance of nucleic acids and proteins. The ratio of OD_{260} to OD_{280} can be used as a guide to protein purity, with a ratio of 1.06 and below signifying an excess of 95% protein content (Goldring 2015). After purification, the concentration of each Tpm was determined using a Bradford protein assay.

The purity of each protein was subsequently determined by SDS-PAGE analysis (Figure 5.2) and mass spectrometry (Table 5.2). The Cerulean3 fused proteins migrated to the predicted size of ~47 kDa due to the fluorescent protein whereas mutant and WT Cdc8 migrated to the predicted size of ~19 kDa. No contaminating bands were seen in any of the samples and the equivalent intensities of the purified protein bands gave confidence the concentrations had been accurately determined. An example of mass spectrometry data is given in Figure 5.2 for Cdc8- E36K^{ACE}. A dominant single peak was seen for each Tpm protein and each protein matched the predicated mass based on amino acid sequence within 1 kDa with the exception of the Cerulean labelled Cdc8 proteins. The Cerulean labelled proteins have a mass 18 kDa lower than predicted from the mass sum of individual amino acids, this is due to the hydrolysis of a water molecule during the formation of the chromophore (Table 5.2) (Tsien 1998).

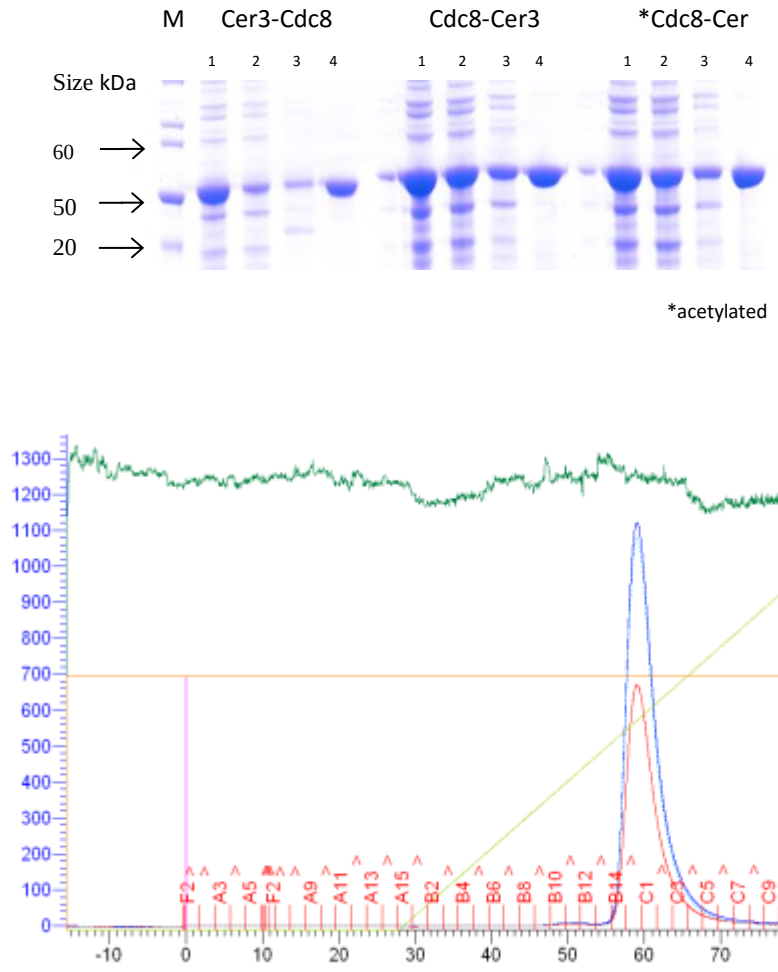

Figure 5.1 Expression and purification of Cerulean3 labelled Cdc8 proteins from *E. coli.* (A) An SDS-PAGE gel showing molecular weight marker (M), nickel column purification samples of *E. coli* expressing, from left to right, Cer3-Cdc8, Cdc8-Cer3, Cdc8-Cer3^{ACE}. (1) Pre-purification, (2) Flow through, (3) Wash, (4) Elution. (B) FPLC trace taken from the second purification run on the HiTrap Q column for acetylated Cer3-Cdc8, eluted using a gradient of 0 to 1 M NaCl. Each sample was sent for mass spectrometry.

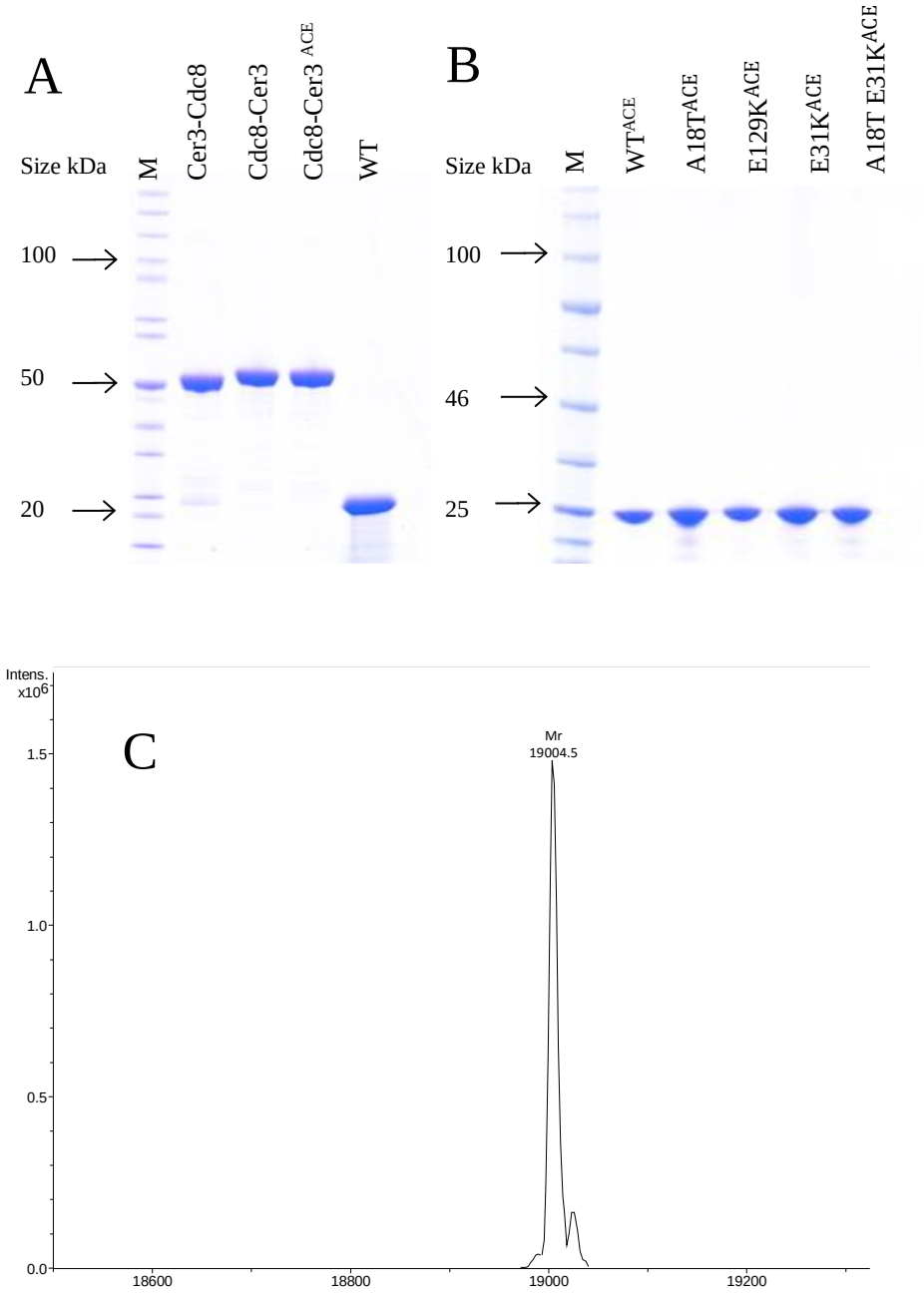

Figure 5.2 Purity of cerulean tagged and mutant Cdc8 proteins (A) A coomassie stained SDS-PAGE gel showing WT and cerulean tagged Cdc8 proteins. (B) A coomassie stained SDS-PAGE gel showing WT and Cdc8 mutants. (C) A mass spectroscopy trace showing a dominant peak for mutant Cdc8-E31K^{ACE}. M corresponds to molecular weight marker.

Tropomyosin	Source	Predicted Mass (Da)	Mass (Da)	Δ Mass (Da)
Cdc8	*E. coli*	18,964	18,963.9	-0.1
Cdc8^{ACE}	*E. coli*	19,006	19,006.4	-0.4
Cer3-Cdc8	*E. coli*	47,020	47,001.6	-18.4
Cdc8-Cer3	*E. coli*	46,889	46,871	-18
Cdc8-Cer3^{ACE}	*E. coli*	46,931	46,913	-18
Cdc8-A18T ^{ACE}	*E. coli*	19,036	19,035.8	-0.2
Cdc8-E129K ^{ACE}	*E. coli*	19,005	19,004.9	-0.1
Cdc8-E31K ^{ACE}	*E. coli*	19,005	19,004.9	-0.1
Cdc8-A18T E31K ^{ACE}	*E. coli*	19,035	19,035	0

Table 5.2 A summary of protein mass spectroscopy data. Electrospray mass spectroscopy was used to confirm the relative molecular mass of each protein. All proteins were within a 1 kDa of that predicted with the exception of the cerulean tagged proteins which displayed a reduction of 18 kDa due to the loss of a water molecule buried adjacent to the chromophore.

5.5 *In vitro* analysis of Cdc8

5.5.1 Point mutations and fluorescent fusions alter the thermo-stability of Cdc8

As the *cdc8-110* and *cdc8-27* mutants result in loss of cell viability when shifted to the restrictive temperature of 36°C, thermal unfolding experiments using circular dichroism (CD) were performed to investigate the effects the various amino acid mutations and fluorescent protein fusions had upon the thermostability of Cdc8. The CD spectra for highly helical structures is characterised by distinctive minima at 208 nm and 222 nm, as shown in the CD spectrum for the amino terminally tagged Cer3-Cdc8 (Figure 5.3).

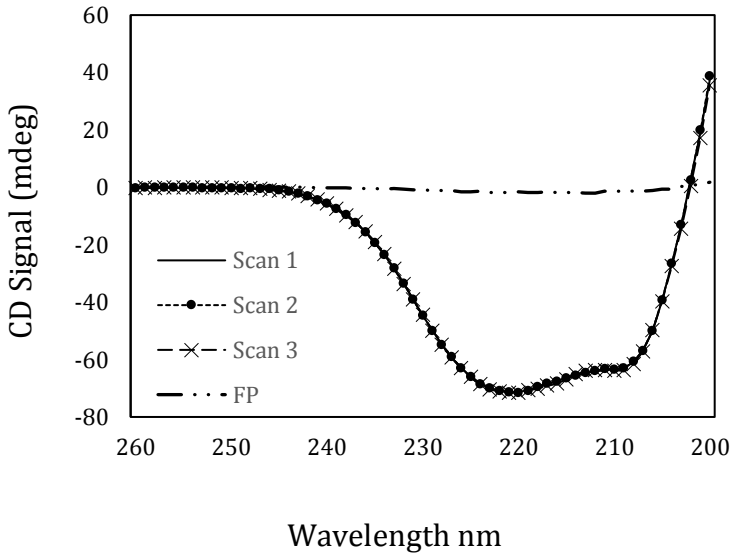

Figure 5.3 Circular Dichroism Spectrum. CD spectra for Cer3-Cdc8 showing distinctive minima at 208 nm and 222 nm. Overlay alignment of each scan indicates Cer3-Cdc8 was able to rapidly refold to its original state. CD signal of the fluorescent protein (FP) showed the presence of the Cerulean3 fusion had no significant impact upon the overall Cdc8 spectra.

This characteristic helical spectrum was evident for all Tpm proteins. Melting curve data for each protein was acquired by monitoring the molar ellipticity at 222 nm continuously in the temperature range from 10°C to 60°C. Once each melting curve was acquired, the protein was cooled and subjected to two further runs. CD spectra were acquired at the start of each run. Each scan showed complete overlay alignment, indicating each Tpm was able to rapidly refold to its original state (Figure 5.3). To determine whether the Cerulean3 fusion impacted the Cdc8 spectra, an equivalent amount of fluorescent protein (FP) (cyan) was analysed using CD under the same conditions. The scan showed the presence of a fluorescent protein fusion will have no significant impact upon the overall CD spectra, as the relative CD signal of an equivalent amount of FP alone is 5% of that observed for the dimeric coiled-coil Tpm proteins (Figure 5.3).

First derivative plots of the melting curve data (Figure 5.4) were used to analyse both the cooperative folding and mid-point melting temperatures (T_m) of each protein. Mid-point of unfolding was calculated from Gausian fits to the first differential of the unfolding profiles (Figure 5.5). Highly cooperative unfolding of a protein is characterised by a sharp single-phase sigmoidal curve, which indicates the protein existed initially as a compact, well-folded structure. A very gradual or bi-phasic melting reaction however, indicates the protein existed as a very flexible, partially unfolded protein or the dimer is non-cooperatively bound. Wild-type Cdc8 and Cdc8^{ACE} display single phase melting curves, showing each dimer is cooperatively bound with the rate of unfolding constant.

The T_m for WT Cdc8 was 33.4°C whereas Cdc8^{ACE} had a higher T_m of 35.4°C due to the additional stability generated by acetylation, equivalent to values established previously (East et al. 2011) The addition of a cerulean tag to the to the amino terminus resulted in an increased melting temperature of 2.1°C when compared to unacetylated WT Cdc8, giving it an equivalent melting temperature to acetylated WT Cdc8.

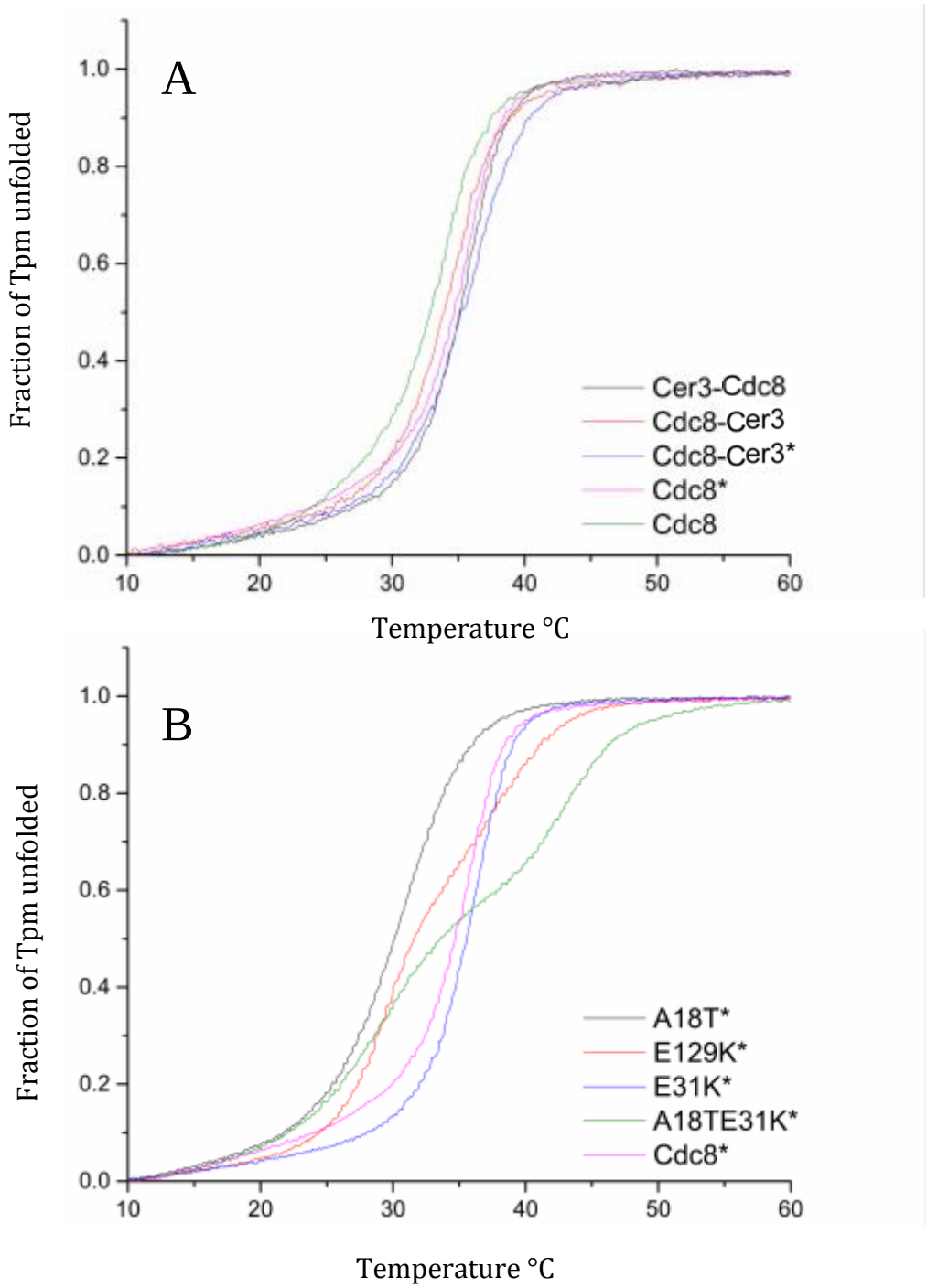

Figure 5.4 Normalised CD absorbance at 222nm as a function of temperature. A) Cerulean-tagged Cdc8 proteins. B) Mutant Cdc8 proteins. * Refers to acetylation.

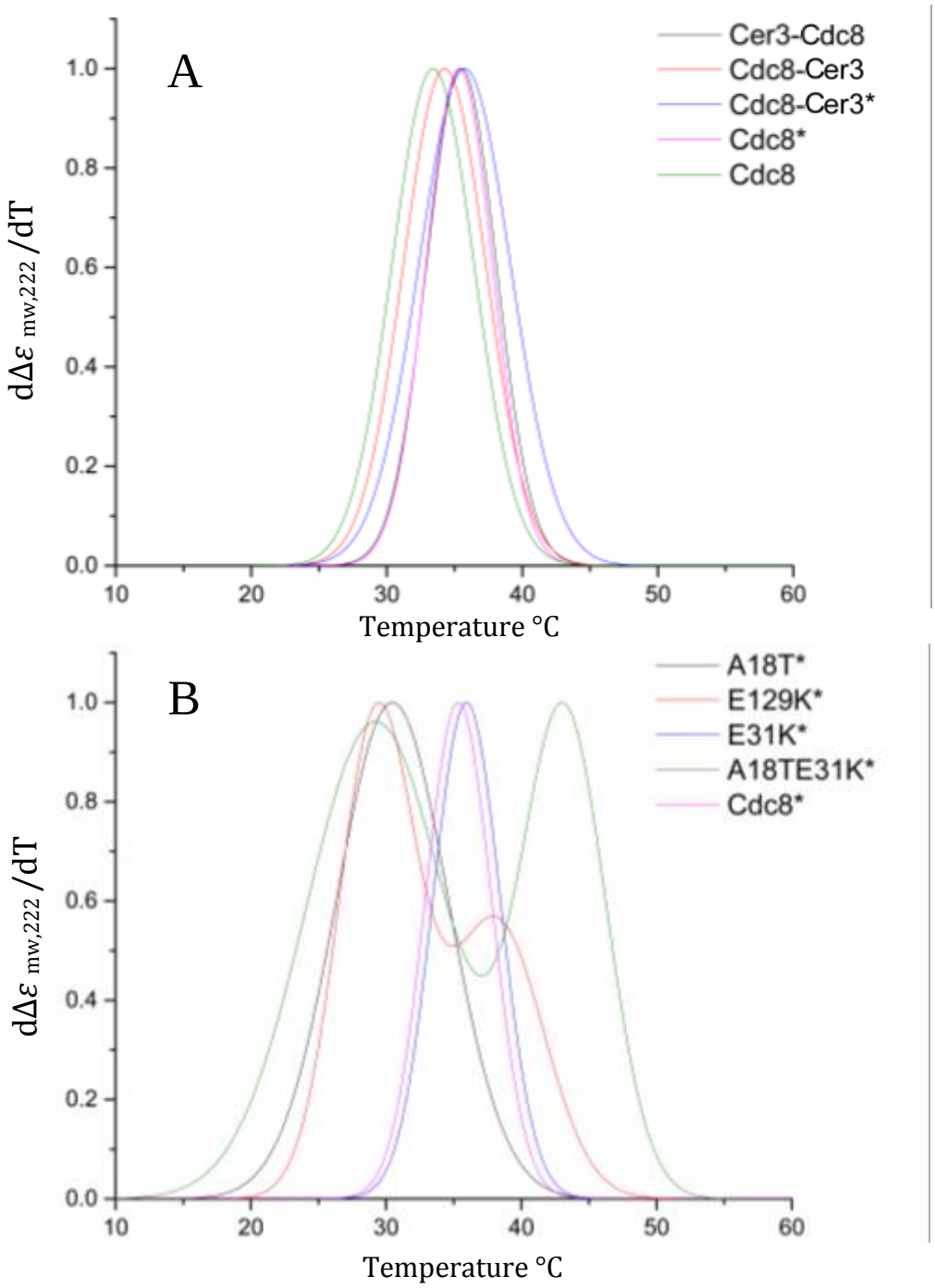

Figure 5.5 First derivative midpoint melting curves. A, Cerulean-tagged Cdc8 proteins. B, Mutant Cdc8 proteins. * Refers to acetylation.

Tropomyosin	T_m(°C)
Cdc8^{ACE}	35.4
Cdc8	33.4
Cer3-cdc8	35.5
Cdc8-cer3	34.3
Cdc8-cer3^{ACE}	35.7
Cdc8-A18T ^{ACE}	30.5
Cdc8-E129K ^{ACE}	29.3, 38.1
Cdc8-E31K ^{ACE}	35.9
Cdc8-A18T E31K ^{ACE}	29.2, 43.2

Table 5.3 Summary of WT, cerulean tagged and Cdc8 mutant midpoint melting temperatures. Midpoint of unfolding were calculated from Gausian fits to the first differential of the unfolding profile.

Similarly, addition of the cerulean tag to the carboxyl terminus of unacetylated Cdc8 increased the temperature by 0.9°C whereas in the acetylated form, the melting temperature was moderately higher than acetylated WT Cdc8 at 35.7°C. All of the melting curves generated for the cerulean tagged Cdc8 protein fusions displayed single phase melting curves indicating the addition of the cerulean tag had no effect on the binding cooperativity of each dimer. Mutants; A18T^{ACE} and E31K^{ACE}

displayed single-phase melting curves however, when compared to WT Cdc8^{ACE}, A18T^{ACE} appears to significantly de-stabilise the protein reducing the melting temperature by 4.9°C, whereas E31K^{ACE} appears to stabilise the α-helix increasing the melting temperature by 0.5°C. Unlike the other mutant Cdc8 proteins, E129K^{ACE} and the combined mutant A18TE31K^{ACE} both show a distinctive two-phase melting profile with ~ 60% of the CD change occurring during the lower temperature transition. For E129K^{ACE} the T_m calculated for the first phase was 29.3°C whereas for the double mutation the lower transition occurs at 29.2ºC. The upper unfolding transition for E129K^{ACE} and A18TE31K^{ACE} indicate the proteins are significantly more stable with T_m's of 38.1ºC and 43.2ºC respectively, significantly higher than the single unfolding transition of WT Cdc8^{ACE}.

5.5.2 Cdc8 fluorescent fusions affect end-to-end interactions

Cdc8 dimers polymerise by end-to-end interactions formed between the amino- and carboxyl- terminus of the Tpm protein (Frye, Klenchin & Rayment 2010a). Due to its size, the addition of a fluorescent protein fusion to each terminal of Cdc8 had potential to impact the ability of the protein to polymerise. To investigate the effect of Cerulean3-Tpm fusions upon the ability of the protein to form filaments, a viscosity assay was undertaken. Viscosity measurements were taken over an increasing salt gradient, as salt disrupts the ionic interactions that facilitate Cdc8 polymerisation and thus can be used to measure the strength of the end-to-end interactions.

Kinematic viscosity was calculated using the manufacturer's predetermined micro-viscometer kinematic viscosity constant (0.03235) and the average efflux time calculated from five observations per sample at each NaCl concentration. A higher viscosity reading corresponds to a greater propensity to form filaments. This assay was carried out at 22^0C using a salt gradient of 0 mM to 200 mM, Tpm proteins concentrations were set at 20 µM. At 0 mM of NaCl WT Cdc8 has a viscosity of 1.08 centistokes (cSt)

whereas acetylated WT Cdc8 has an increased viscosity of 1.22 cSt, showing acetylation of the protein has a dramatic effect on the ability of Cdc8 to polymerise (Figure 5.6). At 200 mM NaCl, the viscosity of Cdc8^{ACE} is still much higher than Cdc8, therefore in addition to increasing the propensity of the protein to form filaments, acetylation also increases the strength of the end-to-end interactions. The viscosity data for the Cerulean3 tagged Cdc8 proteins indicates the end-to-end interactions for all of the proteins have been affected as a result of the fluorophore.

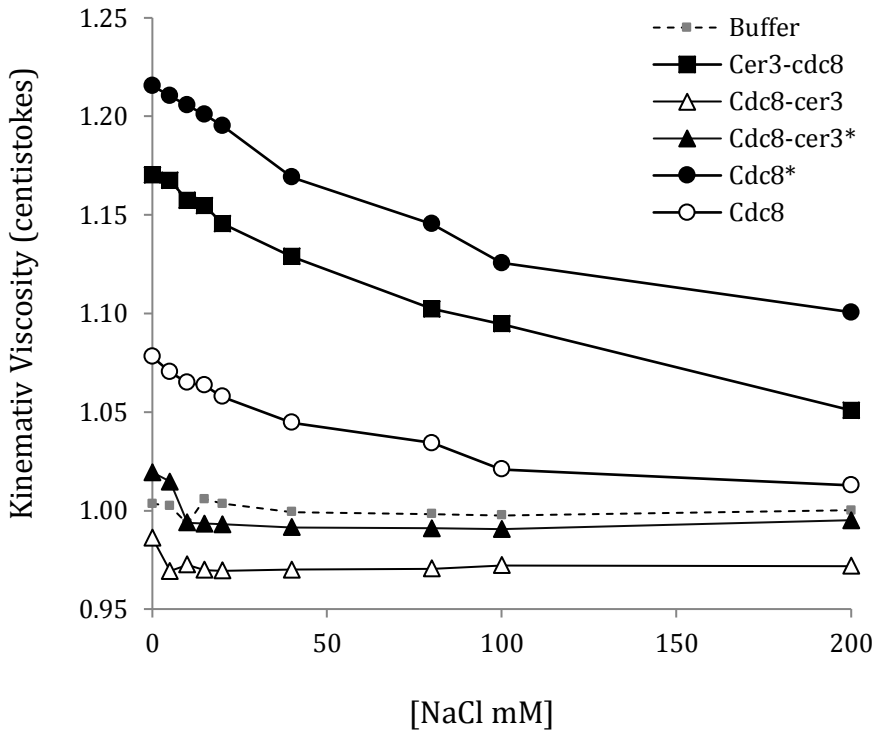

Figure 5.6 Viscosity assay of WT and cerulean tagged Cdc8 proteins. Amino tagging of Cdc8 increases the strength of end-to-end interactions increasing viscosity to levels comparable to acetylated WT Cdc8. Carboxyl tagging of Cdc8 however, abolishes the proteins ability to form end-to-end interactions.

At 0 mM of NaCl the amino terminal tagged Cdc8 was able to form end-to-end interactions and gave a viscosity reading of 1.17 cSt (Figure 5.6). This indicates tagging Cdc8 with cerulean at its amino terminus does not affect the ability of the protein to polymerise but rather partially mimics acetylation, increasing the strength of the end-to-end interactions giving a higher viscosity reading than unacetylated WT Cdc8, although not quite as high as $Cdc8^{ACE}$.

Similarly, at 200 mM NaCl the end-to-end interactions are still stronger than unmodified Cdc8. In contrast, the carboxyl terminal tagging of Cdc8 with a cerulean fluorophore had a significant impact on the proteins ability to polymerise, with Cdc8-Cer3 and $Cdc8\text{-}Cer3^{ACE}$ giving viscosity readings of 0.99 and 1.02 cSt respectively (Figure 5.6). As the viscosity of these proteins remained the same as the buffer throughout the experiment, the data indicates these proteins are unable to form any kind of end-to-end interaction.

Mutant	Viscosity (cSt)
Buffer	1.00
Cdc8	1.08
$Cdc8^{ACE}$	1.22
Cer3-Cdc8	1.17
Cdc8-Cer3	0.99
$Cdc8\text{-}Cer3^{ACE}$	1.02

Table 5.4 A summary of WT and cerulean tagged Cdc8 viscosity. Viscosity values given for 0 mM NaCl at 22 ^{0}C. Kinematic viscosity was calculated using the manufacturer's predetermined microviscometer kinematic viscosity constant (0.03235) and the average efflux time calculated from five observations per sample at each NaCl concentration

5.5.3 Amino and carboxyl cerulean fusions modify the affinity of Cdc8 for actin

Previously it has been shown small alterations to the amino terminus of Tpm not only impairs its ability to form end-to-end interactions but also negatively impacts its affinity for actin (Hitchcock-DeGregori 2008). As the addition of the Cerulean3 fluorophore significantly altered the ability of the protein to

form end-to-end interactions, co-sedimentation experiments were performed to determine whether the addition of the FP had an impact on the ability of Cdc8 to interact with actin (methods). Increasing concentrations of the tagged Cdc8 proteins were incubated at 25 ^{0}C with 10 µM of actin, centrifuged at high speed then the pellets and supernatants were subjected to SDS-PAGE. Gels were stained with coomassie and analyzed by densitrometry. Figure 5.7. shows example SDS-PAGE gels used to determine the binding affinity of the tagged Cdc8 proteins.

Actin can be seen in the bottom band of the SDS-PAGE gels with the density of each well remaining approximately constant, whereas the top band is the tagged Cer3-Cdc8 protein. The density of these wells increases as the concentration of Tpm increases from 0.5 µM left to 12 µM on the right (Figure 5.7A). The Cer3-Cdc8 tagged protein shows actin binding, as the top band in the pellet gel shows saturation of Tpm around 6 µM. Both the carboxyl-terminal tagged Cdc8 proteins however showed weak actin binding. Although much higher concentrations of Cdc8-Cer3 and Cdc8-Cer3^{ACE} were used, only a small proportion of the protein was observed in the pellet fractions whilst a large amount remained in the supernatant.

Repeats of the co-sedimentation assays under the same conditions consistently showed Cdc8-Cer3 and Cdc8-Cer3^{ACE} were unable to reach a binding saturation point. The gels were subsequently analyzed by densitometry and the values were used to calculate the binding coefficients of each Tpm for actin by fitting the data to binding curves using the Hill equation. Unacetylated WT Cdc8 has a binding affinity of around 2.7 µM, whereas acetylated WT Cdc8 has an increased affinity for actin, giving a binding constant of around 0.46 µM (East et al. 2011).

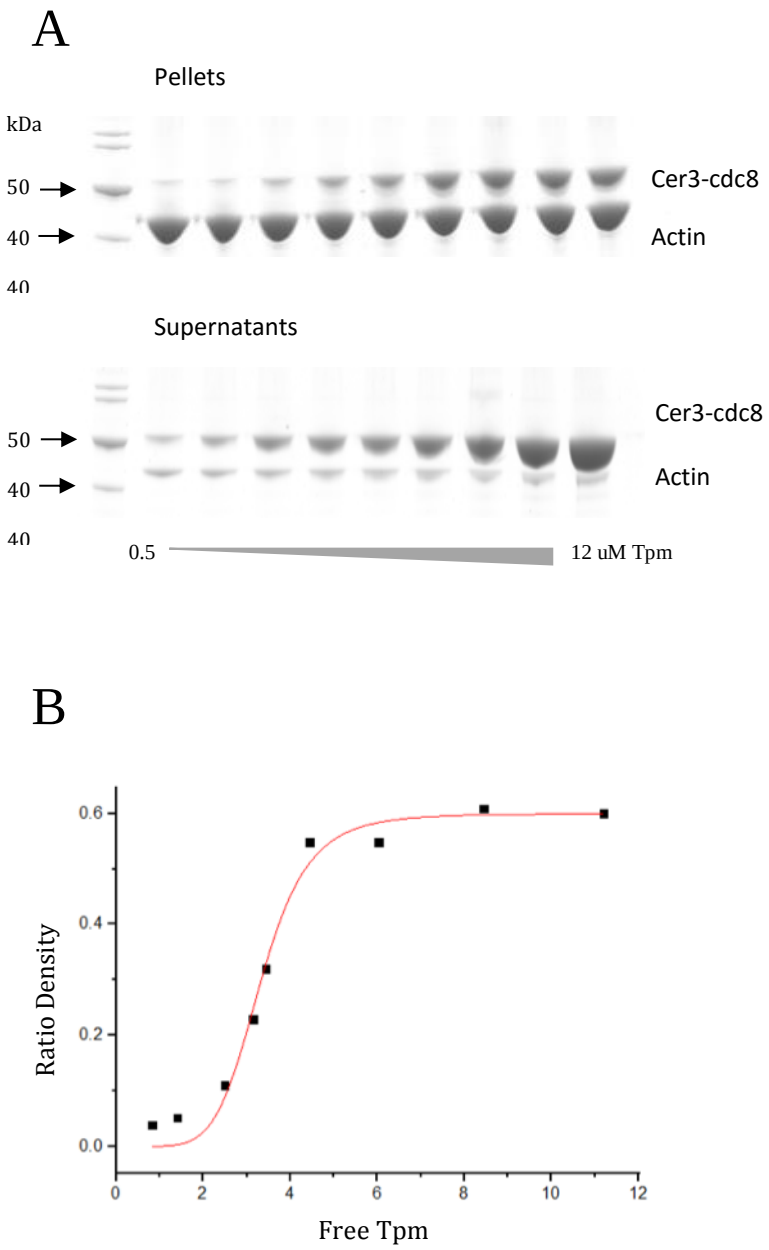

Figure 5.7 Example SDS-PAGE gel and binding curve for cerulean tagged Cdc8 co-sedimentation with actin. A) Example SDS-PAGE gels of the pellet and supernatant from the co-sedimentation experiments of Cer3-cdc8 with actin over increasing Tpm concentrations. B) Binding curve data measured by densitometry of co-sedimentation SDS-PAGE gels. Curves represent Hill equation lines of best fit.

The binding coefficient for Cer3-Cdc8 was calculated to be 0.69 µM, however for the carboxyl tagged Cdc8 proteins the binding was extremely weak to actin and a binding curve could not be generated using this assay. When centrifuged in the absence of actin, the Cdc8-Cer3^{ACE} protein was observed in the pellet. Several attempts to determine a value using varying salt concentrations from 100 mM to 500 mM and lower centrifugation speeds were also unsuccessful. It was therefore not possible to determine the actin affinity for the carboxyl labeled Cdc8 proteins.

5.6 *In vivo* analysis of Cdc8

5.6.1 Cerulean tagged Cdc8 can dimerize with endogenous Cdc8 *in vivo*

Although information on the physical properties of the Cerulean3 tagged Cdc8 proteins had been acquired *in vitro* it was important to relate these results to how the proteins would behave *in vivo*. To explore the ability of each fusion to localize and complement the function of the endogenous Cdc8 protein, amino and carboxyl terminally tagged *cdc8*$^{+}$ cDNAs were cloned into an *S.pombe* expression plasmid under the control of the pREP41 promoter. Previously, it has been established that expression levels of GFP-Cdc8 from the *nmt41* promoter reflect Cdc8 levels from the endogenous locus, therefore Cdc8 fusions were expressed using the same repressible promoter (Skoumpla et al. 2007)

The plasmids were transformed into a wild-type *S. pombe* strain, then grown in minimal EMMG media in the presence of 5 mM thiamine to suppress protein expression, at 25°C for 24 hours until reaching mid-log. Cells were then washed into – thiamine and cultured for a further 24 hours before mounting onto coverslips using 100 mg/ml lectin and imaging.

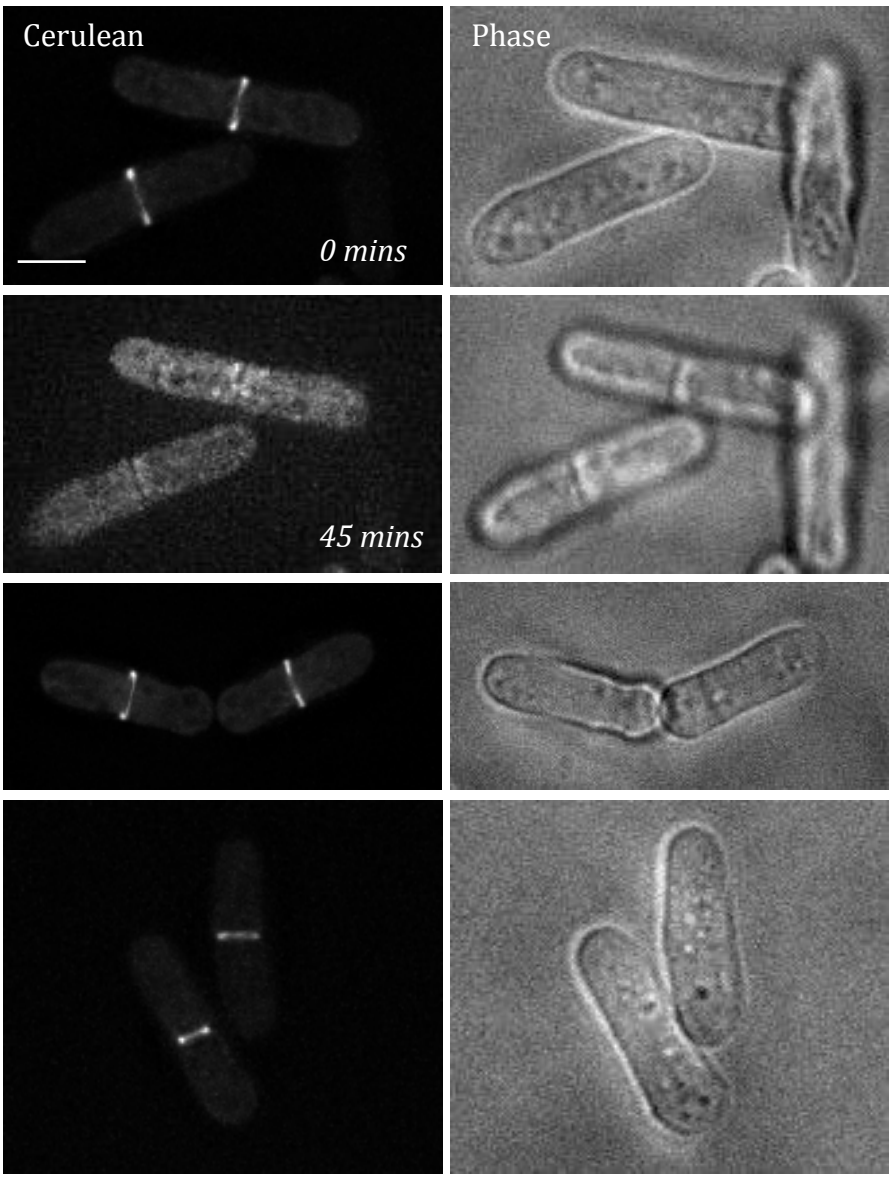

Figure 5.8 Images of wild-type *S. pombe* cells expressing Cer3-Cdc8. Wild-type cells expressing pREP41Cer3-Cdc8 (left) show protein localisation to the CAR with cells undergoing normal cytokinesis within 45 mins. Phase contrast images (right) show cells display a wild-type phenotype. Scale bar is 10 µM.

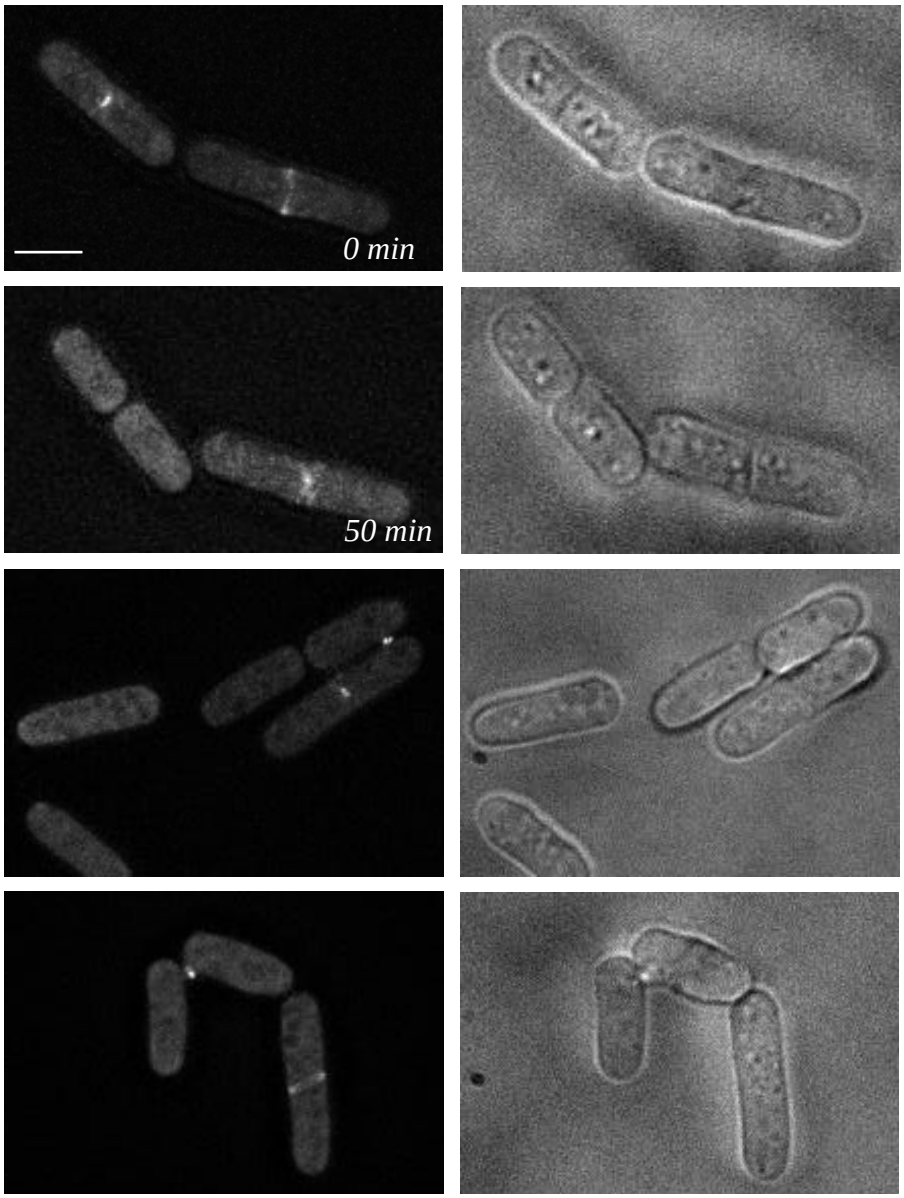

Figure 5.9 Images of *S. pombe* cells expressing Cdc8-Cer3. Wild-type cells expressing pREP41Cdc8-Cer3 (left) show protein localisation to the CAR with cells undergoing cytokinesis within 50 mins, however some cells develop misplaced rings or protein aggregates preventing full separation of cells. Phase contrast images (right) show some cells to have polarized associated growth defects. Scale bar is 10 µM.

Cells expressing Cdc8 tagged at its amino terminus displayed a wild-type morphology and showed the protein was able to associate with the actin polymers within the contractile CAR (Figure 5.8). Average septation of *S. pombe* cells takes between 45 – 55 minutes therefore cells were able to undergo normal cytokinesis, indicating the amino terminally tagged Cdc8 protein is able to dimerize with the endogenous Cdc8. Although cells expressing Cdc8-Cer3 also showed protein localisation to the contractile ring, the presence of Cdc8-Cer3 appears to have a dominant negative effect, as cells expressing the protein displayed misplaced rings (Figure 5.9). Although some cells were able to undergo cytokinesis, aggregates of the protein could be seen at sites of old cell division, suggesting the protein was unable to fully dissociate, thus preventing cells from fully separating.

5.6.2 Cdc8 tagged at the amino terminus complements endogenous Tpm

To further explore the ability of the Cerulean3 tagged Tpm proteins to complement WT Cdc8 function, the *S. pombe* expression plasmids containing the fluorescent fusions were introduced into a temperature sensitive *cdc8-110* strain in which the mutant genomic *cdc8*$^{+}$ allele is fully functional at the permissive temperature of 25 ^{0}C however, is non-functional at the restrictive temperature of 36 ^{0}C. *S. pombe* cells expressing plasmids containing WT *cdc8*$^{+}$ and an empty *pREP41*$^{+}$ vector were used as controls.

To compare the growth of each of these strains, growth curves were generated at both 25 ^{0}C and 36 ^{0}C in the presence and absence of thiamine (Figure 5.10) (methods). Growth rates were calculated by measuring the slope of the curve in the middle of the exponential growth phase and expressed as a change in OD_{600} per hour relative to the control *cdc8-110* strain carrying the empty expression vector *pREP41+.*

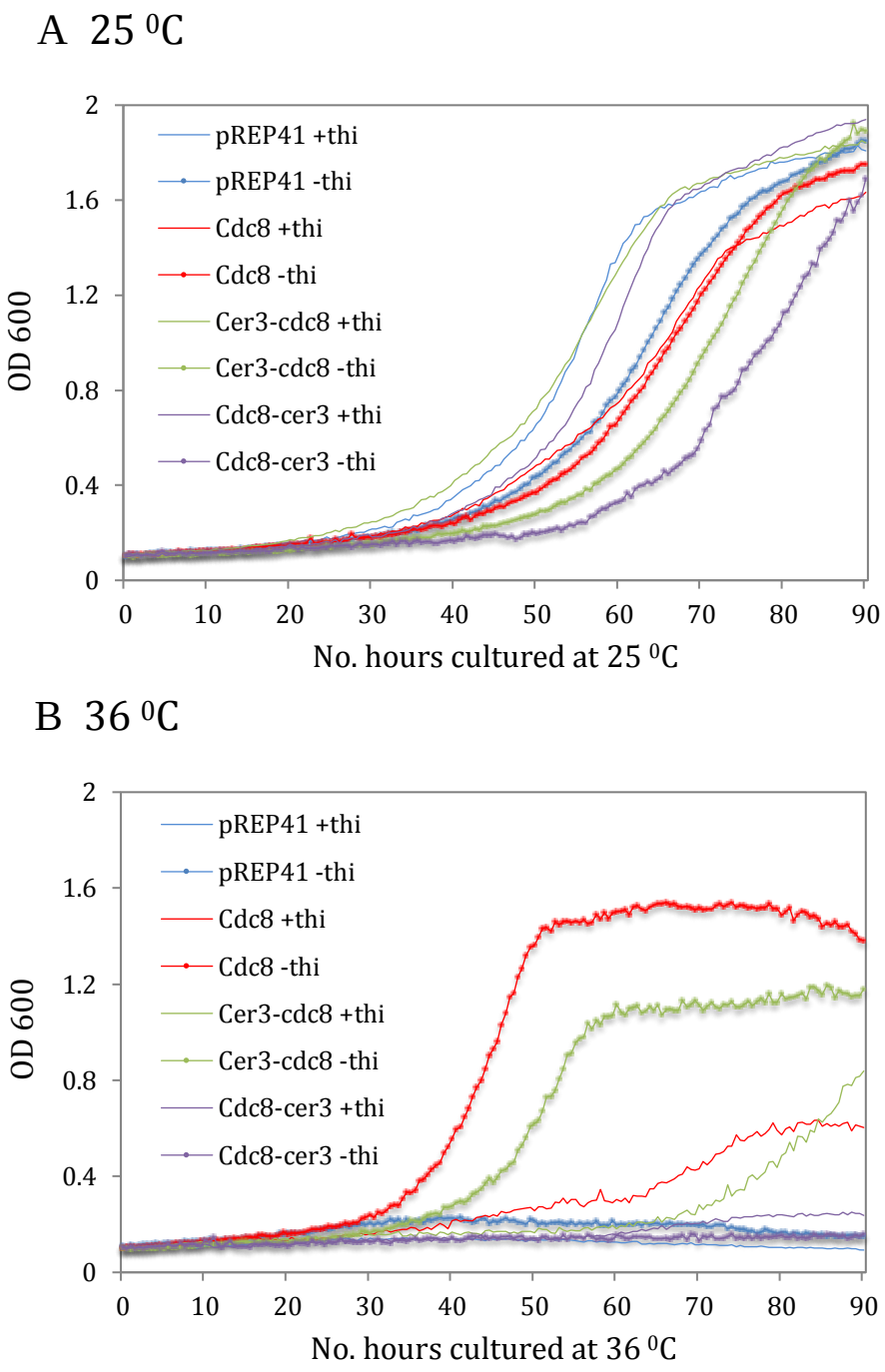

Figure 5.10 Growth curves of *cdc8-110* cells expressing pREP41, WT and cerulean Cdc8 fusions. The OD_{600} for *cdc8-110* cells expressing pREP41, WT Cdc8, Cdc8-Cer3 and Cer3-Cdc8 over 90 hours at in the presence and absence of 5 mM thiamine.

Allele	Growth rate 25°C (ΔOD_{600} $hours^{-1}$)	Relative to pREP +thi	Growth rate 36°C (ΔOD_{600} $hours^{-1}$)	Relative to Initial rate
pREP +	0.047	1.00	0.000	0.00
pREP -	0.042	0.89	0.000	0.00
cdc8^{+} +	0.041	0.87	0.022	0.54
cdc8^{+} -	0.048	1.02	0.055	1.15
cer3-cdc8 +	0.049	1.04	0.033	0.67
cer3-cdc8 -	0.043	0.91	0.047	1.09
cdc8-cer3 +	0.047	1.00	0.000	0.00
cdc8-cer3 -	0.032	0.68	0.000	0.00

Table 5.5 Growth rates of *cdc8-110* cells expressing pREP41, WT and cerulean Cdc8 fusions. Growth rates for each strain calculated from the steepest section of the growth curve at 25 ^{0}C and 36 ^{0}C, expressed in OD600 per hour. Relative growth rates calculated using *cdc8-110 cells* carrying an empty vector (pREP41) + thiamine as the standard. Relative growth rates at 36 ^{0}C calculated against initial growth rates at 25 ^{0}C. + indicates presence of thiamine, - indicates absence of thiamine.

At the permissive temperature of 25 ^{0}C, *cdc8-110* cells containing the empty expression vector grew at a rate of 0.047 ΔOD_{600} hours^{-1} in the presence of thiamine and 0.042 ΔOD_{600} hours^{-1} in the absence of thiamine. When comparing the relative growth rates at the permissive temperature of 25 ^{0}C (Table 5.5), *cdc8-110* cells containing *cdc8*$^+$ and *cer3-cdc8*$^+$ gave comparable growth kinetics to the empty plasmid control, both in the presence and absence of thiamine. *cdc8-110* cells containing *cdc8-cer3*$^+$ however, showed a notable reduction in growth rate to 0.032 ΔOD_{600} hours^{-1} when grown in the absence of thiamine, therefore reducing cell growth rates by ~ 30% when compared to the empty control. As this is not seen in *cdc8-110* cells containing *cdc8-cer3*$^+$ grown in the presence of thiamine, it indicates the expression of Cdc8-Cer3 is toxic to the cells.

When grown at the restrictive temperature of 36^{0}C, *cdc8-110* cells containing the empty pREP41 plasmid lacked a functional Cdc8 protein and were no longer viable. Initially cells lacking functional Tpm show an increase in OD due to cells continuing to grow in length, however cells are unable to divide. *cdc8-110* cells containing the carboxyl – terminal fusions were also unable to grow at the restrictive temperature, indicating fluorescently tagging Cdc8 at its carboxyl terminus renders the protein inactive and therefore once shifted to 36^{0}C, cells lacked a functional Cdc8 protein. Comparison of growth kinetics between *cdc8-110* cells containing plasmid born copies of wild type *cdc8*+ and *cer3-cdc8*$^+$ showed the amino-terminal fusion grown in the absence of thiamine permitted growth at a rate approaching that of wild type (Table 5.5).

5.6.3 *In vivo* fluorescent imaging of Cerulean3 Cdc8 fusions in *cdc8-110* cells

To further explore the localisation of Cer3-Cdc8 and Cdc8-Cer3 in cells lacking functional endogenous Cdc8, *cdc8-110* cells containing plasmid born copies of wild type *cdc8*$^{+}$, *cer3-cdc8*$^{+}$, *cdc8-cer3*$^{+}$ and *pREP41*$^{+}$ were grown in EMMG at 25 ^{0}C in the absence of thiamine. After 2 days, the cells were shifted to the restrictive temperature of 36 ^{0}C for 6 hours. Cells were then mounted onto cover-slips using 100 mg/ml of lectin and imaged.

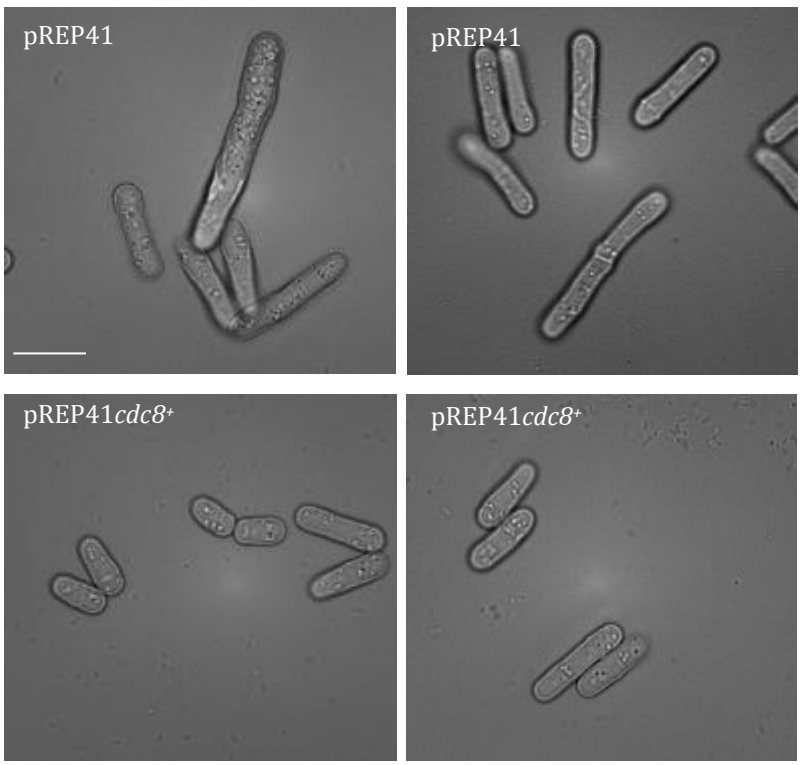

Figure 5.11 Phase images of *cdc8-110* cells expressing pREP41 and WT Cdc8. At the restrictive temperature of 36^{0}C, cells with non-functioning Cdc8 become elongated and are unable to divide. Expression of plasmid *cdc8*$^{+}$ complements loss of endogenous Cdc8 with cells appearing wild-type. Scale bar is 10 µm.

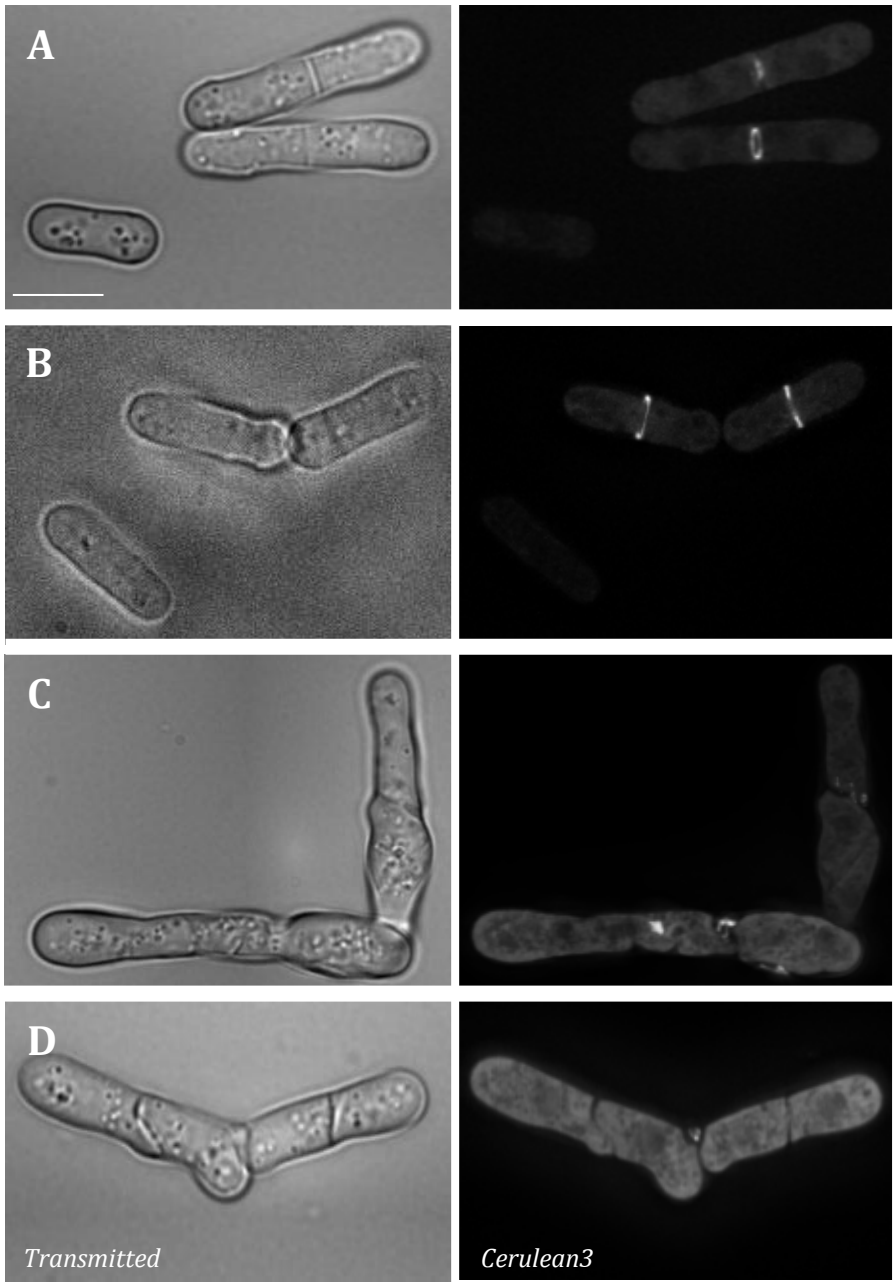

Figure 5.12 Phase and fluorescent images of *cdc8-110* cells expressing A,B) Cer3-Cdc8 and C,D) Cdc8-cer3. At the restrictive temperature of 36 ^{0}C, Cer3-Cdc8 is able to complement Cdc8 function although cells are elongated, Cdc8-Cer3 however is non-functional, therefore cells are unable to divide and become elongated with polarized associated growth defects. Scale bar is 10 µm.

Once shifted to the restrictive temperature of 36 ^{0}C, *cdc8-110* cells containing the empty *pREP41*$^{+}$ became elongated and were unable to divide due to the absence of functional Cdc8 (Figure 5.11). Cells containing plasmid born copies of *cdc8*$^{+}$ however appeared wild-type displaying a normal cell size with no disruption to the normal timing of cell division (Figure 5.11). Although growth kinetics revealed in the absence of thiamine, *cdc8-110* cells containing *cer3-cdc8*$^{+}$ grew at equivalent rates to those expressing WT Cdc8 at 36 ^{0}C, imaging revealed cells were significantly longer than wild type demonstrating the normal timing of cell division was disrupted (Figure 5.12). In contrast *cdc8-110* cells containing *cdc8-cer3*$^{+}$ grown at the restrictive temperature of 36 ^{0}C became elongated and were unable to divide confirming the loss of functional Cdc8. In addition, cells displayed severe polarized associated growth defects, with aggregates of Cdc8-Cer3 appearing randomly within the cell. The data therefore indicates that the Cerulean3 Cdc8 fusions may be able to form heterodimers with endogenous unlabelled tropomyosin, however only the amino-terminal Cer3-Cdc8 fusion was able to form dimers with the capacity to form filaments and associate with actin in the absence of the wild type protein.

5.6.4 *In vivo* fluorescent imaging of cerulean Cdc8 fusions in *cdc8-110 myo2-mCherry* cells

Cdc8 plays a key role in regulating the motor activity of the class II myosin; Myo2, the only essential myosin within the *S. pombe* cell (East & Mulvihill 2011). Required for the assembly of the CAR from acto-myosin containing medial nodes, Myo2 also provides the major contractile force during actin ring constriction (Mulvihill & Hyams 2003). To determine how the Cerulean3 fusions affected the ability of the coiled-coil protein to regulate myosin motor activity *in vivo, cdc8-110* cells with fluorescently labelled Myo2mCherry containing plasmids encoding *cdc8*$^{+}$*, cer3-cdc8*$^{+}$ and *cdc8-cer3*$^{+}$*,* were grown in EMMG at 25 ^{0}C in the absence of thiamine for two days.

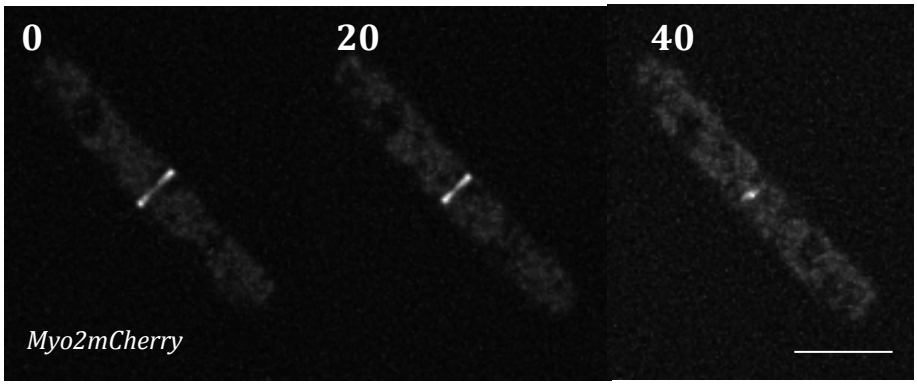

Figure 5.13 Montage of *myo2.mCherry pREP41cdc8^{+} cdc8-110* cells. Fluorescent images of *cdc8-110 myo2.mCherry pREP41cdc8^{+}* cells shifted to 36 ^{0}C show normal ring constriction. Timings are shown in minutes. Scale bar is 10 µm.

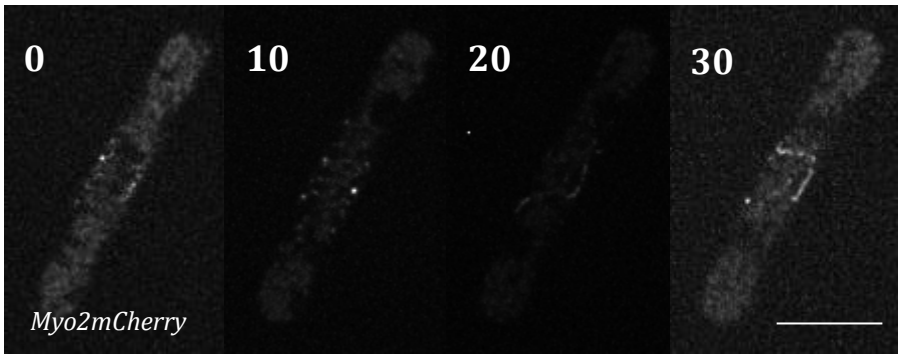

Figure 5.14 Montage of *myo2.mCherry pREP41cdc8-cer3^{+} cdc8-110* cells grown at 36^{0}C. As Cdc8-Cer3 did not localise, images are only given for Myo2mCherry. Although Myo2 is being recruited to the cell equator cells are unable to form stable acto-myosin rings, therefore Myo2 foci concentrate into randomly organised contractile filaments or aggregates Timings are shown in minutes Scale bar is 10 µm.

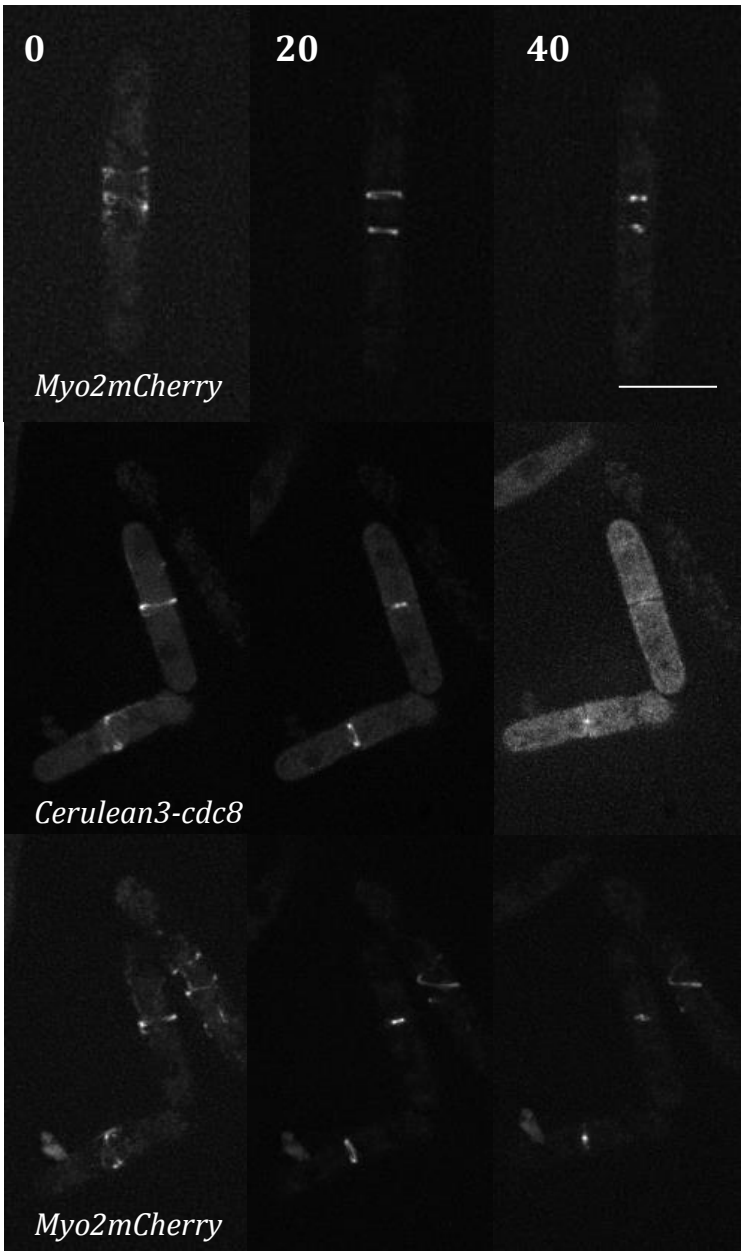

Figure 5.15 Montage of *myo2.mCherry pREP41cer3-cdc8*$^{+}$ *cdc8-110* cells grown at 36 ^{0}C. Images show Myo2mCherry and Cer3-Cdc8. Cells were able to undergo normal cytokinesis, with some of the population incorporating Myo2 into multiple contractile acto-myosin rings. Timings are shown in minutes Scale bar is 10 µm.

Cells were then shifted to the restrictive temperature of 36 ^{0}C for 6 hours. Consistent with previous data, the *myo2.mCherry* allele is functional at the restrictive temperature of 36 ºC however endogenous *cdc8*$^{+}$ is not (M. Johnson et al. 2014). Cells expressing *cdc8*$^{+}$ and *cer3-cdc8*$^{+}$ from episomal plasmids formed normal contractile rings.

To therefore quantify the ability of each fusion protein to regulate the contractile activity of Myo2, the rate of CAR constriction was measured in *myo2.mCherry cdc8.110* cells at 36 ºC. Cells expressing Cdc8 constricted at an average rate of 0.088 ± 0.014 µmmin-1 (mean ∆CAR-diameter rate ± s.d.) (Figure 5.13). In comparable cells expressing Cdc8-Cer3, Myo2mCherry was being recruited to the cell equator, however foci concentrated into randomly organised contractile filaments or aggregates (Figure 5.14). The rate of constriction could therefore not be calculated as cells failed to form stable contractile rings, leading to loss of viability.

In cells expressing Cer3-Cdc8, the CAR constricted at a rate of 0.09 ± 0.007 µmmin-1, however in more than 30% of these mitotic cells multiple contractile acto-myosin rings formed, to which Myo2 was incorporated. Although this indicates the expression of Cer3-Cdc8 disrupted the regulation of node dependent CAR formation, once formed the actin-Cer3-Cdc8 co-polymers were capable of regulating normal Myo2 dependent contraction (Figure 5.15).

5.6.5 *In vivo* fluorescent imaging of cerulean Cdc8 fusions in *cdc8-110 myo52mNeongreen* cells

In addition to regulating the motor activity of Myo2, Cdc8 also plays a key role in modulating the duty-ratio of the fission yeast myosin V; Myo52 to promote processive movement upon actin filaments. During interphase, Myo52 associates with interphase actin-Cdc8 filaments to deliver cellular cargoes to the growing tips of the cell. To explore the impact tagging Cdc8

has on the ability of the protein to regulate and facilitate the actin dependent movement of Myo52, *myo52.mNeongreen* cdc*8-110* strains containing plasmids encoding *cdc8*$^{+}$*, cer3-cdc8*$^{+}$ and *cdc8-cer3*$^{+}$ were cultured in EMMG at 25 ^{0}C in the absence of thiamine for two days, then shifted to the restrictive temperature of 36 ^{0}C for 6 hours.

In cells lacking functional Cdc8, Myo52 is unable to associate with actin and therefore fails to accumulate to the growing ends of the cells. In *myo52.mNeogreen cdc8-110* cells expressing wild type Cdc8 or the amino terminal Cer3-Cdc8 fusion, Myo52 was seen to localise to the ends of the cell (Figure 5.16). When compared however, cells expressing Cer3-Cdc8 showed fewer Myo52 movements within the cytosol than cells expressing WT Cdc8. In contrast, *myo52.mNeogreen cdc8-110* cells expressing Cdc8-Cer3 showed no localisation of Myo52 at the ends of the cells which is consistent with the inability of Myo52 to associate with actin.

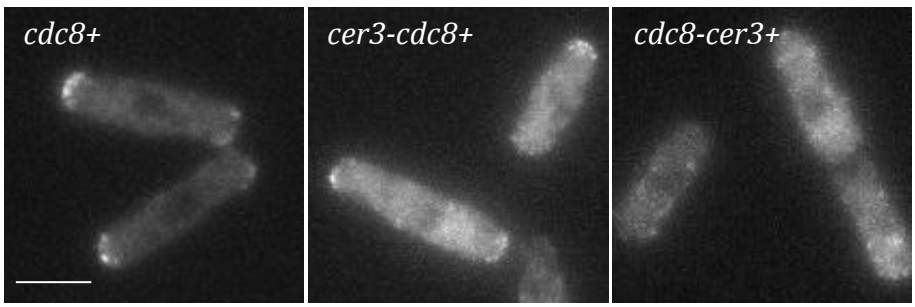

Figure 5.16 Micrographs of *myo52.mNeongreen cdc8-110 cells* encoding *cdc8*$^{+}$*, cer3-cdc8*$^{+}$ *and cdc8-cer3*$^{+}$. At 36 ^{0}C, cells expressing Cdc8 or Cer3-Cdc8 show Myo52 localise at the ends of the cell, however cells expressing Cdc8-Cer3 show no discrete localisation of Myo52. Scale bar is 10 µm.

5.7 Discussion

In order to investigate the basis of temperature sensitivity in the fission yeast *cdc8-110* and *cdc8-27* mutants, thermal unfolding assays were performed at high salt concentrations (500 mM) using circular dichroism. This was to prevent Tpm polymerizing end-to-end at the protein concentrations required for the CD measurements, ensuring the observed results were a consequence of dimer dissociation and denaturation of the α-helix. CD spectra acquired for all Cdc8 proteins at the start of each run showed distinctive minima for highly helical structures and gave identical spectra indicating each Cdc8 protein was able to rapidly refold to its original state.

Melting curve data for unmodified Cdc8 gave a mid-point melting temperature (T_m) of 33.4°C and unfolds with a single thermal transition, indicating the Cdc8 dimer dissociated at the same time as the protein denatured. Amino terminal acetylation of Cdc8 results in stabilisation of the single unfolding transition, increasing the T_m to 35.4°C, equivalent to values established previously (East et al. 2011). This is consistent with observations that acetylation masks the charge of the amino-terminal methionine allowing the amino terminus to adopt a more stable, fully helical conformation (Brown et al. 2001).

The single point mutations A18T and E31K, both unfolded with a single thermal transition however, A18T resulted in loss of stability giving a T_m 4.9°C lower than $Cdc8^{ACE}$ whereas E31K stabilised the protein increasing the T_m by 0.5°C. The point mutations A18T and E31K are found in the *cdc8-110* strain, however as E31K is marginally more stable than $Cdc8^{ACE,}$ it is possible the A18T mutation alone leads to yeast cell temperature sensitivity. Thermal transitions for mutants E129K and the double mutant A18T/E31K reveal biphasic melting profiles giving T_m's of 29.3/38.1 and 29.2/43.3 respectively, with ~60% of the CD change occurring during the lower temperature transition, which is 6.1 and 6.2°C lower than $Cdc8^{ACE}$. The upper, smaller unfolding transition for E129K and A18T/E31K is significantly

more stable than Cdc8^{ACE}, giving T_m's of 38.1ºC and 43.2ºC respectively. This is significantly higher than the single unfolding transition T_m of the wild type protein. In the absence of a high-resolution Tpm structure it is difficult to give a precise interpretation of the stabilising/ destabilising effect of each mutation, however some features can be inferred from the position of the residue in the heptad repeat (Figure 15). Ala18 is in the core *d* position of the heptad repeat, a position normally occupied by small hydrophobic residues. Sequence analysis of Cdc8 reveals A18 is part of an alanine cluster (A11-T15-A18-A22-A25) between two strong hydrophobic clusters (Figure 5.17).

Alanine clusters are thought to introduce sharp bends in the axis of the Tpm by reducing the density of side-chain packing, creating a source of semi-flexibility for the molecule. Replacing hydrophobic A18 with a Thr introduces a polar residue with some hydrophilic character and a larger side chain into the core of the Tpm and also places two Thr close together. This is likely the cause of the destabilisation of the coiled-coil. Residue Glu31 falls into the *c* position, usually occupied by polar or charged residues on the surface of the molecule facing the surrounding aqueous environment. Although unlikely to play any role in stabilising the coiled-coil structure due to its surface location, E31K is located in a region which interacts with actin therefore changing a negatively charged side chain to a positive charge could have a significant impact on the Tpm's ability to bind actin.

Glu129 is found in the *g* position of the heptad repeat, a position often occupied by charged amino acid residues which form salt bridges between the two neighbouring chains, defining the parallel orientation of each strand and further stabilising the coiled coil structure (Jampani et al. 2012). As the equivalent *e* position is also a negatively charged Glu, it is impossible for this residue to be involved in the formation of a salt bridge however mutation to a positively charged Lys might be expected to stabilise the coiled-coil.

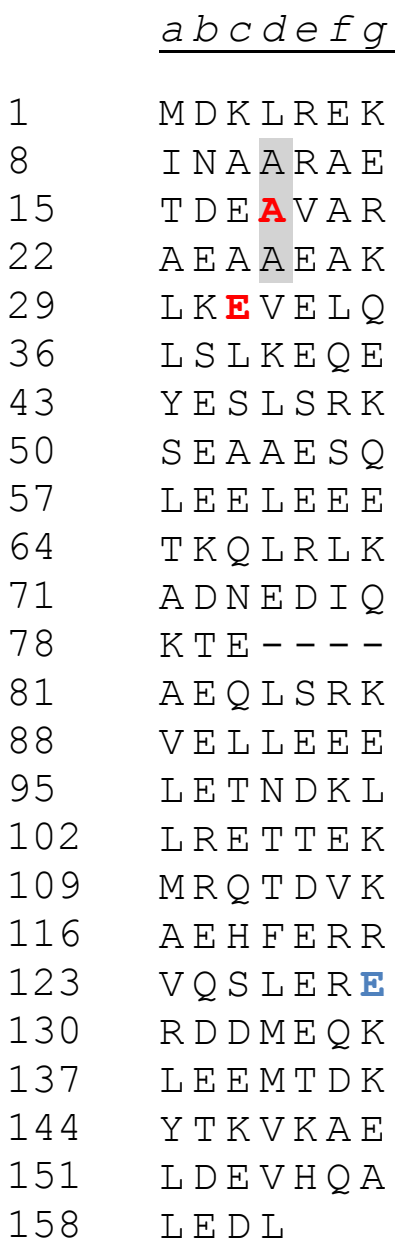

Figure 5.17 Alignment of Cdc8 sequence to heptad repeat. The amino acid sequence of Cdc8 aligned vertically in groups of heptad repeats. Mutations identified in the *cdc8-110* and *cdc8-27* genes are highlighted in red and blue respectively. Alanine cluster highlighted in grey.

A closer look at the local protein sequence also reveals an Arg in the following *a* position, normally occupied by a polar residue therefore this local structure is unlikely to conform to the standard coiled-coil.Although from these results, temperature sensitivity in *cdc8-110* cells appears to be the result of the A18T mutation, as E31K alone has little impact on Cdc8 thermostability, the location of E31K in a region which interacts with actin could greatly reduce the proteins affinity for actin, therefore the combined substitutions might explain the dramatic effect of these temperature sensitive mutations. Actin binding assays and expression from a plasmid in *cdc8-110* cells using the individual mutations would allow the role of each of the amino acid substitution to be further explored.

As both E129K and A18T/E31K showed bi-phasic melting transitions, it is possible amino-terminal acetylation stabilises a proportion of the protein corresponding to the upper thermal transition, allowing both proteins to remain partially folded at 36 ºC. This could mean that in *cdc8-110* and *cdc8-27* cells, the Tpm does not get rapidly cleared by the cell through proteolysis, but remains present in a semi-folded state allowing rapid refolding and reactivation of the protein when shifted back to a permissive temperature. In addition to assessing the effects of single amino acid substitutions on protein stability, circular dichroism and thermal unfolding assays were also performed using the amino and carboxyl Cerulean3 tagged Cdc8 proteins to investigate the impact FP-Tpm fusions had upon the biophysical properties of Cdc8. CD spectra acquired for all FP-Tpm fusions gave the characteristic highly helical spectra, identical after each run indicating the FP fusion has little effect on protein folding. CD data acquired for the FP alone confirmed the fluorophore had no significant impact upon the overall CD spectra.

Normalised melting curve data showed each protein unfolds with a single thermal transition, indicating the presence of the FP has little impact on the binding cooperativity of Cdc8. The addition of Cerulean3 to the carboxyl terminus of Cdc8 had a minimal effect on thermostability, increasing the T_m

from 33.4°C to 34.3°C when compared to unacetylated Cdc8. Similarly, acetylation of the amino terminal methionine of Cdc8-Cer3 gave a slight increase in T_m of 0.3°C when compared to $Cdc8^{ACE}$. In contrast, fusing Cerulean3 to the amino-terminus of Cdc8 had a more significant effect, increasing the thermal stability of the protein to 35.5°C, equal to that of wild-type $Cdc8^{ACE}$. These results therefore indicate the addition of Cerulean3 to the carboxyl terminus of the protein has no significant effect upon the stability or binding cooperativity of the Cdc8 coiled-coil protein, however addition of the FP to the amino terminus stabilizes the protein to equivalent levels of acetylation.

The amino and carboxyl terminus of Cdc8 is required for the formation of end-to-end interactions, due to the amino terminus of one Tpm inserting into the splayed carboxyl terminus of the adjacent Tpm (Palm et al. 2003). Modifications to the amino acid sequence can therefore alter the ability of the protein to form polymers. The additional mass of ~ 28 kDa at the amino or carboxyl terminus from the Cerulean3 FP has the potential to impact the ability of the protein to polymerise, therefore a viscometry assay was used to investigate the effect the addition of the fluorescent protein had upon the ability of Cdc8 to form filaments. A high viscosity correlates with a greater capacity to form filaments, with increasing salt concentrations used to disrupt the strength of ionic interactions between Tpm proteins, revealing the strength of such interactions.

The viscosity of each protein in the absence of salt revealed at 0 mM NaCl, unmodified Cdc8 has a viscosity of 1.08 centistokes (cSt) whereas $Cdc8^{ACE}$ has an increased viscosity of 1.22 cSt, however in the presence of 200 mM NaCl the viscosity decreases to 1.01 cSt and 1.10 cSt respectively. These results therefore indicate, even at high salt concentrations, acetylation stabilises the Tpm filaments to levels higher than unmodified Cdc8 in no salt. It has been suggested that the amino terminus of Tpm must be able to form a fully folded helix for a strong overlap complex with the carboxyl terminus. These results are consistent with the first two residues of

unacetylated Cdc8 being non-helical resulting in weaker interactions, whereas acetylation is thought to complete the helical structure of the amino terminus therefore greatly increasing the propensity of the protein to form filaments (Brown et al. 2001). The viscosity data for all Cdc8 FP fusions indicated the end-to-end interactions between adjacent Tpm dimers are affected by the addition of the Cerulean3 fluorophore. In the absence of salt, amino terminally tagged Cdc8 gave a viscosity reading of 1.17 cSt, which is higher than unmodified Cdc8 but lower than $Cdc8^{ACE}$, indicating the addition of the FP at the amino terminus partially mimics acetylation and increases the ability of the Tpm to polymerise. Similarly to $Cdc8^{ACE}$, in 200 mM NaCl these end-to-end interactions are more stable than those seen for Cdc8. In contrast, the unacetylated and acetylated carboxyl terminal fusion gave viscosity readings equivalent to the buffer only control, indicating the addition of the FP to the carboxyl terminus completely abolished the ability of the protein to form end-to-end interactions.

The affinity of individual Tpm dimers for actin is low, however is increased when dimers polymerise via end-to-end interactions. As the FP fusions significantly impacted the ability of the protein to form filaments, co-sedimentations assays were used to investigate the impact FP fusions had on the proteins affinity to actin. Binding coefficients ($K_{50\%}$) established previously for Cdc8 and $Cdc8^{ACE}$ gave values of 2.76 µM and 0.46 µM respectively (East et al. 2011). Tagging Cdc8 at its amino terminus increased the proteins affinity for actin, resulting in a binding coefficient of 0.69 µM. Consistent with viscosity data, fusing Cerulean3 to the amino terminus of Cdc8 appears to partially mimic acetylation and therefore increases the proteins affinity for actin to levels more comparable to $Cdc8^{ACE}$.

Previously it has been shown small alterations to the amino terminus of Tpm not only impairs its ability to form end-to-end interactions but also negatively impacts its affinity for actin (Hitchcock-DeGregori 2008). Comparable to these findings, carboxyl terminal FP fusions abolished both the proteins

affinity to form filaments and interact with actin. Due to its extremely weak affinity for actin, binding curves and thus binding coefficients could not be generated for Cdc8-Cer3 or Cdc8-Cer3^{ACE}. Even at increased salt concentrations, the protein was seen to pellet during centrifugation in the absence of actin, therefore the binding coefficients were estimated to be greater than 20 µM. *In vivo* analysis of FP fusions revealed both amino and carboxyl tagged Cdc8 were capable of localising to the CAR in cells possessing the wild type *cdc8*$^{+}$ allele however, only amino terminally tagged Cdc8 was able to localise and support growth in the absence of functional endogenous Cdc8. This indicates that although the carboxyl-terminal fusion is capable of forming heterodimers with endogenous Tpm, its ability to decorate actin polymers in a cell does not provide any indication of its level of functionality, as it was shown to be unable to form end-to-end polymers or associate with actin *in vitro*.

The cellular distribution of Cdc8 and its interactions with actin and myosin have been shown previously to be modulated by amino-terminal acetylation. Consistent with these findings, Cer3-Cdc8 binds to actin and regulates Myo2 activity during CAR constriction however, its expression often disrupts initial polymerisation events with more than 30% of mitotic cells forming multiple contractile acto-myosin rings. Once formed the actin-Cer3-Cdc8 co-polymers were capable of regulating normal Myo2 dependent contraction, giving equivalent constriction rates to wild type Cdc8. Contrariwise, cells expressing Cdc8-Cer3 were unable to form stable contractile rings, therefore foci of Myo2 concentrated into randomly organised contractile filaments or aggregates with cells failing to complete cytokinesis, leading to loss of viability.

In line with both *in vitro* and *in vivo* data, in the absence of functional endogenous Cdc8, cells expressing wild type Cdc8 from a plasmid or the amino terminal Cer3-Cdc8 fusion showed Myo52 localise to the ends of the cell, however cells expressing Cdc8-Cer3 showed no discrete localisation, consistent with the inability of Myo52 to associate with actin. Closer analysis revealed cells expressing Cer3-Cdc8 showed fewer Myo52 movements

within the cytosol than WT, therefore the addition of FP tags to the end of the Tpm changes the landscape at the end of the actin polymer, disrupting normal amino-terminal signalling, therefore supporting models which predict the Tpm amino terminus is crucial during actin-Tpm co-filament nucleation and growth.

5.7 Conclusion

Despite the discovery *of cdc8-110* and *cdc8-27* more than 40 years ago, the basis of temperature sensitivity for each of these well-defined mutants is only just starting to be defined. The results obtained during this study indicate the amino acid substitutions within the *cdc8*$^{+}$ gene for both mutants result in a two-step thermal unfolding transition of the protein, with the majority of the protein unfolding at temperatures lower than those required for unacetylated wild-type Cdc8, therefore rendering the protein inactive at restrictive temperatures.

Data for unmodified versions of each Cdc8 mutant acquired within the lab by Chloe Johnson, revealed amino-terminal acetylation resulted in an increase in the thermal stability of each protein to varying degrees. Interestingly, non-acetylated *cdc8-110* and *cdc8-27* mutations displayed single phase unfolding transitions which gave T_m values of 27.9 ºC and 29.3 ºC respectively, therefore it is likely acetylation separates the unfolding into two distinct transitions. This indicates that acetylation is important not just for stabilising the amino-terminus and allowing interaction between the amino and carboxyl termini of the Tpm polymer on actin, but also for the stability of the whole molecule.

Biochemical analysis of Cdc8 FP fusions showed addition of the Cerulean3 fluorophore to the amino or carboxyl terminus did not impact the helical content or thermal stability of the protein, however *in vitro* and *in vivo* analysis showed that the addition of a fluorescent protein to the amino

terminus gives Cdc8 properties that closely mimic those of the acetylated endogenous Cdc8. Fusion of the FP to the carboxyl terminus, inhibited both the ability of Tpm to form end-to-end contacts and the ability to associate with actin. Whilst the impact of fusing a fluorescent protein to the terminus of Tpm is likely to vary between different isoforms and cell types, these results demonstrate the importance of defining the functionality and biophysical properties of the modified protein compared to those of the wild type protein, before drawing any conclusions from data generated using such fusions.

Chapter 6: Use of hydrostatic pressure to perturb the cell cycle

6.1 Introduction

Pressure is a key physical parameter which continually influences the evolution and distribution of both macro and micro-organisms, living in any environment from the planet surfaces to the most extensive habitats of the biosphere (Winter 2015; Bartlett 2002). Previous research has shown that small changes in hydrostatic pressure alter the ability of key molecules within a cell to interact and thus communicate which can result in growth inhibition, growth arrest, cellular death and breakdown of cellular structures (Iwahashi 2015). Cells have been shown to temporarily adapt to pressure changes by altering gene expression, indicating that specific cellular processes may be activated during different ranges of hydrostatic pressure, allowing for cell survival (Iwahashi 2015).

Offering a number of advantages that conventional methods such as temperature and pH perturbations do not, the use of hydrostatic pressure provides a non-invasive method for dissecting the cellular functions of proteins both *in vivo* and *in vitro*, with often fully-reversible effects. As all life is dependent upon the ability of a cell to rapidly respond to changes in its environment through modulation of diverse signalling pathways, development of a unique hydrostatic pressure system could provide an invaluable insight into functional dependencies and molecular interactions within a cell.

During this study, we aimed to develop a novel pressure chamber which can be incorporated into any inverted live cell imaging system, allowing the visualisation of cells during pressure perturbation experiments, creating a system which can be readily available to other research group. As fluorescent live-cell imaging methods allow intracellular protein dynamics and molecules to be followed in real time, we also aimed to combine the hydrostatic pressure imaging system with sensitive EMCCD cameras and

high numerical aperture lenses so it could be used to visualise fluorescent proteins within live cells. This meant developing a system which gave better image resolution, higher photon capture and higher speed of image collection. Due to the simplicity of its cell cycle, unique shape and ease of genetic manipulation, the fission yeast *S. pombe.* offers an ideal model organism to investigate the effects of pressure on the cell cycle and the cell cytoskeleton, identifying which molecules are involved in cell cycle progression and which stress pathways may be activated.

6.1 Development of the hydrostatic pressure chamber

6.1.1 Prototype I

The first design of the hydrostatic pressure chamber was a proof of concept prototype which served to provide specifications for a real working system rather than a theoretical one. As the first model, prototype I was used to evaluate and verify some key functional aspects of the pressure cell design required for the functionality of the final product. The initial design of the hydrostatic pressure system had three main components; the pressure-cell, the HPLC pump and the software for system control and data acquisition.

The hydrostatic pressure-cell made from stainless steel, was specifically designed to take pressures of up to 200 bar, which could be held constant over a number of hours. The main chamber of the pressure-cell was designed to contain the liquid media used during the experiment (Figure 6.1 A). It featured two optical windows. The first was a 10 mm thick Perspex window at the top of the chamber, used for standard illumination and phase imaging. The choice of thickness for the second window was dictated by the specific level of pressure application and measurement to be acquired, however was limited to between 0.08 and 1 mm due to the working distance of the microscope lenses. This window held the sample and was located on the underside of the chamber facing the objective of the inverted fluorescent microscope.

In the initial design, windows were mounted onto highly polished stainless steel metal window support disks with small 2 mm openings at the centre of each disk, which allowed the sample to be illuminated and imaged using an inverted research microscope (Figure 6.1 B). Due to constraints in manufacturing these support disks, an upgrade was introduced which removed the centre portion of the support disk (Figure 6.1 B). This allowed for the introduction of a flat, highly polished 0.9 mm aluminium metal disk which sat between the window support and the optical window.

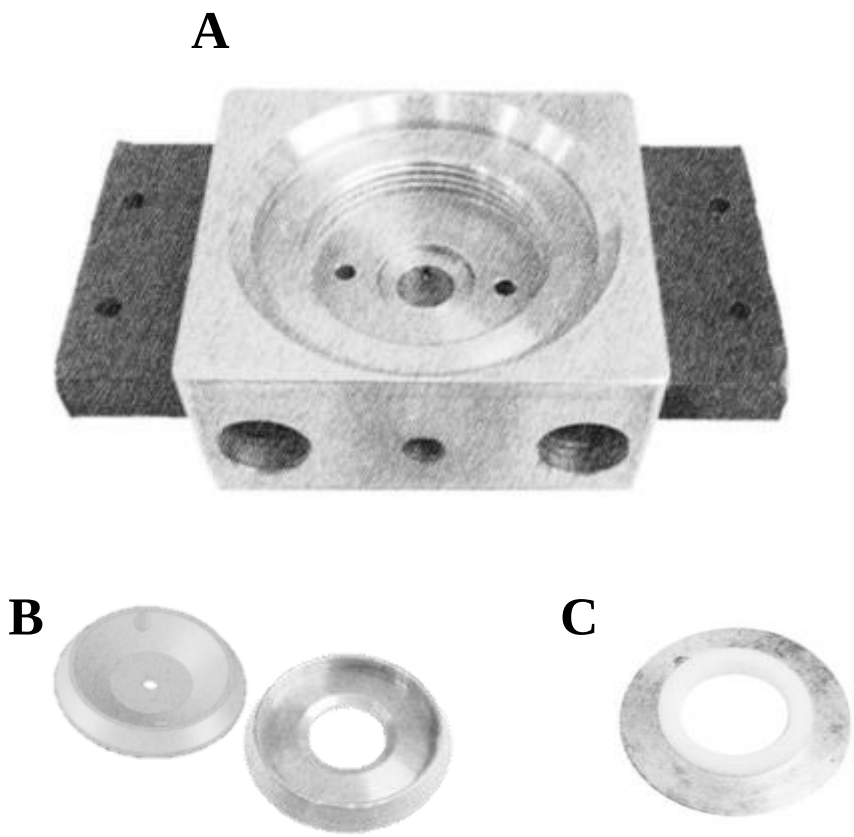

Figure 6.1 Pressure cell prototype I, window support disk and seal. A) The main body of the pressure cell which housed the liquid medium and sample used during experiments. One side of the cell contained a water pipe inlet with the outlet located on the opposite side. Plastic extensions each side (black) of the cell are required for mounting onto the microscope. B) Custom designed metal window support disk. In the initial design, the sample window fixed directly onto the support disk, however an upgrade was made that removed the central piece of metal, with the window assembled first onto a metal disk then attached to the support disk. C) White Teflon seal that assembled onto the window support disk, held in place by a metal ring.

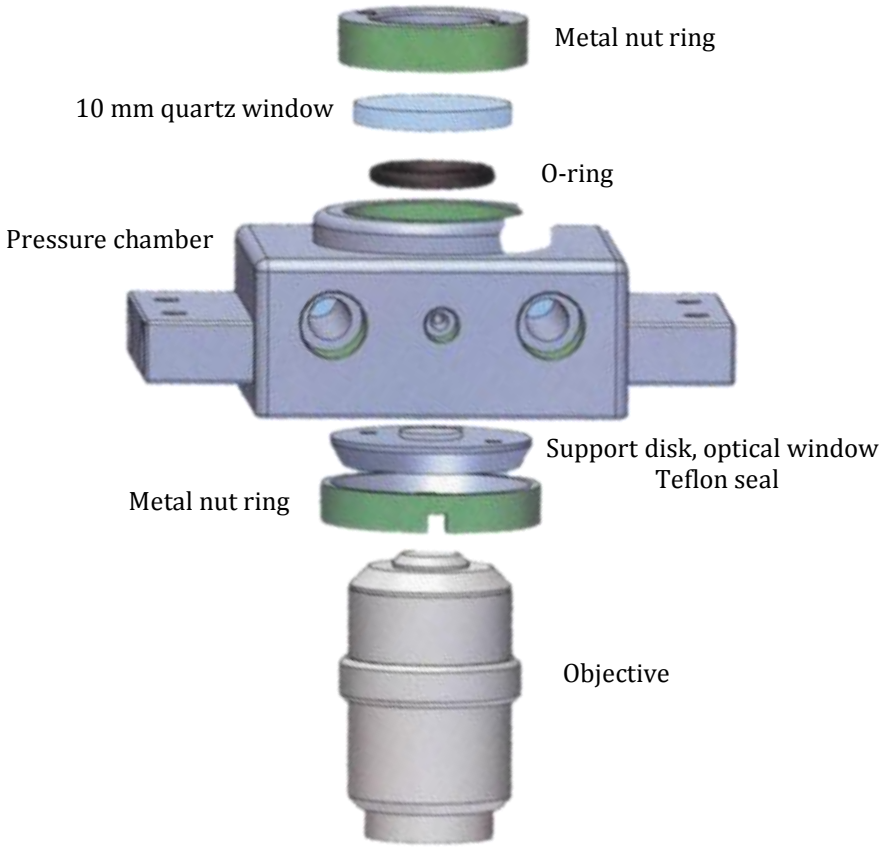

Figure 6.2 Schematic drawing of prototype I pressure system components. A 10 mm quartz window sits on a rubber O-ring in the top of the pressure cell and is secured by a metal nut ring (green), The sample window is mounted onto a highly polished metal window support disk along with a Teflon seal. This is then inserted into the underside of the pressure chamber and secured by a metal nut ring (green), creating a seal that enables the cell to be pressurised. Fluid pipe inlet and outlets (green) are located either side of the cell. Plastic extensions are attached each side of the cell for mounting onto the microscope. Location of microscope objective shown underneath pressure-cell components.

Objective	NA	Working distance (mm)	Immersion medium
40x	0.6	2.7 - 4	Air
60x	0.7	1.5 – 2.2	Air
60x	1.0	2	Water
60x	1.4	0.1	Oil

Table 6.1 Microscope objective specifications. Specifications for the numerical aperture, working distance and immersion medium of each microscope objective.

This allowed for quick modifications to metal thickness and central hole size, as the flat metal disks were cheaper and more easily sourced. To withstand the pressures used within the pressure-cell, the stainless-steel metal support disks required a minimum thickness of 0.8 mm, however the microscope objectives each have maximum working distances due to their numerical apertures (NA) (Table 6.1). To accommodate this, the metal support disks were custom made to the exact specifications of the objectives so that the bevelled edges needed to give the optical windows extra support, would not block access by the objective. The metal disks and optical windows were held in place on the support disks using a cellulose-based glue dissolved in acetone. In combination with sensitive EMCCD cameras, this system only allowed samples to be imagined using the three lenses with a working distance of 2 mm and above.

The chamber was sealed using a Teflon seal, which was assembled onto the metal support disk and metal nut ring (Figure 6.1 C), which was secured using a conventional thread mechanism. Custom made interlocking tools made from stainless steel were used to seal the pressure-cell. A nut tool handle slotted into a window nut tool that also attached to a metal block. The metal block slotted into custom designed grooves on the metal nut ring.

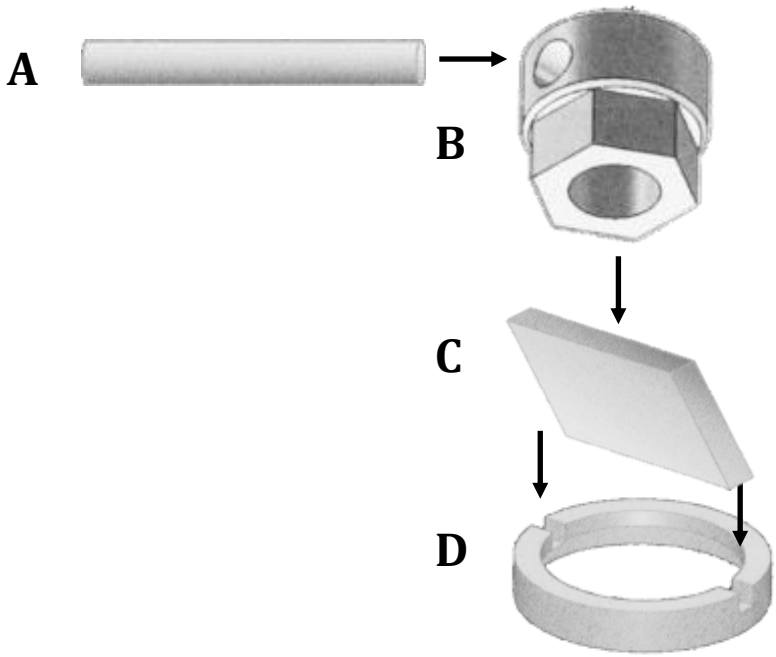

Figure 6.3 Schematic representation of interlocking tools used to seal prototype I pressure cell A) Nut tool handle slots into a B) window nut tool. This attaches onto the C) metal block which slots into custom designed grooves on the D) metal nut ring. This tightens the thread and compresses down the components of the chamber creating a seal that enabled the cell to be pressurised.

Once in place, the tools tightened the thread of the metal nut ring into the pressure cell, compressing the underside components of the chamber together, creating a seal that enabled the system to be pressurised (Figure 6.3). Hydrostatic pressure was generated and regulated through a computer controlled Kontron HPLC 422 master pump equipped with 0.01-2 mL/min piston heads in a master-slave configuration. The pump was directly connected to a fluid pipe inlet on the pressure cell via stainless-steel tubing. On the parallel side of the cell was a water pipe outlet connected to a pressure relief valve which allowed the pressurised fluid to flow out of an auxiliary passage, providing an additional mechanism to control and limit the pressure within the system.

Value of pressure was indicated by the pump which was located next to the hydrostatic pressure system and by the in-house LabVIEW® based software interface, developed within this lab. Although any fluid can be utilised as a pressure medium, each experiment was tailored to the sample being used, for instance during live cell imaging experiments, specific growth media was used for culturing samples to maximise longevity of the sample and therefore experiments. Although the first prototype of the pressure-cell enabled the system to pressurise up to 200 bar within several seconds, the design of the cell held a number of disadvantages.

The first major issue was the instability of the pressure within the system. Although pressure could be held within the system over a number of hours, fluctuations ranged within 20-30 bar. These large fluctuations exposed the sample windows to repetitive stress via flexing and therefore windows frequently shattered. In addition, the pressure against the sample windows often resulted in the formation of indents in the surface of the stainless-steel support disks making them ineffectual at sealing the system in future experiments. Although an initial upgrade introduced cheaper more easily sourced metal disks that were more dispensable to circumvent this issue, continually replacing the disks became expensive and impractical.

Whilst the original cellulose based glue was only adopted to aid in holding the optical window in position until the system was pressurized, it was quickly found to be inadequate. Once the system was subjected to over 20 bar of pressure the windows would often dislodge from the support disk allowing fluid to leak out of the system and thus lose pressure. In addition, these large fluctuations in pressure enhanced the build-up of sugars coming out of the media solution within the HPLC pump, causing the valves of the pumps to cease working and remain in the open position making the system inoperable.

Although prototype I highlighted design floors within the main body of the pressure - cell, it also emphasised the need for a more reliable method of sealing the system. The Teflon seal was found to quickly lose shape, making it inadequate to seal the system in subsequent experiments, therefore it needed to be frequently changed. The custom-made tools also made the system difficult for the user to seal for experiments, as the tools often slipped out from the grooves holding them in place. Even after the addition of a bench bracket which held the chamber whilst tightening, the current tool design made the system non-user friendly.

6.1.2 Prototype II

As the initial pressure-cell was a proof of concept prototype, it was used to evaluate the design and capabilities of the system, exposing a high degree of design flexibility for potential improvements that would enhance the function and precision of the hydrostatic pressure system. This enabled prototype II to become a working prototype with more functionality. Based on the original design, prototype II also contained three major components; the pressure-cell, the HPLC pump and the software for system control and data acquisition. In prototype II, the main body of the cell was designed very closely to that of prototype I, however instead of using a metal nut ring mechanism to seal the chamber which previously made the system less

user friendly, a metal flange was designed which contained a nitrile O-ring (Figure 6.4 A,B). To this metal flange, a highly polished 0.5-0.9 mm thick aluminium metal disk, similar to those used in prototype I, was attached to which the optical window would then be assembled. Both the optical window and metal disk were held in place using Araldite professional adhesive.

This design allowed the metal flange to be inserted into the main body of the cell with ease, creating a seal with the O-ring, bypassing the need to use the interlocking tools. It was then kept in position with six easily adjustable threaded screws during pressure experiments. Standard illumination from above the pressure cell for phase imaging was upgraded to an LED 12 light halo. As in the previous system, hydrostatic pressure was generated and regulated through a computer controlled Kontron HPLC 422 master pump. Although similar in design to the original chamber, the second prototype was able to hold the pressure in the system stable for over 20 hours, showing only minor fluctuations in pressure within a 5 bar range (Figure 6.5). These minor fluctuations enabled a reduction in flow rate, resulting in less repetitive strain on the optical windows. This increased the duration of experiments and also resulted in less build-up of sugar - syrup around the pump valves, increasing the functionality of the pumps.

Once the system was functional and could be held stable for a number of hours without much user intervention, a series of experiments were undertaken to investigate the effects of hydrostatic pressure on image quality and capture. This would also highlight any restrictions the use of hydrostatic pressure imparted on fluorescent microscopy based techniques.

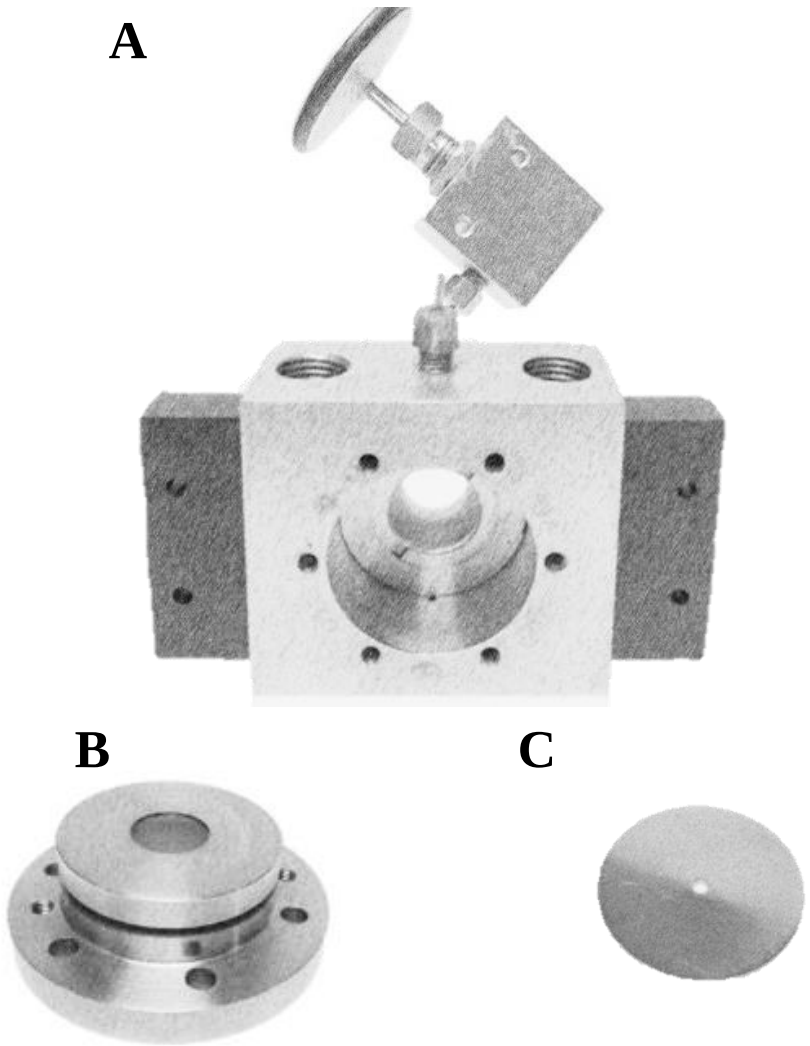

Figure 6.4 Prototype II pressure cell components. A) The main body of the pressure cell, with a similar design to prototype I. Water pipe outlet shown with relief valve at the top of the cell. B) Custom designed metal forma with nitrile O-ring used to seal the system. Once in place the forma was secured using six screws. C) Window support disk that attached to the metal forma and optical window.

A

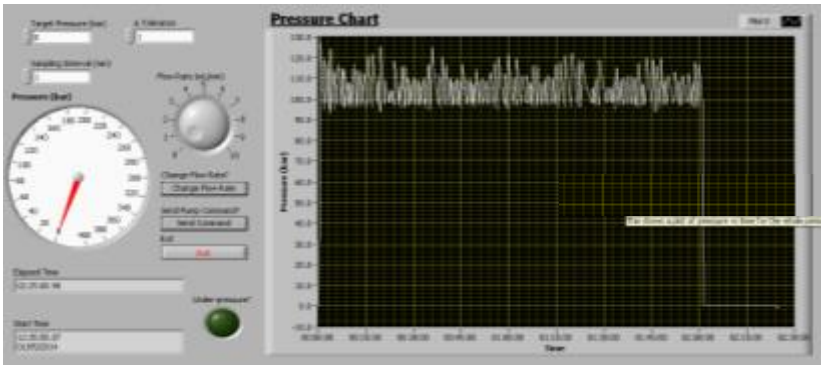

B

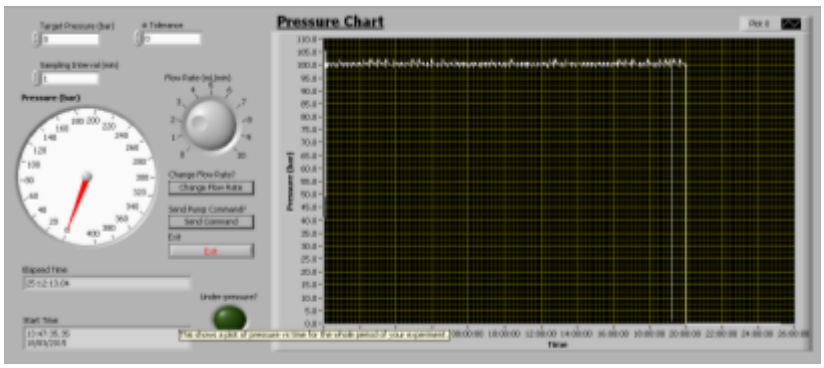

Figure 6.5 Pressure trace comparison at 100 bar of prototype I and II using a 1 mm thick quartz window. A. Pressure graph for prototype I over 2 hours, shows continual pressure fluctuations within a 20 - 30 bar range. B. Pressure graph for prototype II taken over a 20 hour period, shows pressure held constant for the entire duration with only minor fluctuations within a 5 bar range.

6.2 Resolution of the system is limited by the lens working distance and coverslip thickness

The working distance of each objective affects the numerical aperture (NA). NA is measured by the ability of the lens to gather light and resolve fine specimen detail at a fixed object distance and is in turn partially determined by the refractive index of the medium filling the space between the sample and the lens. A high NA improves both the brightness and resolution of an image, however often reduces the working distance of the lens. As a consequence of this, the quality of the images that could be captured using this system were limited to the choice of lenses available, as were the choice of optical windows that could be mounted into the pressure cell.

To assess the differences in image quality and resolution observed using different window thicknesses, immuno-fluorescently labelled alpha-tubulin Human Embryonic Kidney (HEK) cells kindly provided by Anne Roobol, were mounted onto optical windows ranging from 0.08 mm up to 1.0 mm. Images were captured using a 60 x 0.7 NA air lens. HEK cells were chosen as they are 13 µmin size, much larger than *S. pombe* cells. Once immune-fluorescently labelled, various structures such as the mitotic spindle within the cell are revealed with a high level of detail.

The image acquired using the 0.08 mm thick glass window clearly gave the best image quality and resolution, with a great level of detail shown for the tubulin structures and chromosome segregation. The 0.5 mm quartz window also gave good resolution of the various tubulin structures but as the working distance was increased some resolution was lost when compared to the previous image. The 1.0 mm quartz window shows a significant reduction in image resolution and quality when compared to both the 0.08 and 0.5 mm window with structures less defined than seen previously. Although this window is still within the working distance of the 60 x 0.7 NA air lens, there is loss of fine detail and there is more detectable

background light present even after image de-convolution, that is not a desired primary or indirect fluorescent emission (Figure 6.6).

As the choice of lens that could be used for fluorescent image capture was restricted by the working distance of the system, the next step was to determine the significance of numerical aperture (NA) and magnification on image quality, resolution and signal intensity. For this *S. pombe* Cam1-GFP labelled cells were chosen. Cam1 localizes to endocytic patches and the spindle pole bodies as well as the cell division septum (Moser et al. 1997). High resolution images are needed to capture localisation at the cell poles or the spindle pole bodies as fluorescent signal is low, however lower resolution images are still sufficiently sensitive to capture localisation at the cell equator as fluorescent signal is much brighter. Cam1-GFP labelled cells were therefore chosen as they allowed a good comparison of image resolution and sensitivity within a single cell. *cam1-gfp* cells were mounted into the chamber on glass optical windows of 1.0 mm, 0.8 mm, 0.5 mm and 0.19 mm in thickness. Images were captured at atmospheric pressure using a 60 x water lens, 60 x air lens, 60 x oil lens and a 40 x air lens (Figure 6.7, 6.8).

When comparing images captured using the same optical window thickness, the difference in image quality between all of the 60 x lenses gives a clear demonstration of the effect numerical aperture has on the quality of resolution obtainable. The image captured using the 60 x oil lens and 0.19 mm window (Figure 6.7D) gives very clear detail of Cam1 localisation, displaying individual foci at the tips and equator of the cells as well as the spindle pole bodies. This is due to the lens having the highest NA and a much better refractive index due to the oil immersion technique.

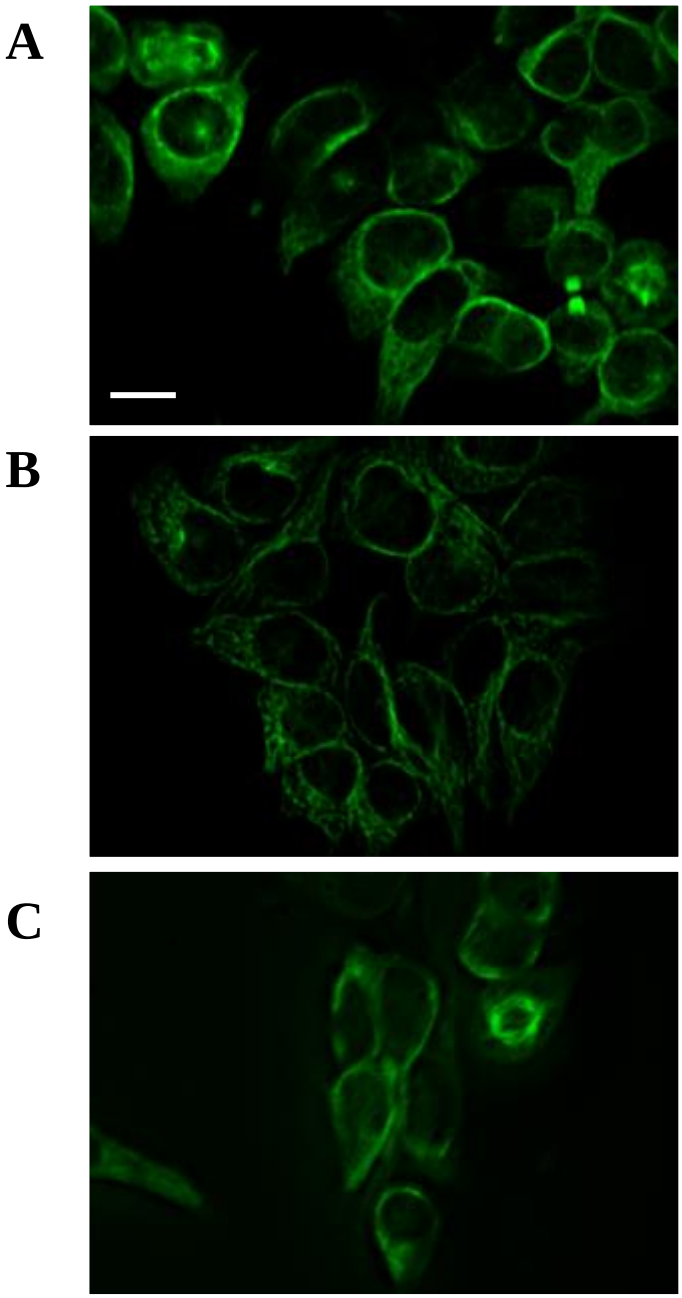

Figure 6.6 HEK2 alpha tubulin labelled cells imaged using a 60x air lens. A. 0.08mm glass. **B.** 0.5mm quartz. **C.** 1.0mm quartz. There is a direct correlation between window thickness and image resolution. The lower the thickness of window the clearer the is clearly demonstrated. Scale bar is 10 μm.

The image captured using the same thickness optical window with the 60 x water lens also gives a high level of detail however some resolution has been lost due to the lower NA (Figure 6.7C). The image captured using the 60 x air lens gives the lowest resolution, with much fainter signal of Cam-1-GFP, displaying a blur at the cell equator and weaker signal at the cell tips (Figure 8H). This is due to the lower NA of this lens and lower refractive index due to air being present between the sample and the lens. For the same reasons, the 40 x air lens further exacerbates the loss of image quality and resolution when comparing images captured using a 0.19mm glass optical window (Figure 6.8D).

In addition to highlighting the loss of resolution with lower NA lenses, these images reveal a direct correlation between NA and the level of background noise which is greatly increased when the NA of the lens is decreased. They also reaffirm the loss of resolution when increasing window thickness. Due to the small working distance of the oil lens, it is not compatible with use for imaging the pressure system. Similarly, the 60 x water lens is not suitable for use with the pressure system as during long term experiments the water droplet would evaporate. After testing a range of different window thicknesses and materials to optimise image quality and resolution when using the pressure system, it was found optical windows with a thickness of below 1.0 mm were unable to withstand pressures of 100 bar for long periods of time. Changing the material of the optical window had little effect on window durability or image quality and resolution.

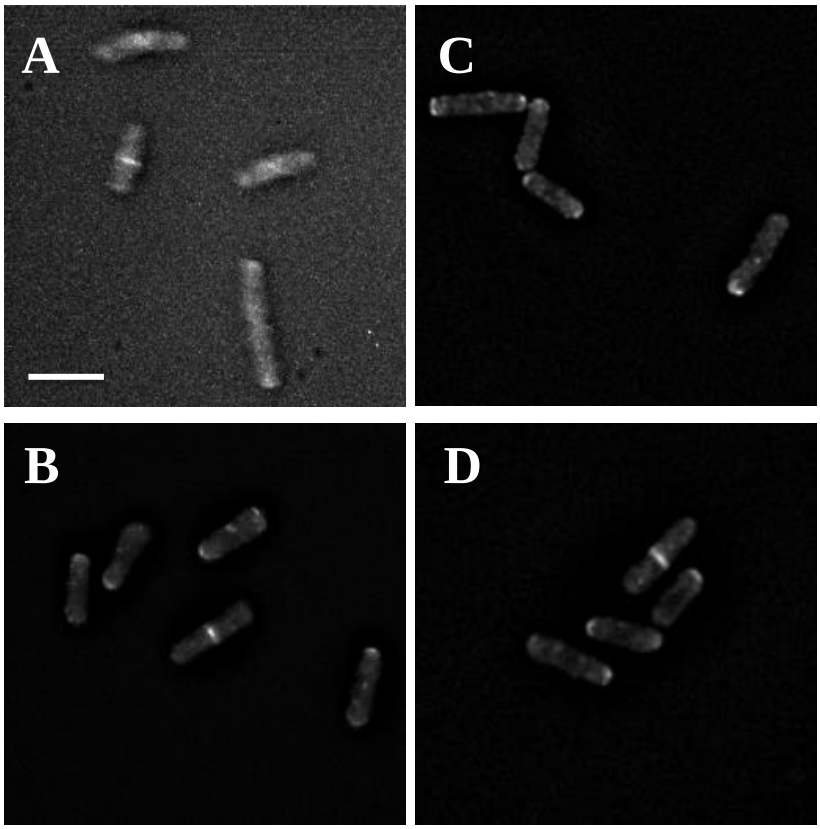

Figure 6.7 Comparison of Cam1-GFP images captured with 60 x 1.0 NA water lens (A-C) and a 60 x 1.4 NA oil lens (D). A. 0.8mm quartz. **B.** 0.5mm quartz. **C, D.** 0.19mm glass. Scale bar is 10 μm.

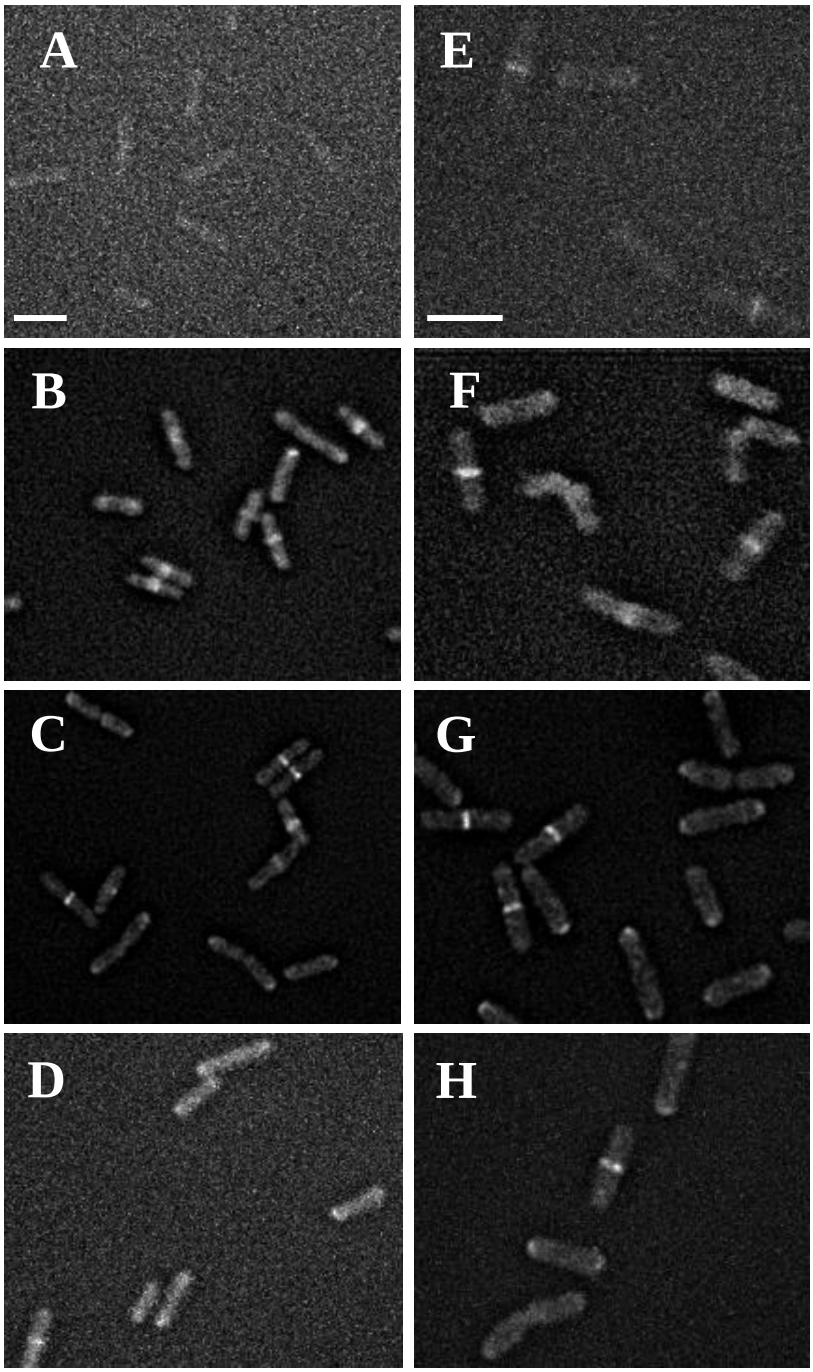

Figure 6.8 Comparison of Cam1-GFP images captured with 40 x 0.6 NA air lens (A-D) and a 60 x 0.7 NA air lens (E-H). A, E. 1mm quartz. **B, F.** 0.8mm quartz. **C, G.** 0.5mm quartz. **D, H.** 0.19mm glass. Scale bar is 10 μm.

6.3 Pressure does not cause optical aberrations

Although the choice of lens and window thickness had an effect on image resolution and imposed restrictions on fluorescent imaging of the system, the effects of pressure induced optical aberrations still needed to be defined. Optical aberrations are a distortion in the image formed by an optical system compared to the original and can arise for a number of reasons such as the placement of optical elements within a system or by the limitations of optical components such as lens shape itself. To therefore investigate the effects of pressure on optical aberrations, wild-type *S. pombe* cells were mounted onto a 1.0 mm borosilicate window. A 1.0 mm optical window could be used for this experiment as resolution of cellular detail was not required.

The cells were focused at atmospheric pressure (1 bar) and then subjected to 100 bar. Once the system reached 100 bar an image was captured and the microscope was refocused (Figure 6.9). The pressure was dropped at 10 bar intervals and an accompanying image was captured. At the end of the experiment an image was taken at 1 bar and then again once the cells had been refocused. The results clearly demonstrate that the application of pressure had a significant impact on the focus of the field in view. This is due to a flex in the window to which the cells were mounted. Once the cells were refocused however, there appeared to be no differences in the images taken at both 1 bar and at 100 bar.

As optical aberrations will always degrade image quality, these results indicate pressure has little effect on the optical system and therefore image quality, with no noticeable distortions seen in images captured under the various pressures. In order to quantify the effects of pressure on image quality, rabbit muscle fibres were mounted into the pressure system. The mean resting sarcomere length is approximately 2.4 μm, with each sarcomere an identical distance apart, therefore using rabbit muscle fibres allowed for the quantification of changes in each image.

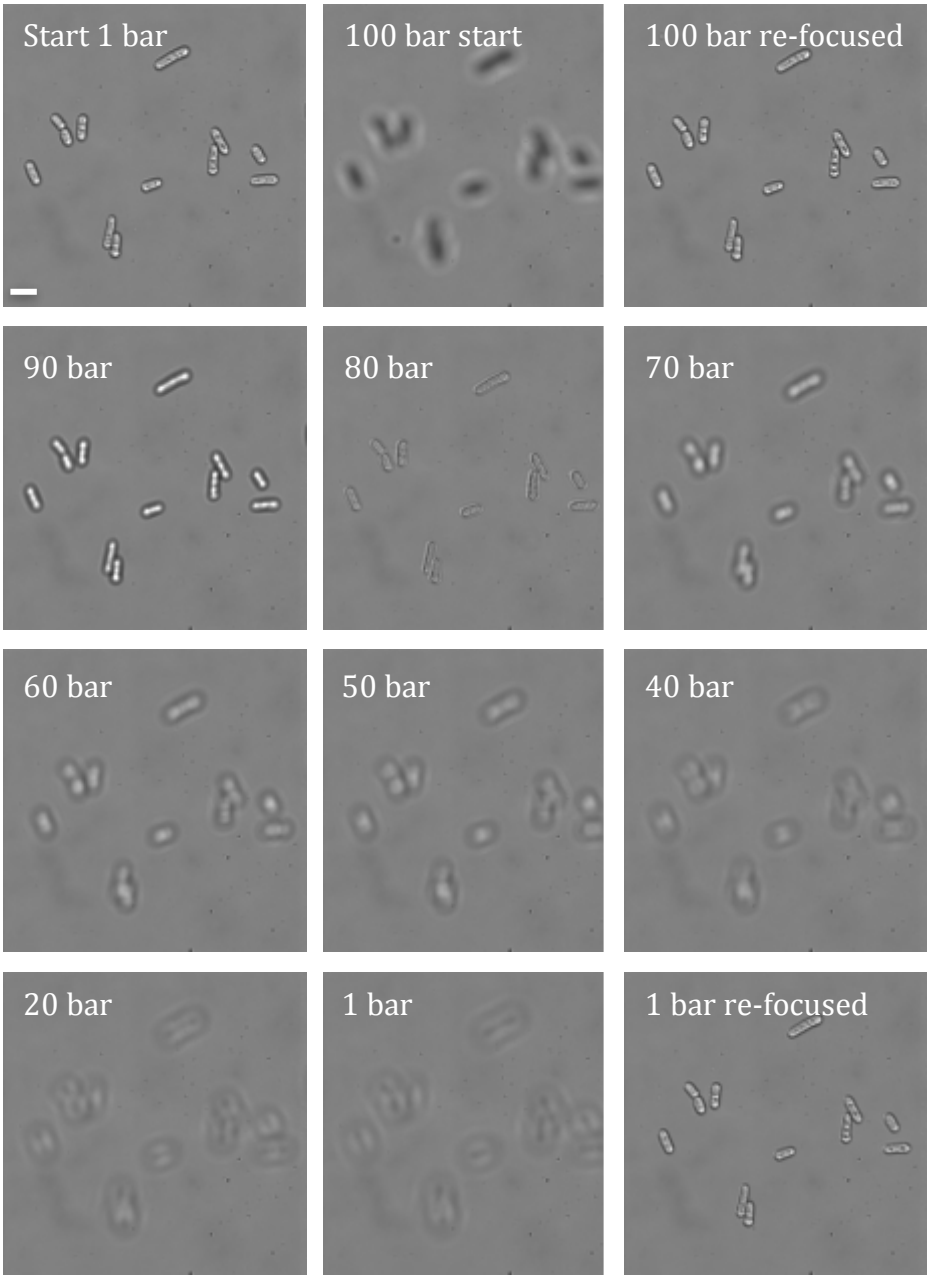

Figure 6.9 Effects of pressure on image quality using *S. pombe*. Images went out of focus as a result of changes in pressure however the images captured at 1 and 100 bar look identical indicating pressure has little effect on image quality. Scale bar is 10 µm.

Rabbit muscle fibres were mounted onto a 1 mm borosilicate optical window and subjected to 1 and 130 bar, at each point an image was captured. Images were then analysed using MicroManager software. Using a standard line tool a line profile was ascertained, computed from a line drawn at the same point across each image with the subsequent results plotted (Figure 6.10). The peaks displayed on the line profile correspond to the A band of each sarcomere and are therefore approximately equidistant apart.

Both line profiles for each image show directly comparable data. The slight shift in position of the graph at 130 bar is likely due to a slightly different starting point of the line used to analyse the image however, the distance between each sarcomere at each pressure remained constant giving confidence that the application of pressure had little effect on image quality and did not cause optical aberrations.

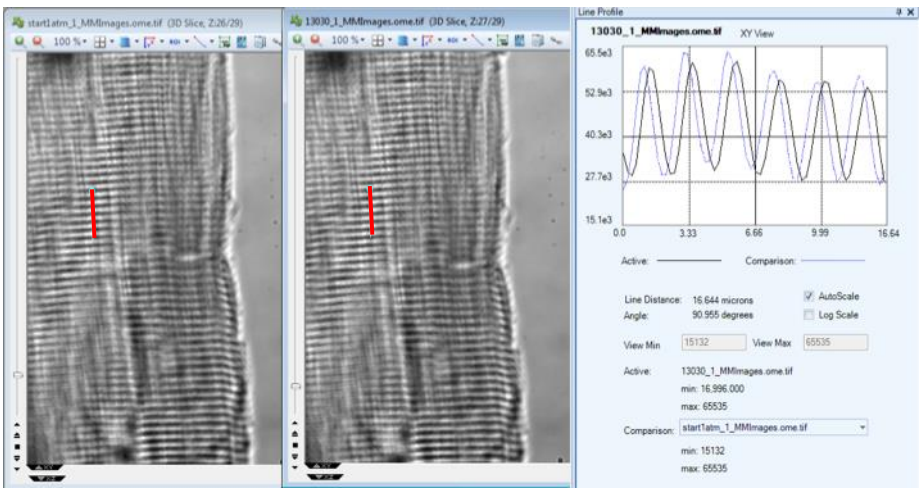

Figure 6.10 Rabbit muscle fibre line graph. A line profile, computed from a line drawn at the same point across each image -1 bar (left) and 130 bar (right) of the same rabbit muscle fibre gives near identical line traces indicating pressure has little effect on image quality.

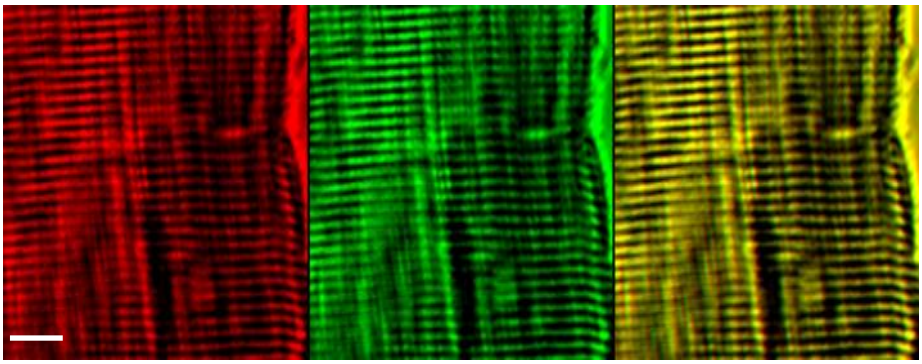

Figure 6.11 Rabbit muscle fibre image overlay. Rabbit muscle fibre images captured at 1 and 130 bar display almost complete structural overlay indicating pressure had no observable effect on image quality. Scale bar is 10 μm.

To further confirm there were no changes in sample structure an image overlay comparison was made, with the composite image confirming the application of pressure caused no apparent changes in the structure of the muscle fibres (Figure 6.11). To further test for optical aberrations in samples of a much smaller size, porcine red blood cells were mounted into the pressure chamber using a 1 mm borosilicate optical window. Porcine red blood cells measure ~ 6 μm. Images were captured at 1 and 100 bar then analysed using MicroManager software. A standard line tool was used to generate a line profile of the same red blood cell using the images captured at 1 and 100 bar. As previously seen with the rabbit muscle fibre, the application of pressure had very little impact on image quality or the structure of the sample under investigation.

The combined results of the rabbit muscle fibre and of the porcine red blood cell therefore indicate that hydrostatic pressure does not distort the image or affect the quality of image obtainable at pressures of between 100 and

130 bar on a sample of variable size. In addition, refocussing the image does not affect the quality of the resolution.

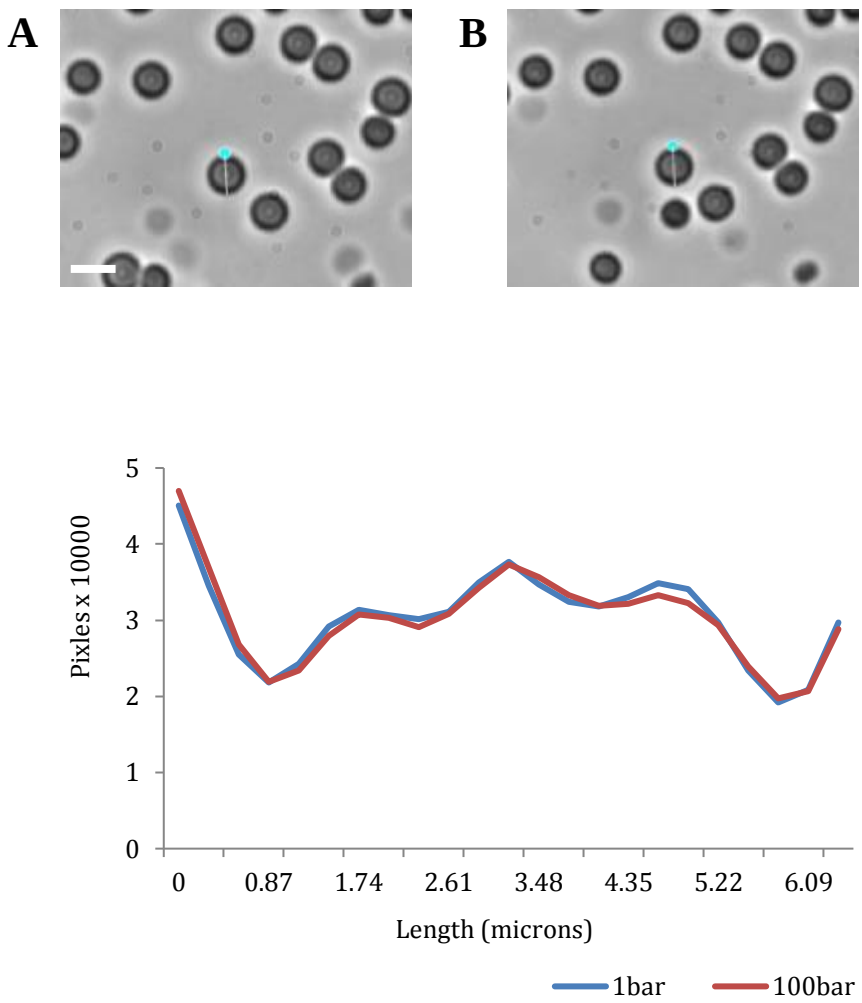

Figure 6.12 Porcine red blood cell line graph. A line profile, computed from a line drawn across the same red blood cell at A) 1 bar and B) 100 bar gives near identical line traces indicating pressure does not cause optical aberrations. Scale bar corresponds to 10 µm.

6.4 The pressure cell does not affect normal *S. pombe* growth

Although information on the possible optical aberrations the application of hydrostatic pressure might create on image capture had been acquired, it was important to understand the effects of culturing cells in the hydrostatic pressure system. To ensure any changes in growth rate were a result of hydrostatic pressure, prototroph *S. pombe* cells with a GFP tagged histone were cultured for 2 days at 25°C to a density of 2 x 10^6 (mid-log) then mounted into the 25°C chamber using lectin and kept at atmospheric pressure over a 16-hour time period (Figure 6.13).

In eukaryotes, histones are core components of the nucleosome involved in packaging and condensing DNA into chromatin (Timmermann et al. 2001). This strain of *S. pombe* was therefore chosen for initial live cell experiments in the pressure chamber, as the tagged histone allowed us to follow mitotic progression and the very bright GFP signal enabled cells to be imaged using an optical window of 1 mm thickness.

Due to the low density of the culture needed, *S. pombe* cells grown in the chamber using fresh minimal EMMG media showed an initial delay in growth, however following acclimatization to the chamber cells displayed a generation time of roughly four hours, which is in line with the typical *S. pombe* generation time at 25°C. To circumvent the need for cells to acclimatize to the chamber, *S. pombe* cells were subsequently grown in cell conditioned media. Cell conditioned media is generated by partially culturing the same strain of cells in the required media to a density of 1-2 x 10^6. Cells are then removed from the culture by centrifugation. Although the media is depleted of some components, it is enriched with cell derived material including small amounts of growth factors, proteins, cytokines and chemicals supporting growth of cells at a much lower density.

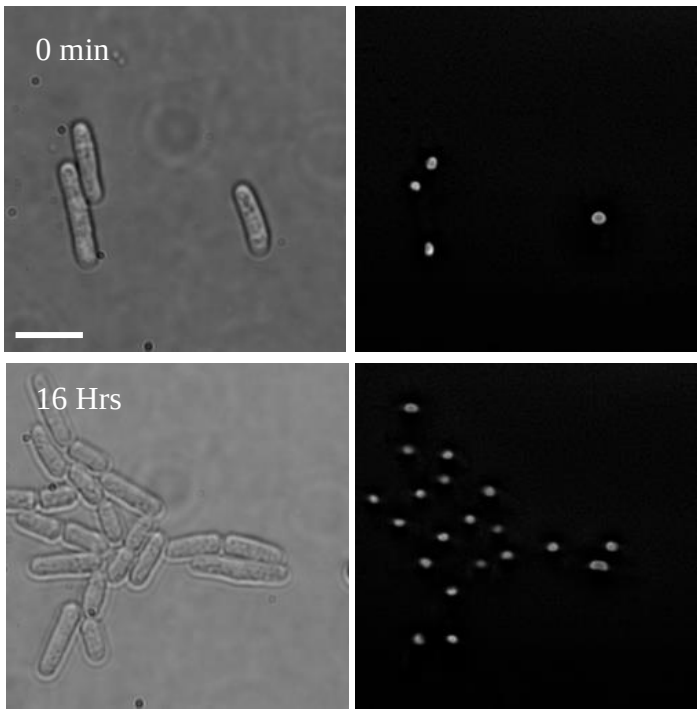

Figure 6.13 *S. pombe* cells grown in the pressure cell at 1 bar. Phase images (left) and gfp images (right) of gfp-histone tagged *S. pombe* cells cultured in the pressure cell using cell conditioned media at 25°C showed a typical generation time of 4 hours. Scale bar is 10 µm

6.4.1 *S.pombe* cells do not lose viability at 100 bar pressure

Once it was clear culturing cells within the pressure system had no effect on normal cell growth, it was possible to investigate the effects of pressure on cell viability, with confidence that any changes in growth rate were a result of exposure to hydrostatic pressures. To test cell viability a wild type prototroph *S.pombe* strain was cultured for two days at 25°C until reaching a density of 2 x 10^6. To maintain a level of consistency throughout pressure experiments only prototroph *S. pombe* strains were selected for experiments. The cells were mounted into a different type of pressure cell

that could not be imaged and kept at 25°C whilst being subjected to 100 bar for varying lengths of time. Once removed from the chamber the cells were diluted to 200 cells / 100 µl and plated onto a triplicate of EMMG agar plates. The plates were then incubated at 25°C for 5 days and the colonies formed counted. Relative viability was calculated by dividing the number of colonies obtained by the number of cells the culture was diluted to, therefore for these viability experiments the number of colonies was divided by 200 (cells / 100 µl). The results showed that cells subjected to 100 bar for up to 24 hours did not lose any viability, however previous data acquired by Agnieszka Wieckowska within the lab showed a 25% decrease in viability when subjected to 200 bar after two hours. Viability then further decreased as the exposure time increased, until a loss of 100% viability after 24 hours (Figure 6.14).

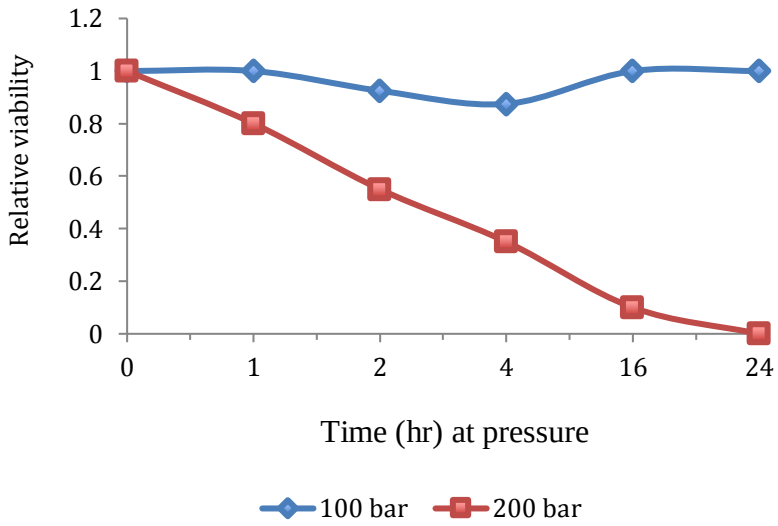

Figure 6.14 Cell Viability. Exposure of wild-type *S.pombe* cells to 100 bar for varying lengths of time has no effect on relative viability, however exposure to 200 bar decreases cell viability after 2 hours with 100% of cell viability lost after 24 hours.

6.4.2 100 bar pressure disrupts normal cell cycle progression of *S.pombe* cells

Having established the application of 100 bar had no observable effect upon fission yeast cell viability, cells were loaded into the imaging pressure cell to determine the effects pressure perturbation had on the cell cycle and proteins *in vivo.* A prototrophic *S. pombe* strain with a GFP labelled histone was selected as it produced bright fluorescent signal in addition to providing a good marker for progression of the cell cycle.

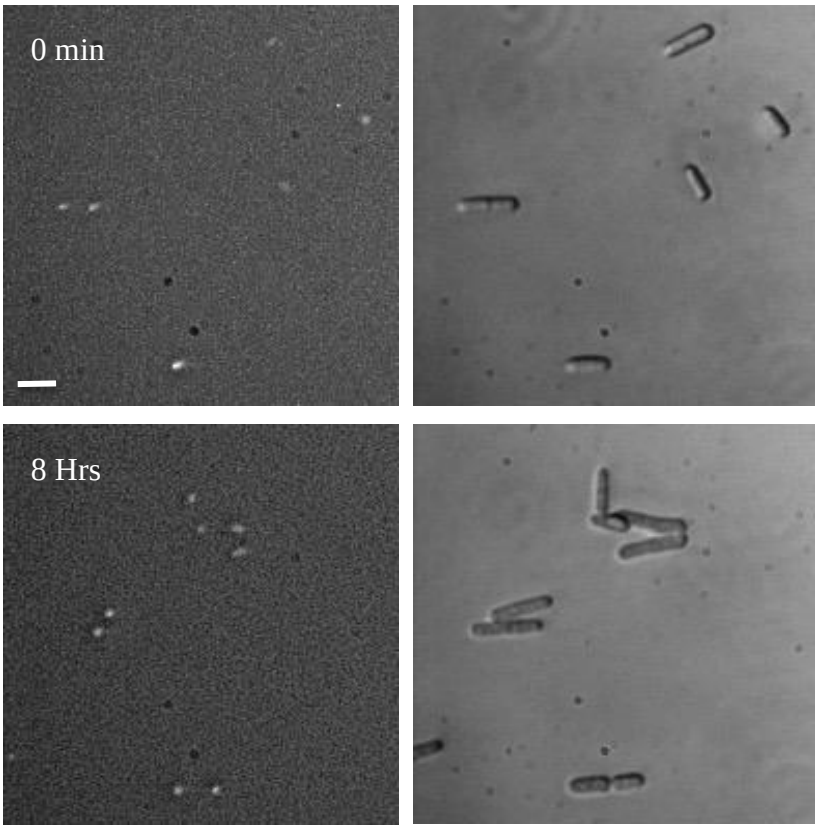

Figure 6.15 S. pombe cells grown in the pressure cell at 100 bar. *S. pombe* cells subjected to 100 bar displayed a reduced growth rate with cells becoming elongated and unable to undergo normal cell division. Cells were released to atmospheric pressure after 20 hours. Scale bar is 10 µm.

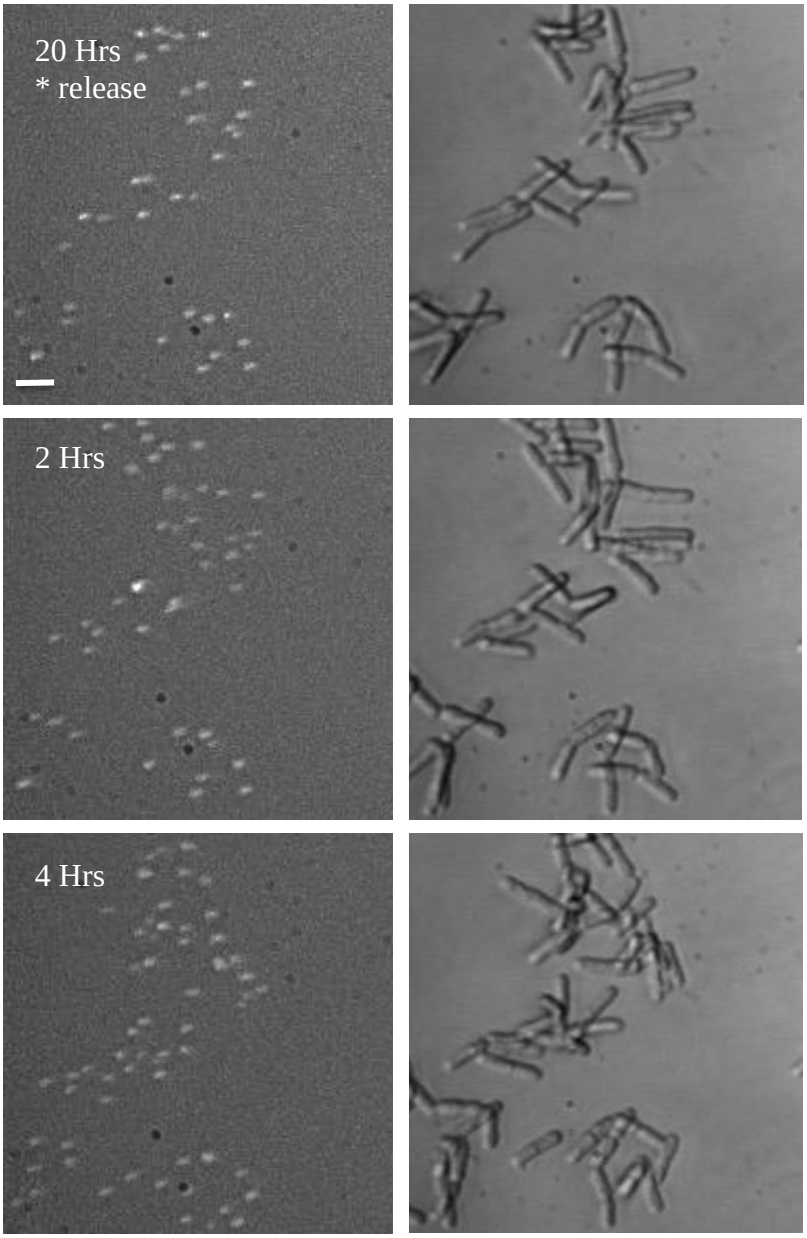

Figure 6.16 *S. pombe* cells released from 100 to 1 bar after. Following release after 20 hours at 100 bar cells appeared to quickly enter mitosis with rapid cell division seen. Cells then appeared to recover back to standard wild type phenotype. Scale bar is 10 µm.

Cells were cultured for two days until reaching mid log and mounted into the pressure cell using lectin onto a 1 mm borosilicate optical window. Cells were then subjected to 100 bar for a period of 20 hours. Exposure to the sub-lethal level of hydrostatic pressure, resulted in cells displaying an elongated phenotype, with a reduction in growth rate of approximately 50% with only a small proportion of the population able to undergo cytokinesis (Figure 6.15). Upon release of pressure to 1 bar after 20 hours, cells appeared to rapidly enter mitosis (Figure 6.16).

To quantify these results the average number of nuclei per cell was calculated throughout the experiment and compared to average cell length for 300 cells. At the beginning of the experiment cells showed a slight decrease in the number of nuclei as a few underwent cell division as a stress response to the changes in hydrostatic pressure. After ~ 3 hours, the average number of nuclei per cell started to increase as cells began to reach the critical cell length of ~ 14 µm and enter mitosis (Figure 6.17). Following cell division by some of the population the average number of nuclei decreased, however the average cell length continued to increase surpassing the *S. pombe* critical cell length until reaching a peak of 18 µm at 9.5 hours.

Since the delays were observed in both nuclear division and septation, the data suggests that the cell cycle delay was either in late G2 or in early mitosis, prior to nuclear division even though cells had exceeded the necessary length to proceed past the cell geometry-sensing checkpoint. Once cells reached a length of ~ 18 µm however, it appears mitosis and subsequently cell division were initiated. The peak at ~ 10 hours in cell length coincides with a peak in average number of nuclei as cells underwent mitosis and cell division, however the average cell length does not fall below ~ 16 µm, indicating cells were unable to recover to a wild-type phenotype. Upon release after 20 hours the data shows the average number of nuclei almost instantaneously increase along with a rapid decrease in average cell length.

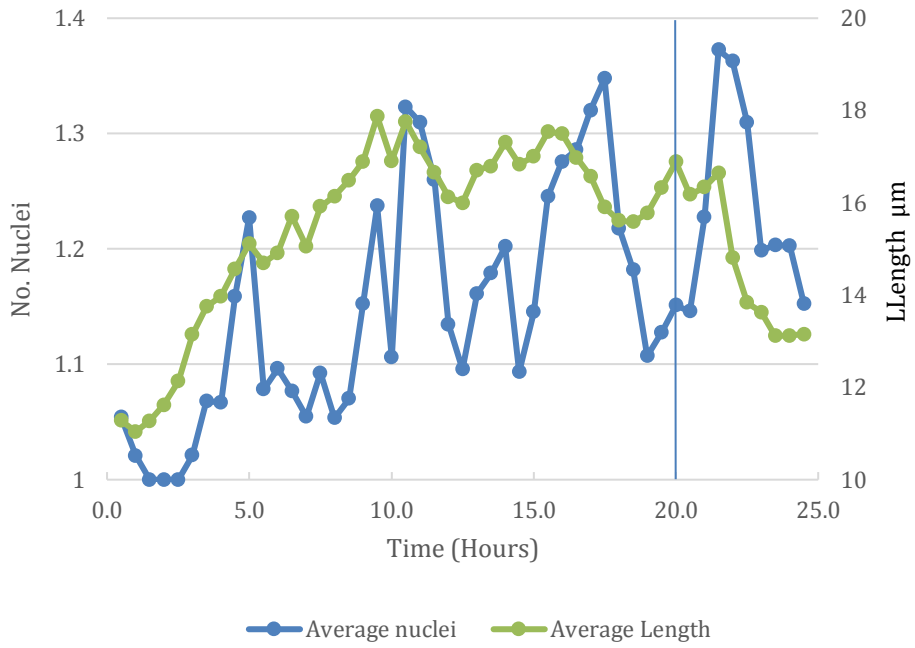

Figure 6.17 Comparing the average cell length of *S. pombe* with number of nuclei over time at 100 bar. Average cell length increases with delayed cell division. Following release after 20 hours at 100 bar cells appeared to quickly enter mitosis with rapid cell division resulting in a decrease in average cell length.

The continual rise in average number of nuclei even after a fall in average cell length suggests that daughter cells that were larger than the critical size were also able to rapidly re-enter mitosis without going through the cell cycle size-phase, resulting in a further drop in average cell length. Although the data indicates exposure to 100 bar of hydrostatic pressure does not surcease the cell cycle in all cells it clearly causes a delay in mitosis and cytokinesis. After release to atmospheric pressure however, these changes appear to be fully reversible, with cells quickly recovering back to a typical wild-type phenotype after only 3 hours. As the cells were growing in

exponential phase when mounted into the chamber, the pattern of mitosis and change in cell length seen over the duration of the experiment suggests the application of 100 bar of pressure induced a potential circadian rhythm-like effect with cells beginning to display a synchronized cell cycle.

6.5 100 bar induces pseudohyphal growth in *Candida albicans*

As the application of 100 bar had a significant impact on the fission yeast cell cycle, *C. albicans* was used to further explore whether these effects were conserved among different species of yeast. A wild type *C. albicans* strain was cultured for two days until reaching mid log. The cells were then mounted into the pressure cell using lectin and subjected to 100 bar for a period of 22 hours. A previous experiment culturing *C. albicans* in the pressure cell at 1 bar revealed no changes in growth with cells displaying a typical generation time of roughly 2 hours, therefore giving confidence that any changes in growth rate were a result of hydrostatic pressure.

Unlike *S. pombe, C. albicans* is dimorphic and can grow in a number of different morphological forms under different environmental conditions (Whiteway & Bachewich 2007). Standard culture conditions favour the yeast form of the organism, which reproduce by budding however a change in physiological conditions such as temperature or pH can result in the development of pseudohyphae or true hyphael growth (Sudbery 2011). Pseudohyphae are elongated cells which have constriction sites of septation, appearing as filamentous cell chains with both unipolar, bipolar and axial budding patterns where as true hyphae have no constrictions at the site of septation and form long tube like filaments with completely parallel sides (Sudbery 2011).

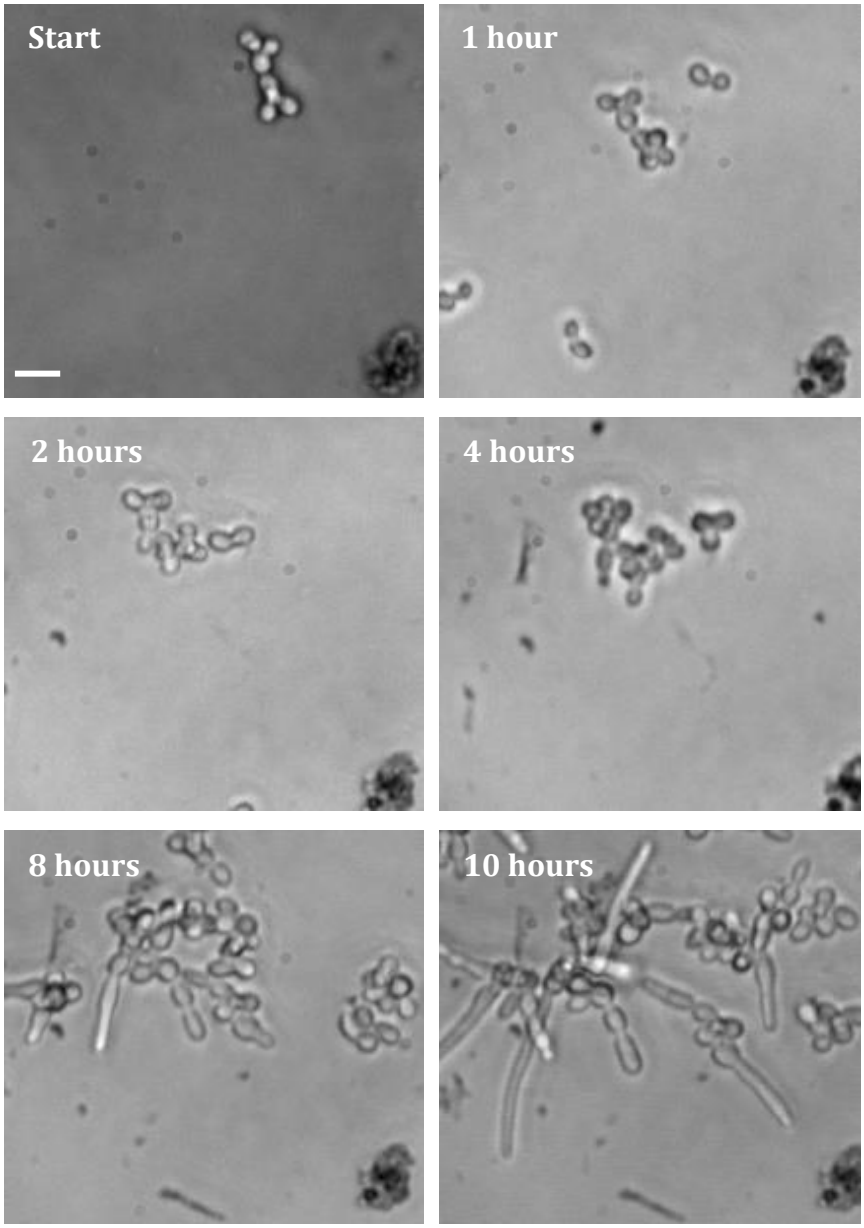

Figure 6.18 *C. albicans* cells grown in the pressure cell at 100 bar. Under standard culture conditions, *C. albicans* reproduces by budding. *C. albicans* cells subjected to 100 bar pressure however displayed a severe delay in the cell cycle with cells switching to pseudohyphal growth. Scale bar is 10 µm.

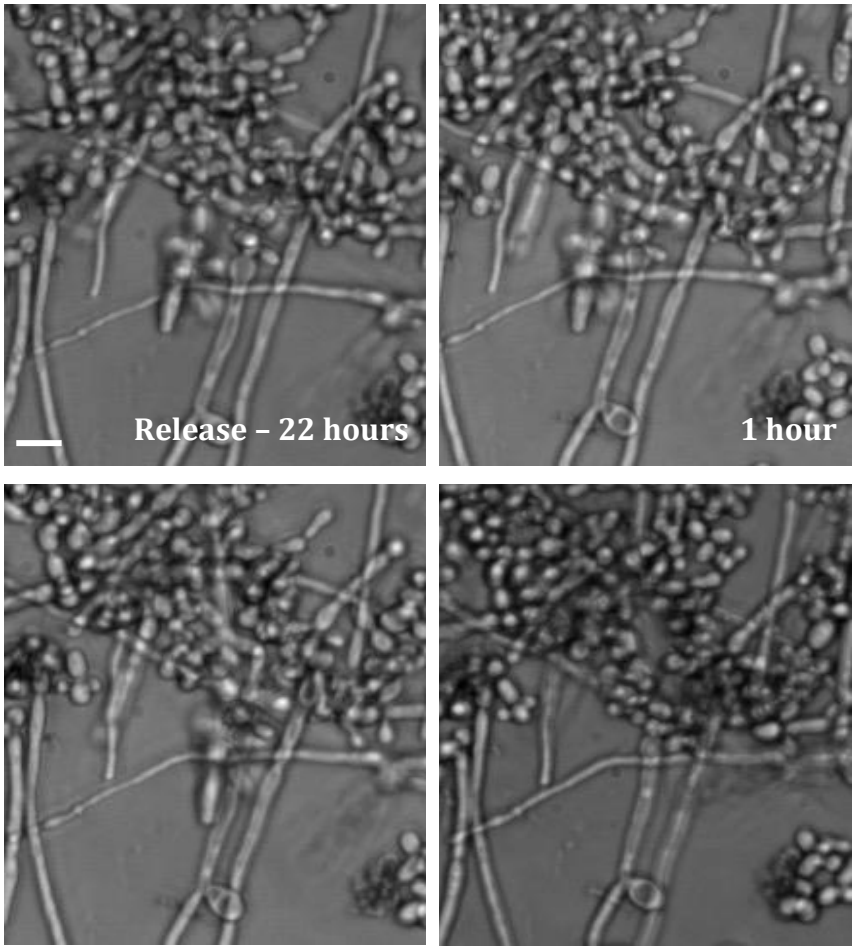

Figure 6.19 Release of *C. albicans* cells grown in the pressure cell at 100 bar. Once released back to atmospheric pressure after 22 hours at 100 bar, *C. albicans* cells appeared to slowly recover back to a typical generation time. Scale bar is 10 µm.

C. albicans grown in the pressure cell at atmospheric pressure displayed the standard yeast form of growth, reproducing by budding. Cells grown at 100 bar however, showed a severe delay in budding as well as a switch in morphology to filamentous growth resulting in the formation of

pseudohyphae (Figure 6.18). In addition to switching the growth form, cells were also producing chlamydospores; large spherical, enigmatic thick walled cells (Whiteway & Bachewich 2007). Although the biological function of chlamydospores still remains unknown, they typically form under suboptimal growth conditions and have been proposed to allow for survival in harsh environmental conditions (Staib & Morschhauser 2007). Unlike *S. pombe*, pressurized *C albicans* cells appeared to have a slower response to hydrostatic pressure and also took longer to recover normal growth indicating that even after cells had been relieved from the pressure stress, they were still suffering from metabolic changes and were responding to this stress (Figure 6.19).

6.6 Discussion

Prototype I of the pressure cell provided a proof of concept pressure system which enabled the rapid modulation of hydrostatic pressure upon biological samples of varying size. Although the initial design contained a number of disadvantages, it highlighted numerous specification upgrades required to develop a real working system in Prototype II. Prototype II established the feasibility of the experimental approach, providing a more functional system that enabled the rapid modulation of hydrostatic pressure within a more easily sealed and user- friendly system, however a number of limitations remained.

One major disadvantage of the current pressure system is the restriction on the working distance of the various lenses when using fluorescent microscopy. Optical windows with a thickness of less than 1 mm were found to be unable to withstand pressures of ~100 bar, the pressure required to perturb the cell cycle, however increasing the thickness of the optical window resulted in a substantial loss in the quality and resolution of the fluorescent images captured. Even when using much larger cells with

clearer structures such as HEK2 cells, a significant level of detail and resolution was lost between the 0.5 mm and 1 mm window.

To try and circumvent this issue, optical windows made from different materials were tested, however no effect on image quality, window durability or optical properties were seen. Long distance lenses were used to try and overcome the issue of reduced image quality with thicker windows, however a higher working distance of the lens resulted in a decreased numerical aperture, this increased the signal to noise ratio further worsening the quality of the images obtainable. Thinner metal disks were next used to try and compensate for the thicker optical windows but this had little effect on optimising the system as metal disks with a thickness of less than 0.8 mm could not withstand the pressures of the system and would quickly bend out of shape or the optical window would cause an indent in the disk making it ineffectual at sealing the system in subsequent experiments.

Reducing the size of the hole in the centre of the disk to give it more support also had little effect on disk durability. As sub-lethal pressures of 100 bar did not affect *S. pombe* viability but readily perturbed the cell cycle, the current system limits real time fluorescent imaging to cells which express proteins with bright fluorescent signal. Although the method of imaging was limited by the system, the application of hydrostatic pressure was shown to not cause any significant optical aberrations, with image quality equivalent at atmospheric pressure and pressures over 100 bar. The system can therefore be used to phase image cells in real time, as thicker optical windows can be used and subsequently higher pressures since fluorescent cellular detail is not required.

In addition to optical limitations, the pressure cell still contained a number of design flaws. Although the original glue was inadequate at holding the optical windows in place, it was chosen because its thickness could easily be adjusted and once the experiment was finished it could simply be removed using acetone. Araldite however, is difficult to remove once set as it requires soaking in methanol for a number of hours. In addition, it is difficult

to change the consistency as it requires a ratio mix of two compounds. If an optical window shattered during an experiment, the construction of the current system does therefore not allow for the components to be changed quickly causing long experimental delays.

The upgraded method of sealing the system using a nitrile O ring on the newly designed metal flange successfully removed the difficulty of using the custom-made tools, however after use during a few experiments, pressure within the system led to the flange bending out of shape, making it ineffectual at sealing the system in subsequent experiments. As the flange was a large stainless steel custom made component of the system, it was very expensive to replace after only a few experiments. During higher pressure experiments the six screws that secured the flange were found to be inadequate at holding it in place, leading to the screws breaking and the flange popping out of the cell. Although this method of sealing the system had a number of draw backs, it was able to successfully hold the system at pressure for a number of hours with only minor fluctuations, therefore once experiments were running, little user intervention was required.

Although the reduction in flow rate due to a better seal of the system reduced the build-up of sugars coming out of the media solution, having the media flow through the pumps for long periods of time still resulted in a build-up of syrup around the valves making it an ongoing issue. Having media pump through the system for long periods of time at 25°C also meant the system was very difficult to keep sterile during experiments, with contamination a frequent problem. In the current design, the hydrostatic pressure within the system is monitored by the HPLC pump which feeds back into the computer software, therefore if the pump is not correctly calibrated the pressure read out could be wrong. Installing a calibrated mechanical pressure gauge between the HPLC pump and the chamber would help resolve this issue, however it would add another component into the system increasing the difficulty of sterile experiments. The custom-made software currently used to monitor and control the HPLC pump is very basic

and often crashed during long term experiments therefore it would require upgrading for use with subsequent designs.

During preliminary pressure perturbation experiments, it was found exposure of *S. pombe* and *C. albicans* to increased hydrostatic pressures of ~ 100 bar for extended periods of time resulted in reduced growth rates and a delay in cell division. *S. pombe* cells expressing the GFP-tagged histone showed a clear delay in both nuclear division and septation, indicating the cell cycle delay is in late G2 or in early mitosis prior to nuclear division. The constraints of the current system meant imaging of GFP labelled histone *C. albicans* was not possible due to the weak fluorescent signal, however in the yeast S. *cerevisiae,* it is thought an extended G2 phase is responsible for the elongated growth of pseudohyphal buds like those seen in the culture of *C. albicans*. The data therefore indicates the application of hydrostatic pressure results in a delay in G2 in both *S. pombe* and *C. albicans* however how this occurs, still remains unknown.

The mechanisms by which the cell cycle can be modulated in response to stress have been extensively studied, revealing a wide spectrum of checkpoints the cell must complete for entry into mitosis including a DNA integrity, cytokinesis and cell size check point. Damage induced from exposure to hydrostatic pressure may lead to the simultaneous activation of more than one of these checkpoints therefore causing a cell cycle delay. Further investigations using *S. pombe* strains with deleted proteins central to cell cycle checkpoints such as *rad3*$^{+}$, *wee1*$^{+}$ or *clp1*$^{+}$ could potentially reveal the cell cycle stages targeted by pressure stress without the need to use fluorescently labelled proteins. Similarly, *S. pombe* strains with deletion of *sty1*$^{+}$ would allow investigation into cell cycle progression in response to environmental influences.

Deletion of the highly conserved kinase Rad3 would prevent cells from arresting at the G2/M transition as a result of damaged or un-replicated DNA (Alao & Sunnerhagen 2008). Similarly, deletion of the kinase Wee1 would allow cells to bypass the cell size checkpoint due to the loss of Wee1

mediated inactivation of Cdk1. Deletion of Clp1 or Sty1 would allow further investigation into the cytokinesis checkpoint and cellular responses to various environmental stresses respectively (Wolfe et al. 2006; Forsburg 1991). Although the system potentially offers insight on the adaptation of life to high pressure environments, the limitations on fluorescent microscopy technique's make the interrogation of many molecular and cellular interactions difficult.

Alternatively, as certain cytoskeletal polymers such as those formed from actin and tubulin are more susceptible to pressure changes than others, the application of hydrostatic pressure could have resulted in protein denaturation or protein dissociations thereby abolishing certain intracellular structures required for cell division. It has previously been reported that exposure of *S. pombe* and *Candida tropicalis* to increased hydrostatic pressure of ~ 1000 bar for short periods of time resulted in reduced growth rates, abnormal distribution of microtubules and microfilaments (Sato et al. 1996). As GFP-tagged histone cells showed a clear delay in nuclear division, disruption of the cell cycle could be a consequence of the abnormal distribution and formation of microtubules.

This is also supported by the data acquired from cells released to atmospheric pressure from 100 bar after several hours as some *S. pombe* cells underwent consecutive cell divisions, indicating cells contained the necessary proteins required to proceed through the cell cycle checkpoints but were unable to complete mitosis. Some denatured proteins are able to return to the original state when the denaturant is removed, therefore if hydrostatic pressure causes disruption of microtubules, it is likely the perturbation is fully reversible as the rate of recovery was rapid with cells appearing to instantaneously trigger entry to mitosis upon release from pressure. Although there was a significant delay in the *S. pombe* cell cycle at 100 bar, some cells were still able to undergo mitosis. This could be due to an accumulation of proteins forcibly pushing the cell through certain cell cycle activated check points and into mitosis or it could be due to cells

developing barotolerance, therefore adapting to the environmental changes enabling cells to survive and grow in higher pressure environments.

6.7 Conclusions

Pressure is an equally important thermodynamic parameter as more conventional methods such as temperature and pH, however pressure studies using fluorescently labelled proteins are considerably less frequent in the literature due to the difficulties associated with pressure experiments. The main aims of this project were to enhance a hydrostatic pressure imaging system which gave better image resolution, higher photon capture and higher speed of image collection, producing a system which could be readily used by other research groups.

Although the current design of the hydrostatic pressure chamber enables rapid changes in pressure and real time imaging of cells during pressure perturbation studies with minimal optical aberrations, the limitations imposed by the system currently make it largely incompatible with fluorescent microscopy. For this pressure system to become a reliable, fully functional user-friendly system additional modifications to the mechanism by which it is sealed, pressure monitored and constructed are required. It could then be used to explore the full potential of rapid pressure changes on a range of cell types from prokaryotes to higher eukaryotes.

Chapter 7: Discussion

7.1 Introduction

During the course of this study a variety of molecular and biochemical techniques were used to study various components of the actin cytoskeleton using the two model organisms *Caenorhabditis elegans* and *Schizosaccharomyces pombe.* In addition, a novel hydrostatic pressure imaging system was developed which aimed to allow fluorescently labelled protein dynamics to be captured in real time within a live cell context.

7.2 Characterisation of myosin I

In order to characterise the *C. elegans* class I myosins HUM-1 and HUM-5, fluorescent protein fusions were generated for expression and localisation studies. In addition, phenotyping analysis was undertaken using strains in which the endogenous genes had been disrupted. High resolution confocal microscopy revealed HUM-1 was expressed in a variety of tissues including the chemo/ odour sensilla, pharyngeal-intestinal valve, intestinal rectal valve, reproductive system and the phasmid/PHC sensilla. Conversely, HUM-5 was expressed exclusively in the PVD, FLP and CEP neurons.

No co-localisation of HUM-1 or HUM-5 could be seen in any tissues or structures, indicating each gene has a different anatomical focus, therefore supporting the hypothesis: HUM-1 and HUM-5 have discrete localisations. Although both proteins are expressed in clearly defined tissues, the plasmid born copies of each gene are under the control of their own promoters therefore it is unlikely expression of these plasmids is as tightly regulated as the endogenous gene. This is due to the lack of additional regulatory mechanisms such as chromatin remodelling which is bypassed by the plasmid DNA. Western blot analysis would enable a comparison of expression levels of the plasmid HUM-1 proteins to the endogenous protein.

Phenotyping assays revealed HUM-1 and HUM-5 are non-essential to *C. elegans* viability however disruption of HUM-1 causes a reduction in maximal brood size with delayed embryo release, whereas disruption of HUM-5 had no observable effects. Introduction of a HUM-1 transgene was able to rescue the brood phenotype, confirming the protein was functional *in vivo* and the reduction of brood was HUM-1 dependent. Additional studies of the reproductive system would allow us to determine whether the effect was dependent on the hermaphrodite self-sperm or due to loss of function within the tissues of the reproductive system. Although the exact function of HUM-1 and HUM-5 remains to be elucidated, based on the expression and function of other Myo1e and Myo1d homologs it is likely HUM-1 is involved in endocytosis and actin membrane dynamics and HUM-5 plays an important role in the membrane recycling pathway and neurodevelopment, supporting the hypothesis: HUM-1 and HUM-5 have discrete functions.

To next explore the impact of a conserved phosphorylation event on myosin Ie function, mutations were introduced into a conserved serine residue present in the *C. elegans* and *S. pombe* homologs: HUM-1 and Myo1 respectively. The first mutation prevented phosphorylation whereas the second acted as a phosphorylation mimic. Each protein was then fused with a fluorescent marker to allow for localisation studies.

Both mutations altered the subcellular localisation of HUM-1 to varying degrees, indicting tissue-specific phosphorylation fine tunes protein activity to fulfil the specific needs of each tissue. Introduction of the HUM-1S734A or HUM-1S734D transgenes were unable to rescue the brood phenotype suggesting both forms of the protein are required for correct functioning within the reproductive system. Similarly, both mutations abolished Myo1 membrane associations therefore Myo1 localisation appeared entirely cytoplasmic. This was a surprising result given phosphorylation often results in a conformational change in the structure of a protein, causing it to become activated or deactivated therefore it was expected the two mutations would have dissimilar effects. The similar results could however be due to the

aspartic acid failing to mimic phosphorylation, therefore giving the same results as the non-phosphorylated form. In addition, expression of Myo1S782A or Myo1S782D also induced spore formation although spores were non-viable, lacking correct DNA content. The combined results from Myo1 and HUM-1 studies therefore support the hypotheses: phosphorylation of this serine residue is required for protein localisation and protein function.

7.3 Characterisation of fission yeast Cdc8

In order to explore the impact of fluorescent protein fusions and the temperature sensitive mutations *cdc8-110* and *cdc8-27*, upon the the stability and function of fission yeast tropomyosin, Cdc8, a combined *in vitro* and *in vivo* study was undertaken. *In vitro* results for *cdc8-110* and *cdc8-27* mutants revealed both proteins had a two-step thermal unfolding transition, lower than that of wild-type Cdc8. Although the majority of each protein will unfold at lower temperatures the upper unfolding transition is higher than wild-type Cdc8, therefore it is possible the proteins can remain partially folded within the cell whilst kept at restrictive temperatures.

In vitro results also revealed addition of a fluorophore tag to the amino- or carboxyl- terminus of Cdc8 does not impact protein stability, however amino- terminal fusions mimic acetylation whereas carboxyl- terminal fusions abolished Cdc8 polymerization and functionality. *In vivo* analysis revealed addition of the fluorophore tag to the amino- terminus had little effect on Cdc8 activity with cells able to form contractile rings and undergo cell division however fusion to the carboxyl- terminus abolished Cdc8 polymerisation, localisation and functionality.

7.4 Development of a hydrostatic pressure imaging system

Although this project was largely successful in developing a system which enabled rapid changes in pressure and real-time imaging of cells during pressure perturbation studies, the limitations imposed by the system made it largely incompatible with fluorescent microscopy.

Preliminary data showed the application of 100 bar of pressure induced a cell cycle delay in both *S. pombe* and *C. albicans,* likely in late G2 or in early mitosis prior to nuclear division. *S. pombe* cells appeared elongated but recovered rapidly once released from pressure whereas *C. albicans* switched to pseudohyphal growth and displayed an extended recovery period.

If optimized the hydrostatic pressure imaging system could be a useful tool to perturb the cell cycle with fully reversible effects allowing long term imaging of live cells, however the materials available for optical windows at this time make it unlikely to be used in conjunction with fluorescent imaging.

7.5 Summary

Overall this study has made several significant contributions to furthering our knowledge of the actin cytoskeleton and its various components. It has increased our understanding of the *C. elegans* class I myosins, which since discovery have remained largely unexplored (Baker et al. 1997). It has also given more insight into regulation of myosin Ie activity via phosphorylation of a conserved serine residue found within the TH1 domain.

This study has also provided insight into the basis of temperature sensitivity in the fission yeast *cdc8-110* and *cdc8-27* mutants as well as emphasising the effects of fluorescent protein labels on protein function, highlighting interesting areas for further investigation.

In addition, the methodical approach to developing a novel hydrostatic pressure imaging system has identified several important factors which limit the use of the system with fluorescent microscopy. Preliminary data revealed a conserved cell cycle delay due to hydrostatic perturbations which was fully reversible highlighting the *in vitro* advantages of the system.

Bibliography

Aamodt, E., 2006. *The Neurobiology of C. elegans*, Academic Press.

Akasaka, K. & Matsuki, H., 2015. *High Pressure Bioscience* K. Akasaka & H. Matsuki, eds., Dordrecht: Springer.

Alao, J.P. & Sunnerhagen, P., 2008. Rad3 and Sty1 function in Schizosaccharomyces pombe: an integrated response to DNA damage and environmental stress? *Molecular microbiology*, 68(2), pp.246–254.

Albeg, A. et al., 2011. C. elegans multi-dendritic sensory neurons: Morphology and function. *Molecular and Cellular Neuroscience*, 46(1), pp.308–317.

Alberts, B. et al., 2014. *Molecular Biology of the Cell*, Garland Science.

Anokye-Danso, F. et al., 2008. Transcription Factors GATA/ELT-2 and Forkhead/HNF-3/PHA-4 Regulate the Tropomyosin Gene Expression in the Pharynx and Intestine of Caenorhabditis elegans. *Journal of molecular biology*, 379(2), pp.201–211.

Athanasiou, K.A. et al., 2015. Harnessing biomechanics to develop cartilage regeneration strategies. *Journal of biomechanical engineering*, 137(2), p.020901.

Attanapola, S.L., Alexander, C.J. & Mulvihill, D.P., 2009. Ste20-kinase-dependent TEDS-site phosphorylation modulates the dynamic localisation and endocytic function of the fission yeast class I myosin, Myo1. *Journal of cell science*, 122(Pt 21), pp.3856–3861.

Bae, Y.-K. & Barr, M.M., 2008. Sensory roles of neuronal cilia: cilia development, morphogenesis, and function in C. elegans. *Frontiers in bioscience : a journal and virtual library*, 13, pp.5959–5974.

Baker, J.P. & Titus, M.A., 1997. A family of unconventional myosins from the nematode Caenorhabditis elegans. *Journal of molecular biology*, 272(4), pp.523–535.

Balasubramanian, M., Helfman, D. & Hemmingsen, S., 1992. A new tropomyosin essential for cytokinesis in the fission yeast S.pombe. *Nature*, 360, pp.1–4.

Balny, C., Masson, P. & Heremans, K., 2002b. High pressure effects on biological macromolecules: from structural changes to alteration of cellular processes. *Biochimica et biophysica acta*, 1595(1-2), pp.3–10.

Barciszewski, J. et al., 1999. The role of water structure in conformational changes of nucleic acids in ambient and high-pressure conditions. *European journal of biochemistry / FEBS*, 260(2), pp.293–307.

Bargmann, C., 2006. Chemosensation in C. elegans. *WormBook : the online review of C. elegans biology*.

Bartlett, D.H., 2002. Pressure effects on in vivo microbial processes. *Biochimica et biophysica acta*, pp.367–381.

Barua, B., 2013. Periodicities designed in the tropomyosin sequence and structure define its functions. *Bioarchitecture*, 3(3), pp.51–56.

Bähler, M. et al., 1994. Rat myr 4 defines a novel subclass of myosin I: identification, distribution, localisation, and mapping of calmodulin-binding sites with differential calcium sensitivity. *The Journal of cell biology*, 126(2), pp.375–389.

Bement, W.M. & Mooseker, M.S., 1995. TEDS rule: A molecular rationale for differential regulation of myosins by phosphorylation of the heavy chain head. *Cell motility and the cytoskeleton*, 31(2), pp.87–92.

Benesh, A.E. et al., 2012. Expression and localisation of myosin-1d in the developing nervous system. *Brain research*, 1440, pp.9–22.

Berg, J.S., Powell, B.C. & Cheney, R.E., 2001. A millennial myosin census. *Molecular biology of the cell*, 12(4), pp.780–794.

Bird, A.F. & Bird, J., 2012. *The Structure of Nematodes*, Academic Press.

Bounoutas, A. & Chalfie, M., 2007. Touch sensitivity in Caenorhabditis elegans. *Pflügers Archiv - European Journal of Physiology*, 454(5), pp.691–702.

Brenner, S., 1974. The genetics of Caenorhabditis Elegans. *Genetics*, 77, pp.1–24.

Bridgman, P.C., 2004. Myosin-dependent transport in neurons. *Developmental Neurobiology*, 58(2), pp.164–174.

Brooks, A. & Johnson, T.E., 1991. Genetic specification of life span and self-fertility in recombinant-inbred strains of Caenorhabditis elegans. *Heredity*, 67(1), pp.19–28.

Brown, J.H., 2010. How sequence directs bending in tropomyosin and other two-stranded alpha-helical coiled coils. *Protein Science*, 19(7), pp.1366–1375.

Brown, J.H. et al., 2001. Deciphering the design of the tropomyosin molecule. *Proceedings of the National Academy of Sciences of the United States of America*, 98(15), pp.8496–8501.

Bumbarger, D.J. et al., 2009. Three-dimensional reconstruction of the amphid sensilla in the microbial feeding nematode, Acrobeles complexus(nematoda: Rhabditida). *The Journal of Comparative Neurology*, 512(2), pp.271–281.

C. elegans Sequencing Consortium, 1998. Genome sequence of the nematode C. elegans: a platform for investigating biology. *Science (New York, N.Y.)*, 282(5396), pp.2012–2018.

Carlier, M.F. et al., 1997. Actin depolymerizing factor (ADF/cofilin) enhances the rate of filament turnover: implication in actin-based motility. *The Journal of cell biology*, 136(6), pp.1307–1322.

Caterina, M.J. & Julius, D., 1999. Sense and specificity: a molecular identity for nociceptors. *Current Opinion in Neurobiology*, 9(5), pp.525–530.

Chalfie, M. et al., 2014. Assaying mechanosensation. *WormBook : the online review of C. elegans biology*.

Chen, H., Bernstein, B.W. & Bamburg, J.R., 2000. Regulating actin-filament dynamics in vivo. *Trends in biochemical sciences*, 25(1), pp.19–23.

Cheng, J., Grassart, A. & Drubin, D.G., 2012. Myosin 1E coordinates actin assembly and cargo trafficking during clathrin-mediated endocytosis. *Molecular biology of the cell*, 23(15), pp.2891–2904.

Cho, A. et al., 2016. An Atypical Tropomyosin in Drosophila with Intermediate Filament-like Properties. *Cell reports*, 16(4), pp.928–938.

Chung, B.-M., Rotty, J.D. & Coulombe, P.A., 2013. Networking galore: intermediate filaments and cell migration. *Current opinion in cell biology*, 25(5), pp.600–612.

Clay, M.R. & Sherwood, D.R., 2015. Basement Membranes in the Worm: A Dynamic Scaffolding that Instructs Cellular Behaviors and Shapes Tissues. *Current topics in membranes*, 76, pp.337–371.

Coluccio, L.M., 2007. *Myosins*, Springer Science & Business Media.

Cooper, G.M., 2000. *The Cell*, Sinauer Associates.

Cooper, G.M. & Hausman, R.E., 2009. *The Cell*, Sinauer Associates Incorporated.

Corsi, A.K., Wightman, B. & Chalfie, M., 2015. A Transparent Window into Biology: A Primer on Caenorhabditis elegans. *Genetics*, 200(2), pp.387–407.

de Forges, H., Bouissou, A. & Perez, F., 2012. The International Journal of Biochemistry & Cell Biology. *International Journal of Biochemistry and Cell Biology*, 44(2), pp.266–274.

Dixon, S.J. & Roy, P.J., 2005. Muscle arm development in Caenorhabditis elegans. *Development (Cambridge, England)*, 132(13), pp.3079–3092.

Doberstein, S.K. & Pollard, T.D., 1992. Localization and specificity of the phospholipid and actin binding sites on the tail of Acanthamoeba myosin IC. *The Journal of cell biology*, 117(6), pp.1241–1249.

Dominguez, R., 2011. Tropomyosin: the gatekeeper's view of the actin filament revealed. *Biophysical Journal*, 100(4), pp.797–798.

Donaudy, F. et al., 2003. Multiple Mutations ofMYO1A, a Cochlear-Expressed Gene, in Sensorineural Hearing Loss. *The American Journal of Human Genetics*, 72(6), pp.1571–1577.

Drazic, A. et al., 2016. The world of protein acetylation. *Biochimica et biophysica acta*, 1864(10), pp.1372–1401.

Drees, B. et al., 1995. Tropomyosin is essential in yeast, yet the TPM1 and TPM2 products perform distinct functions. *The Journal of cell biology*, 128(3), pp.383–392.

Dupin, I., Sakamoto, Y. & Etienne-Manneville, S., 2011. Cytoplasmic intermediate filaments mediate actin-driven positioning of the nucleus. *Journal of cell science*, 124(Pt 6), pp.865–872.

East, D.A. & Mulvihill, D.P., 2011. Regulation and function of the fission yeast myosins. *Journal of cell science*, 124(Pt 9), pp.1383–1390.

East, D.A. et al., 2011. Altering the stability of the Cdc8 overlap region modulates the ability of this tropomyosin to bind co-operatively to actin and regulate myosin. *The Biochemical journal*, 438(2), pp.265–273.

El-Mezgueldi, M. et al., 2002. The Kinetic Mechanism of Myo1e (Human Myosin-IC). *The Journal of biological chemistry*, 277(24), pp.21514–21521.

Evangelista, M., Zigmond, S. & Boone, C., 2003. Formins: signaling effectors for assembly and polarization of actin filaments. *Journal of cell science*, 116(Pt 13), pp.2603–2611.

Feeser, E.A. et al., 2010. Myo1e Binds Anionic Phospholipids with High Affinity. *Biochemistry*, 49(43), pp.9353–9360.

Fletcher, L. & Muschel, R.J., 2006. The centrosome and the DNA damage induced checkpoint. *Cancer letters*, 243(1), pp.1–8.

Forsburg, S., 1991. Cell Cycle Regulation In The Yeasts Saccharomyces Cerevisiae And Schizosaccharomyces-Pombe. *Annual Review of Cell and Developmental Biology*, 7(1), pp.227–256.

Forsburg, S.L. & Rhind, N., 2006. Basic methods for fission yeast. *Yeast (Chichester, England)*, 23(3), pp.173–183.

Fortune, N.S., Geeves, M.A. & Ranatunga, K.W., 1991. Tension responses to rapid pressure release in glycerinated rabbit muscle fibers. *Proceedings of the National Academy of Sciences of the United States of America*, 88(16), pp.7323–7327.

Frye, J., Klenchin, V.A. & Rayment, I., 2010a. Structure of the tropomyosin overlap complex from chicken smooth muscle: insight into the diversity of N-terminal recognition. *Biochemistry*, 49(23), pp.4908–4920.

Garcia, A., Zanic, M. & Howard, J., 2013. Microtubule catastrophe and rescue. *Current opinion in cell biology*, 25(1), pp.14–22.

Gautier, J. et al., 1988. Purified maturation-promoting factor contains the product of a Xenopus homolog of the fission yeast cell cycle control gene cdc2+. *Cell*, 54(3), pp.433–439.

Goins, L.M. & Mullins, R.D., 2015. A novel tropomyosin isoform functions at the mitotic spindle and Golgi in Drosophila. *Molecular biology of the cell*, 26(13), pp.2491–2504.

Goldring, J.P.D., 2015. Spectrophotometric methods to determine protein concentration. *Methods in molecular biology (Clifton, N.J.)*, 1312(Chapter 7), pp.41–47.

Goley, E.D. & Welch, M.D., 2006. The ARP2/3 complex: an actin nucleator comes of age. *Nature reviews. Molecular cell biology*, 7(10), pp.713–726.

Greenberg, M.J. & Ostap, E.M., 2013. Regulation and control of myosin-I by the motor and light chain-binding domains. *Trends in cell biology*, 23(2), pp.81–89.

Gross, M. & Jaenicke, R., 1994. Proteins under pressure. The influence of high hydrostatic pressure on structure, function and assembly of proteins and protein complexes. *European journal of biochemistry / FEBS*, 221(2), pp.617–630.

Gunning, P., O'Neill, G. & Hardeman, E., 2008. Tropomyosin-based regulation of the actin cytoskeleton in time and space. *Physiological reviews*, 88(1), pp.1–35.

Gunning, P.W., Ghoshdastider, U., et al., 2015. The evolution of compositionally and functionally distinct actin filaments. *Journal of cell science*, 128(11), pp.2009–2019.

Gunning, P.W., Hardeman, E.C., et al., 2015. Tropomyosin - master regulator of actin filament function in the cytoskeleton. *Journal of cell science*, 128(16), pp.2965–2974.

Hagan, I. & Nurse, P., 2016. *Fission Yeast*,

Hall, D.H. & Altun, Z.F., 2008. *C. Elegans Atlas*, CSHL Press.

Hall, D.H. & Treinin, M., 2011. How does morphology relate to function in sensory arbors? *Trends in Neurosciences*, 34(9), pp.443–451.

Hartman, M.A. & Spudich, J.A., 2012. The myosin superfamily at a glance. *Journal of cell science*, 125(Pt 7), pp.1627–1632.

Heissler, S.M. & Sellers, J.R., 2016. Various Themes of Myosin Regulation. *Journal of molecular biology*, 428(9), pp.1927–1946.

Hillson, N., Onuchic, J. & Garcia, A., 1999. Pressure-induced protein-folding/ unfolding kinetics. *Journal of theoretical biology*, pp.1–6.

Hitchcock-DeGregori, S.E., 2008. Tropomyosin: Function Follows Structure. In P. Gunning, ed. *Tropomyosin*. Advances in Experimental Medicine and Biology. New York, NY: Springer New York, pp. 60–72.

Hitchcock-DeGregori, S.E. & Heald, R.W., 1987. Altered actin and troponin binding of amino-terminal variants of chicken striated muscle alpha-tropomyosin expressed in Escherichia coli. *The Journal of biological chemistry*, 262(20), pp.9730–9735.

Hoffman, C.S., Wood, V. & Fantes, P.A., 2015. An Ancient Yeast for Young Geneticists: A Primer on the Schizosaccharomyces pombe Model System. *Genetics*, 201(2), pp.403–423.

Huang, J. et al., 2012. Residual body removal during spermatogenesis in C. elegans requires genes that mediate cell corpse clearance. *Development (Cambridge, England)*, 139(24), pp.4613–4622.

Hunt-Newbury, R. et al., 2007. High-throughput in vivo analysis of gene expression in Caenorhabditis elegans. J. Sulston, ed. *PLoS biology*, 5(9), p.e237.

Huttlin, E.L. et al., 2010. A tissue-specific atlas of mouse protein phosphorylation and expression. *Cell*, 143(7), pp.1174–1189.

Ichetovkin, I. et al., 2000. Actin filaments are severed by both native and recombinant dictyostelium cofilin but to different extents. *Cell motility and the cytoskeleton*, 45(4), pp.293–306.

Inglis, P.N. et al., 2007. The sensory cilia of Caenorhabditis elegans. *WormBook : the online review of C. elegans biology*, pp.1–22.

Ishii, A. et al., 2009. Human myelin proteome and comparative analysis with mouse myelin. *Proceedings of the National Academy of Sciences of the United States of America*, 106(34), pp.14605–14610.

Iwahashi, H., 2015. Pressure-Dependent Gene Activation in Yeast Cells. *Sub-cellular biochemistry*, 72(Chapter 20), pp.407–422.

Jampani, N.R. et al., 2012. Structural Analysis of Smooth Muscle Tropomyosin Alpha and Beta Isoforms. *Biophysical Journal*, 102(3), p.375a.

Jauregui, A.R. et al., 2008. The Caenorhabditis elegansnephrocystins act as global modifiers of cilium structure. *The Journal of cell biology*, 180(5), pp.973–988.

Johnson, L.N., 2009. The regulation of protein phosphorylation. *Biochemical Society transactions*, 37(Pt 4), pp.627–641.

Johnson, M. et al., 2010. Targeted amino-terminal acetylation of recombinant proteins in E. coli. *PloS one*, 5(12), p.e15801.

Johnson, M., East, D.A. & Mulvihill, D.P., 2014. Formins determine the functional properties of actin filaments in yeast. *Current biology : CB*, 24(13), pp.1525–1530.

Johnson, M., Geeves, M.A. & Mulvihill, D.P., 2013. Production of amino-terminally acetylated recombinant proteins in E. coli. *Methods in molecular biology (Clifton, N.J.)*, 981, pp.193–200.

Kelley, L.A. et al., 2015. The Phyre2 web portal for protein modeling, prediction and analysis. *Nature protocols*, 10(6), pp.845–858.

Kim, S.V. & Flavell, R.A., 2008. Myosin I: from yeast to human. *Cellular and molecular life sciences : CMLS*, 65(14), pp.2128–2137.

Kim, S.V. et al., 2006. Modulation of cell adhesion and motility in the immune system by Myo1f. *Science (New York, N.Y.)*, 314(5796), pp.136–139.

Kornblatt, J.A. & Kornblatt, M.J., 2002. The effects of osmotic and hydrostatic pressures on macromolecular systems. *Biochimica et biophysica acta*, 1595(1-2), pp.30–47.

Kramer, J.M. et al., 1990. The Caenorhabditis elegans rol-6 gene, which interacts with the sqt-1 collagen gene to determine organismal morphology, encodes a collagen. *Molecular and cellular biology*, 10(5), pp.2081–2089.

Krendel, M. & Mooseker, M.S., 2005. Myosins: tails (and heads) of functional diversity. *Physiology (Bethesda, Md.)*, 20, pp.239–251.

Krendel, M. et al., 2009. Disruption of Myosin 1e promotes podocyte injury. *Journal of the American Society of Nephrology : JASN*, 20(1), pp.86–94.

Krendel, M., Osterweil, E. & Mooseker, M., 2008. Myosin 1E interacts with synaptojanin-1 and dynamin via its SH3 domain. pp.1–16.

Kurahashi, H., Imai, Y. & Yamamoto, M., 2002. Tropomyosin is required for the cell fusion process during conjugation in fission yeast. *Genes to cells : devoted to molecular & cellular mechanisms*, 7(4), pp.375–384.

Lee, W.L., Bezanilla, M. & Pollard, T.D., 2000. Fission yeast myosin-I, Myo1p, stimulates actin assembly by Arp2/3 complex and shares functions with WASp. *The Journal of cell biology*, 151(4), pp.789–800.

Li, F. et al., 2011. A direct method for site-specific protein acetylation. *Angewandte Chemie (International ed. in English)*, 50(41), pp.9611–9614.

Li, J., Lu, Q. & Zhang, M., 2016. Structural Basis of Cargo Recognition by Unconventional Myosins in Cellular Trafficking. *Traffic (Copenhagen, Denmark)*.

Li, S. et al., 2010. Loss of post-translational modification sites in disease. *Pacific Symposium on Biocomputing. Pacific Symposium on Biocomputing*, pp.337–347.

Li, X.E. et al., 2014. Structure and flexibility of the tropomyosin overlap junction. *Biochemical and biophysical research communications*, 446(1), pp.304–308.

Lin, J.J.-C. et al., 2008. Human tropomyosin isoforms in the regulation of cytoskeleton functions. *Advances in experimental medicine and biology*, 644, pp.201–222.

Ljubetič, A. et al., 2016. Designing the structure and folding pathway of modular topological bionanostructures. *Chemical communications (Cambridge, England)*, 52(30), pp.5220–5229.

López-Otín, C. & Hunter, T., 2010. The regulatory crosstalk between kinases and proteases in cancer. *Nature reviews. Cancer*, 10(4), pp.278–292.

Mango, S.E., 2007. The C. elegans pharynx: a model for organogenesis. *WormBook : the online review of C. elegans biology*, pp.1–26.

Maravillas-Montero, J.L. et al., 2014. Myosin 1g regulates cytoskeleton plasticity, cell migration, exocytosis, and endocytosis in B lymphocytes. *European Journal of Immunology*, 44(3), pp.877–886.

Margie, O., Palmer, C. & Chin-Sang, I., 2013. C. elegans Chemotaxis Assay. *Journal of visualized experiments : JoVE*, (74), pp.1–6.

Markwardt, M.L. et al., 2011. An improved cerulean fluorescent protein with enhanced brightness and reduced reversible photoswitching. *PloS one*, 6(3), p.e17896.

Masters, T.A., Kendrick-Jones, J. & Buss, F., 2017. Myosins: Domain Organisation, Motor Properties, Physiological Roles and Cellular Functions. *Handbook of experimental pharmacology*, 235(24), pp.77–122.

May, R.C., 2001. The Arp2/3 complex: a central regulator of the actin cytoskeleton. *Cellular and molecular life sciences : CMLS*, 58(11), pp.1607–1626.

Mazzolini, R. et al., 2012. Brush border myosin Ia has tumor suppressor activity in the intestine. *Proceedings of the National Academy of Sciences of the United States of America*, 109(5), pp.1530–1535.

McCarter, J. et al., 1997. Soma-germ cell interactions in Caenorhabditis elegans: multiple events of hermaphrodite germline development require the somatic sheath and spermathecal lineages. *Developmental biology*, 181(2), pp.121–143.

McIntosh, B.B. & Ostap, E.M., 2016. Myosin-I molecular motors at a glance. *Journal of cell science*, 129(14), pp.2689–2695.

McKillop, D.F. & Geeves, M.A., 1993. Regulation of the interaction between actin and myosin subfragment 1: evidence for three states of the thin filament. *Biophysical Journal*, 65(2), pp.693–701.

Mele, C. et al., 2011. MYO1EMutations and Childhood Familial Focal Segmental Glomerulosclerosis. *New England Journal of Medicine*, 365(4), pp.295–306.

Menini, A., Hart, A.C. & Chao, M.Y., 2010. From Odors to Behaviors in Caenorhabditis elegans.

Moreno, S., Klar, A. & Nurse, P., 1991. Molecular genetic analysis of fission yeast Schizosaccharomyces pombe. *Methods in enzymology*, 194, pp.795–823.

Morgan, D.O., 2007. *The Cell Cycle*, New Science Press.

Mori, I., 1999. Genetics of Chemotaxis and Thermotaxis in the Nematode Caenorhabditis Elegans. *Annual Review of Genetics*, 33(1), pp.399–422.

Moser, M.J., Flory, M.R. & Davis, T.N., 1997. Calmodulin localizes to the spindle pole body of Schizosaccharomyces pombe and performs an essential function in chromosome segregation. *Journal of cell science*, 110 (Pt 15), pp.1805–1812.

Mostowy, S. & Cossart, P., 2012. Septins: the fourth component of the cytoskeleton. *Nature reviews. Molecular cell biology*, 13(3), pp.183–194.

Muller, J. et al., 2005. Sequence and comparative genomic analysis of actin-related proteins. *Molecular biology of the cell*, 16(12), pp.5736–5748.

Mullins, R.D., Heuser, J.A. & Pollard, T.D., 1998. The interaction of Arp2/3 complex with actin: nucleation, high affinity pointed end capping, and formation of branching networks of filaments. *Proceedings of the National Academy of Sciences of the United States of America*, 95(11), pp.6181–6186.

Mulvihill, D.P. & Hyams, J.S., 2003. Role of the two type II myosins, Myo2 and Myp2, in cytokinetic actomyosin ring formation and function in fission yeast. *Cell motility and the cytoskeleton*, 54(3), pp.208–216.

Muschiol, D., Schroeder, F. & Traunspurger, W., 2009. Life cycle and population growth rate of Caenorhabditis elegans studied by a new method. *BMC ecology*, 9(1), p.14.

Nakano, K. & Mabuchi, I., 2006. Actin-depolymerizing protein Adf1 is required for formation and maintenance of the contractile ring during cytokinesis in fission yeast. *Molecular biology of the cell*, 17(4), pp.1933–1945.

Nambiar, R., McConnell, R.E. & Tyska, M.J., 2009. Control of cell membrane tension by myosin-I. *Proceedings of the National Academy of Sciences of the United States of America*, 106(29), pp.11972–11977.

Newman, A.P., White, J.G. & Sternberg, P.W., 1996. Morphogenesis of the C. elegans hermaphrodite uterus. *Development (Cambridge, England)*, 122(11), pp.3617–3626.

Nitanai, Y. et al., 2007. Crystal structures of tropomyosin: flexible coiled-coil. *Advances in experimental medicine and biology*, 592(Chapter 13), pp.137–151.

Oda, T. et al., 2009. The nature of the globular- to fibrous-actin transition. *Nature*, 457(7228), pp.441–445.

Odronitz, F. & Kollmar, M., 2007. Drawing the tree of eukaryotic life based on the analysis of 2,269 manually annotated myosins from 328 species. *Genome biology*, 8(9), p.R196.

Palm, T., Greenfield, N.J. & Hitchcock-DeGregori, S.E., 2003. Tropomyosin ends determine the stability and functionality of overlap and troponin T complexes. *Biophysical Journal*, 84(5), pp.3181–3189.

Paul, A.S. et al., 2008. The role of the FH1 domain and profilin in formin-mediated actin-filament elongation and nucleation. *Current biology : CB*, 18(1), pp.9–19.

Pfaendtner, J., La Cruz, De, E.M. & Voth, G.A., 2010. Actin filament remodeling by actin depolymerization factor/cofilin. *Proceedings of the National Academy of Sciences of the United States of America*, 107(16), pp.7299–7304.

Pollard, T., 1991. Myosin-I. *Annual Review of Physiology*, 53(1), pp.653–681.

Pollard, T.D., 1986. Assembly and dynamics of the actin filament system in nonmuscle cells. *Journal of cellular biochemistry*, 31(2), pp.87–95.

Pollard, T.D. et al., 1973. Acanthamoeba myosin. I. Isolation from Acanthamoeba castellanii of an enzyme similar to muscle myosin. *The Journal of biological chemistry*, 248(13), pp.4682–4690.

Portet, S., 2013. Dynamics of in vitro intermediate filament length distributions. *Journal of theoretical biology*, 332, pp.20–29.

Purves, W.K. et al., 2003. *Life: The Science of Biology: Volume IV*, Macmillan.

Rao, V.S., Marongelli, E.N. & Guilford, W.H., 2009. Phosphorylation of tropomyosin extends cooperative binding of myosin beyond a single regulatory unit. *Cell motility and the cytoskeleton*, 66(1), pp.10–23.

Rath, O. & Kozielski, F., 2012. Kinesins and cancer. *Nature reviews. Cancer*, 12(8), pp.527–539.

Riddle, D.L., 1997. *C. Elegans II*, Firefly Books.

Roche, J. et al., 2013. Impact of hydrostatic pressure on an intrinsically disordered protein: a high-pressure NMR study of α-synuclein. *Chembiochem : a European journal of chemical biology*, 14(14), pp.1754–1761.

Sahota, V.K. et al., 2009. Troponin I and Tropomyosin regulate chromosomal stability and cell polarity. *Journal of cell science*, 122(Pt 15), pp.2623–2631.

Salas-Cortes, L. et al., 2005. Myosin Ib modulates the morphology and the protein transport within multi-vesicular sorting endosomes. *Journal of cell science*, 118(Pt 20), pp.4823–4832.

San Martín, M.F., Barbosa-Cánovas, G.V. & Swanson, B.G., 2002. Food processing by high hydrostatic pressure. *Critical reviews in food science and nutrition*, 42(6), pp.627–645.

Sanders, J. et al., 2013. The Caenorhabditis elegans interneuron ALA is (also) a high-threshold mechanosensor. *BMC Neuroscience*, 14(1), p.156.

Sato, M. et al., 1996. Schizosaccharomyces pombe is more sensitive to pressure stress than Saccharomyces cerevisiae. *Cell structure and function*, 21(3), pp.167–174.

Sawin, K.E., 2002. Cell polarity: following formin function. *Current biology : CB*, 12(1), pp.R6–8.

Sawin, K.E. & Tran, P.T., 2006. Cytoplasmic microtubule organization in fission yeast. *Yeast (Chichester, England)*, 23(13), pp.1001–1014.

Schafer, W., 2016. Nematode nervous systems. *Current Biology*, 26(20), pp.R955–R959.

Schevzov, G. et al., 2014. Tropomyosin isoforms and reagents. *Bioarchitecture*, 1(4), pp.135–164.

Schulenburg, H. & Ewbank, J.J., 2007. The genetics of pathogen avoidance in Caenorhabditis elegans. *Molecular microbiology*, 66(3), pp.563–570.

Sellers, J.R., 2000. Myosins: a diverse superfamily. *Biochimica et biophysica acta*, 1496(1), pp.3–22.

Senda, S. et al., 2001. Recruitment of a Specific Amoeboid Myosin I Isoform to the Plasma Membrane in Chemotactic DictyosteliumCells. *The Journal of biological chemistry*, 276(4), pp.2898–2904.

Siddiqui, S.S. & Culotti, J.G., 2007. Examination of neurons in wild type and mutants of Caenorhabditis elegans using antibodies to horseradish peroxidase. *Journal of neurogenetics*, 21(4), pp.271–289.

Sieburth, D. et al., 2005. Systematic analysis of genes required for synapse structure and function. *Nature*, 436(7050), pp.510–517.

Sielski, N.L. et al., 2014. Tissue specific expression of myosin IC isoforms. *BMC cell biology*, 15(1), p.8.

Silva, J.L. et al., 2009. Ligand Binding and Hydration in Protein Misfolding: Insights from Studies of Prion and p53 Tumor Suppressor Proteins†. *Accounts of Chemical Research*, 43(2), pp.271–279.

Skoumpla, K. et al., 2007. Acetylation regulates tropomyosin function in the fission yeast Schizosaccharomyces pombe. *Journal of cell science*, 120(Pt 9), pp.1635–1645.

Sloboda, R.D., 2015. Isolation and analysis of microtubules and associated proteins. *Cold Spring Harbor Protocols*, 2015(2), pp.152–154.

Smith, J.A., 1982. The cell cycle and related concepts in cell proliferation. *The Journal of pathology*, 136(2), pp.149–166.

Snaith, H.A. et al., 2010. New and Old Reagents for Fluorescent Protein Tagging of Microtubules in Fission Yeast. In *Microtubules: in vivo*. Methods in Cell Biology. Elsevier, pp. 147–172.

Spang, A. et al., 2015. Complex archaea that bridge the gap between prokaryotes and eukaryotes. *Nature*, 521(7551), pp.173–179.

Staib, P. & Morschhauser, J., 2007. Chlamydospore formation in Candida albicans and Candida dubliniensis--an enigmatic developmental programme. *Mycoses*, 50(1), pp.1–12.

Starheim, K.K., Gevaert, K. & Arnesen, T., 2012. Protein N-terminal acetyltransferases: when the start matters. *Trends in biochemical sciences*, 37(4), pp.152–161.

Stewart, A. & Phillips, P., 2002. Selection and Maintenance of Androdioecy in Caenorhabditis elegans. *Genetics*, pp.1–8.

Stiernagle, T., 2006. Maintenance of C. elegans. *WormBook : the online review of C. elegans biology*, pp.1–11.

Sudbery, P.E., 2011. Growth of Candida albicans hyphae. *Nature Reviews Microbiology*, 9(10), pp.737–748.

Suter, D.M., 2010. *Functions of Myosin Motor Proteins in the Nervous System*, New York, NY: Springer New York.

Syamaladevi, D.P., Spudich, J.A. & Sowdhamini, R., 2012. Structural and functional insights on the Myosin superfamily. *Bioinformatics and biology insights*, 6, pp.11–21.

Tassopoulou-Fishell, M. et al., 2012. Genetic variation in myosin 1H contributes to mandibular prognathism. *American journal of orthodontics and dentofacial orthopedics : official publication of the American Association of Orthodontists, its constituent societies, and the American Board of Orthodontics*, 141(1), pp.51–59.

Timmermann, S. et al., 2001. Histone acetylation and disease. *Cellular and molecular life sciences : CMLS*, 58(5-6), pp.728–736.

Toya, M. et al., 2001. Identification and functional analysis of the gene for type I myosin in fission yeast. *Genes to cells : devoted to molecular & cellular mechanisms*, 6(3), pp.187–199.

Tsien, R.Y., 1998. THE GREEN FLUORESCENT PROTEIN. *Annual review of biochemistry*, 67(1), pp.509–544.

Tyanova, S. et al., 2013. Phosphorylation variation during the cell cycle scales with structural propensities of proteins. *PLoS computational biology*, 9(1), p.e1002842.

Vrhovski, B., Thézé, N. & Thiébaud, P., 2008. Structure and evolution of tropomyosin genes. *Advances in experimental medicine and biology*, 644, pp.6–26.

Walklate, J., Ujfalusi, Z. & Geeves, M.A., 2016. Myosin isoforms and the mechanochemical cross-bridge cycle. *The Journal of experimental biology*, 219(Pt 2), pp.168–174.

Wang, Y. et al., 2014. EKPD: a hierarchical database of eukaryotic protein kinases and protein phosphatases. *Nucleic acids research*, 42(Database issue), pp.D496–502.

Wang, Y.-C., Peterson, S.E. & Loring, J.F., 2013. Protein post-translational modifications and regulation of pluripotency in human stem cells. *Cell Research*, 24(2), pp.143–160.

Ward, S. et al., 1975. Electron microscopical reconstruction of the anterior sensory anatomy of the nematode Caenorhabditis elegans.?2UU. *The Journal of Comparative Neurology*, 160(3), pp.313–337.

Whiteway, M. & Bachewich, C., 2007. Morphogenesis in Candida albicans. *Annual Review of Microbiology*, 61(1), pp.529–553.

Williams, G.H. & Stoeber, K., 2012. The cell cycle and cancer. *The Journal of pathology*, 226(2), pp.352–364.

Winter, R., 2015. Pressure Effects on Artificial and Cellular Membranes. *Sub-cellular biochemistry*, 72(Chapter 17), pp.345–370.

Wirshing, A.C., 2017. Myosin activity drives actomyosin bundle formation and organization in contractile cells of the C. elegans spermatheca. pp.1–31.

Woese, C.R. & Fox, G.E., 1977. Phylogenetic structure of the prokaryotic domain: the primary kingdoms. *Proceedings of the National Academy of Sciences of the United States of America*, 74(11), pp.5088–5090.

Wolfe, B.A. et al., 2006. Phospho-Regulation of the Cdc14/Clp1 Phosphatase Delays Late Mitotic Events in S. pombe. *Developmental Cell*, 11(3), pp.423–430.

Wood, V. et al., 2002. The genome sequence of Schizosaccharomyces pombe. *Nature*, 415(6874), pp.871–880.

Yamazaki, R. et al., 2016. Knockdown of Unconventional Myosin ID Expression Induced Morphological Change in Oligodendrocytes. *ASN neuro*, 8(5).

Zadro, C. et al., 2009. Are MYO1C and MYO1F associated with hearing loss? *Biochimica et biophysica acta*, 1792(1), pp.27–32.

Zonia, L. & Munnik, T., 2007. Life under pressure: hydrostatic pressure in cell growth and function. *Trends in plant science*, 12(3), pp.90–97.

Zuryn, S. & Jarriault, S., 2013. Deep sequencing strategies for mapping and identifying mutations from genetic screens. *Worm*, 2(3), p.e25081.

Appendix: Publications from this thesis